TECHNIQUES FOR HOMODYNE DECHIRP-ON-RECEIVE LINEARLY FREQUENCY MODULATED RADAR

Robert J. C. Middleton

A Thesis Submitted for the Degree of PhD
at the
University of St Andrews

2011

Techniques for Homodyne Dechirp-on-Receive Linearly Frequency Modulated Radar

R J C Middleton

Thesis submitted for the degree of Doctor of Philosophy of the University of St Andrews

October, 2010

Abstract

This thesis presents work done to extend and improve the operation of homodyne dechirp-on-receive linearly frequency modulated radars.

First, an investigation of the effect of common phase errors on the point response function of the radar is described. The dependence on the window function of the degradation due to phase errors is investigated, and a simple, precise, and general approach for calculating the degraded Point Spread Function (PSF) is described and demonstrated. This method is shown to be particularly useful when investigating the effect of chirp nonlinearity on the PSF.

Next, a method for focussing range profiles that are degraded by chirp nonlinearity is described. This method is based on two established methods, the Phase Gradient Algorithm (PGA) and a time-domain re-sampling technique. The technique is entirely hardware independent, allowing any homodyne dechirp-on-receive linearly frequency modulated radar to be focussed. Where suitable archive signal data exists, focussed imagery can even be produced from radars that no longer exist. The complete algorithm and details of the implementation are described, and the technique is demonstrated on three representative radar cases: extreme chirp nonlinearity, typical chirp nonlinearity, and a retrospective case. In all of the cases, it was shown that the PSF was dramatically improved.

A technique based on down conversion by aliasing for reducing the required sampling rate is described, and a simple technique for calculating suitable sampling rates is presented. This method is demonstrated for a typical application in which sampling rate reduction might be required, namely Moving Target Indication (MTI). The MTI application is described and quantified, including a simple technique for choosing suitable radar operation parameters. The MTI technique with subsampling was demonstrated in software simulations and in a simple radar experiment.

A Synthetic Aperture Radar (SAR) test bench for researching component performance and scatterer properties in the context of SAR was developed. An appropriate image formation processing algorithm was found and modified to better suit the task of a short data collection baseline and drifting centre frequencies, both of which are present in the test bench situation. Software was written to collect data, to control the hardware, and to process the signals into SAR images. A data simulator was written to test the image formation algorithm implementation; it also served as a useful tool for investigating the effect of signal errors on the quality of the resultant SAR imagery. A suitable oscillator was chosen for the task, based on phase noise and centre frequency stability considerations, both of which are quantified and discussed. Preliminary SAR imagery was produced, indicating that the system operates correctly and in agreement with comparable systems.

Declarations

Candidate's declaration

I, R J C Middleton, hereby certify that this thesis, which is approximately 44,000 words in length, has been written by me, that it is the record of work carried out by me and that it has not been submitted in any previous application for a higher degree.

I was admitted as a research student in September, 2006 and as a candidate for the degree of PhD in September, 2007; the higher study for which this is a record was carried out in the University of St Andrews between 2006 and 2010.

Date: December 19, 2010

Signature of candidate:

R J C Middleton

Supervisor's declaration

I hereby certify that the candidate has fulfilled the conditions of the Resolution and Regulations appropriate for the degree of PhD in the University of St Andrews and that the candidate is qualified to submit this thesis in application for that degree.

Date: December 19, 2010

Signature of supervisor:

Dr D A Robertson

Signature of supervisor:

Dr G M Smith

Permission for electronic publication

In submitting this thesis to the University of St Andrews I understand that I am giving permission for it to be made available for use in accordance with the regulations of the University Library for the time being in force, subject to any copyright vested in the work not being affected thereby. I also understand that the title and the abstract will be published, and that a copy of the work may be made and supplied to any bona fide library or research worker, that my thesis will be electronically accessible for personal or research use unless exempt by award of an embargo as requested below, and that the library has the right to migrate my thesis into new electronic forms as required to ensure continued access to the thesis. I have obtained any third-party copyright permissions that may be required in order to allow such access and migration, or have requested the appropriate embargo below.

The following is an agreed request by candidate and supervisor regarding the electronic publication of this thesis:

Embargo on both the printed copy and electronic copy for the same fixed period of two years on the following grounds: publication would preclude future publication.

Date: December 19, 2010

Signature of candidate:

R J C Middleton

Signature of supervisor:

Dr D A Robertson

Signature of supervisor:

Dr G M Smith

Acknowledgments

I would like to thank the following people for their help and support during the research and writing of this PhD thesis:

My primary supervisor, Dr Duncan Robertson, for helping to make this PhD educational, interesting, and enjoyable. I would also like to thank Duncan for his advice during the preparation of this thesis and for proofreading the typescript.

My secondary supervisor, Dr Graham Smith, for his encouragement and excellent academic, financial, and technical support.

Dr David Macfarlane for many helpful and interesting technical discussions and practical help with many of the radar experiments.

Dr David Bolton for many interesting technical discussions and helpful electronics advice.

Alan Blake of QinetiQ, Great Malvern, for proofreading the Synthetic Aperture Radar chapter.

Tom Gallacher and Peter Speirs for their willing and skillful assistance in many of the experiments.

Dr Paul Cruickshank and Dr Robert Hunter for their helpful advice.

Scott Johnston, Steven Balfour, David Steven, Callum Smith, Mark Robertson, Mark Ross, and Chris Booth for providing expert advice and help with the fabrication of the mechanical and electronic aspects of the research.

My family for their support during the last three and a half years, and Elizabeth Thomsen for many interesting non-technical discussions.

Robert Middleton
Nottinghamshire
October, 2010

Publications

The following publications are based on the research presented in this thesis:

> ‘Predicting range point response from chirp nonlinearity’ was presented at the Radar 2008 International Radar Conference in Adelaide, Australia.
>
> ‘Range autofocus for linearly frequency modulated continuous wave radar’ has been accepted for publication in the IET Radar, Sonar, and Navigation journal.
>
> ‘High range resolution moving target indication at long stand-off ranges using minimal sampling rates in linear FMCW radar’ was presented as an Invited Keynote paper at the 2010 IRMMW-THz International Conference in Rome, Italy.

Acronyms

AM	Amplitude Modulation
AVTIS	All-weather Volcano Topography Imaging Sensor
BPA	Back Projection Algorithm
BPF	Band Pass Filter
dc	direct current (or 0 Hz)
DDS	Direct Digital Synthesizer
FBPA	Factorized Back Projection Algorithm
FCP	Fourier Cross Processing
FFT	Fast Fourier Transform
FMCW	Frequency Modulated Continuous Wave
FOD	Foreign Object Debris
FoPen	Foliage Penetrating
FWHM	Full Width Half Maximum
GPS	Global Positioning System
IF	Intermediate Frequency
IMPATT	IMPact ionization Avalanche Transit Time
LMS	Least Mean Squares
LPI	Low Probability of Intercept
LO	Local Oscillator
MTI	Moving Target Indication
PFA	Polar Format Algorithm
PGA	Phase Gradient Algorithm
PM	Phase Modulation
PMYTO	Permanent YIG Tuned Oscillator
PPI	Plan Position Indicator
PPP	Prominent Point Processing
PSD	Power Spectral Density
PSF	Point Spread Function

QPE	Quadratic Phase Error
RCS	Radar Cross Section
RF	Radio Frequency
RMA	Range Migration Algorithm
RMS	Root Mean Square
RVP	Residual Video Phase
SAR	Synthetic Aperture Radar
SAW	Surface Acoustic Wave
SNR	Signal to Noise Ratio
STALO	STable Local Oscillator
TTL	Transistor Transistor Logic
VCO	Voltage Controlled Oscillator
YIG	Yttrium Iron Garnet

List of Figures

List of Tables

Contents

Chapter 1

Introduction

1.1 Homodyne Dechirp-on-Receive Linearly Frequency Modulated Radar

This thesis is concerned with simple signal processing and parameter selection techniques to expand and improve the operation of a particular kind of radar: Homodyne Dechirp-on-Receive Linearly Frequency Modulated radar.

This kind of radar measures the range and size of objects by transmitting a linearly frequency-swept ('chirped') signal towards the scene. The echoes that are reflected back to the radar are received and down converted against the transmitting signal. The duration of the sweep is chosen to be much longer than the round-trip time to the scene, so the transmitting signal and its echoes from the scene more-or-less completely overlap.

Because the frequency profile of the signal is linear, the difference between the frequency of the transmitted signal and that of an echo is just the product of the round-trip time and the frequency sweep rate. So the frequency of each down-converted echo is constant and proportional to the range of the object that reflected that echo. If more than one scatterer is present, the received signal is the superposition of the echoes, and the down-converted signal is the superposition of down-converted echoes. The amplitude of each echo is proportional to the square root of the Radar Cross Section (RCS) of the scatterer that reflected it.

Fourier transforming the down-converted (or 'de-chirped') signal gives the radar range profile of the scene, i.e. a plot of reflected energy versus range.

It is worth noting that this kind of radar is often realized as a continu-

ous wave radar, i.e. one that permanently transmits radiation with a constant amplitude. This type of radar is commonly called Frequency Modulated Continuous Wave (FMCW) radar. Strictly, this thesis is not limited to continuous wave operation but *is* limited to Homodyne Dechirp-on-Receive Linearly Frequency Modulated radar. However, in most cases, this is what is implied by the name FMCW, and this is how they are often referred to in papers and text books. Accordingly, from here on I shall call them FMCW radars.

FMCW radars have some attractive features:

1. frequency of operation: they can operate at any frequency, including very high frequencies, where it is difficult to build other types of radar. For example, FMCW radars commonly operate at mm-wave and sub mm-wave frequencies, e.g. 94 GHz [1] and 670 GHz [2]. High frequencies are desirable because they offer narrow beam widths and fine cross-range resolution from relatively small antennas. Similarly, if large swept bandwidths are required for fine resolution, these are achieved more easily at higher carrier frequencies (1% relative bandwidth at W-band versus 10% relative bandwidth at X-band). Also, some applications inherently require high frequencies, e.g. cloud profiling, in which the size of water droplets and Mie scattering require that the radiation have mm wavelength [3].

2. in FMCW radars, the bulk of the signal processing is done in analogue hardware, so a very high swept bandwidth signal (i.e. very fine range resolution radar) can be achieved with moderate sampling requirements and digital signal processing. This is because only the IF signal need be unambiguously sampled and the IF signal frequency is not necessarily very high;

3. because the range resolution is determined by the bandwidth and not by the duration of the signal, large time-bandwidth products can be achieved. The Signal to Noise Ratio (SNR) of the compressed signal is proportional to the time-bandwidth product, so FMCW radar (like any other high time-bandwidth product radar) can have a very high SNR, a feature common to matched filter range compression techniques;

4. the range compression and the associated processing gain allow very long, very weak signals to be transmitted. This has several important and desirable consequences:

(a) low-power, low-voltage, light-weight, robust and stable solid-state components can be used;

(b) the solid-state components offer relatively low-power operation and operate at room temperature so do not need cooling. The power supply requirements are relatively modest (often a car battery is sufficient to run the radar and the signal processing for many hours on end). Low supply voltage and power are also an important safety feature for people working on and around the radars;

(c) low transmit power also has advantages where it is undesirable to interact with other electronic systems. These might be control and communications systems, or they might be the detector systems of an opponent in a military application, i.e. FMCW can confer a Low Probability of Intercept (LPI) [4];

5. FMCW radar can operate with very close scenes, in some cases as close as the antenna. This is useful for close-range operation, e.g. in mining [5, 6], where short-range visibility might be obscured by dust; automotive parking assistant radars [7, 8] operate at 24 GHz and must be able to range objects as close as tens of centimetres; Silo depth gauges (effectively short range altimeters), which also operate at 24 GHz, must also be able to range very close objects.

Of course, this type of radar has disadvantages, too:

1. even subtle imperfections in the linearity of the frequency sweep can introduce large phase errors in the dechirped signal that scale with range. This is often the factor that limits the valid range of operation of FMCW radars [9–12];

2. because the IF frequency of an echo is the product of the frequency sweep rate and the round-trip time to the scatterer, the IF signals in fine resolution, long standoff range situations can become problematic, placing demanding requirements on the digital sampling and signal processing;

3. the linear frequency modulation translates range into IF frequency, but relative motion between the radar and a scatterer introduces a Doppler

frequency into the IF signal of that scatterer. This Doppler shift is indistinguishable from the frequency due to range offset, making the response to the scatterer ambiguous in range and radial speed;

4. the sweep length must be long compared to the round-trip time of the farthest scatterer to be imaged;

5. because the radar simultaneously transmits and receives signals, the two signals must be separated if the receiver is not to be damaged or desensitized by an apparently very large scatterer at very close range.

1.2 mm-Wave radar

The work discussed in this thesis is not particular to any frequency. In fact, it could equally well be applied to sonar, which is the acoustic equivalent of radar. However, because FMCW radar is capable of operating at very high carrier frequencies and with very large swept bandwidths (which often implies high carrier frequency), FMCW systems are often found being used at high frequencies, e.g. 94 GHz.

In certain applications, high-frequency signals also have some inherent advantages over lower frequency ones:

1. they provide narrow beams from relatively small antennas, giving fine cross-range resolution from compact radar systems;

2. large absolute bandwidths are available, giving fine range resolution;

3. reasonable range resolution can be obtained with radiation that can pass relatively unhindered though dust and fog that would obscure an optical system [6, 13];

4. high-frequency regions of the spectrum are reasonably uncluttered by communications systems and other radars (at the moment). Also, the atmospheric attenuation of the radiation can limit the range at which the radar beam will pose an interference problem or be intercepted;

5. there is an extensive range of components, equipment and expertise available at certain high frequencies for historical, scientific (particularly astronomy and spectroscopy), and commercial reasons [1].

1.3 Examples of mm-wave homodyne dechirp-on-receive linearly frequency modulated continuous wave radars

mm-Waves have long been used for fine-resolution compact radar operation and are becoming increasingly popular. Some typical and emerging applications of mm-wave FMCW radar include:

1. aeronautical: radars providing landing guidance in zero visibility conditions, e.g. BAE's Autonomous Landing Guide [14] and [15–17], and those providing vision in very dusty 'brownout' conditions that occur when helicopters land in dusty conditions [18, 19];

2. industrial: use of mm-wave radars to see through dust to mining workfaces [6];

3. scientific: mapping of volcano topography [13], mapping of icefields [20–22];

4. meteorological: measuring weather systems [23];

5. military and security: detecting concealed weapons [24–26], detecting buried explosives [27], ordnance guidance (e.g. Raytheon and Boeing's Joint Air To Ground Missile), and battlefield surveillance [28, 29];

6. automotive: cruise control, collision avoidance, and parking assistants [7, 8, 30–34].

To illustrate the diversity of the types and applications of mm-wave FMCW radar, I shall discuss three distinct and important examples in the following subsections.

1.3.1 A small, inexpensive, mass-produced, robust, low-power, and reliable radar with good resolution for 0 to 200 m ranges for automotive applications

Automotive radar is a good example of a mass-produced, low-power, robust, short-range, homodyne FMCW radar. They are produced cheaply, typically US$50 each, and have many of the components integrated into a single device

[7, 35, 36]. A typical miniature radar integrated into a single circuit is shown in Figure 1.1.

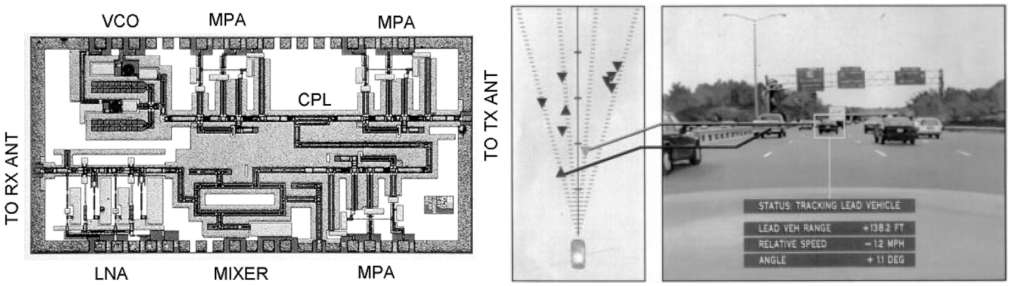

Figure 1.1: A compact monolithic radar, such as those used for automotive radar, and a representation of the typical output information. Reproduced from [35] and [7] respectively.

This type of radar is highly specialized, performing a particular task to produce particular information. This degree of specialization allows low-cost production of very reliable devices.

1.3.2 A high-performance, highly portable scientific instrument for monitoring volcano lava domes

A millimeter-wave terrain-mapping radar, the All-weather Volcano Topography Imaging Sensor (AVTIS) [10, 13], was designed and built to produce three-dimensional imagery of volcano lava domes [37]. mm-Wave FMCW radars are ideal for this application because they offer low power requirements and 10 m cross-range resolution at 1 km long standoff ranges with a compact antenna (30 cm diameter).

mm-Waves also penetrate cloud and dust sufficiently well to image the lava domes of volcanoes, something that visible light cannot do. Additionally, the mm-wave front end can be switched into a passive radiometer mode in order to perform thermal measurements, which are important for volcano imaging [38]. The mm-wave FMCW radar allows the system to be extremely portable and to be able to operate for long periods of time (i.e. days) on portable low-voltage batteries. The compact system and a typical image are shown in Figure 1.2.

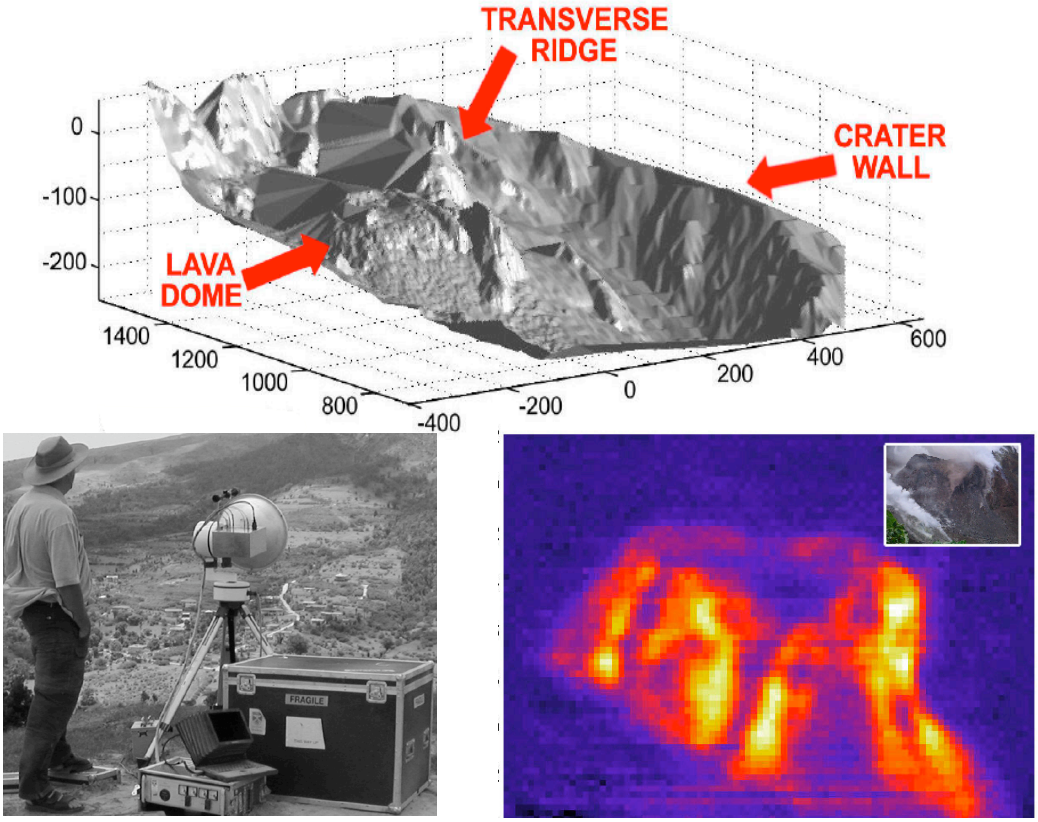

Figure 1.2: The AVTIS radar, power supply, and signal processors with operator on a hilltop overlooking a volcano in Montserrat, West Indies. A topographic image is shown and a thermal image (with corresponding photograph) is shown digitally 'draped' over a digital elevation model produced by AVTIS. The equipment photograph is reproduced from [39], the imagery is reproduced from [38].

1.3.3 A high-performance, aviation-safe, production radar for monitoring debris on airport runways

On the 25th of July 2000 a 3 cm × 43 cm piece of titanium debris from a DC 10 aeroplane punctured the tyre of Air France Concorde Flight 4590, causing a piece of rubber to damage the number-five fuel tank, ultimately causing the aeroplane to crash, which in turn killed all 109 people on board and four people on the ground.

In response to the danger presented by Foreign Object Debris (FOD) on the runway, QinetiQ (formerly DERA) developed the Tarsier radar as a means of automatically and rigorously inspecting runways.

The requirements of the radar are very fine resolution, very high sensitivity,

and low transmit power: an M12 bolt head must be detectable at 1 km standoff range [40], and the signal must not interfere with the communications and control systems found in the aeroplanes and airport infrastructure. In practice, the imagery is good as far as 2 km from the radar.

The mm-wave FMCW radars, which stand on tall towers, shown in Figure 1.3, provide 0.2° fan beams with 0.25 m range resolution. The dual-antenna (one for transmitting and one for receiving) radars are rotated at $3°s^{-1}$ to provide up to 360° field of view. Examples of the kind of imagery produced are shown in Figure 1.4.

Figure 1.3: The tarsier radar on a tower at an airport. Reproduced from [41].

A custom network of radars is set up to cover all the required runway surfaces, and automatic change detection and object identification software

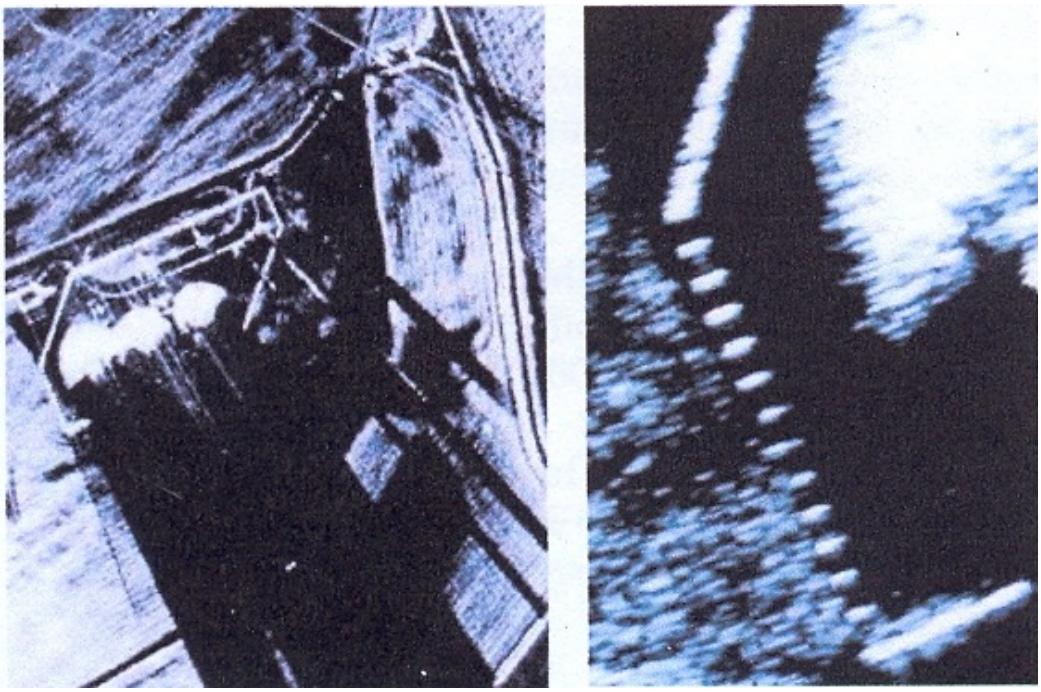

Figure 1.4: Typical imagery produced by Tarsier. Reproduced from [40].

monitors live images, which are updated about once every minute. If an object is found, a human user is alerted who then uses optical cameras to investigate further. If required, a FOD collection team is deployed to clear the debris from the runway at a GPS location provided by the Tarsier system.

This automated approach replaces a manual visual inspection performed by driving up the runway once every four hours. During the manual search, aeroplanes cannot use the runway, which is clearly a problem for busy airports like London's Heathrow.

Tarsier is an exemplary high-performance mm-wave FMCW radar, exhibiting excellent linearity, excellent noise performance, and, consequently, excellent sensitivity as far as 2 km from the radar.

1.4 Areas of research presented in this thesis

In this section, I shall discuss the particular areas that I have studied and the research that I shall present in the remainder of this thesis, outlining the problems, the work already done, and the approaches I have taken in solving

them.

1.4.1 Understanding allowable signal errors

When designing new radars to meet some specification or evaluating the suitability of an existing radar or component for some purpose, it is necessary to be able to connect the performance of the radar to the properties of the hardware and signal processing. Perhaps the single most important metric of a radar's performance is its Point Spread Function (PSF). The PSF is the range profile of a single point-like scatterer and is a function of scatterer range.

The PSF contains information about the sensitivity of the radar, its resolution, its dynamic range, and its geometric accuracy (where the response appears in the range profile compared to where it was in space). It can be measured using a test range with very low clutter and a point-like reference reflector. Alternatively it can be measured using a delay line of the appropriate length (which can be difficult if long-range operation is required).

However, it is not always possible to test a radar: it might not exist to be tested if it is in the design stage, or it might be impossible to test without difficult and expensive experiments (e.g. long range, satellite-borne radar). It is very useful to be able to predict the performance of the radar from the components and, conversely, to be able derive the required component specifications from the required performance.

One of the most significant factors degrading the shape of the PSF, especially the dynamic range, is phase and amplitude noise. The effect of these signal imperfections on the PSF has been studied, and using modulation theory Stove [11] presents a precise connection between phase (represented as frequency) and amplitude noise and the degraded PSF. This connection is essentially a relationship between the Power Spectral Density (PSD) of the noise process and the resultant sidebands in the PSF.

Amplitude and phase noise are typically broadband random processes. In addition to these, there is also low-order deterministic Phase Modulation (PM) and Amplitude Modulation (AM). These mostly result in defocussing, distortion, displacement and desensitization of the PSF. Perez-Martinez et al. [42] consider the effects of PM due to group delay and conclude that, while the errors are small by current standards, they may be problematic in the next generation of radars. However, although phase errors due to group delay are generally small, phase errors due to nonlinearity in the chirp are not. Estimat-

ing and removing the nonlinearity, or compensating for its effects, is a very important aspect of the FMCW radar design process and forms a large part of the work described in this thesis.

It is useful to know what phase errors and amplitude errors can be tolerated in a system. Although work has been done to make mathematical connections between models of the low-order deterministic phase and amplitude errors and their effects on the PSF [43–45], the connections are often complicated to implement, and their description of the effect on the PSF is sometimes hard to understand and not always complete.

In order to gain a practical understanding of the effects of AM and PM on the point response, I numerically simulated FMCW radar signal processing for various different combinations and degrees of error. This is discussed in Chapter 3, where I also repeated these tests with different window functions. The results show that there is a wide variety in the effect of any given error on the PSF depending on the type of window function. But the resulting catalogue of results indicates the allowable limits on low-order phase and amplitude errors. This indicates the usefulness of both the exact, direct numerical simulation (which can accommodate arbitrary signal defects and window weighting functions) and the resulting catalogue, each providing a useful design tool.

It is also useful to have a parametric model (e.g. for fitting to data) of the ideal PSF resulting from a given window function. Such a model is developed for all window functions built from sums of cosine functions, which includes Hamming, Hann, Blackman-Harris, Flat-top, and several others.

1.4.2 Chirp nonlinearity: estimation and correction

For radars with Voltage Controlled Oscillator (VCO) based signal generation schemes, the most significant source of phase errors in the dechirped signal is nonlinearity in the chirp. This is usually because the oscillator providing the radar signal is chirped through the required bandwidth by a modulated control voltage that determines the natural oscillation of a physical system, e.g. a Gunn diode. However, the relationship between the applied control voltage and the resultant frequency is not necessarily a linear one. Additionally, if the system is being swept very rapidly, e.g. one chirp every 50 μs, the frequency response of the driver circuit and oscillator system may distort the ramp.

The effects of chirp nonlinearity are exactly those of any kind of PM, with the added feature that the PM due to chirp nonlinearity increases as the range

to the scatterer increases.

Work has been done to characterize the effects of chirp nonlinearity on the PSF. Piper [46] derives the effect of sinusoidal nonlinearities on the range resolution, and Scheiblhofer [47] derives the bias and variation of the peak of the PSF due to a general frequency nonlinearity. Another method [48] also yields an estimate of the range error and the image phase error from an estimate of the frequency nonlinearity. These are very useful and valuable techniques, but they do not tell us about the actual shape of the PSF, which is important to know: it is convolved with the underlying scene structure to give the radar image.

In Chapter 3, I shall describe a simple and intuitive technique analogous to the ambiguity diagram (the PSF plotted against Doppler shift [49]) that provides a rich and precise calculation of the PSF without approximation. The technique is to simulate the FMCW radar signal processing at all offset ranges of interest. This direct simulation method can accommodate arbitrary phase errors, amplitude errors, and window weighting functions. The result is a two-dimensional plot of the range PSF as a function of range to the scatterer. The plots show the effect of the signal errors on resolution, sensitivity, PSF shape, dynamic range, and geometric accuracy.

There are many methods of estimating chirp nonlinearity and correcting for it. Most simply, the frequency as a function of applied voltage (the tuning curve) can be found by stepping through the required voltage range and measuring the frequency. The applied waveform is then deliberately pre-distorted to linearize the chirp. Burke [50] achieves this distortion with an analogue circuit. The distorted control voltage removes any bulk nonlinearity but does not take into account subtle non-linearities or the slowly changing nature of the tuning curve as the radar warms up or cools down. Also, it does not take into account the difference between the dynamic tuning curve (slewing etc.) and the static tuning curve.

Withers [51] describes a more sophisticated method of evaluating the frequency error in which a delay line (a feature of many linearization techniques) and a phase detector are used to make a frequency discriminator.

Kulpa et al. [52] describe a software technique for estimating the nonlinear PM that is defocussing the radar. The method works by hypothesizing the parameter values of a low-order model of the phase error in the dechirped signal. The dechirped signal is then matched filtered using the hypothesized phase error. The integral of the filtered signal (which is bigger the better the

hypothesis) is then stored against the parameter combination that gave rise to it. After a sufficiently wide and closely spaced range of hypotheses has been tested, the results are searched for the peak, which indicates the best hypothesis. However, this method is computationally intensive, especially for precisely fitted, high-order models.

Another method involves Hilbert transforming the dechirped signal derived from a delay line. The resulting frequency error estimate is not order-based and does not require a search through parameter space. Once the frequency error has been found, the voltage waveform that chirps the oscillator can be modified to compensate for any nonlinearity. In the example developed by Yang et al. [53], the modified chirp voltage waveform is stored in memory and 'played' out to chirp the VCO.

Another method, described by Fuchs et al. [54], uses a similar technique to derive the frequency error but uses a resampling time warping technique to linearize the phase in all of the dechirped signal components simultaneously.

Closed-loop techniques, which often involve delay lines and phase detectors to form frequency discriminators, can be used to correct the control voltage in real time as it is swept [55, 56].

Very often, a surface acoustic wave (SAW) delay device [56] is used to obtain a sufficient delay in a compact unit. However, a different approach is described in [57] in which an ultra-sonic reference signal is simultaneously transmitted at the scene being imaged by the radar. The ultra-sonic signal is easily kept linear owing to the nature of the technology. The phases of the radar and the ultra-sonic dechirped signals are compared and used to derive a time-warping as in the techniques mentioned above.

Warping the signal to linearize the phase is a powerful idea and is used in a similar manner in a method described by Vossiek et al. [58], where the reference signal is derived from a delay line. In all of the approaches mentioned that use a time warping, the signal is sampled then interpolatively resampled in software, warping the time domain. However, the sampling can also be adjusted in real time as the dechirped signal is collected [59].

The methods mentioned above all provide excellent results, but they all require dedicated hardware provision to derive an estimate of the nonlinearity. Such hardware provision is not always convenient. In some cases, the radar may already exist but require linearization or further linearization in addition to an existing technique. Alternatively, the radar may be an instrumentation radar for assessing the performance of components, in which case it might not

be desirable or possible to provide dedicated linearization hardware. Some miniature, low-power radar systems might not have the space or the electrical or computational power to provide linearization as the data are collected.

Next, I shall discuss the background and motivation for an 'autofocus' system that estimates nonlinearity and compensates for it entirely in software. Such a system is developed from two existing techniques and is presented in Chapter 4.

A useful method for estimating phase errors in notionally monochromatic signals is known as the Phase Gradient Algorithm (PGA) [60]. This method, which is used to autofocus Synthetic Aperture Radar (SAR) imagery, exploits the persistent nature of the deterministic phase error. Multiple images of a reference scatterer can be collected, and a stable estimate of the deterministic part of the phase error can be derived from them. Because the PGA is extremely robust against noise, it can estimate the phase errors in the dechirped signal of a real-world reflector, and so there is no need to use a delay line.

The PGA can be used to estimate phase errors of any kind, but in this thesis I will combine it with the time warping technique to form a completely software-based technique for measuring and compensating for chirp nonlinearity. This new approach based on the combination of two software techniques has the advantages that it can be applied to any FMCW radar system and does not require hardware modification, delay lines for example, or the ability to be able to modify the chirping control voltage.

Another advantage of the technique is that it produces high-quality estimates of the dynamic tuning curve of the oscillator that take into account typical operation conditions (chirp rate, bandwidth, temperature etc.).

Because it is entirely software based, the method described and demonstrated in Chapter 4 can be applied retrospectively to archive data (provided that suitable calibration data have been collected), as has been demonstrated in that chapter.

1.4.3 Subsampling downconversion with a special application to Moving Target Indication

AVTIS [13] is an integrated radar and radiometer system designed to produce fine-resolution radar and thermal 'snapshots' of volcano lava domes [37]. Such radar systems are useful because, while most people are familiar with footage and photographs of volcano lava domes, in many cases the active

parts are obscured by cloud, dust, and ash.

Volcanologists can use information about evolving lava domes to study the volcano and to predict eruptions [61, 62]. It is useful for volcanologists to be able to measure the speed of the material emerging from the volcano [63], a measurement made possible by measuring the Doppler shift of particles in the beam. However, AVTIS does not currently have the capability to measure Doppler shifts. It is desirable to be able to add this feature to AVTIS without any significant hardware modification whilst maintaining very high range resolution at a large standoff range.

The most widely used technique to estimate the velocity of targets is to repeatedly and coherently image the scene in quick succession and then to Fourier transform the stacked range profiles in the constant-range direction. The Fourier transform sorts the signal energy at each range by rate of change of phase of the peak of the PSF, the 'image phase'. This rate of change of phase is directly proportional to the radial speed of the moving scatterers. Each Fourier transform gives a graph of the distribution of scatterer velocity for the range cell.

The maximum detectable velocity that can be found (unambiguously) with the Fourier technique is inversely proportional to the time between successive radar range measurements. This requirement means that, for a large range of velocities, a short chirp is required.

Short chirp durations combined with long standoff ranges and fine range resolution result in very high dechirped signal frequencies. To accommodate large dechirped signal frequencies, the data could be sampled very quickly. However, the sampling rate in AVTIS is fixed and is not sufficient for fine range resolution, long standoff range, and large measurable reflector velocities simultaneously. Typical requirements would result in many hundreds of MHz dechirped bandwidth; to sample such signals unambiguously requires very fast and very expensive sampling cards. Avoiding fast sampling requirements is usually desirable, where possible.

A neat hardware method is to band-pass filter the required part of the dechirped signal corresponding to the scene and then to down convert using a mixer and a coherent reference signal before sampling the dechirped signal. But this method is not possible for AVTIS because the hardware has already been designed and built.

There is a further complication, associated with very short chirp length. If the round-trip time to the scene is larger than the chirp length, then the radar

will be transmitting a subsequent chirp when the echoes of a given chirp arrive back at the radar.

Down conversion of echoes with subsequent chirps would make the dechirped signal frequencies small and would allow long-range, high-resolution Doppler radar. However, this approach is not possible here because AVTIS is not coherent from chirp to chirp (although the dechirped signals are).

The method just described also has an undesirable side effect. The range profile will become ambiguous because reflections from scatterers nearer and farther than the volcano will be indistinguishable from those from the volcano. This ambiguity might not be a problem if there is a clear line of sight to the volcano, which also blocks the beam.

However, there is another, preferred method with no requirement for chirp-to-chirp coherence. It is based on the concept of down conversion by subsampling, which allows for clutter between the radar and the volcano and beyond by band-pass filtering. This subsampling technique would also be useful for reducing the required sampling rate for very-fine resolution, long standoff radars.

In Chapter 5, I shall describe the requirements for Doppler radar and the special case presented by AVTIS. With numerical simulations and an educational demonstration radar analogous to AVTIS, I will demonstrate a technique (IF downconversion by subsampling) for reducing the sampling rate.

1.4.4 mm-Wave synthetic aperture radar test bench

Synthetic Aperture Radar (SAR) is a technique that achieves cross-range resolution by computationally synthesizing an aperture from the signals collected by a radar as it is translated in the cross-range direction.

SAR is a well-known technique and has been used with a variety of radars for a variety of ends. At the low-frequency end, there is Foliage Penetrating (FoPen) radar [64]. A great deal of SAR operates in the X-band (8–12 GHz) region, and work has been done at frequencies up to W-band (75–110 GHz) [65].

SAR is more difficult at higher frequencies than at lower ones because the positional accuracy of the radar required to achieve good results is proportional to the wavelength. It is much more difficult to make a moving radar, perhaps on an aeroplane, move within millimetres of a nominal path than it is to fly within 10 cm of a nominal path, as at X-band.

In fact, most SAR systems use sophisticated techniques using GPS and accelerometers to track the exact position of the radar and then to correct the data for any non-ideality in the track [66, 67]. Additionally, autofocus techniques can be used to remove low-order errors in the track's linearity [60].

Some processing algorithms, e.g. backprojection [68], can directly use data collected from arbitrary tracks, but others, e.g. the Range Migration Algorithm (RMA), assume a linear data collection track, so the data must be interpolatively corrected before processing if errors are present [67].

In most SAR processing algorithms, it is usual to assume that the radar is stationary during each data transmit-and-receive cycle along the synthetic aperture. For pulsed systems, which transmit relatively short bursts of radiation, this is usually a good approximation. However, FMCW radars usually transmit long bursts of radiation, which means that the radar may well move through a significant distance during the data collection. This will result in degradation of the image quality.

Work has been done to re-derive the data processing algorithms to cope with long chirps [69], and in some circumstances the chirp time is small enough not to be a problem.

An advantage of a shorter wavelength is that the size of the synthetic aperture needn't be as long as for longer wavelengths: the resolution achievable with a given synthetic aperture is proportional to the wavelength.

mm-Wave FMCW radar systems can be cheap, compact, reliable, and have low computational and electical power requirements. This makes them attractive for small-scale, compact SAR applications.

In order to develop mm-wave SAR capability, it is desirable to have a SAR test bench: a system that can be used to investigate the quality of SAR images given particular components, signal processing, and scatterer structures and materials. To this end, in Chapter 6, I will develop and demonstrate a simple mm-wave SAR system that uses a mechanically translated radar to form SAR images of a small (10 m square) scene at a short standoff range (30 m). The radar is stationary at each point along a straight track so exactly satisfies the stop-start assumption.

I shall describe the RMA, which was chosen to process the data, and highlight the modifications that I have made to it. These include a modification to enable a large scene to be imaged with a short along-track signal collection interval and a modification to remove errors introduced by a drifting master oscillator and fluctuating 'dc' signal component.

The properties of the available signal generators (analogue chirped PMYTO and a DDS-based system) are considered and evaluated for suitability in this application.

A SAR data simulator is used to investigate the sensitivity of the RMA to radar position error and oscillator centre frequency drift.

Some sample test imagery, generated from both synthetic data and data collected at a small outdoor range, is shown, and the quality of the imagery is analysed and discussed.

1.5 Thesis structure

In Chapter 2, I shall describe the basic theory of FMCW radar systems. In Chapter 3, I shall investigate the effect of phase and amplitude errors on the PSF. I shall also develop a technique that generates diagrams analogous to the Ambiguity Diagram for calculating and displaying the effect of chirp nonlinearity (and other signal defects) on the PSF as a function of reflector range. Following on from this, in Chapter 4, I shall develop and demonstrate a software-based technique for estimating and compensating for chirp nonlinearity in FMCW radars. In Chapter 5, I will develop and demonstrate a technique for achieving MTI in high-resolution, long-range FMCW radars without the need for major hardware modification and with low sampling rates. Finally, in Chapter 6, I will implement a mm-wave SAR test bench system and discuss the component selection, algorithm modifications, and resultant image quality.

Chapter 2

Introduction to FMCW radar

In this is chapter, I shall describe and quantify the operation of Homodyne Dechirp-on-receive Linearly Frequency Modulated (also often known as FMCW) Radar.

2.1 Why not use pulses?

The primary purpose of radars is to measure the range of objects. One way of doing this is to transmit a short pulse of radiation and then to plot the time record of the echoes. The delay of the echo corresponds to the range of the reflector, and the size of the echo corresponds to its reflectivity. So-called 'pulse radar' is a well-used technique, and many radars work perfectly well like this.

However, as the range resolution achieved by this technique is directly proportional to the pulse length, if fine range resolution is required, then the length of the pulses must be small. If the required resolution is 10 cm, the maximum duration of the pulses is of order 2/3 ns.

Transmitting such short signals is problematic for several reasons: firstly, making the transmitter electronics switch on and off at this speed is a difficult problem in its own right [70, 71]; and secondly, the radar must transmit sufficient power that the received echo is strong enough to be detected satisfactorily. The necessary large peak transmit power requires large, expensive, delicate, and inefficient high-voltage vacuum technology.

In contrast to pulse radars, FMCW radars offer fine range resolution and low-power operation from simple architectures that use reliable, robust, and

relatively cheap solid-state components.

2.2 FMCW radar – measuring range

The type of radar discussed in this thesis, homodyne dechirp-on-receive linearly frequency modulated radar, does not generally transmit short intense bursts of radiation; in many cases it transmits a continuous low-power signal all of the time. But transmitting a constant frequency signal towards the scene and recording the echo does not provide information about the range of any reflectors in beam. It reveals the presence of reflectors and provides information about any radial motion via Doppler shifts but does not indicate the range of those reflectors.

To have range resolution, the radar must have non-zero bandwidth. That is to say, some aspect of the signal must vary in time. This can be achieved by time-modulating the properties of the signal (usually frequency, phase or amplitude) as it is transmitted, but the particular method used in FMCW radar has many advantages.

In FMCW radar, the frequency of the transmitted radiation is swept linearly through a range of frequencies, B, 'chirping' the radiation, as illustrated in Figure 2.1-(a). The frequency of the transmitted signal has the following form

$$f_{\mathrm{t}}(t) = f_0 - \frac{B}{2} + \frac{B}{T}t, \tag{2.1}$$

where f_0 is the carrier frequency and T is the duration of the chirp. t is the time since the start of the current chirp.

The chirp can be swept up or down, i.e. B can be negative in (2.1). But the value of B is conventionally reported as being positive, and the chirp is referred to being 'up' or 'down'.

The difference in frequency between the transmitting signal and a slightly delayed copy, an echo, is proportional to the delay and is given by

$$f_{\mathrm{diff}}(t) = f_{\mathrm{t}}(t) - f_{\mathrm{t}}(t-\tau) = \frac{B\tau}{T}. \tag{2.2}$$

τ is the round-trip time and is given by

$$\tau = \frac{2R}{\mathrm{c}}, \tag{2.3}$$

where R is the range to the reflector and c is the speed of light.

So, the frequency difference between the transmitting signal and the echo is

$$f_{\text{diff}} = \frac{2BR}{\text{c}T}. \tag{2.4}$$

Equation (2.4) is central to FMCW radar processing: the difference in frequency between the transmitted and the received signals is constant and proportional to the range of the scatterer that reflected the echo. This is illustrated in Figure 2.1-(b). By finding the difference between the instantaneous frequency of an echo and that of the transmitting signal, the radar can be used to measure range.

2.3 Hardware signal processing: dechirp on receive

One of the advantages of FMCW radar processing is that it lends itself to a hardware-based signal processing technique called 'dechirp on receive'.

In homodyne dechirp-on-receive radars, the echoes are down converted by the transmitting signal, which achieves a frequency subtraction. In fact, the mixer subtracts the phase of the transmitting signal from the phase of each of the echoes. The down-converted echoes (also called the Intermediate Frequency (IF) signal) have frequencies given by (2.4) and are usually much smaller than either the carrier or the chirped bandwidth, so are easier to sample and process.

The down conversion can be done using a mixer, a device that subtracts the phase of the reference (also called the Local Oscillator – LO) signal from the phase of each component of the received (also called the Radio Frequency – RF) signal.

The mixer works by switching the polarity of the RF signal at the frequency of the LO signal. In fact, only an ideal mixer exactly switches the polarity, more realistic mixers are described in Section 3.4.2. This polarity switching effectively multiplies each component in the RF signal by a square wave with the same phase as the LO signal.

From the Fourier series of a square wave, $A_{\text{sw}}(t)$ with instantaneous frequency $f_{\text{inst.}}$,

$$A_{\text{sw}}(t) = \frac{4}{\pi} \sum_{n=1,3,5\ldots} \frac{1}{n} \sin\left(2\pi f_{\text{inst.}} t\right), \tag{2.5}$$

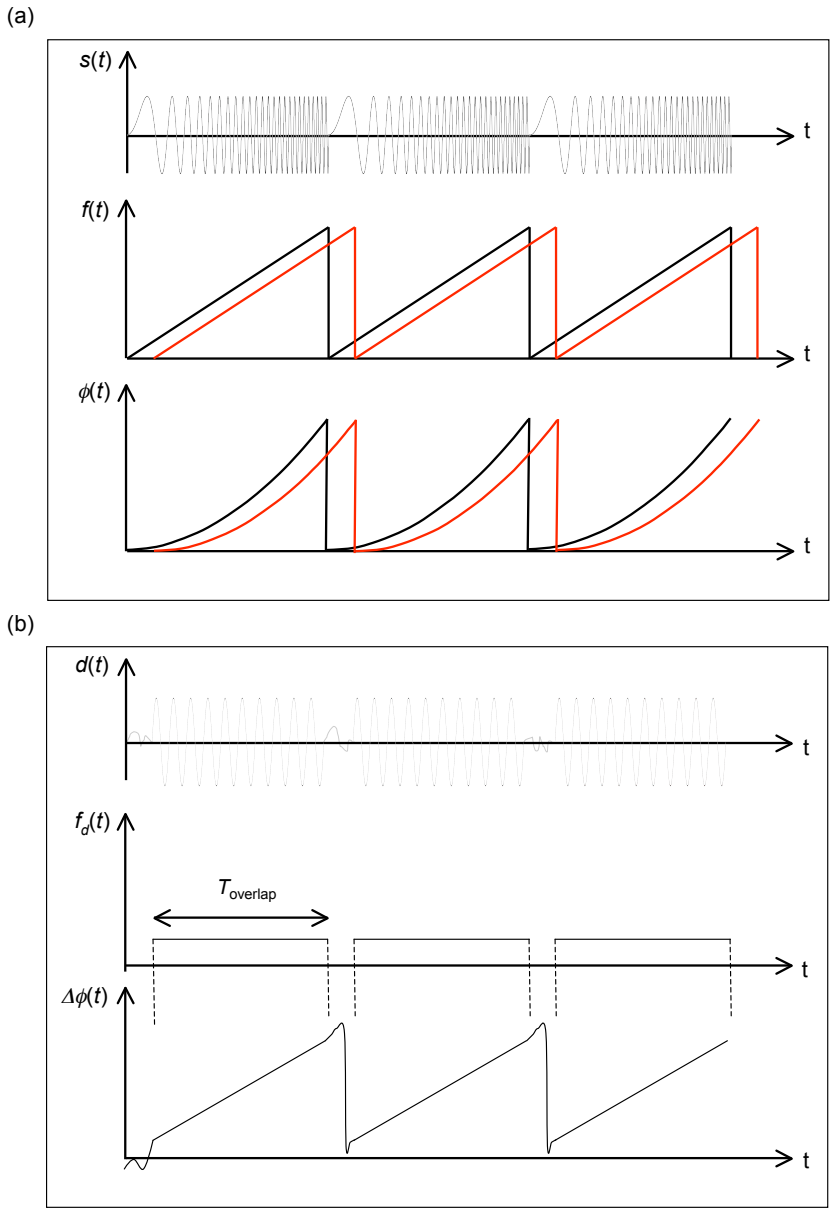

Figure 2.1: (a) The transmitted radar signal, $s(t)$, the frequency profiles, $f(t)$, of the transmitted signal (in black) and the echo (in red), and the phase profiles, $\phi(t)$, of the transmitted signal and echo. (b) The dechirped signal, $d(t)$, the frequency profile, $f_{\mathrm{d}}(t)$ of dechirped signal, and the phase $\Delta\phi(t)$ of the dechirped signal. The time interval labelled T_{overlap} is the duration of the overlapping signals so is the longest duration of the signal that can be used for the spectral analysis required to form a radar image.

the fundamental component of the square wave is $\propto \sin\left(\phi_{\mathrm{LO}}(t)\right)$. Only the fundamental component is required in the calculation because the frequency difference between the echoes and all the higher harmonics are above the pass band of the mixer.

The signal leaving the Intermediate Frequency (IF) port is the product of the fundamental frequency component of a square wave with the same phase as the signal entering the LO port and the signal entering the RF port. For a single echo signal in the RF port, $\sin\phi_{\mathrm{RF}}(t)$, this is

$$s_{\mathrm{IF}}(t) \propto \sin\phi_{\mathrm{LO}}(t)\sin\phi_{\mathrm{RF}}(t), \tag{2.6}$$

which can be written in the following form,

$$s_{\mathrm{IF}}(t) \propto \cos[\phi_{LO}(t) - \phi_{\mathrm{RF}}(t)] - \cos[\phi_{LO}(t) + \phi_{\mathrm{RF}}(t)], \tag{2.7}$$

but as only the low frequency term passes through the IF port, the signal leaving the IF port of the mixer is

$$s_{\mathrm{IF}}(t) \propto \cos[\phi_{LO}(t) - \phi_{\mathrm{RF}}(t)], \tag{2.8}$$

from which it can be seen that the required phase subtraction has been achieved.

This process is linear for the RF input signal, so the phase subtraction applies to all of the components in the RF signal.

In order for the echoes to be down converted by the transmitting signal, the duration of the chirp must be long enough that the chirp is still transmitting when the echoes arrive back at the radar.

If a heterodyne system is used, this requirement is removed. Alternatively, a long delay line of length comparable to the round-trip distance to the scene could be inserted between the source and the LO port of the mixer.

In most cases, the duration of the chirp will be hundreds of times the duration of the delay from the farthest target. This means that the echoes from all of the scatterers in the scene and the transmitting signal more-or-less completely overlap.

In fact, using a long chirp with long ranges (large τ) or high resolution (large B) is also desirable because, as can be seen in (2.4), increasing the value of T reduces the frequency of the IF components, which in turn reduces the required sampling rates.

A long signal is also desirable from an SNR point of view. The time bandwidth product of the signal indicates the compression ratio of the transmitted

chirp to the final peak response of the radar. The larger the product, the greater the integrated energy of the signal compared to that of the noise.

The compound dechirped signal resulting from the homodyne FMCW radar, which is pictured in Figure 2.3, is a sum of single frequency signals. This sum of signals is much the same as a musical chord. It is not possible simply to measure the frequency of the signal to find the range of the reflectors, unless there is only one of them, which is sometimes true, for instance in altimeters and silo depth gauges. Spectral analysis in the form of window weighting and Fourier transformation can be used to present the signal energy as a distribution in frequency and so in range, too. This allows the reflections from multiple reflectors to be separated – they occupy a small region of the spectrum, but the entirety of the time-domain signal history. Conservation of energy also dictates that single frequency signals benefit from compression gain, which improves the peak SNR. Apart from unit conversions and scalings, Fourier transformation is the final step in the image formation process.

The result of the above process, often referred to as a 'range profile', is a plot of the energy reflected back from the scene as a function of scatterer range. In this thesis, I will often refer to this as an 'image'. It is not an image in the usual sense: it is complex and not necessarily two-dimensional. However, it is the result of the radar imaging process.

It is worth noting that homodyne FMCW signal processing is a form of matched filtering, which maximizes the SNR of the range-compressed signal [49]. Identifying the mode of range compression discussed in this thesis as matched filtering is useful because a great deal is known about matched filtering and the general properties of the resulting range profiles.

2.4 Resolution in dechirp-on-receive linearly frequency modulated radars

The resolution of an FMCW radar can be determined by the frequency resolution and the frequency-to-range scaling. The frequency resolution is given by the duration of the signal used to form the spectrum of the dechirped signal. Only the part of the IF signal in which the echoes from the scene overlap with the transmitting chirp can be used for spectral analysis. The maximum duration that can be used is indicated in Figure 2.1 by the quantity T_{overlap} for the farthest reflector to be included in the image.

If the duration of the signal used to form the spectrum is T_{F}, then the frequency bin width is δf and is given by

$$\delta f = \frac{1}{T_{\mathrm{F}}}. \tag{2.9}$$

The range bin width is found using the incremental form of the fundamental FMCW equation, (2.4),

$$\delta f_{\mathrm{diff}} = \frac{2B}{\mathrm{c}T}\delta R, \tag{2.10}$$

so that

$$\delta R = \frac{\mathrm{c}T}{2BT_{\mathrm{F}}}. \tag{2.11}$$

Equation (2.11) gives the unambiguous range sampling interval in the radar range profile and is the distance from the origin to the first null on the sinc response arising from a truncated spectral analysis region. However, the unambiguous sample spacing is not always a practical measure of resolution and does not take into account window weighting.

By choosing the form of the window weighting function carefully [72], sidelobes can be appropriately suppressed. Windowing is usually necessary because the sidelobe structure of a sinc function is unacceptably high for many purposes. This can be seen in Figure 2.2, which compares PSFs resulting from different window weighting functions.

However, the cost of reducing sidelobe levels is a modified point response shape, and windowing usually results in broadening of the mainlobe. This is often an acceptable cost of reducing sidelobes and can be compensated for by increasing the chirp bandwidth. This is discussed in Chapter 3.

To take this broadening into account and to convert the bin width to the Full Width Half Maximum (FWHM) power resolution, a scaling factor, κ, is used. For a plain sinc function, i.e. simply converting from the bin width to FWHM, $\kappa = 0.8859$ (4 decimal places). Where other window weighting functions are used, the appropriate value of κ is usually found numerically. Where it is used, I will state the value of κ in the text.

The full form of the notional FWHM FMCW radar resolution, ρ, is

$$\rho = \frac{\kappa \mathrm{c}T}{2BT_{\mathrm{F}}}. \tag{2.12}$$

From this expression, it can be seen that, as T_{F} is usually $\approx T$, then ρ is more-or-less independent of T. So, by chirping through a large enough B,

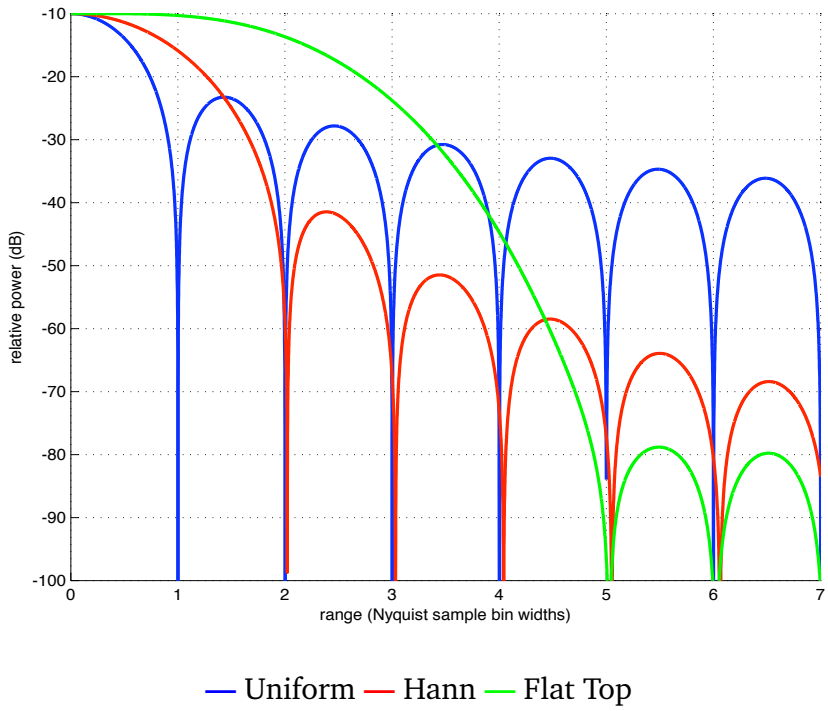

Figure 2.2: The ideal point spread functions due to Uniform window weighting, Hann window weighting, and Flat Top window weighting. It can be seen that the Nyquist resolution (from the peak to the first null of the Uniform response) is much smaller than the FWHM resolution of the Flat Top response.

excellent resolution can be achieved. The resolution is limited not by the chirp time but by the maximum bandwidth available with the radar's transmit and receive signal paths.

Fundamentally, the PSF of a radar is determined by the processable signal bandwidth, the amplitude and phase variations across that bandwidth, and the type of window function used – most generally this is represented as the correlation of the transmitted and received signals. This approach to PSF analysis is discussed in Chapters 3 and 6. The advantages of the approach taken in this chapter are that it provides a useful connection between easily measurable system quantities, and also makes the influence of various stages of the signal processing clear.

It will be shown that (2.12) and the idea that image quality in general can be described by simple parameters are only valid when the radar is working nominally.

2.5 Summary of dechirp-on-receive linearly frequency modulated radar

The radar source produces a signal with a linear frequency ramp. This signal is transmitted towards the scene to be imaged. The echoes arrive back at the radar, where they are mixed with the transmitting signal to produce the dechirped signal. The dechirped signal is then suitably filtered, windowed, and Fourier transformed to yield the range profile of the scene.

The resolution of the radar is determined (predominantly) by the bandwidth of the chirp, so long chirps can be used, which is often desirable in order to obtain a high time-bandwidth product and to maintain a low IF sampling rate.

Homodyne dechirp-on-receive linearly frequency modulated radar operation offers fine range resolution, high SNR, low average transmit power, low computational load, and a simple architecture.

The basic structure of the FMCW radar just described is summarized in Figure 2.3.

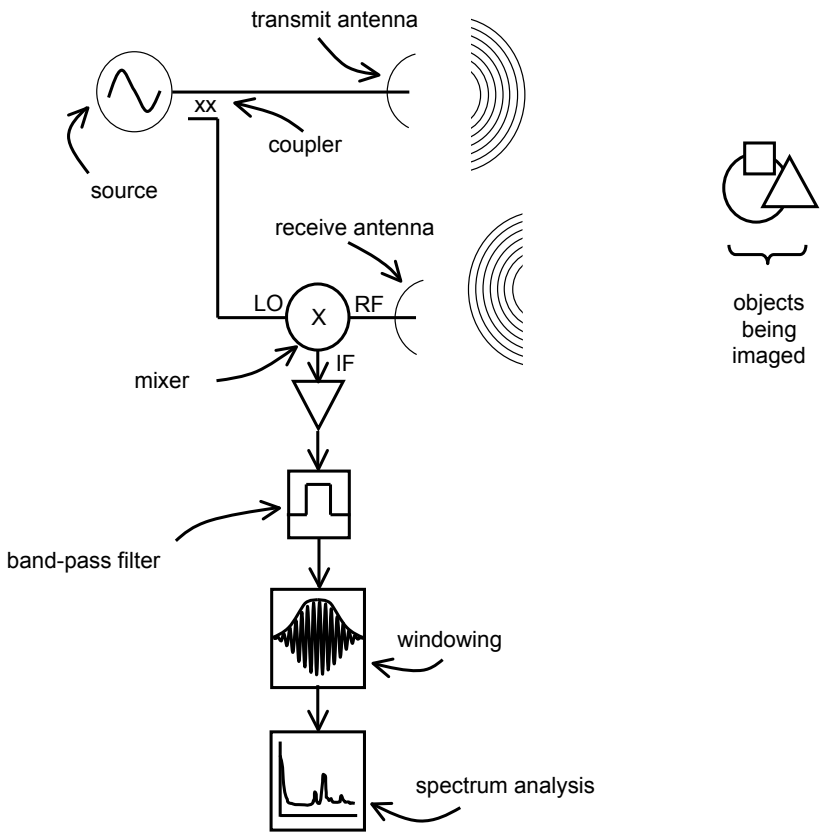

Figure 2.3: The generic structure of the homodyne FMCW radar. In many cases, aided by a three-port circulator, one antenna serves both for transmission and reception. The Local Oscillator (LO) port is the reference signal path, the Radio Frequency (RF) port is the echo signal path, and the Intermediate Frequency (IF) port is the dechirped signal path.

Chapter 3

Range-standoff diagrams

In this chapter, I shall describe and demonstrate a simple and intuitive technique for calculating the radar's response to a point-like scatterer at any range given the dechirped signal's phase and amplitude errors.

Part of the work presented in this chapter was presented as a paper, 'Predicting range point response from chirp nonlinearity', at the Radar 2008 conference in Adelaide, Australia.

3.1 Introduction

The PSF of a radar is the response of that radar to an ideal point-like reflector and is usually a function of range. The image produced by the radar is the convolution of the PSF and the R^{-4} weighted RCS distribution along the radar beam. Accordingly, the PSF tells us about the fundamental properties of the image quality, including resolution, sensitivity, dynamic range, geometric precision, sidelobe level, and image phase accuracy.

Ideally, these properties are determined by just the chirped bandwidth and the window function used to weight the signal, but in practice they depend on the phase and amplitude errors degrading the signal, too.

There are many excellent techniques for calculating the values of these properties based on the signal errors, but they often require complicated analysis and approximations, and they often produce a parametric description of the image quality [42, 43, 46–48, 52, 73, 74]. Additionally, the window function is not always taken into account, and it will be shown that it has a large influence on how signal errors affect the PSF.

In this chapter, I shall describe a simple method for predicting the PSF exactly, taking the window function into account and without making any approximations. This method allows both subtle and extreme changes in the shape of the PSF to be quickly appreciated, something which is not always possible from parametric descriptions. For example, Figure 3.1 shows the degradation of the PSF of a Uniformly weighted signal as increasing degrees of Quadratic Phase Error (QPE) are applied. It can be seen that, for small QPEs, the response simply broadens. But as the QPE becomes large, the PSF can be seen to change shape. In the $3\pi/2$ case, there are two peak responses, a feature that would be hard to depict and understand in a parameter plot. For instance, FWHM resolution would be a meaningless quantity for the $3\pi/2$ response. However, it is clear from the PSF what the impact of such a phase error on the image quality of the radar would be.

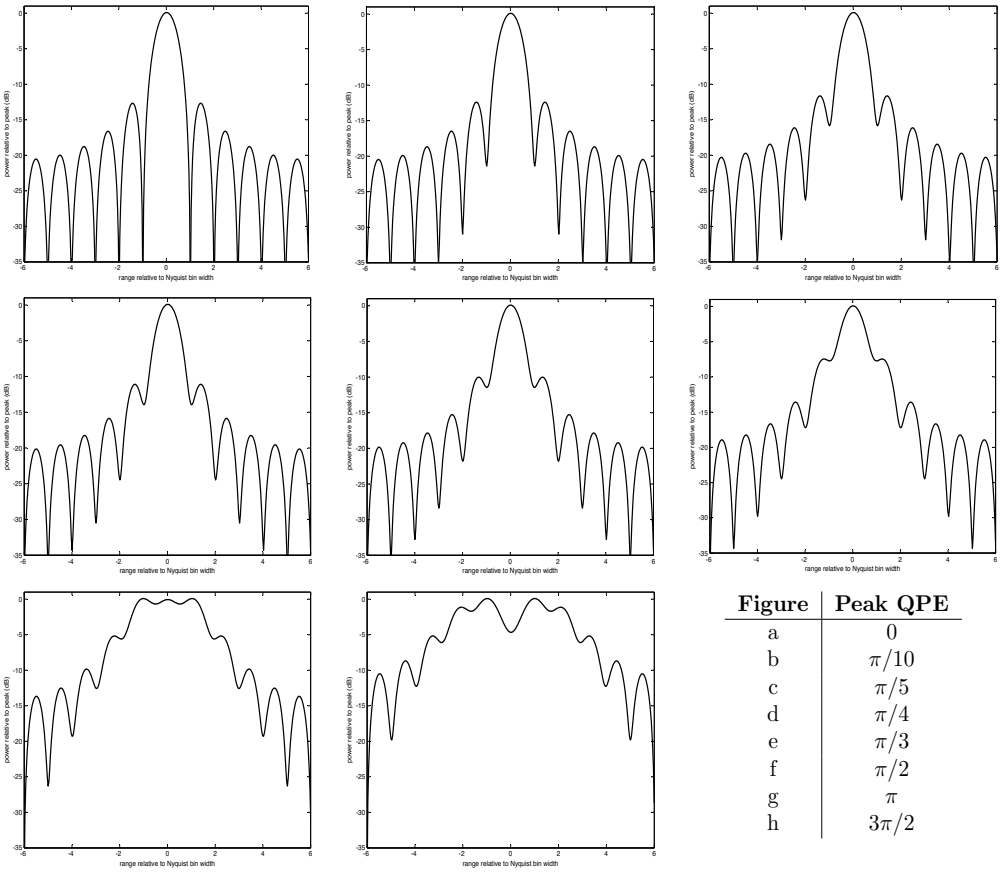

Figure	Peak QPE
a	0
b	$\pi/10$
c	$\pi/5$
d	$\pi/4$
e	$\pi/3$
f	$\pi/2$
g	π
h	$3\pi/2$

Figure 3.1: The degradation of the PSF with increased QPE. A uniform window function was used.

The method described in this chapter is to numerically simulate the radar signal processing for a hypothetical point reflector. This allows the PSF resulting from arbitrary phase and amplitude errors to be computed for a given window weighting function.

In homodyne systems, the same phase error is present in both the LO and the RF signals. This results in partially cancelled phase errors that scale proportionally to the relative delay and so to the range of the reflector, too. This means that the phase error and the defocussing are range dependent. It is useful, then, to be able to plot the PSF as a function of the range of the reflector, the notional standoff range. In this thesis, I shall call this plot a 'range-standoff' diagram because it shows the response of the radar in range relative to the notional standoff range as a function of that notional standoff range.

I shall describe three main categories of error based on their nature and their effect on the PSF.

Although it is possible to calculate the form of the ideal PSF for arbitrary window functions numerically, it is sometimes useful to have an exact parametric description. For example, it is useful to have a parametric model of the ideal response shape to fit to the sampled image of a point-like reference scatterer in order to estimate the range of the reflector and the actual resolution.

In this chapter, I shall describe a general expression that exactly gives the ideal PSF for a specific set of window functions: those defined by a weighted and delayed sum of cosine functions.

The chapter has the following structure: first I shall define the prediction method and diagrams, then I shall calculate and categorize the typical phase and amplitude errors in the radar. I shall then demonstrate the usefulness of the diagrams as descriptions of the PSF. Finally, I shall demonstrate the ability of the diagrams to predict the PSF given a known chirp nonlinearity.

3.2 Calculating the PSF from phase and amplitude errors

The method proposed in this chapter is analogous to ambiguity diagrams [49], which show the changing shape of the PSF as a function of increasing Doppler shift. The method proposed here is to show the changing shape of the PSF as a function of reflector range, with the phase and amplitude errors being (potentially) dependent on the round-trip time.

The method is to calculate the spectrum of the IF signal of a simulated reflector after down conversion to remove the notional phase (a linear ramp of slope $4\pi RB/(\mathrm{c}T)$) of the signal, leaving only the error parts.

The dechirped signal (from a single reference reflector) can be written as

$$s_{\mathrm{d}}(t,R) = A(t,R)e^{i\phi_{\mathrm{d}}(t,R)}. \tag{3.1}$$

In an FMCW radar, $s_{\mathrm{d}}(t)$ would be used in the following computation (a Fourier transform of the windowed IF signal) to form the radar range profile, $P(f)$, as a function of IF frequency,

$$P(f) = \int_{t_1}^{t_2} e^{i2\pi f t} W(t) s_{\mathrm{d}}(t,R)\mathrm{d}t, \tag{3.2}$$

where the limits, t_1 and t_2, are chosen so that only the interval in time when the transmitting chirp and all of the echoes overlap is used in the spectral analysis (see Figure 2.1). In fact, in many cases, $t_1 = 0$ and $t_2 = T$. The window function, $W(t)$, is used to suppress sidelobes in the PSF, and many window functions will also suppresses the incorrectly dechirped parts at either end of the IF signal.

In order to investigate the properties of the PSF, it is useful to down convert the IF signal against its ideal form. This leaves only the error parts of the phase, which means that any range offset and image phase in the PSF are due to phase and amplitude errors rather than the nominal range and image phase of the reference reflector.

Define the phase error to be $\xi(t,R)$ and define the amplitude error such that

$$A(t,R) = A_0[1 + a(t,R)]. \tag{3.3}$$

Removing the ideal part of the phase, writing (3.2) in terms of the signal errors, and using (2.4) to change variables from frequency to range gives the PSF as a function of range, r, relative to the notional range, R, of the reference reflector. This is the nominal PSF of the radar

$$\mathrm{PSF}(r,R) = \int_{t_1}^{t_2} e^{i\frac{4\pi B}{\mathrm{c}T} r t} W(t)[1 + a(t,R)]e^{i\xi(t,R)}\mathrm{d}t. \tag{3.4}$$

An example plot of $\mathrm{PSF}(t,R)$ for a QPE that increases with range is shown in Figure 3.2. The evolution of the shape with increasing range is clearly visible from this type of plot, a range-standoff diagram. However, it is often

easier to see the detail of the PSF at any particular range by taking slices through the diagram at given standoff ranges, R, of interest. This is shown in Figure 3.1 and also in a stacked format in Figure 3.9, which are also both for increasing QPE. Uniform windowing was used for all three cases.

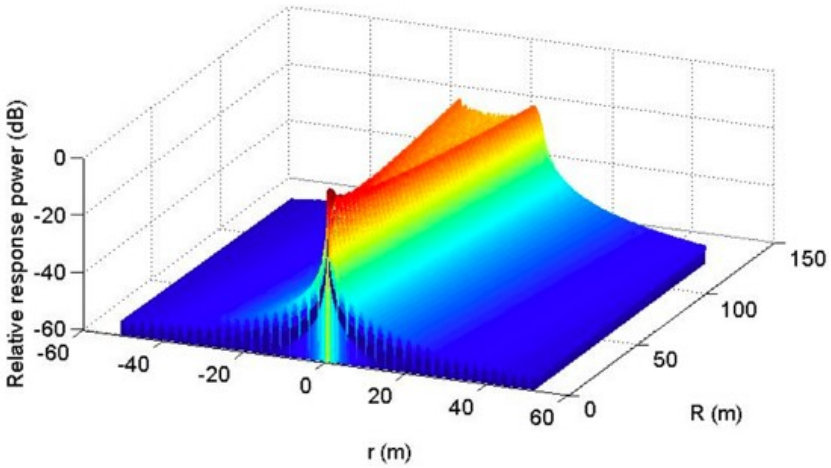

Figure 3.2: Example of the range-standoff diagram, PSF(r,R), for QPE increasing with range. Uniform window weighting was used. This format makes the evolution of the PSF with standoff range clear: the peak can be seen to fall and the response can be seen to broaden, both in a uniform manner. However, presenting the PSFs as slices at particular standoff ranges, R, makes the individual features clearer, as can be seen in Figures 3.1 and 3.9. N.B. r is the range relative to the nominal range, R.

The quantities describing the signal, $a(t)$, $\xi(t)$, $W(t)$, t_1, t_2, T, and B, can be used with (3.4) to calculate the PSF. This gives diagrams that can be inspected or measured. This can be repeated for ranges of quantities to generate look-up tables of resolution, peak power, first sidelobe level etc. as required.

The effect on the PSF of amplitude noise and phase noise of any size and type could be investigated by combining the calculation of PSF(r,R) with Monte Carlo methods. However, excellent techniques based on acceptable approximations have already been developed that provide a good direct connection between the phase and amplitude noise spectra and the PSF [11]. This will be discussed in Chapter 6.

3.3 Calculating the ideal PSF from the window function

It is useful to have a parametric description of the ideal PSF for various applications, e.g. estimation of the resolution and range of a response to a scatterer from coarsely sampled range profiles, as illustrated in Figure 3.3.

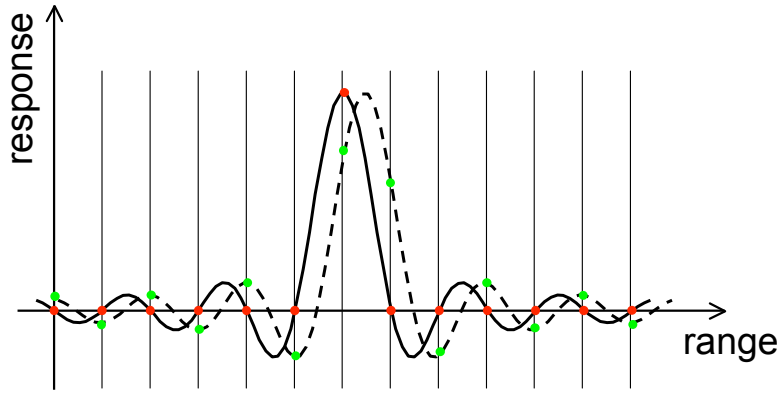

Figure 3.3: In a coarsely sampled range profile, the PSF can appear very asymmetric and attenuated if the response is not aligned with the samples. This is illustrated by the green samples. Cf. the red samples corresponding to the aligned response. Sufficiently oversampling the range profile can also overcome this in most cases.

Such a parametric description is not easy to obtain for the general case. However, a simple expression, parameterized by the quantities that define the weighting, exists to describe the ideal PSF for windows belonging to the cosine family.

The cosine family of windows is specified by the following equation

$$W(t) = \sum_n a_n \cos\left(\frac{2\pi b_n t}{T} + c_n\right), \tag{3.5}$$

where t is between 0 and T.

The PSF of an ideal signal with this weighting is given by the Fourier transform of the weighting function, as in (3.4). The Fourier transform of $W(t)$ is $\widehat{W}(f)$,

$$\widehat{W}(f) = \int_0^T e^{2\pi i f t} W(t) \mathrm{d}t. \tag{3.6}$$

Substituting (3.5) into (3.6) gives

$$\widehat{W}(f) = \sum_n \left[a_n \left(\int_0^T \cos\left(\frac{2\pi b_n t}{T} + c_n \right) e^{2\pi i f t} \mathrm{d}t \right) \right], \tag{3.7}$$

which gives the spectrum, $\widehat{W}(f)$, as a complex sum of symmetrically shifted sinc functions,

$$\widehat{W}(f) = \frac{Te^{i\pi T f}}{2} \sum_n a_n \left[e^{i(\pi b_n + c_n)} \mathrm{sinc}\left(\pi T[f + b_n]\right) + e^{-i(\pi b_n + c_n)} \mathrm{sinc}\left(\pi T[f - b_n]\right) \right]. \tag{3.8}$$

Equation (3.8) provides an exact expression for the PSF due to a window function, $W(t)$, using only the specification of that window function, as defined in (3.5). Some typical cases are given in Table 3.1 [72].

This representation is used in this thesis where a model of the nominal PSF is required.

3.4 Phase and amplitude errors

In FMCW radars, frequency-dependent phase and amplitude errors (e.g. those introduced by the group delay and frequency response of components) become time dependent. This is because the frequency of the signal is related to the time since the start of the chirp by (2.1).

In Sections 3.4.1 and 3.4.2, I shall calculate the phase and amplitude errors that appear in the dechirped signal. I shall not ascribe them to any particular process (apart from the phase due to chirp nonlinearity) but instead ascribe them to a particular part of the radar circuit. The location of their source determines how they combine when the errors in the echoes (RF signal) interact with those in the reference (LO) signal.

3.4.1 Phase errors in the dechirped signal

The sources of signal phase (both ideal and errors) around the homodyne FMCW circuit are illustrated in Figure 3.4.

As discussed in Chapter 2, the phase of each of the dechirped echoes in the IF signal is the phase of the signal at the LO port of the mixer subtracted from that of the echo at the RF port.

Window function	n	a_n	b_n	c_n
Uniform	0	1	0	0
Hann	0	0.5	0	0
	1	−0.5	1	0
Hamming	0	0.54	0	0
	1	−0.46	1	0
Cosine	0	1	0.5	$-\pi/2$
Blackman	0	$(1-\alpha)/2$	0	0
	1	$1/2$	1	0
	2	$\alpha/2$	2	0
Nuttall	0	0.355767	0	0
	1	−0.487396	1	0
	2	0.144232	2	0
	3	−0.012604	3	0
Blackman-Harris	0	0.35875	0	0
	1	−0.48829	1	0
	2	0.14128	2	0
	3	−0.01168	3	0
Blackman-Nuttall	0	0.3635819	0	0
	1	−0.4819775	1	0
	2	0.1365995	2	0
	3	−0.0106411	3	0
Flat Top	0	1	0	0
	1	−1.93	1	0
	2	1.29	2	0
	3	−0.388	3	0
	4	0.032	4	0

Table 3.1: Coefficients for a selection of popular cosine family window functions and their PSFs [72]. The window is given by (3.5) and the corresponding spectrum (their PSF) is given by (3.8). Uniform, Hann, and Blackman-Harris window functions are shown in Figure 3.12.

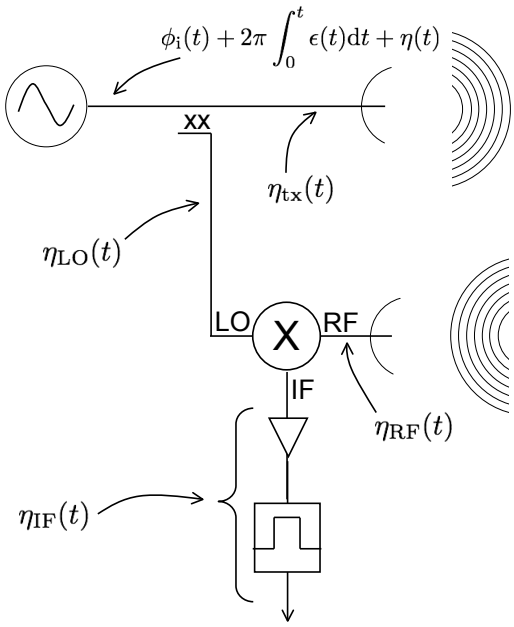

Figure 3.4: The sources of the various additive parts of the signal phase in the homodyne FMCW radar.

The signal entering the LO port of the mixer has the following phase parts:
$\boxed{\phi_{\mathrm{i}}(t)}$ is the nominal phase of the signal.
$\boxed{2\pi \int_0^t \epsilon(t')\mathrm{d}t'}$ is the phase error in the signal leaving the source due to chirp nonlinearity. $\epsilon(t)$ is the frequency error in the chirp and t' is a dummy variable.
$\boxed{\eta(t)}$ is the phase error in the signal leaving the source not due to chirp nonlinearity. This includes noise, group delay etc..
$\boxed{\eta_{\mathrm{LO}}(t)}$ is the phase error, consisting of noise and group delay etc., picked up by the signal after being split into the reference (LO) arm and the transmit (tx) arm. This phase error only appears at the LO port of the mixer.

The total phase of the signal entering the mixer at the LO port is $\phi_{\mathrm{LO}}(t)$, which is given by adding all of the separate parts that are listed and described immediately above:

$$\phi_{\mathrm{LO}}(t) = \phi_{\mathrm{i}}(t) + 2\pi \int_0^t \epsilon(t')\mathrm{d}t' + \eta(t) + \eta_{\mathrm{LO}}(t). \tag{3.9}$$

The same calculation can be done for the phase of the echo entering the RF port of the mixer. This differs slightly from the LO phase because there is

an additional delay, τ, caused by the the round-trip time of the echo.

The phase of the echo entering the RF port of the mixer has the following parts:

$\boxed{\phi_{\mathrm{i}}(t-\tau)}$ is the delayed copy of the nominal phase.

$\boxed{2\pi\int_0^{t-\tau}\epsilon(t')\mathrm{d}t'}$ is the delayed copy of the phase error due to nonlinearity in the chirp.

$\boxed{\eta(t-\tau)}$ is the delayed copy of the phase error in the signal due to group delay and noise etc. leaving the source not due to chirp nonlinearity.

$\boxed{\eta_{\mathrm{tx}}(t-\tau)}$ is the delayed copy of the phase error in the signal due to group delay and noise etc. between the coupler and being transmitted. This phase error only appears at the RF port of the mixer but is affected by the range of the reflector.

$\boxed{\eta_{\mathrm{RF}}(t)}$ is the phase error in the signal due to group delay and noise etc. in the receiver. This phase error only appears in the RF port of the mixer and is not affected by the range of the reflector.

Combining the phase errors listed and described above gives the phase of the signal at the RF port,

$$\phi_{\mathrm{RF}}(t,\tau)=\phi_{\mathrm{i}}(t-\tau)+2\pi\int_0^{t-\tau}\epsilon(t')\mathrm{d}t'+\eta(t-\tau)+\eta_{\mathrm{tx}}(t-\tau)+\eta_{\mathrm{RF}}(t). \quad (3.10)$$

The phase of the IF signal leaving the mixer is given by

$$\phi_{\mathrm{IF}}(t)=\phi_{\mathrm{LO}}(t)-\phi_{\mathrm{RF}}(t,\tau)+\eta_{\mathrm{IF}}(t), \quad (3.11)$$

where $\eta_{\mathrm{IF}}(t)$ is the phase error due to noise and group delay etc. introduced in the IF part of the signal processing.

Substituting for $\phi_{\mathrm{LO}}(t)$ and $\phi_{\mathrm{RF}}(t,\tau)$ in (3.11) using (3.9) and (3.10) gives the total phase of the dechirped signal,

$$\begin{aligned}\phi_{\mathrm{d}}(t,R)=&\underbrace{\phi_{\mathrm{i}}(t)-\phi_{\mathrm{i}}(t-\tau)}_{\text{correlated nominal phase}}+\underbrace{2\pi\left[\int_0^{t}\epsilon(t')\mathrm{d}t'-\int_0^{t-\tau}\epsilon(t')\mathrm{d}t'\right]}_{\text{correlated phase error due to chirp nonlin.}}+\\&\underbrace{\eta(t)-\eta(t-\tau)}_{\text{correlated phase error}}+\underbrace{\eta_{\mathrm{tx}}(t-\tau)+\eta_{\mathrm{RF}}(t)+\eta_{\mathrm{IF}}(t)}_{\text{uncorrelated phase error}},\end{aligned} \quad (3.12)$$

where the R dependence is via the round-trip delay, τ.

The phase error in the dechirped signal from a reflector at range R is $\xi(t,R)$, which is, in general, given by

$$\xi(t,R) = \underbrace{\phi_{\mathrm{d}}(t,R)}_{\text{total dechirped signal phase}} - \underbrace{\left[\phi_{\mathrm{i}}(t) - \phi_{\mathrm{i}}(t-\tau)\right]}_{\text{correlated nominal phase}}, \tag{3.13}$$

and in this case is

$$\xi_{\mathrm{d}}(t,R) = \underbrace{2\pi\left[\int_0^t \epsilon(t')\mathrm{d}t' - \int_0^{t-\tau} \epsilon(t')\mathrm{d}t'\right]}_{\text{correlated phase error due to chirp nonlin.}} + \underbrace{\eta(t) - \eta(t-\tau)}_{\text{correlated phase error}} + \underbrace{\eta_{\mathrm{tx}}(t-\tau) + \eta_{\mathrm{RF}}(t) + \eta_{\mathrm{IF}}(t)}_{\text{uncorrelated phase error}}. \tag{3.14}$$

It can be seen from this example that some parts of the phase error vary with τ and that some do not. Of the parts that vary with τ, some correlate whilst others do not.

For the range-dependent uncorrelated phase errors, the PSF will vary with range because different regions of the amplitude and phase errors span the spectral analysis region. However, this is unlikely to make a significant difference to the PSF as a function of range.

The variation in τ has particular implications for the correlated phase errors because the echoes and transmitting copies interfere in a way that significantly modifies the resultant phase error in the signal.

In the case of chirp nonlinearity, the mixing of the delayed and undelayed copies of the signal results in the net phase error scaling proportionally to the range of the reflector. In the case of noise-like phase errors, the result is a modified phase error spectrum, which will be discussed in more detail in Chapter 6.

3.4.2 Amplitude errors in the dechirped signal

As with the phase error, there are amplitude errors common to the transmitted and received parts of the signal. Similarly, there will also be parts that are unique to either the transmit and/or the receive path.

In this calculation, the signal power is taken to be relative to the nominal power. The oscillator power, the coupling coefficients, and loss associated with divergence to and from the reflector are all left as an overall factor to

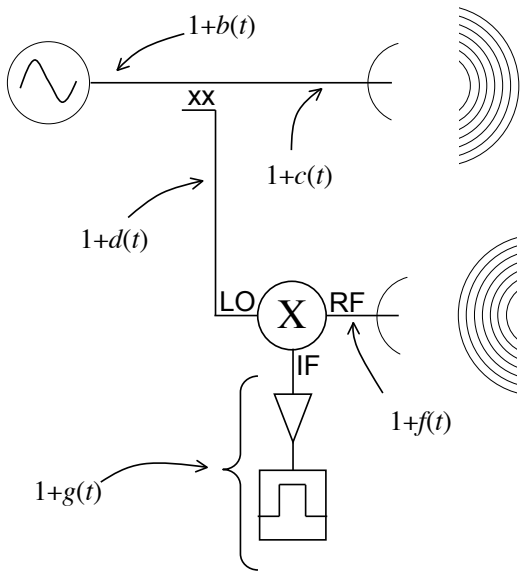

Figure 3.5: The locations of the various multiplicative amplitude modulations around the homodyne FMCW radar.

be determined when calculating the power budget of the radar. The present calculation is concerned with fractional variation relative to constant (in time and frequency) values.

The signal entering the LO port of the mixer has the following amplitude terms:

$\boxed{1+b(t)}$ is the amplitude of the signal leaving the oscillator.

$\boxed{1+d(t)}$ multiplies the signal amplitude as it enters the LO port of the mixer.

The amplitude of the signal entering the LO port of the mixer is $[1+b(t)]\times[1+d(t)]$. This can be written as $1+b(t)+d(t)+b(t)d(t)$.

To take into account the AM suppression of the LO port, the modulation in the LO signal is attenuated, giving the effective LO signal amplitude as

$$1+a_{\mathrm{LO}}(t)=1+\mu\big[b(t)+d(t)+b(t)d(t)\big], \tag{3.15}$$

where μ is the LO AM attenuation factor of the mixer.

Next, the AM in the RF signal is found:

$\boxed{1+b(t-\tau)}$ is the amplitude of the echo as it left the source.

$\boxed{1+c(t-\tau)}$ is the amplitude scaling of the echo as it passed from the source to be transmitted.

$\boxed{1+f(t)}$ is the amplitude scaling of the echo as it passed through the receiver.

The resulting RF signal amplitude (relative to the nominal value) is given by

$$1 + a_{\mathrm{RF}}(t,\tau) = [1 + b(t-\tau)] \times [1 + c(t-\tau)] \times [1 + f(t)]. \tag{3.16}$$

The LO signal is multiplied by the RF signal and passes through the IF signal chain, suffering a further amplitude scaling: $\boxed{1 + g(t)}$.

The amplitude of the output of the mixer is, then

$$1 + a(t,R) = [1 + a_{\mathrm{LO}}(t)] \times [1 + a_{\mathrm{RF}}(t,\tau)] \times [1 + g(t)], \tag{3.17}$$

which gives $a(t,R)$, the effective overall amplitude modulation of the dechirped signal. As with the dechirped signal phase, the R dependence is via τ.

3.4.3 Categorizing the phase and amplitude errors

Although (3.4) would produce valid estimates of the PSF regardless of the origin and form of $a(t)$ and $\xi(t)$, it is useful to categorize the errors based on their form, their origin, and their effect on the PSF.

In many radars, the errors degrading the signal fall into the following categories:

1. deterministic errors that do not correlate. These tend to be low-order phase and amplitude errors that only affect the response close to the mainlobe of the PSF. These are usually quite mild;

2. deterministic errors that do correlate. In practice this means phase errors due to nonlinear chirping. Again, these tend to be low-order phase errors that affect mainly the mainlobe of the PSF. The part due to chirp nonlinearity can be severe;

3. noise-like amplitude and phase errors. These tend to be wideband errors and can affect the PSF a long way from the mainlobe. These can be severe, especially when very bright reflectors are present or where there is transmit-receive leakage in the radar. N.B. some phase errors correlate and so can cancel or reinforce one another.

The first category is not usually a problem for most radars. However, as relative bandwidths, B/f_0, are increased further by ever-higher resolution systems, the roll-off and group delay introduced by amplifiers and band-pass filters might become problematic [42]. In some cases, it might be possible to introduce dummy group delays in the transmit or receive path to balance errors

not inherently common to both with the result that they cancel. In practice, the AM introduced by components like amplifiers and filters is not usually the dominant source of PSF degradation.

The second category of errors (correlated errors) cancel completely at zero range ($\tau = 0$) but increase approximately proportionally with range for small values of τ. Those errors in this category that are due to group delay are usually cancelled sufficiently not to be a problem. However, the phase errors due to chirp nonlinearity can be large and are in practice the largest phase error affecting many radars [11, 46].

The third category accounts for all noise-like (random) signal errors. This type of error tends to extend to higher frequencies so also tends to degrade the PSF much further away from the mainlobe than the phase errors of the first two categories. This category includes correlating and non-correlating errors. The correlating phase errors in this category cancel as do the lower-frequency, deterministic errors in the first category. But because the noise-like errors extend to much higher frequencies, reinforcement is also observed, albeit usually only for far-off reflectors and noisy sources [75]. This is discussed in Chapter 6.

3.5 Demonstration of the range-standoff diagram

In this section, I shall demonstrate the ability of the range-standoff diagrams to produce informative and accurate predictions of the radar's performance given its phase and amplitude errors and given the window function used.

First, I shall demonstrate the ability of the range-standoff diagram to produce curves describing quantities such as FWHM resolution and peak response amplitude. The curves are calculated for Uniform, Hann, and Blackman-Harris weighting functions. The calculated responses, from which the curves are derived, will be shown to be very informative.

Second, I shall demonstrate the ability of the range-standoff diagram to compute the shape of the PSF as a function of range based on the chirp nonlinearity in two radar-based test cases:

1. the first test case is a hardware radar simulation, in which the PSFs were generated for a number of specific chirp nonlinearities;

2. the second test case is an instrumentation radar operating with a deliberately and badly nonlinear chirp at short range.

In each of these test cases, the shape of the PSF obtained with the radar (or hardware simulation) is compared with the PSF generated by calculating the range-standoff diagram with the appropriate chirp nonlinearity at the relevant range.

3.5.1 Effect of quadratic and cubic phase errors on the PSF given different window functions

A computer program was written to compute (3.4) for a range of amplitudes of QPE (range independent) and to measure both the FWHM resolution and the power at the centre of the response, defined here as being the midpoint of the FWHM resolution.

The computer program estimated the PSF for closely spaced values of the peak QPE, Q, as defined in the applied phase error, $\xi(t)$,

$$\xi(t) = \frac{4Q}{T^2}\left(t - \frac{T}{2}\right)^2, \tag{3.18}$$

which is illustrated in Figure 3.6.

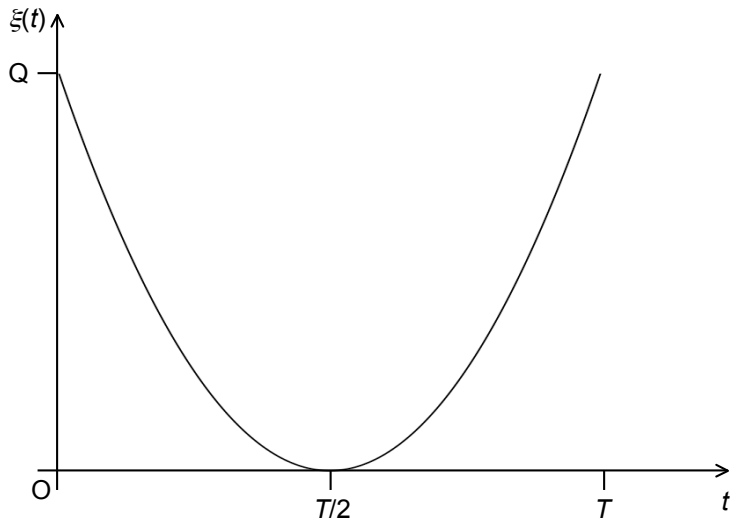

Figure 3.6: Quadratic phase error.

The FWHM resolution and peak amplitude are plotted as a function of Q in Figures 3.7 and 3.8 respectively.

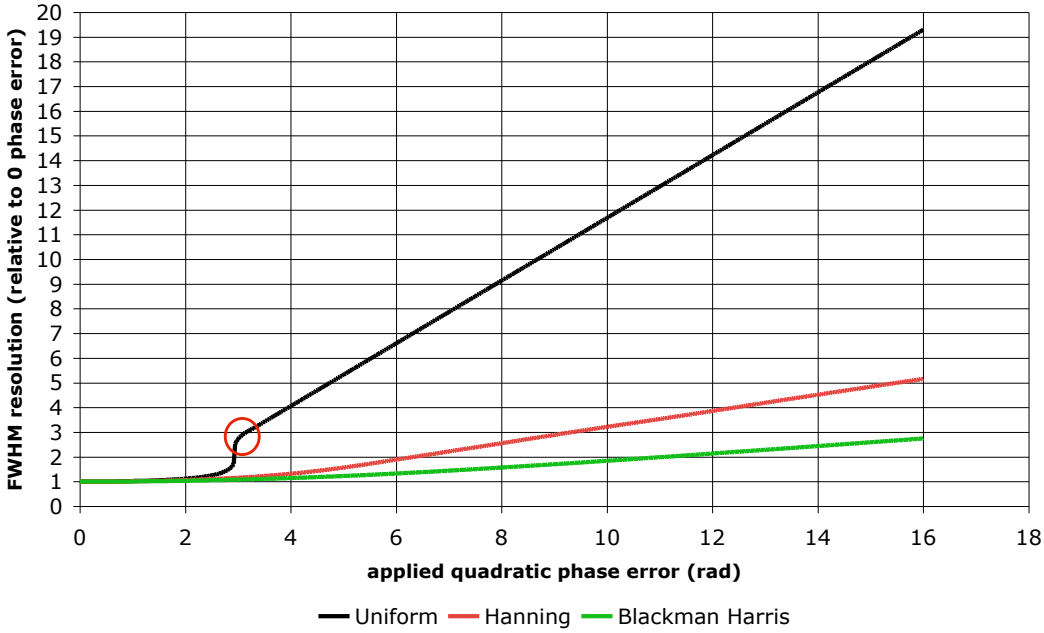

Figure 3.7: FWHM resolution against applied QPE amplitude for Uniformly, Hann, and Blackman-Harris weighted signals. The red circle indicates the splitting of the PSF into two edge peaks. The FWHM width is a poor measure of resolution here.

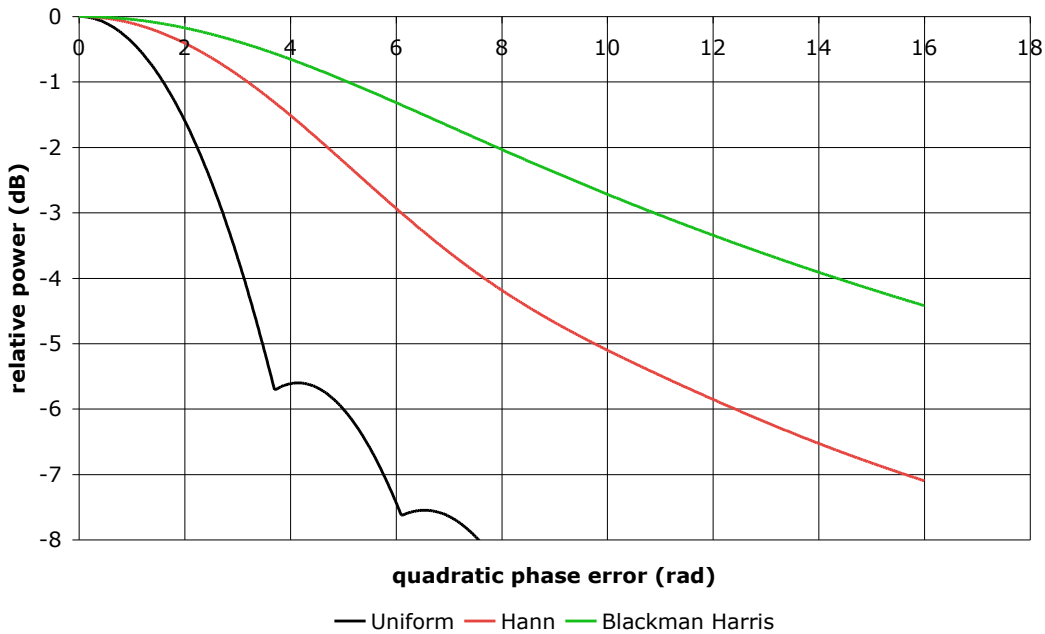

Figure 3.8: Mainlobe power against applied quadratic phase error amplitude for Uniformly, Hann, and Blackman-Harris weighted signals.

It can be seen from Figure 3.1 that, in all the cases, the applied QPE degrades the resolution and the sensitivity of the response but that the choice of window function makes a large difference to the degree of degradation.

The PSFs for a small number of values of Q are shown in Figures 3.9, 3.10, and 3.11 for Uniform, Hann, and Blackman-Harris window weighting functions respectively.

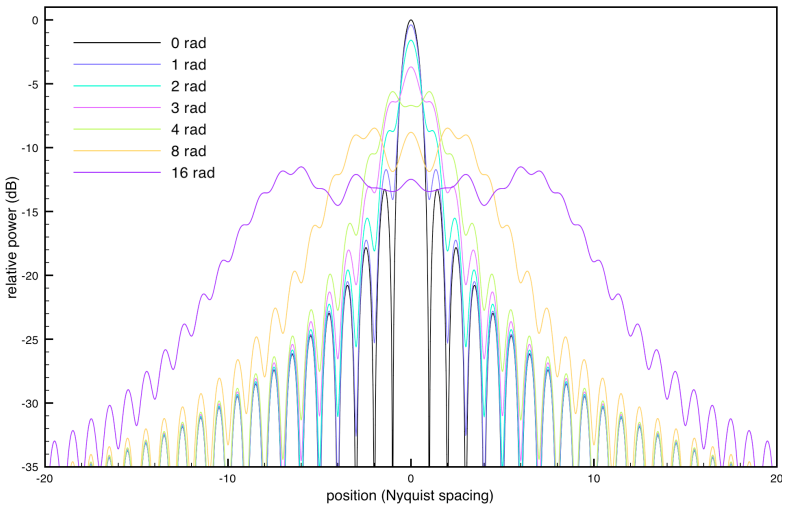

Figure 3.9: The PSFs for a range of applied QPEs. The signal was Uniformly windowed. See also Figure 3.1.

From the PSFs and the plots of FWHM resolution and response amplitude, it can be seen that the Uniformly weighted signal is most severely affected by the quadratic phase error, that the Hann weighted signal is less badly affected, and that the Blackman-Harris signal least affected. This is because the window functions, shown in Figure 3.12, suppress the signal towards its ends, and this is where the most severe phase error occurs. The Uniform signal is equally sensitive to phase errors over its duration, the Hann weighting suppresses the ends, and the Blackman-Harris suppresses the ends of the signal even more strongly.

From the graphs of the PSF at each value of Q, the effect of the increasing QPE can be seen clearly. The shape of the Uniform-weighted PSF is severely distorted by 4 radians of QPE. The peak of the response is split in two, and this explains the jump in the resolution curve, which is circled in Figure 3.7.

However, the windowed signals' PSFs are much less affected, although subtle changes are still revealed in the broadening of the mainlobe and the

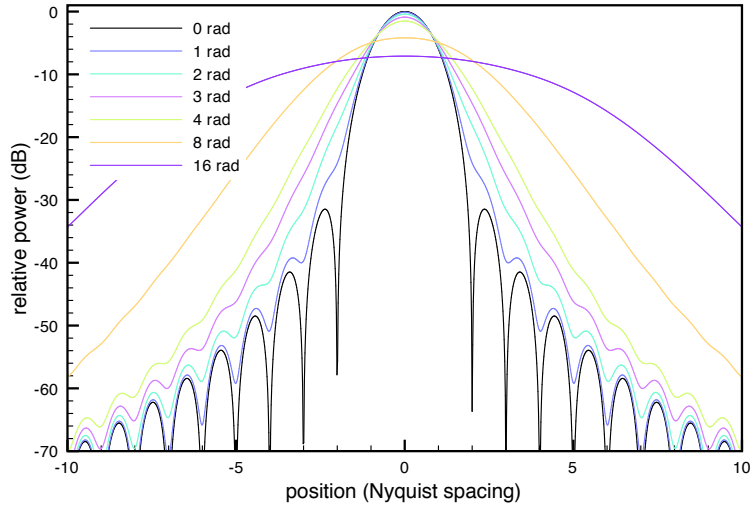

Figure 3.10: The PSFs for a range of applied QPEs. The signal was Hann windowed.

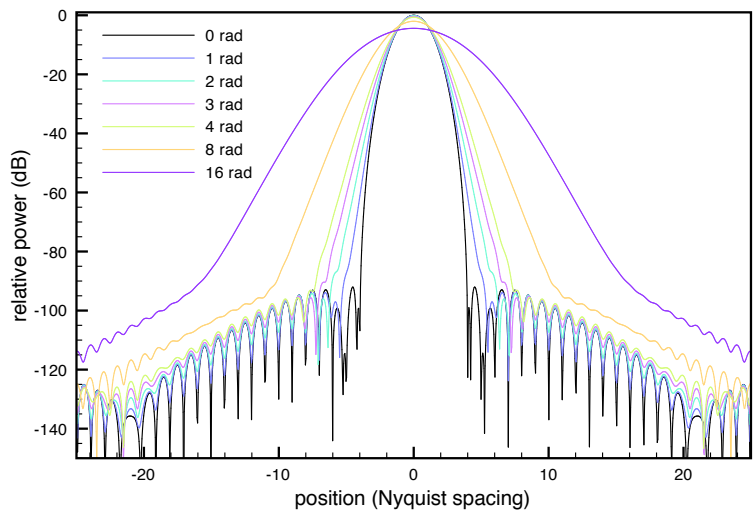

Figure 3.11: The PSFs for a range of applied QPEs. The signal was Blackman-Harris windowed.

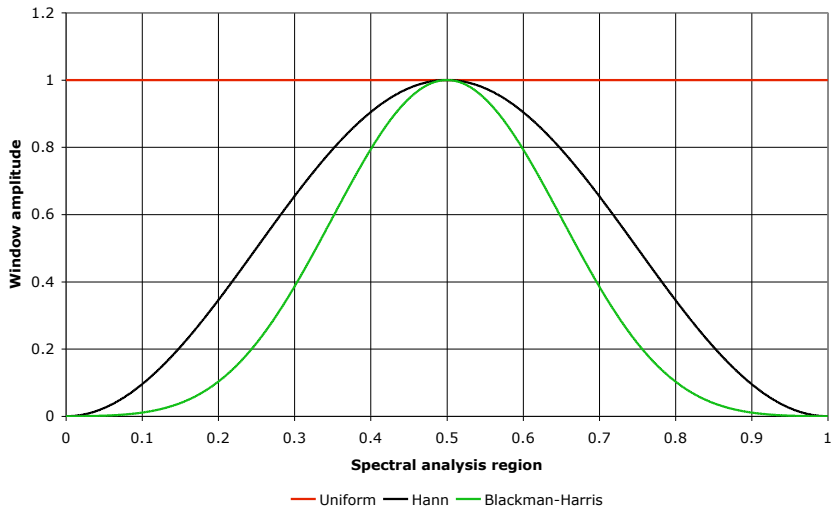

Figure 3.12: The amplitude window functions used in the demonstrations in this chapter. The parameters for these window function are given in Table 3.1. The values in the table specify the window function according to (3.5). Note that the Blackman-Harris window, which has gain in the middle, has been normalized in this plot to aid comparison of the windows.

rising and changing structure of the sidelobes.

Nevertheless, a considerable degree of QPE resistance is conferred by window weighting.

If a cubic phase error of the form

$$\xi(t) = \frac{8C}{T^3}\left(t - \frac{T}{2}\right)^3, \tag{3.19}$$

which is illustrated in Figure 3.13, is applied instead of a quadratic one, then the effect on the PSF is very different. In this case, the resolution, shown in Figure 3.14, and the main response amplitude, shown in Figure 3.15, are relatively unaffected, but the sidelobe levels, shown in Figure 3.16, rise dramatically.

The plots of the PSF, Figures 3.17, 3.18, and 3.19, make it immediately clear that the resolution and amplitude are not relevant measures of image quality for the case of cubic phase errors. In this case, the dramatically rising sidelobes are the most significant degradation.

The resolution, response amplitude, and sidelobe level can all be plotted from the simulations, providing accurate relationships between the quantities and the phase error magnitude.

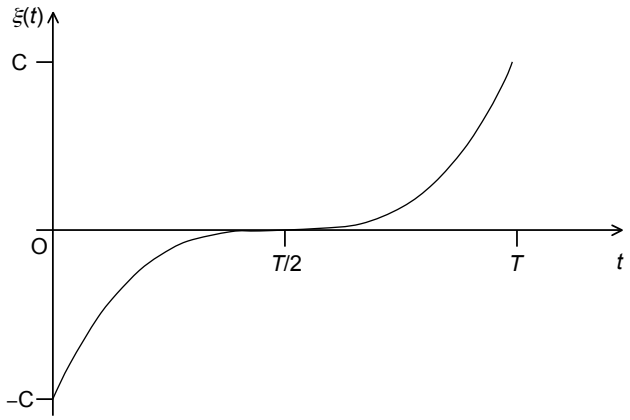

Figure 3.13: Cubic phase error.

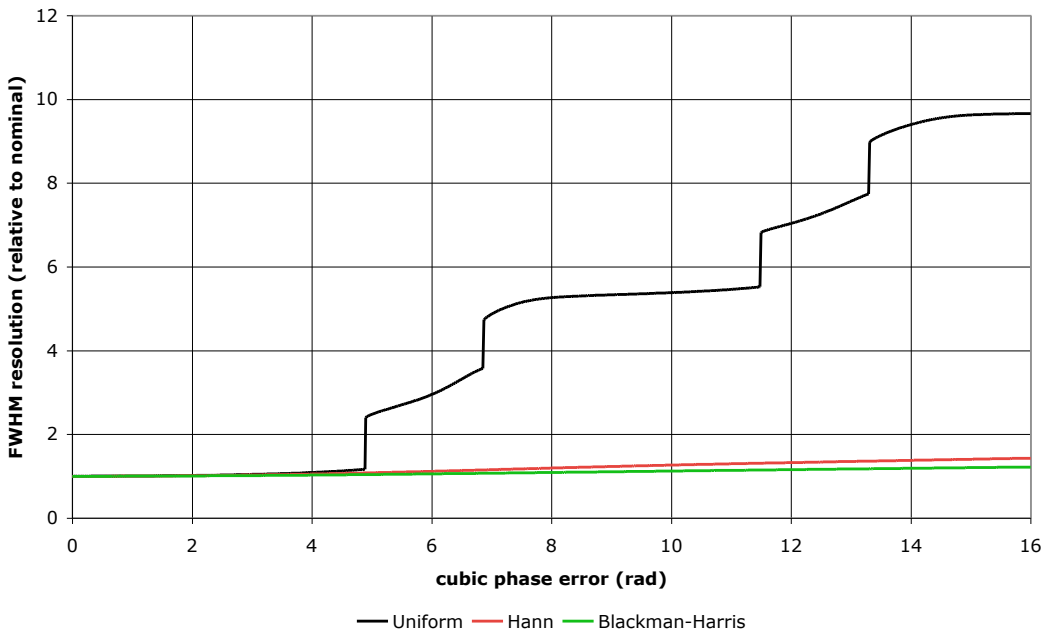

Figure 3.14: The FWHM resolution with increasing peak cubic phase error. The resolution is jumping in the Uniform case because the sidelobes are rising above the −3 dB level relative to the peak. This information is provided clearly by the simulated PSFs, shown in Figure 3.17.

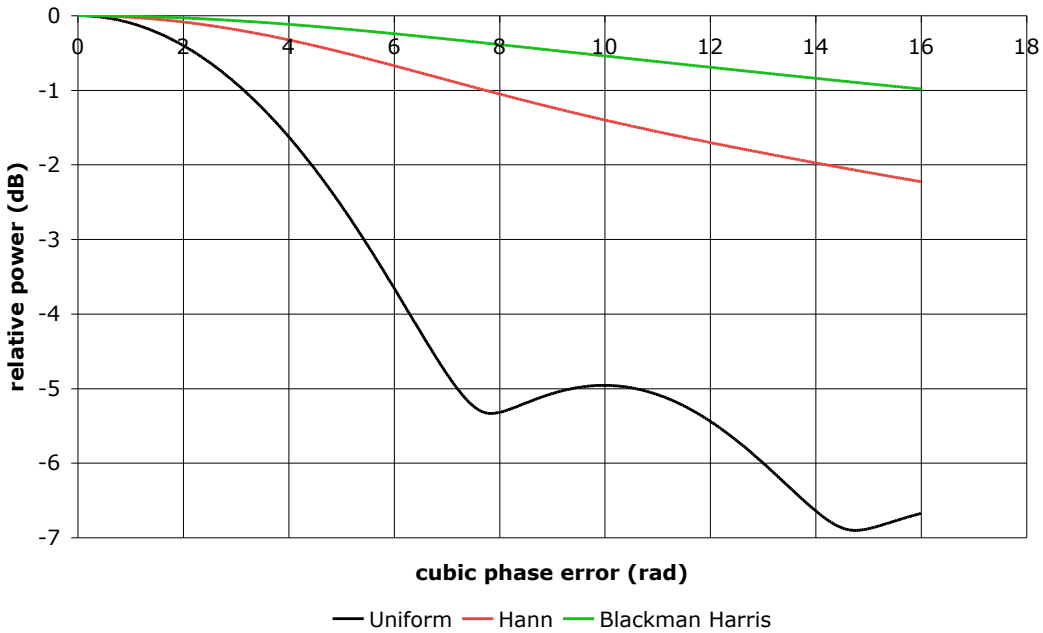

Figure 3.15: Mainlobe power against applied cubic phase error amplitude for Uniformly, Hann, and Blackman-Harris weighted signals.

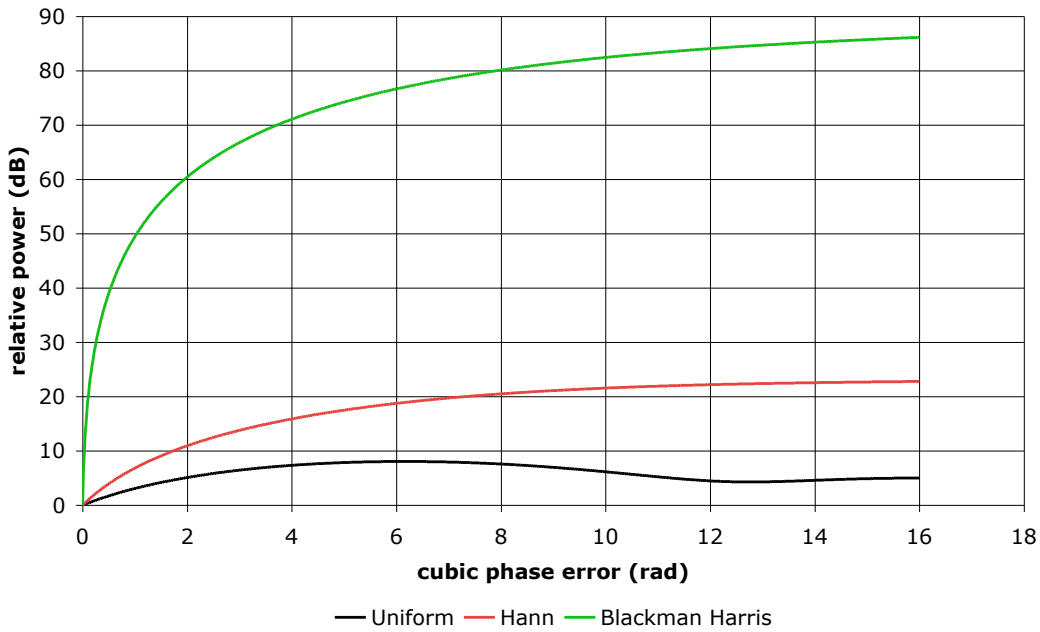

Figure 3.16: First sidelobe power against applied cubic phase error amplitude for Uniformly, Hann, and Blackman-Harris weighted signals.

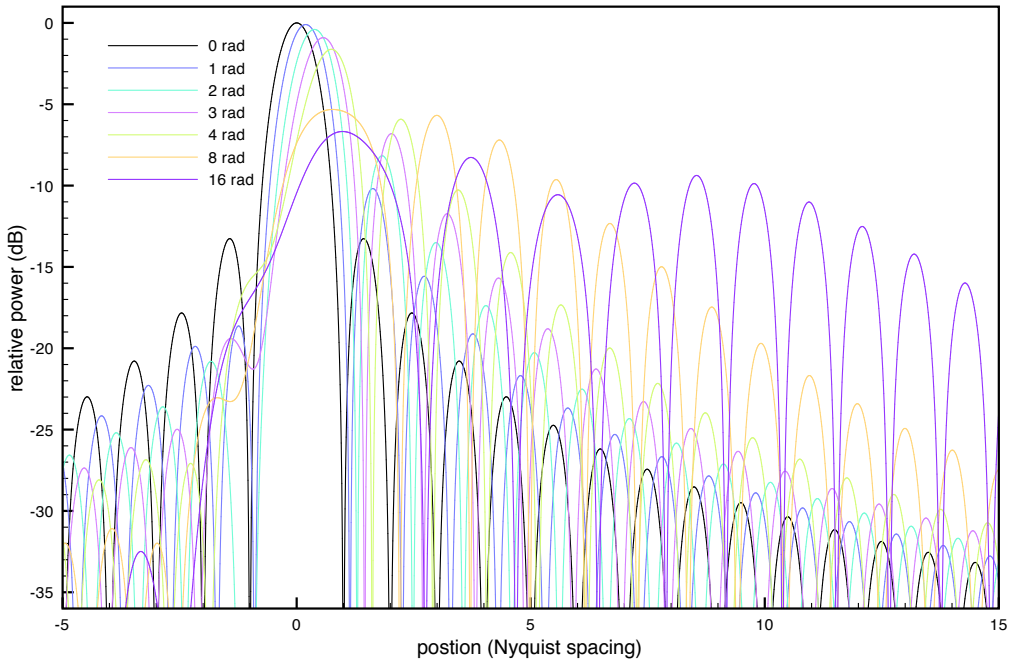

Figure 3.17: The PSFs for a range of applied cubic phase errors. The signal was Uniformly weighted.

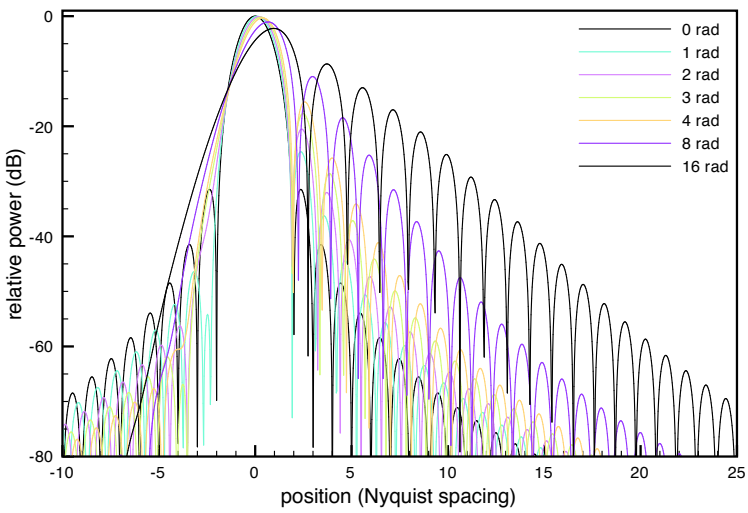

Figure 3.18: The PSFs for a range of applied cubic phase errors. The signal was Hann weighted.

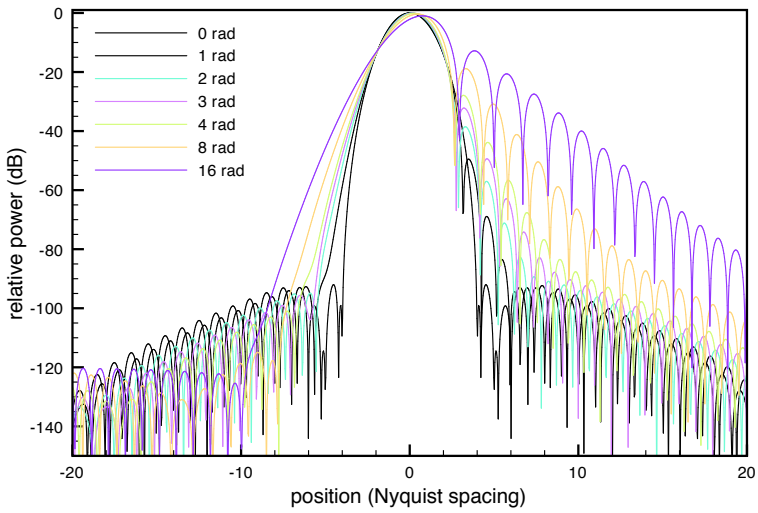

Figure 3.19: The PSFs for a range of applied cubic phase errors. The signal was Blackman-Harris weighted.

This illustrates the usefulness of an at least partly graphical approach to describing the quality of the PSF. For example, it is clear from the graph shown in Figure 3.19 that, in the case of the Blackman-Harris window weighted signal with cubic phase errors, the FWHM resolution is not a useful measure of the image quality.

It is clear that much useful information is available from the graphs. They provide both an easy way of inspecting the PSF for interesting features and a means of calculating curves of relevant quantities, should they be required. This is a very useful technique when establishing tolerances for systems and components.

3.5.2 Hardware simulated radar test

For sufficiently small ranges, the phase error due to chirp nonlinearity scales with the range of the reflector. This can be seen from the form of the phase error in the dechirped signal due to chirp nonlinearity found in Section 3.4.1:

$$\xi_{\text{nonlin.}}(t,R) = 2\pi \left[\int_0^t \epsilon(t')\mathrm{d}t' - \int_0^{t-\tau} \epsilon(t')\mathrm{d}t' \right]. \tag{3.20}$$

For small values of τ, this can be approximated to give

$$\xi_{\text{nonlin.}}(t,R) \approx 2\pi\tau\epsilon(t) = \frac{4\pi R}{\text{c}}\epsilon(t), \tag{3.21}$$

which illustrates the scaling with reflector range.

The small-τ approximation is nearly always valid but is unnecessary for the range-standoff diagrams, which can use the exact form of the phase error given by (3.20).

In Chapter 4, a method based on the Phase Gradient Algorithm to find very precise estimates of the chirp frequency error, $\epsilon(t)$, is described .

To demonstrate the ability of the range-standoff diagrams to predict the shape of the PSF in the presence of arbitrary chirp nonlinearity, a low-frequency high-fidelity hardware radar simulator was made. This simulator was based on a desktop computer, a four-channel (two in, two out) sampling card, and a low-frequency mixer.

To avoid using delay lines, two copies of the chirped signal were simultaneously transmitted from the sampling card's two outputs, one copy delayed by an interval corresponding to the round-trip time to a synthetic reflector.

The direct and delayed signals were applied to the mixer's LO and RF ports, and the resulting IF signal was sampled back into the computer, where it was windowed and Fourier transformed.

The low-frequency mixer was required because the transmitted and received signals were generated by a sampling card, a 12-bit ExacqDAQ CH3150, with a maximum digital-to-analogue sampling rate of 20 MHz simultaneously on two channels.

The form of the transmitted signal was

$$s_{\text{tx}}(t) = v_{\text{LO}} \cos\left(2\pi \int_0^t f_0 - \frac{B}{2} + \frac{Bt'}{T} + \epsilon(t')\mathrm{d}t'\right), \tag{3.22}$$

and the delayed signal applied to the RF port was

$$s_{\text{rx}}(t) = v_{\text{RF}} \cos\left(2\pi \int_0^{t-\tau} f_0 - \frac{B}{2} + \frac{Bt'}{T} + \epsilon(t')\mathrm{d}t'\right), \tag{3.23}$$

where v_{LO} and v_{RF} are suitable signal voltages for the two ports of the mixer.

Whilst mixers used at higher frequencies are passive devices, the mixer used in the demonstration is an active circuit based on an MC1496 chip. A

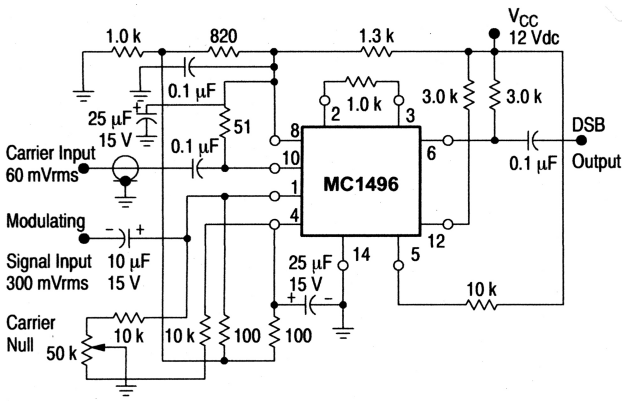

Figure 3.20: Schematic diagram for radio-frequency mixer circuit. (Reproduced from ON Digital MC1496 data sheet.)

Case	Form of nonlinearity (Hz)
Ideal	0
Small quadratic	$1.2 \times 10^{10} t^2$
Big quadratic	$4.0 \times 10^{10} t^2$
Cubic	$10^{14} t^3$
Sinusoidal	$5 \times 10^3 \sin\left(\frac{4\pi t}{T_{\text{chirp}}}\right)$
Polynomial	$-10^{11} t^2 + 10^{14} t^3 - 10^{17} t^4 + 10^{20} t^5 + 10^{23} t^6 - 10^{26} t^7$

Table 3.2: The types of chirp nonlinearity used in the radio frequency radar simulation to validate the Range Standoff Diagrams.

mixer circuit is described in the data sheet for the chip and is reproduced in Figure 3.20.

To reduce unwanted capacitance and leakage, the circuit was point-to-point wired rather than constructed on strip board.

To demonstrate the effect of nonlinear chirps, the hardware radar simulator was run with various forms of nonlinearity, which are shown in Table 3.2. The nominal system parameter values are shown in Table 3.3, and Hann window weighting was used.

The results of the radar measurements and the corresponding predictions produced using the range-standoff diagrams are shown for each case in Figures 3.22, 3.23, 3.24, 3.25, and 3.26.

From all of the examples, it can be seen that there is good agreement between the predicted and the measured forms of the PSF. The shape of the

Parameter	Nominal Value
B	300 kHz
T	0.001 s
f_0	400 kHz
τ	0.1 µs ($R = 15$ km)

Table 3.3: The nominal values of the low-frequency hardware radar simulation.

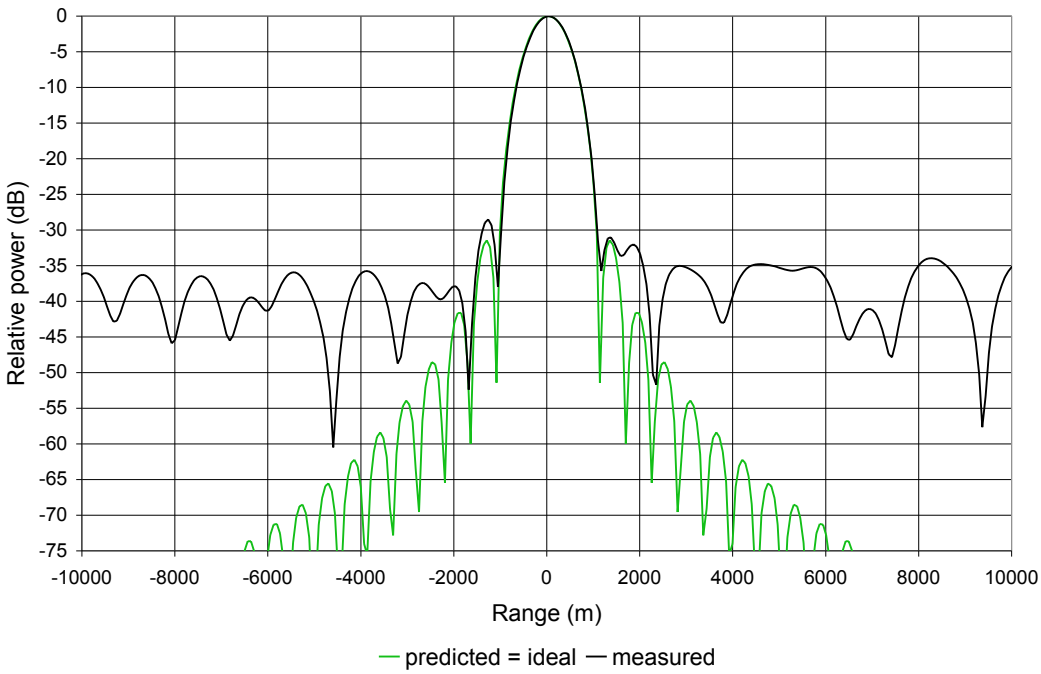

Figure 3.21: The measured and simulated PSF for the ideal case.

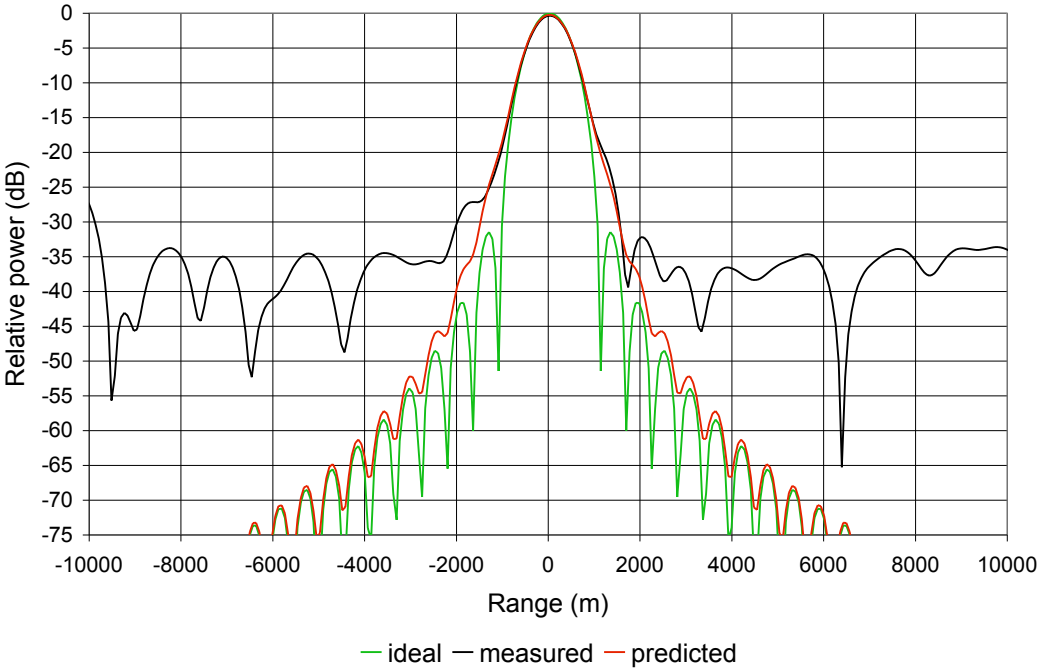

Figure 3.22: The measured and simulated PSF for the small quadratic case.

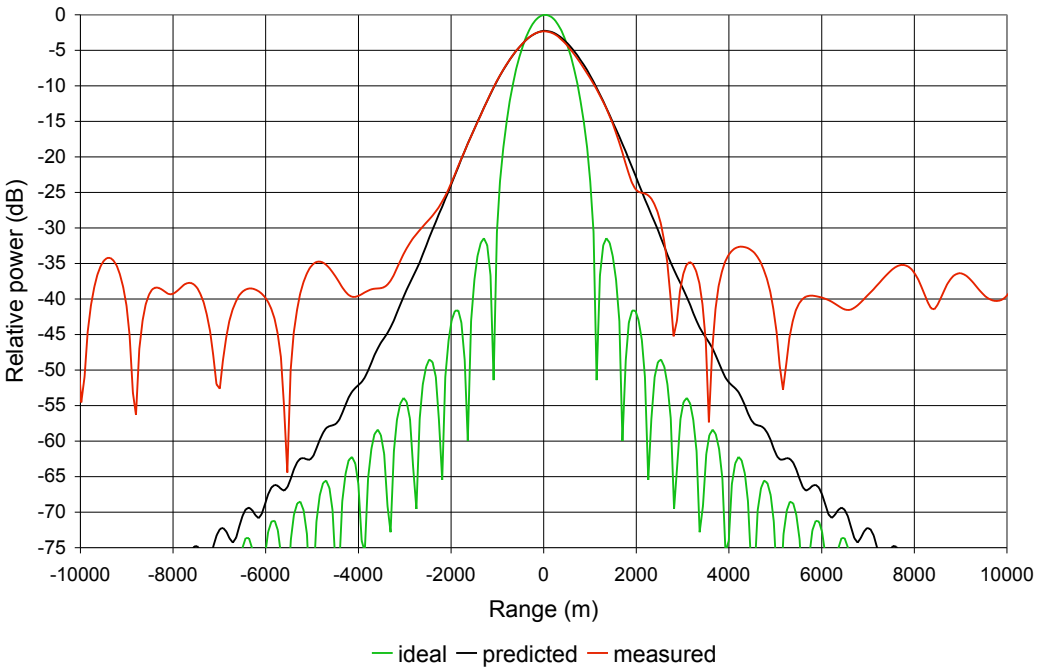

Figure 3.23: The measured and simulated PSF for the large quadratic case.

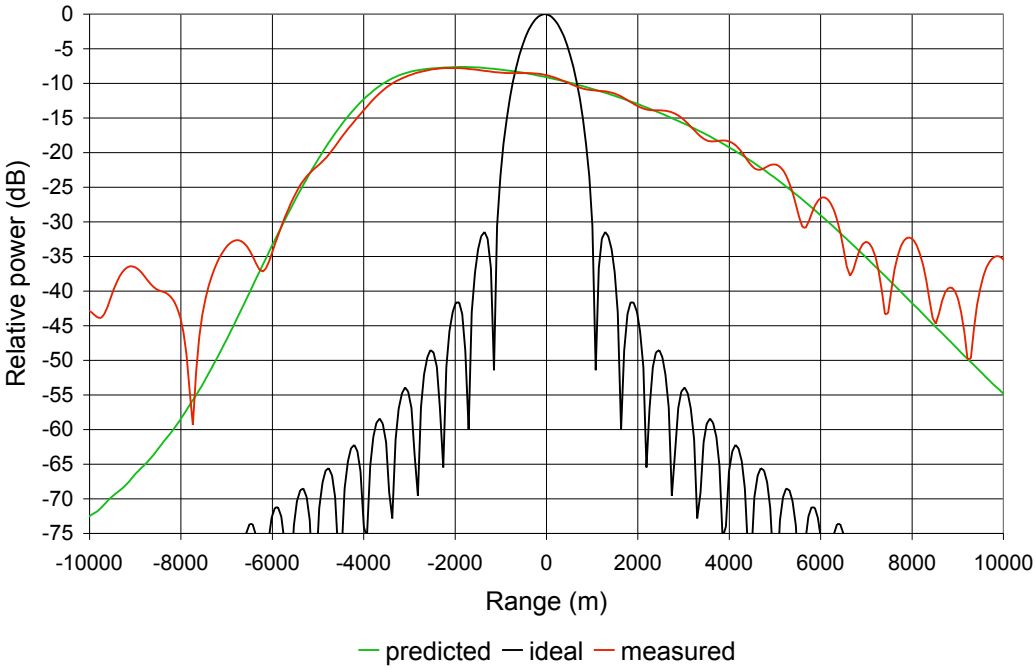

Figure 3.24: The measured and simulated PSF for the cubic case.

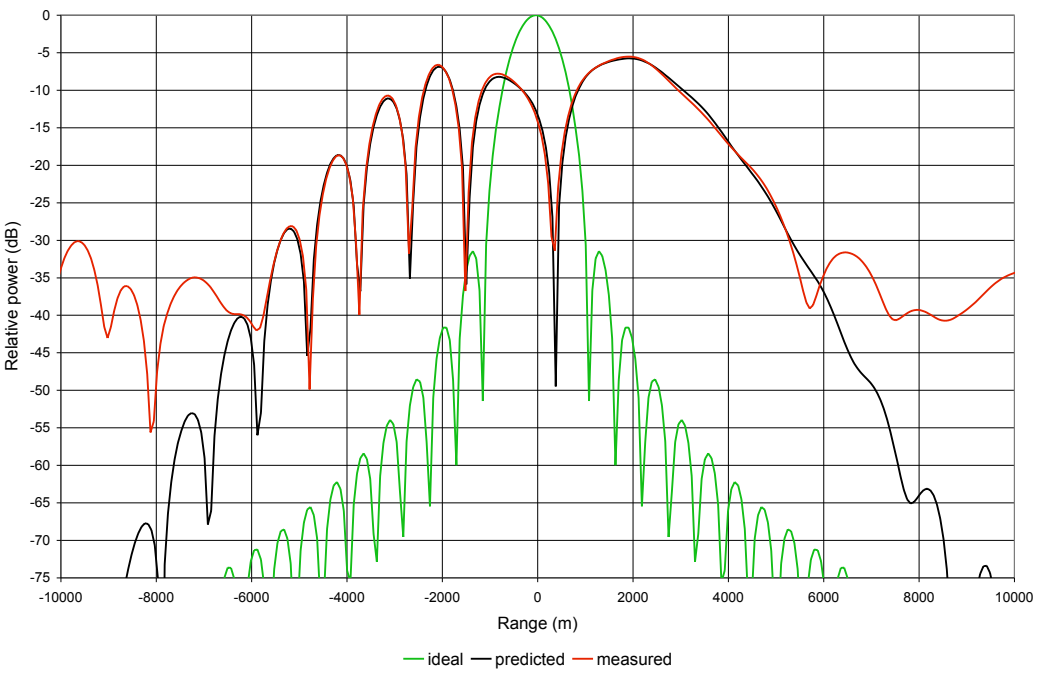

Figure 3.25: The measured and simulated PSF for the sinusoidal case.

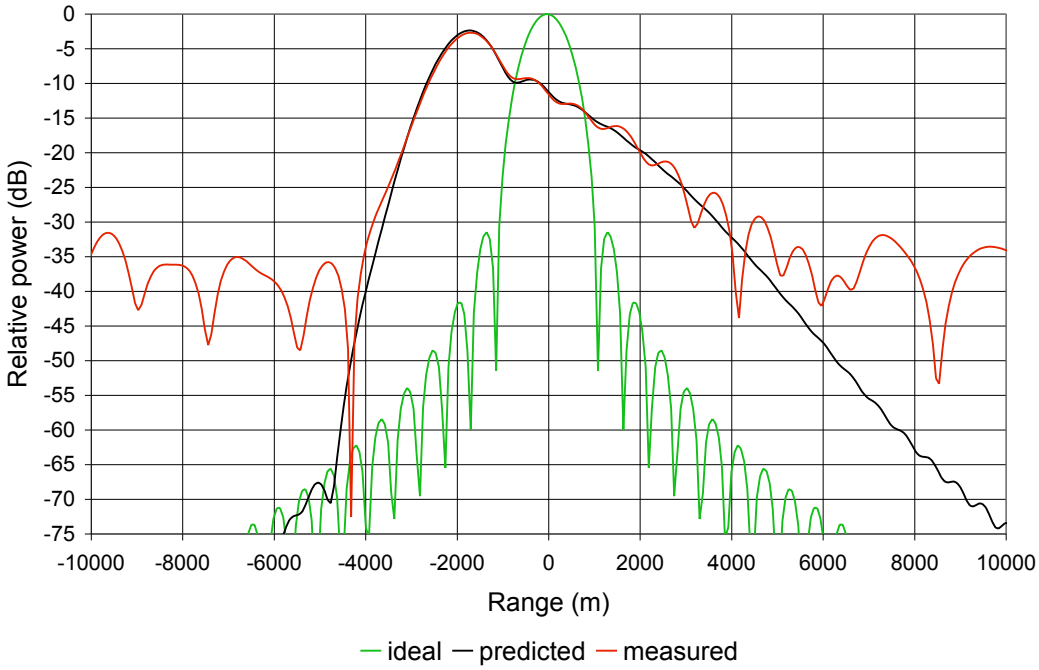

Figure 3.26: The measured and simulated PSF for the polynomial case.

Case	Predicted	Measured
Ideal	0	50
Small quadratic	600	660
Big quadratic	2000	2100
Cubic	5000	5000
Sinusoidal	305	100
Polynomial	0	120

Table 3.4: Simulated and measured range of PSF found using range-standoff diagrams. The notional FWHM resolution is 730 m.

response is predicted, with subtle detail being accurately represented.

In each of the graphs, the predicted and actual PSFs were finely registered (shifted in range and power) to aid comparison of the shape. However, there was generally good agreement between the predicted and the actual range offsets and powers, as shown in Table 3.4. Prior to registration, the predicted and measured power agreed to within 0.1 dB in all of the cases. Similarly, the range offsets agreed to within 1/3 of the nominal FWHM resolution, the nominal FWHM resolution being 730 m.

3.5.3 Short-range instrumentation radar test

An instrumentation radar provided a test platform to demonstrate the ability of the range-standoff technique to compute the PSF of a real radar with a badly nonlinear chirp.

The radar [76] had been developed for testing radar components and architectures. A schematic diagram is shown in Figure 3.27, from which it can be seen that the radar is a dual-horn, homodyne FMCW radar.

The oscillator used is a 7.833 GHz Micro Lambda Wireless MLPF 1463FM Permanent Magnet YIG Tuned Oscillator (PMYTO) with 78 MHz per volt tuning sensitivity. The PMYTO is swept by a Hewlett Packard HP33120A digital arbitrary signal generator. The signal from the PMYTO is multiplied by 12 to 94 GHz by an ELVA-1 IAFM-10/94/12 IMPact ionization Avalanche Transit Time (IMPATT) multiplier.

The separate corrugated transmit and receive horns have their Gaussian beams focussed by a pair of plastic lenses to produce 1° wide overlapping beams (about 70% overlap at 40 m).

The dechirped signal is amplified using a Wenzel Blue Top LNAA-30-0 amplifier, low-pass filtered (1.9 MHz) to prevent aliasing, and then sampled into a Pentium 4 Dell desktop personal computer using a 40 MHz, 12 bit CH3150 ExacqDAQ sampling card.

The reflector arrangement is shown in Figure 3.28, in which the precision trihedral reflector can be seen. Two reflectors were used, a 20 dBsm precision trihdral at 56 m and a 30 dBsm precision trihdral at 85 m.

The radar was run in the following configuration: the carrier frequency was 94 GHz, the nominal chirp bandwidth was 600 MHz, and Uniform window weighting was used. The chirp was made nonlinear by a sinusoidal frequency nonlinearity of amplitude 48 MHz and period equal to that of the chirp.

The two reflectors were imaged using the radar, and the resulting imagery and the corresponding predictions are shown in Figures 3.29 and 3.30. By comparing the plots in each figure, it can be seen that there is reasonable agreement between the prediction and the measurement.

The overall sense of shape is indicated, but the response fades slightly with decreasing range. This is not predicted by the range standoff diagrams and is not expected for this kind of chirp nonlinearity. This might suggest a method for establishing the frequency response of the pre-dechirp stages of a radar.

The measured responses do not follow the predictions very far down the power scale for two reasons: firstly, the degraded response is convolved with the clutter in the scene, reducing the dynamic range of the image; secondly the noise floor due to the phase noise of the frequency multiplied PMYTO signal and the spurs introduced by the HP signal generator chirping the oscillator (which are smeared out by the frequency error) is no better than −40 to −30 dB. Further tests could be done with low-clutter scenes and larger RCS reference reflectors.

It should be noted that, as before, the profiles have been minutely registered in range ($< \rho/3$) and amplitude (< 0.1 dB) to ease comparison of the PSF shapes.

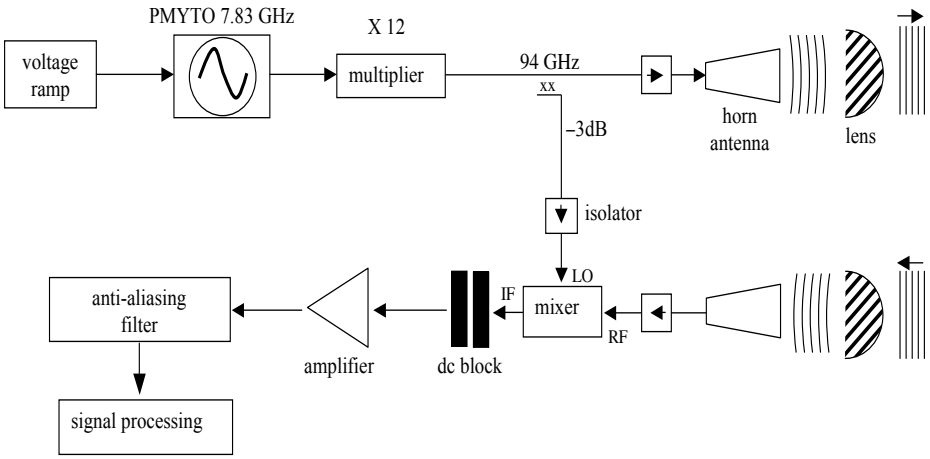

Figure 3.27: The circuit diagram of the instrumentation radar used in tests to validate the range standoff diagram technique.

3.6 Conclusions

In this chapter, I have described a simple technique (Range Standoff diagrams) for calculating and graphically presenting the effects of phase and amplitude error on the PSF of an FMCW radar. I have also described a simple formula for calculating the ideal PSF given signal window weighting for the cosine family of window weighting functions.

The ability of the Range Standoff method to highlight detailed and subtle effects on the PSF for a variety of errors was demonstrated, illustrating the

Figure 3.28: A photograph of the radar test range. The radar can be seen in the open laboratory window.

points that, firstly, simple metrics of PSF quality are not always ideal measures of image quality and, secondly, numerical methods can provide easy and accurate methods for predicting radar performance.

The ability of the technique to predict PSF degradation at a given range was demonstrated for a variety of cases.

In future work, more sensitive measurements could be made to validate the image phase prediction and the prediction of the effects of amplitude modulation.

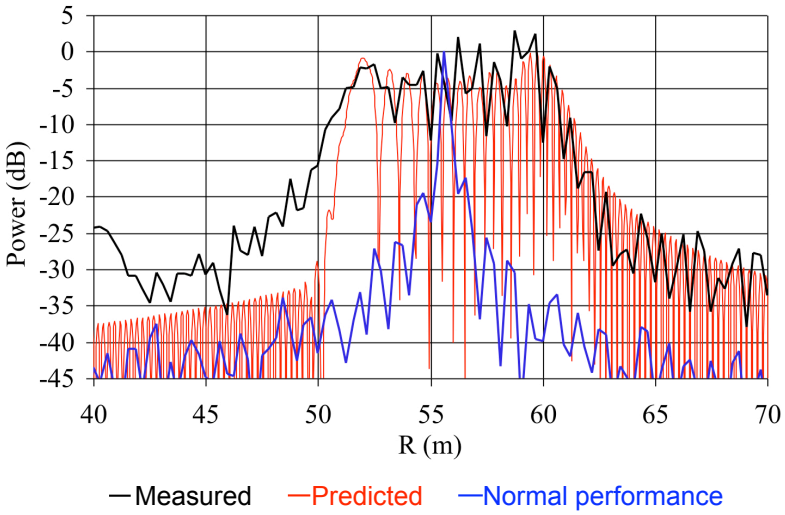

Figure 3.29: The measured normal, measured nonlinear, and predicted nonlinear chirp responses of the instrumentation radar to the close trihedral. It can be seen that there is good agreement between the measured PSF and that predicted using the range-standoff diagram.

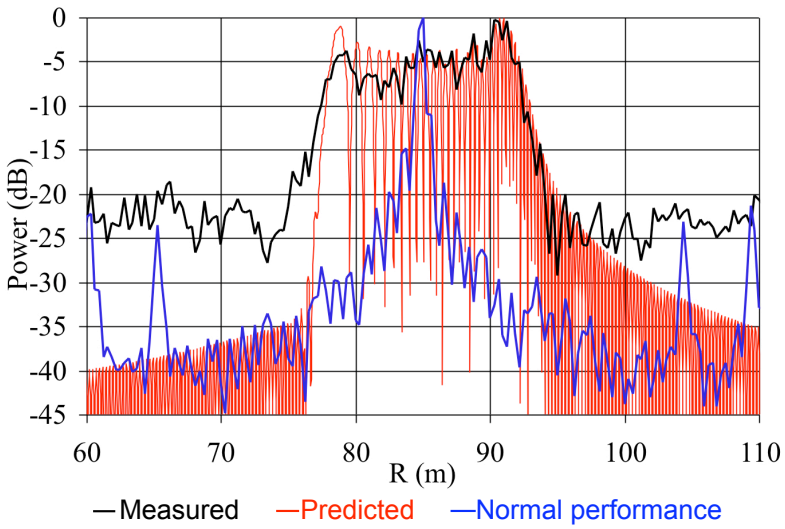

Figure 3.30: The measured normal, measured nonlinear, and predicted nonlinear chirp responses of the instrumentation radar to the far trihedral. It can be seen that there is good agreement between the measured PSF and that predicted using the range-standoff diagram. N.B. the noise floor in the 'measured' plot can be seen to be due to the swept out spurs in the 'normal performance' plot.

Chapter 4

Range autofocus for FMCW radar

In this chapter, I shall describe a software-based method for estimating and compensating for chirp nonlinearity in FMCW radars. The method is based on two existing techniques: the Phase Gradient Algorithm (PGA) and time-domain warping of the dechirped signal. I shall demonstrate the new method on both typically and severely nonlinear chirps. I shall also demonstrate retrospective application of the method on archive radar data.

Part of the work described in this chapter forms a paper accepted for publication in IET Radar Sonar Navigation under the title 'Range Autofocus for Linearly Frequency Modulated Continuous Wave Radar'.

4.1 Introduction

FMCW radar requires a highly linear frequency chirp if the resultant imagery is to have near-ideal resolution, dynamic range, SNR, and geometric precision [10, 43, 47, 48, 77, 78].

Many methods of achieving good chirp linearity exist, including characterization of the chirp nonlinearity and pre-distortion of the control voltage applied to the oscillator [50]; use of feedback via delay lines to modify the voltage control [55, 56]; use of a frequency divider and a Direct Digital Synthesizer (DDS) to linearize the chirp [79]; and phase locked loops [80, 81].

In certain circumstances, it is necessary or desirable not to make hardware provision to linearize the chirp. For example, in a test radar, it might be impossible to include linearization components without modifying the performance of the components under test. Another example might be provision

of a correction/compensation for an existing radar that cannot be modified to include extra hardware. In some circumstances, it might be desirable to keep the hardware to a minimum, for reasons of physical size, electrical power requirements, or cost. In many cases, it would simply be easier not to have to use hardware linearization.

The method proposed in this chapter provides an entirely software-based autofocus technique that enables any FMCW radar to be focussed to near ideal performance.

The method comprises two existing techniques: the PGA [60, 82, 83], which is used to estimate the phase error that is defocussing the PSF of a reference reflector, and a time-domain warping of the signal [54, 58], which is used to simultaneously correct the signal for all ranges, focussing the entire range profile.

This method does not require hardware modification to measure the phase error because the reference phase error can be obtained from a real reflector in the radar's beam. This is made possible by the ability of the PGA to produce a stable estimate of the signal phase directly from the defocussed images of a reference reflector produced by the radar. The PGA achieves this by exploiting both the underlying repeatable nature of the phase error due to the chirp nonlinearity and the random nature of the phase error due to noise. By combining the phase errors that defocus multiple notionally identical images of the same reference reflector, the phase error due to chirp nonlinearity can be stably estimated.

From this stable estimate of the IF phase error due to chirp nonlinearity, a time-domain signal warping can be derived that will distort all of the nonlinear phases, making them linear.

The method proposed in this chapter is called an autofocus technique because the information to focus the radar's PSF is extracted from the defocussed PSF itself. This type of technique, including the PGA, is widely used in SAR, where two-dimensional imagery is focussed in the cross-range direction to remove errors chiefly introduced by nonlinearity in the nominally linear trajectory of the radar.

This chapter has the following structure: in Section 4.2, the proposed method is described and explained. In Section 4.3, the method is demonstrated using a VCO-based radar: first on a deliberately (and badly) nonlinear case over a moderate chirp bandwidth and second using the same radar's inherent (and slight) nonlinearity over a large chirp bandwidth. Finally, the

method is demonstrated on archive data acquired with a long-range terrain-mapping radar, demonstrating retrospective application, which enables poorly focused archive data to be focussed.

4.2 Theory

In this section, the description of FMCW signal phase errors established in Chapter 3 is developed for the specific case of nonlinear chirps. The two underlying techniques, the PGA and time warping, are described, and their combination to provide an FMCW range autofocus is described.

The proposed method comprises three distinct stages, an error estimation stage, a warping calculation stage, and a signal correction stage. All of these stages can be operated independently.

4.2.1 Stage 1: Estimating the phase error

The first stage, based on the PGA, calculates a stable estimate of the repeatable part of the phase error defocusing an isolated point-like reference reflector at a known range.

The phase error defocussing the PSF is described by the expression for the signal phase found in Section 3.4.1. Equation (3.12) gives the phase of the dechirped signal. In this chapter, it is the first two parts that are relavant. The first part, the nominal phase, is the linear phase ramp that determines the range and image phase of the response. The second part is the error in the phase due to the nonlinearity of the frequency chirp.

For a radar that is ideal apart from chirp nonlinearity, the phase of the dechirped echo from a single reflector is, using (3.12), (2.3), (3.20), and (3.21), given to a good approximation by

$$\phi_{\text{nonlin.}}(t,R) \approx 2\pi\tau\left(\frac{Bt}{T} + \epsilon(t)\right), \tag{4.1}$$

from which it can be seen that both the nominal part and the part due to chirp nonlinearity scale directly with reflector range via the round-trip delay, $\tau = 2R/\text{c}$.

In many cases where the radar is static or involved in system testing, it should be possible to site a reference reflector at some known range. But, in most cases, a sufficiently point-like reflector of opportunity could be used,

provided that its range is precisely known. This range could be found with a laser range finder or GPS.

The reference reflector is imaged repeatedly using the uncorrected radar. Each time, a region around the point response is extracted from the range profile, the centre of which is chosen to the be at the peak of the actual response. The apparent range of the reflector can be used to correct the chirp for an overall error in B: the actual bandwidth of the chirp is given by

$$B_{\text{actual}} = \frac{R_{\text{apparent}}}{R_{\text{actual}}} B, \tag{4.2}$$

and this value should be used to revise the nominal value, B. This removes the linear part of the frequency error by accepting the actual bandwidth value as the nominal one. This assumes that the actual value of T matches the nominal one. If this were not the case, then T could be adjusted, too.

If the true range of the reference reflector were not known, e.g. in the case of opportunistic reference reflectors, the linear part of the phase error could be ignored and the apparent range could be used. The resulting focussing would not necessarily hold very well at ranges different to that of the reference reflector, but might provide good enough focussing to allow the true range to be found from the context of the imagery. For example, the scatterer may be identified on a map.

The width of the extracted region determines the bandwidth of the autofocus response. Usually, as the method is iterated and the point response sharpens, the width can be reduced, further improving the SNR of the autofocus solution.

The extracted part is zero-padded then inverse Fourier transformed, yielding the oversampled dechirped signal of the reference scatterer, which is also downconverted relative to the notional dechirped frequency (at the centre of the extracted region). It is labelled $s(t)$ and, following the notation in Chapter 3, is given by

$$s(t) = A(t)e^{i\xi(t)} + N(t), \tag{4.3}$$

where $A(t)$ is real, positive, and the amplitude of the signal. $\xi(t)$ is real and the phase error in the signal. Note that, after down conversion, the ideal phase of a dechirped signal is constant.

Here, the phase error labelled $\xi(t)$ is taken to be due solely to the chirp nonlinearity, and $A(t)$ is taken to be due solely to filter roll off etc.. A complex quantity, $N(t)$, represents all noise due to thermal effects, interference etc.,

and the spurious part of the signal due to clutter. For most situations, the part of the signal due to the reference reflector will significantly dominate.

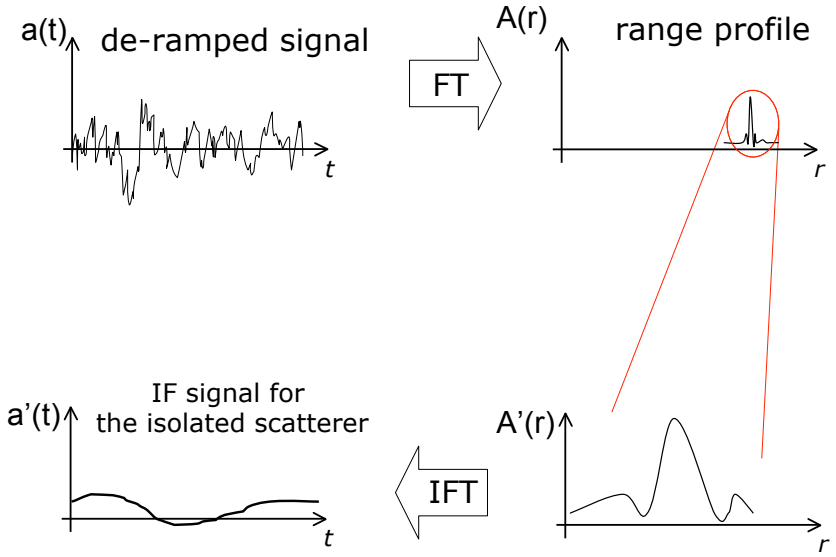

Figure 4.1: The first steps of the PGA: an image is formed, a suitable reference scatterer is isolated and then inverse Fourier transformed to give the signal corresponding to the extracted region. This is essentially a down conversion and band-pass filtering operation on the IF signal.

The aim of this process, which is summarized in Figure 4.1, is to find $\xi(t)$, which is the defocussing phase error. Unfortunately, the presence of noise and arbitrary phase offsets makes it impossible to extract and unwrap the phase of $s(t)$ to estimate $\xi(t)$. In Figure 4.2, the value of the signal in the complex plane is shown for two different images of the same reflector at four different times. It can be seen that estimating the instantaneous phase would not be useful.

The PGA works by finding the *change* in phase from one sample to the next, combining signals derived from multiple images of the same scatterer.

Finding the difference in the phase prevents wrapping. This is because, although $\xi(t)$ varies through large angles, the oversampling makes it vary only slightly from one sample to the next. This means that the phase difference per sample does not wrap. Additionally, working with the differential phase removes any arbitrary phase offsets.

The following expression converts the signal to differential-phase signals

$$u(t) = s(t + \delta t) \times s^*(t), \tag{4.4}$$

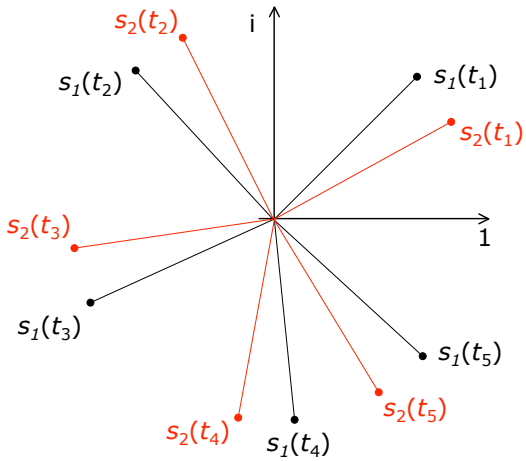

Figure 4.2: The complex values of $s(t)$ for two images of the same reflector at four different times. There is noise and an undetermined overall phase offset between the two signals. Additionally, the phase is wrapped.

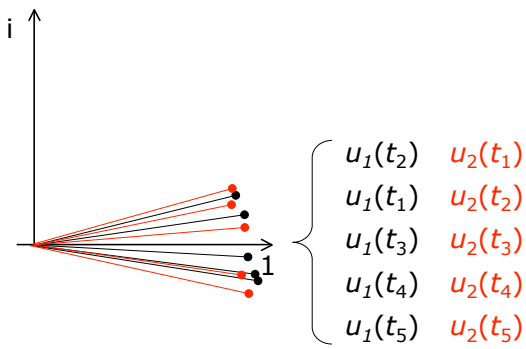

Figure 4.3: The complex values of $u(t)$ for two images of the same reflector at four different times. The arbitrary phase offset has been removed, and the remaining phase angles are small – they do not wrap. Compare this with the phase difference phasors shown in Figure 4.2.

where δt is the duration of one time sample in the signal. This is illustrated in Figure 4.3.

So

$$u(t) = \left[A(t+\delta t)e^{i\xi(t+\delta t)} + \eta(t+\delta t)\right] \times \left[A(t)e^{i\xi(t)} + N(t)\right]^*. \tag{4.5}$$

Multiplying out (4.5) gives

$$u(t) = A(t+\delta t)A(t)e^{i[\xi(t+\delta t)-\xi(t)]} + \overline{N}(t). \tag{4.6}$$

Defining

$$\Delta\xi(t) = \xi(t+\delta t) - \xi(t), \tag{4.7}$$

and

$$\bar{A}(t) = A(t+\delta t)A(t), \tag{4.8}$$

and $\overline{N}(t)$ as the noise part and substituting them into (4.6) gives

$$u(t) = \bar{A}(t)e^{i\Delta\xi(t)} + \overline{N}(t). \tag{4.9}$$

When multiple instances of $u(t)$ (derived from multiple radar range profiles of the reference reflector) are added, the deterministic part adds linearly in amplitude, but the noise part adds linearly in power. Because the deterministic part of $u(t)$ does not vary from one chirp to the next, the sum is a more stable estimate of $\Delta\xi(t)$ than any of the individual $u(t)$ measurements. This is illustrated in Figure 4.4.

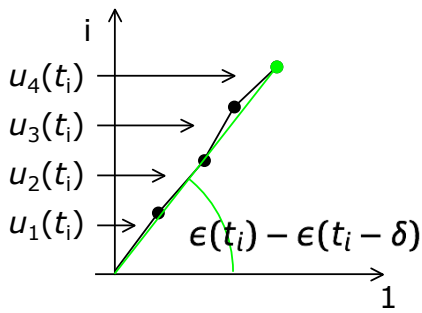

Figure 4.4: The quantity $u(t)$ found from different images of the reflector is accumulated at each value of t. The resulting vector sum (in green in the illustration) is dominated by the part common to all of the individual $u(t)$ values at t. The noise part of the sum does not increase as fast.

It has been assumed that the deterministic part of the phase error is due entirely to chirp nonlinearity, but in practice there will be a certain phase error

due to group delay etc.. However, this is usually very small compared with the phase error due to chirp nonlinearity. If it were a problem, the PGA could be run for reference reflectors at different ranges and the resulting phase errors separated into two parts: a constant part, which is due to group delay etc., and a linearly growing part, which is due to chirp nonlinearity. That is, the phase error could be found for a number of ranges and the following model fitted to the data,

$$\epsilon(t,R) = \epsilon_0(t) + \epsilon_R(t)R. \tag{4.10}$$

The $\epsilon_0(t)$ part indicates the group delay, and the $\epsilon_R(t)$ part indicates the part due to nonlinearity.

So, the reference reflector is repeatedly imaged, and $u(t)$ is found at each time for each image and added to an accumulator, $\Sigma_{\text{diff}}(t)$, where

$$\Sigma_{\text{diff}}(t) = \sum_{\text{images}} u(t). \tag{4.11}$$

$\Sigma_{\text{diff}}(t)$ is then used to find a stable estimate of the phase difference as a function of time,

$$\Delta\xi(t) = \text{Arg}\left[\Sigma_{\text{diff}}(t)\right]. \tag{4.12}$$

The PGA's estimate of $\xi(t)$ is found by accumulating the phase difference in time

$$\xi'(t) = \sum_{i=0}^{t/\delta t} \Delta\xi(i\delta t). \tag{4.13}$$

$\xi'(t)$ differs from $\xi(t)$ by a constant phase offset, which is not important. This completes the PGA.

Once the estimate of the phase error, $\xi'(t)$, has been found, it is useful to fit a curve to it to enable a biased representation of the phase error. This allows estimates of $\xi'(t)$ where the signal is strongest (large $\bar{A}(t)$), and so where the estimate of $\xi'(t)$ is most reliable, to dominate.

In the implementation used for the experiments discussed in Section 4.3, an $\bar{A}(t)$-weighted Least Mean Squares (LMS) fit of a polynomial was used. This discounts the parts where the signal strength drops, so avoids inadvertantly compensating for unrepresentative phase errors. Other curves, e.g. cubic splines, could be used. No deliberate window weighting was used when forming the images used in the PGA because this would desensitize the autofocus to phase errors at the ends of the signal.

4.2.2 Estimating the chirp nonlinearity from the phase error

A useful by-product of this technique is a precise estimate of the chirp nonlinearity, $\epsilon(t)$. For small values of τ, this can be obtained in approximate form directly from the estimate of the signal phase defocussing the reference scatterer using the relationship given in (4.1).

However, the quality of the estimate of the phase error increases with range, so it is useful to have an exact transformation from dechirped signal phase error to frequency nonlinearity for arbitrary (but non-zero) values of τ.

One method is to de-convolve the delay line response with the measurement. Another method for recovering the frequency error, $\epsilon(t)$, is to assume a polynomial form for $\phi(t)$ and to fit the resulting difference phase model to the data to give the coefficients from which the frequency error, $\epsilon(t)$, can be derived.

4.2.3 Stage 2: Calculating the time-domain warping

In its original application, of focussing SAR imagery, the phase error found by the PGA would typically be used directly to correct the wavenumber-domain image signal. The phase error would be removed by multiplying the cross-range Fourier transform of the SAR image by $\exp(-i\xi'(t))$ and then Fourier transforming the signal back into the image domain.

If $\xi'(t)$ were removed from the phase of a real-situation IF signal history, it would focus the response of the radar to reflectors at the same range as the reference reflector. However, as shown in (4.1), the phase error due to chirp nonlinearity is directly proportional to the range of the scatterer, which means that $\xi'(t)$ only applies to reflectors at this specific range.

It is possible to correct the composite dechirped signal simultaneously for all ranges by warping it in time [54]. This can be seen by writing (4.1) with a time warping, $t'(t)$, such that the actual phase takes the form of the ideal phase,

$$\phi_{\text{nonlin.}}\big(t'(t)\big) = \frac{2\pi\tau B t}{T}. \tag{4.14}$$

Substituting for $\phi_{\text{nonlin.}}(t)$ using (4.1) gives

$$\frac{2\pi\tau B t}{T} \approx 2\pi\tau\left(\frac{B}{T}t'(t) + \epsilon\big(t'(t)\big)\right), \tag{4.15}$$

which shows that τ cancels. So, the correction is independent of range (provided τ is small compared to the period of the phase error frequency components).

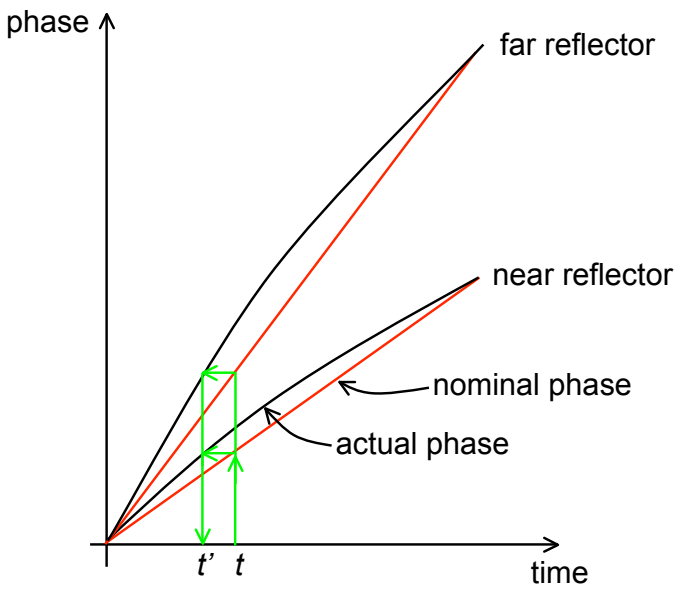

Figure 4.5: The time warping, $t'(t)$, is derived by finding the new time, t', at which the actual phase corresponds to the nominal phase at the current time, t. Because both the phase error and the nominal phase scale with range, the time warping applies at all ranges, as illustrated by the green lines.

To derive the warping, consider the dechirped signal phase, which is expressed in (4.1). This can be written in terms of $\xi'(t)$, which forms the error part of the phase.

$$\phi_{\text{nonlin.}}(t) = \frac{2\pi\tau Bt}{T} + \xi'(t). \tag{4.16}$$

The function $\phi_{\text{nonlin.}}(t)$ is inverted (assuming a monotonic phase) to give $\hat{t}(\phi)$, and this is then applied to both sides of (4.14) to give the time warping as

$$t'(t) = \hat{t}\left(\frac{2\pi\tau Bt}{T}\right). \tag{4.17}$$

The time warp derivation and range independence of the correction are illustrated in Figure 4.5.

4.2.4 Stage 3: Applying the correction warping

The correction is applied by interpolatively warping the dechirped signal using $t'(t)$. This completes the correction procedure.

In the implementation used to demonstrate the method, the IF signal was heavily oversampled and then low-pass filtered using a software convolution filter. A cubic interpolator was then used to resample the signal according to the warping function.

It is usually necessary or desirable to iterate the whole scheme. The correction can be compounded to improve the correction: the more tightly focussed the imagery, the better the SNR and so the better the quality of the error estimate. However, the best correction the autofocus can find is determined by the stability of the signal phase error and the degree of isolation of the reference scatterer from clutter. After a number of iterations, the autofocus correction will change but not improve.

It is worth noting that Meta [84] has developed a sophisticated technique (effectively a spatially-variant filter) for applying a phase correction that is independent of range. This technique is more complicated to apply than the resampling method due to Fuchs [54] and Vossiek [58] used here, but it would provide a more robust solution, especially at long range. The re-sampling technique is sufficient for the typical applications of this kind of radar. If long-range operation were required, it would be easy to replace the re-sampling part of the method with Meta's filtering approach.

4.2.5 Estimating a solution from a set of scatterers

In some applications, it may not be possible to site a bright reference scatterer at a suitable range. However, in its traditional application autofocussing SAR images, the set formed from the brightest scatterer from each range bin is used to provide the set of phase errors to be combined. The PGA exploits the fact that the same phase error defocusses all PSFs.

In the current application, this is not true: the phase error defocussing the PSF increases proportionally with range. However, the increase with range is well understood and can be compensated where necessary, allowing the phase errors defocussing a set of scatterers to be used to estimate the chirp nonlinearity. This would allow a much more diverse range of radar applications to exploit this autofocus technique, especially those in which a two-dimensional scene has been imaged, providing many scatterers.

4.3 Demonstration

In this section, the method described above is demonstrated on three test cases:

1. the badly nonlinear chirp case, in which a deliberately nonlinear ramp voltage is applied to a VCO-based instrumentation radar;

2. the realistic, mildly nonlinear chirp case, in which the same radar is operated with a linear ramp voltage that gives the largest bandwidth available;

3. a retrospective realistic case performed on archive dechirped signal data from a medium range ($R \approx$1400 m) terrain mapping radar.

The hardware and experimental set up are described for each case, and the performances of the radar with and without the autofocus are compared.

In each of the following cases, a tenth-order polynomial phase error representation was fitted to the estimated phase error using an $\bar{A}(t)$-weighted LMS fit.

4.3.1 Badly nonlinear case

The radar used in this demonstration is the experimental radar that is described in Section 3.5.3. However, in these demonstrations, a TTi TG210 analogue signal generator was used to chirp the PMYTO. This substitution was made because, whilst the HP digital arbitrary waveform generator is more versatile, it also produced a noisy PSF. The TTi, however, produced the quietest PSF of all the waveform generators available. The quality of the ramp voltage generation and its effect on PSF quality are discussed in Chapter 6.

The radar was mounted on a sturdy tripod at approximately chest height, and the reference reflector, a 30 dBsm precision trihedral, was mounted at head height on a strong photographic tripod on level grass. The trihedral was placed at 100 m range and the radar boresight aligned with it.

The resolution was chosen to be significantly larger than the tripod and trihedral so that they appeared point like. The designed bandwidth of the chirp was 134 MHz and Hann weighting was used. Using (2.12) with $\kappa = 1.46$ for Hann weighted signals, the designed resolution of the radar is found to be 1.6 m. The chirp time was 1 ms.

The radar image and the theoretical response shape fitted to it in range and resolution are shown in Figure 4.6. It can be seen that the performance of the instrumentation radar is extremely good: 1.7 m FWHM resolution and close to the ideal response shape down to 45 dB below the peak.

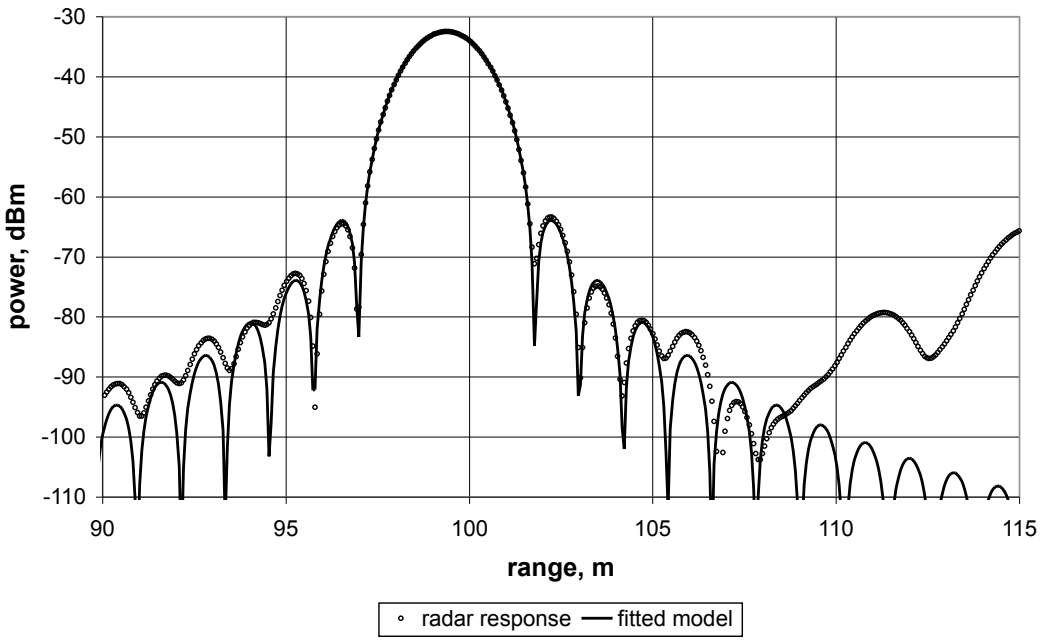

Figure 4.6: The normal response of the instrumentation radar to a trihedral at 100 m. The rising response starting at 107 m is caused by a tree.

Next, the control voltage applied to the PMYTO was deliberately perturbed by using a nonlinear voltage ramp. The radar was then run again to produce a defocussed image of the trihedral. This image is shown in Figure 4.7.

The radar was run with the autofocus to find the phase error and to derive the time warping. The algorithm used 1000 images of the reference reflector. Fewer images could be used, and in practice 100 images appeared to give results as good as those derived from 1000. However, to obtain as good a result as possible and to remove doubt about the SNR, 1000 images were used in each of these tests.

The radar was then run again, this time to focus the radar imagery. The complete process was repeated twice, after which there was no apparent further improvement. The focussed point response is shown in Figure 4.7.

A model of the ideal response, generated using (3.8), is fitted in resolution and range. There is good agreement in the shape of the response, and the FWHM resolution was 1.7 m, agreeing well with the nominal value, 1.6 m.

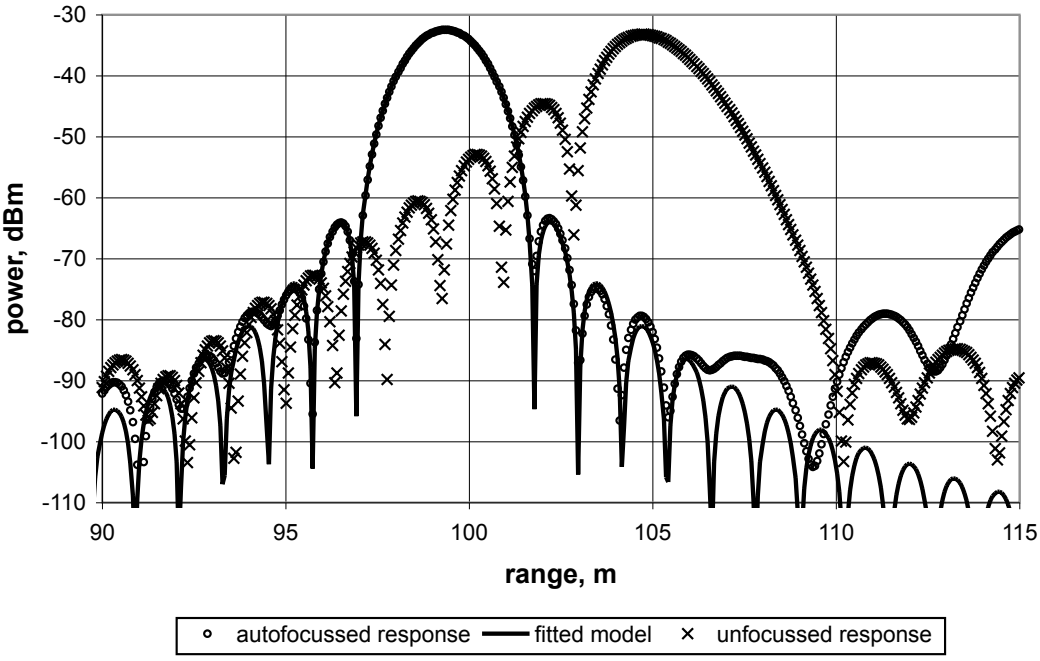

Figure 4.7: Response of the deliberately nonlinear chirp radar to a trihedral at 100 m with and without autofocus (solution derived at 100 m).

The response is at least as good as the normal, unperturbed performance of the radar, indicating some inherent nonlinearity or phase error in the radar, albeit small.

By comparing Figure 4.7 with Figure 4.6, it can be seen that the linear part of the applied chirp frequency error causes a range shift in the autofocussed response (from 104 m to 99 m), which is corrected by the autofocus.

An estimate of the chirp nonlinearity is a valuable by-product of the method. The method provides a very accurate means of finding the dynamic tuning curve of the oscillator while it is operating under realistic conditions (chirp rate, environment etc.). The tuning curve is often estimated by stepping through control voltages and measuring the output frequency. However, such methods take into account neither the frequency responses of the driver circuit and the oscillator, nor any environmental factors. The applied and the estimated nonlinearity agree well, as can be seen in Figure 4.8.

Next, the trihedral was moved to 40 m range. The radar was run again with and without the autofocus correction that was derived in the 100 m case. The results are shown in Figure 4.9, from which it can be seen that, although the defocussed image is not as significantly defocussed as in the 100 m case, it is still badly defocussed. There is good agreement between the focussed

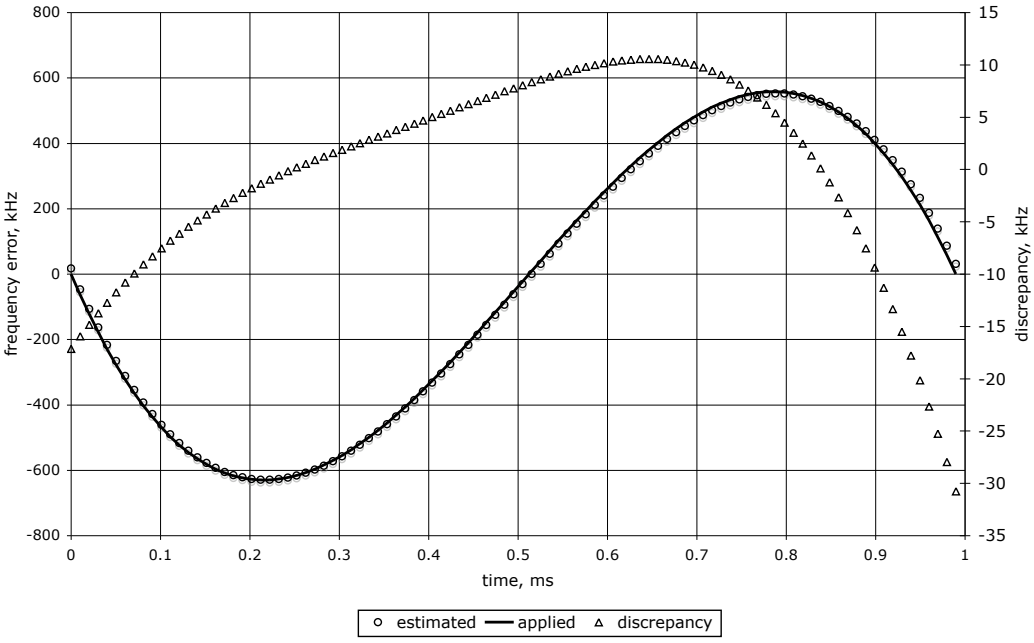

Figure 4.8: The applied and measured (with autofocus and reference reflector at 100 m) chirp nonlinearity over the 134 MHz chirp.

response and the model fitted in range and resolution. The FWHM resolution after autofocus was 1.7 m.

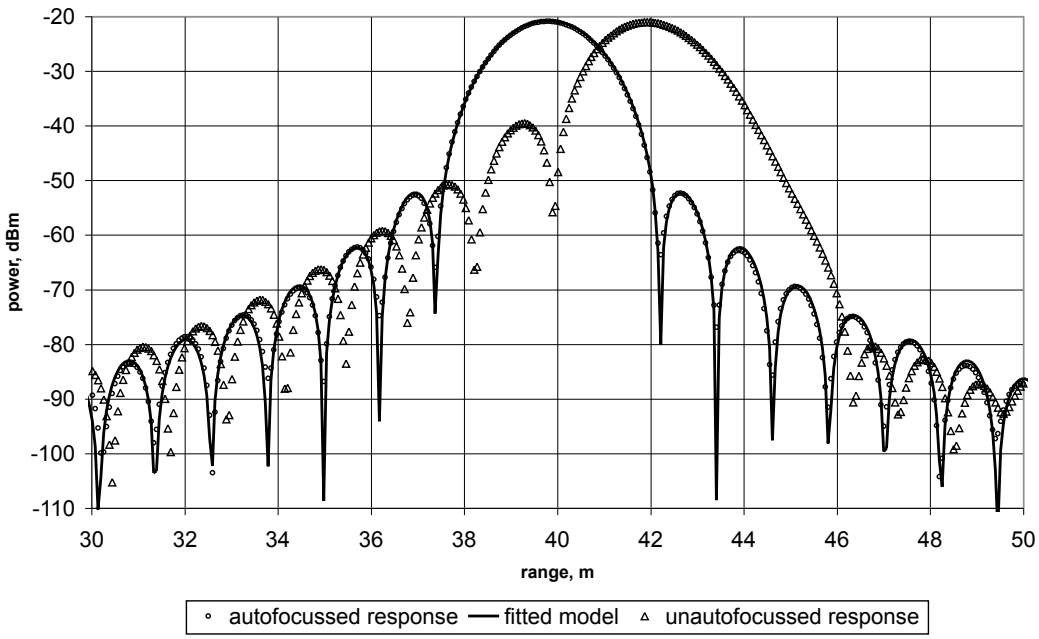

Figure 4.9: Response of the deliberately nonlinear chirp radar to a trihedral at 40 m with and without autofocus (solution derived at 100 m).

Finally, the trihedral was moved to a point 214 m from the radar. The radar was run twice again, with and without the autofocus. The results are shown in Figure 4.10, from which it can be seen that the unfocussed case is extremely distorted. However, the focussed case is much closer to the ideal response and has FWHM resolution 1.7 m.

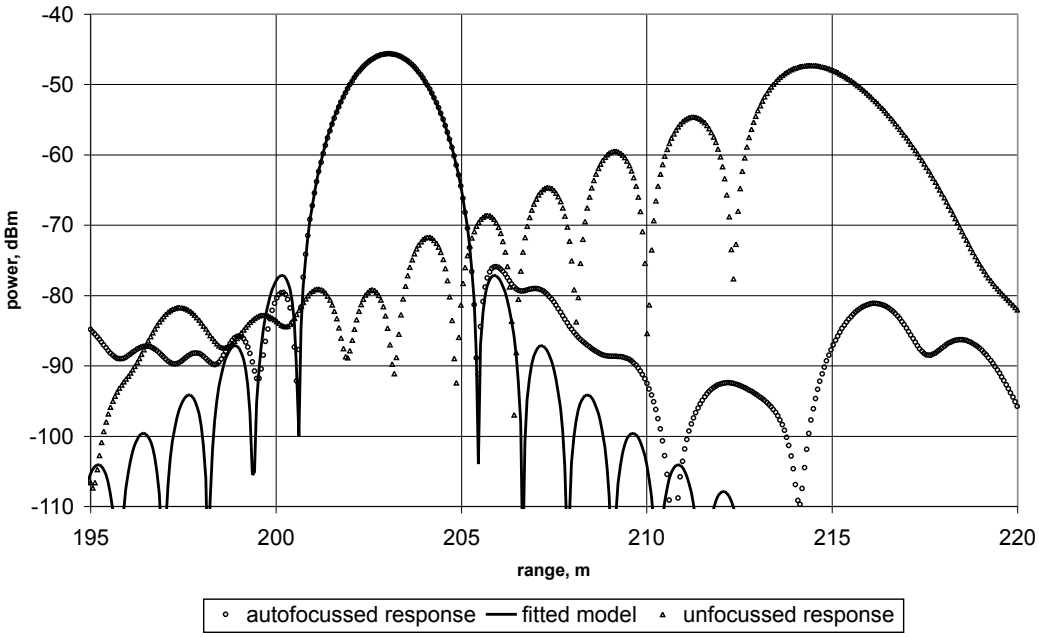

Figure 4.10: Response of the deliberately nonlinear chirp radar to a trihedral at 214 m with and without autofocus (solution derived at 100 m).

Whilst the focussed case is much better than the unfocussed case, it is apparent that the response shape is not as good as at 40 m. This is because the phase error due to the residual nonlinearity scales with range. Correspondingly, while the small-τ approximation holds, the sensitivity of the autofocus increases with increasing reference reflector range.

4.3.2 Mildly nonlinear case

In this case, the radar is run at near-maximum bandwidth (1.2 GHz) and with no deliberate chirp nonlinearity introduced.

Running at the maximum available bandwidth requires the PMTYO to be chirped over a large fraction of its tunable range. Although the PMTYO has excellent linearity, it is not completely linear. At large enough reflector ranges,

the resulting phase errors would become problematic for fine-resolution imaging purposes.

Whilst it is usual to window weight the dechirped signals to reduce sidelobe levels at a cost of broadening of the mainlobe, it also has the beneficial side effect of conferring a degree of immunity to phase errors, as discussed in Chapter 3. Because the degree of nonlinearity is small, to make the comparison of the unfocussed and the focussed response clear, no window weighting was used in this case. Using (2.12) with $\kappa = 0.89$ for Uniform window weighting, the nominal FWHM resolution of the radar is 0.1 m.

The reference reflector was placed at 60 m and the autofocus procedure run three times using 1000 unfocussed images, as in the first case.

At 0.1 m resolution, the tripod and trihedral are not completely point like. They are not extended enough to disrupt the autofocus, but the ideal response of the extended scatterer has lower sidelobes than the ideal. This is because the trihedral and tripod return a distribution of responses which combine to give a very slightly broadened response with slightly lower sidelobes relative to the ideal point response.

Next, the reflector was imaged with and without autofocus for a number of different ranges up to 214 m. The responses were normalized in power to allow comparison of the response shape. This is apparent from Figures 4.9 and 4.10, in which the power can be seen to drop with increasing range.

The range profiles of the trihedral at a number of ranges taken without autofocus are shown in Figure 4.11, whilst in Figure 4.12 the same trihedral is imaged (at the exactly the same positions) with the autofocus correction active. The unfocussed images become noticeably more defocussed as the range is increased. However, in the autofocussed case, the quality of the response is returned to close to the notional value, and the response does not degrade rapidly with increasing range. The FWHM resolution was measured to be 0.1 m, the ideal value.

In Section 4.3.1, it was suggested that the autofocus sensitivity improves with increasing range. To demonstrate this, the error-estimation stage of the autofocus was repeated at 214 m. The trihedral was then imaged with autofocus correction applied at 60 m and 214 m with the autofocus solutions estimated at 60 m and at 214 m. The results are shown in Figure 4.13, from which it can be seen that the correction found at 60 m works well at 60 m but not as well at 214 m, shown by the 165 m (square data marks) plot in Figure 4.13, which has asymmetric sidelobes. The correction found at 214 m works

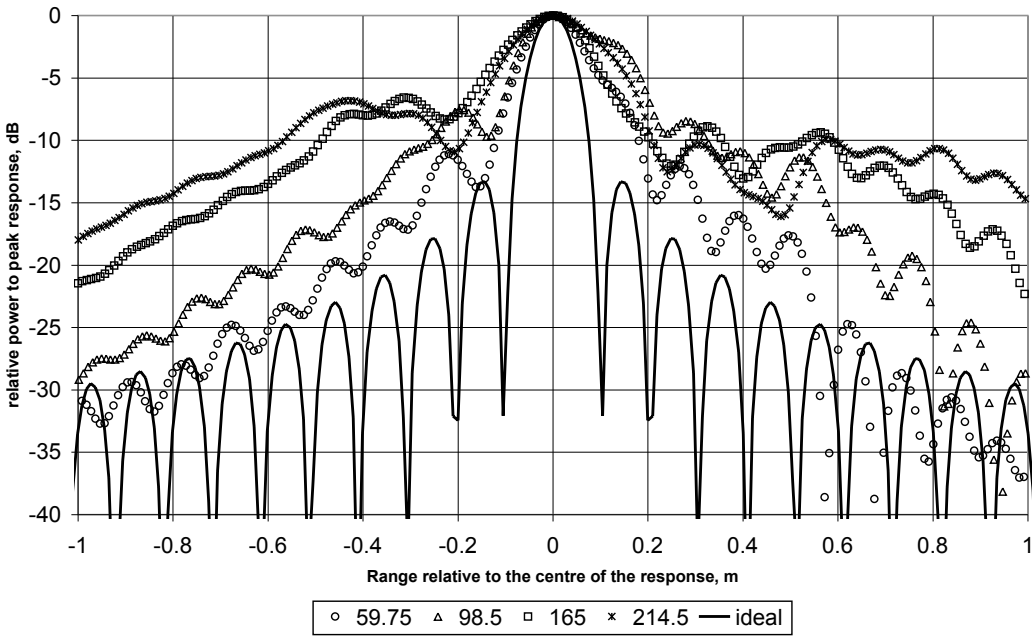

Figure 4.11: The unfocussed responses of the unperturbed high-resolution radar.

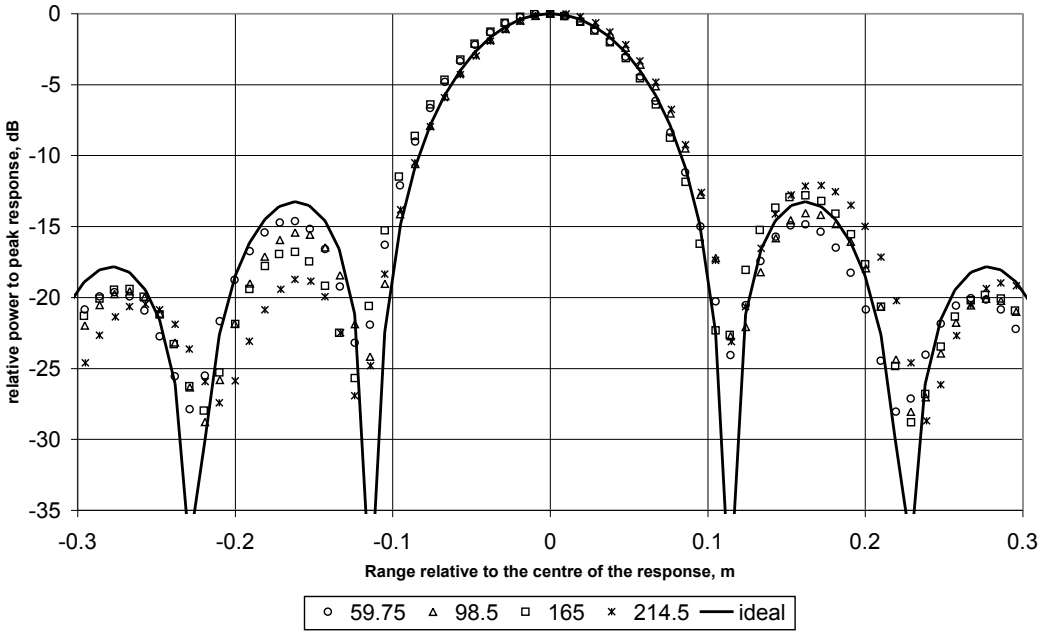

Figure 4.12: The autofocussed responses of the unperturbed high-resolution radar. The autofocus correction was derived at 60 m.

as well as that found at 60 m for the 60 m image and does not deteriorate for the 214 m case.

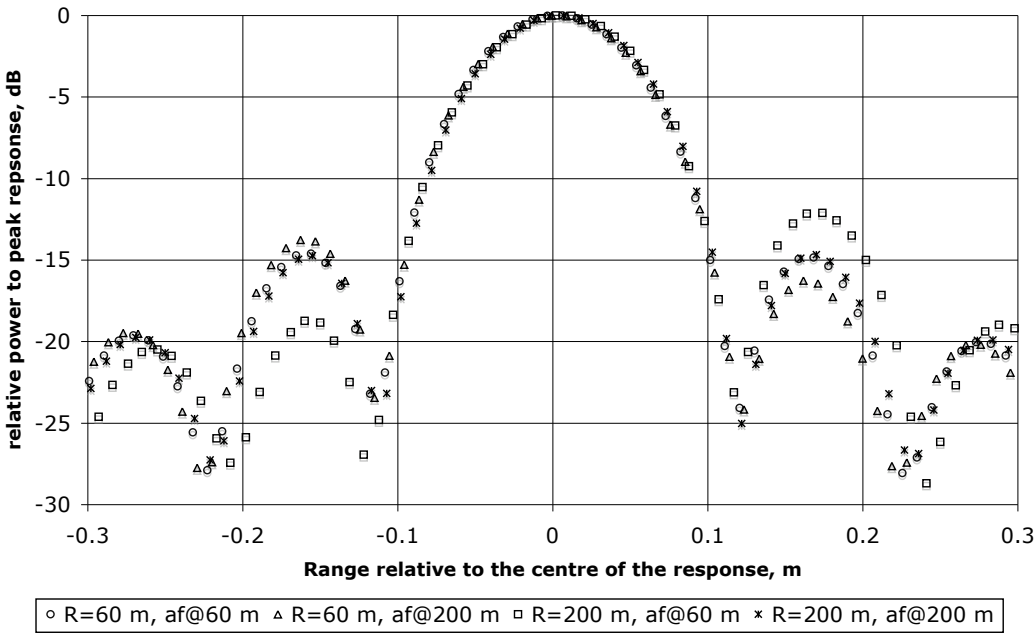

Figure 4.13: The response of the radar at 60 m and 214 m are shown for both the autofocus solutions, one derived at 60 m and one derived at 214 m.

4.3.3 Retrospective case

An important feature of the method described in this chapter is its ability to be applied retrospectively. This has obvious uses in correcting archive data and in off-line data processing applications, e.g. for very low-power data collection.

To demonstrate the autofocus in a retrospective application, data collected several years ago by the AVTIS radar [10, 13, 85] was used with the autofocus to produce focussed range profiles.

AVTIS is a radar developed to make three-dimensional imagery of volcano lava domes, which are often obscured by dust and cloud [37]. AVTIS, a single-antenna homodyne radar, uses a 7.23 GHz Micro Lambda Wireless (MLPF-14-28) PMYTO, which is chirped by an Intersil precision waveform generator (ICL 8038) with 0.1% quoted linearity (deviation from a fitted straight line). The PMYTO signal is amplified by a Ciao CA78-242 amplifier and then frequency-multiplied by 13 by an ELVA-1 (IAFM-10/94/13) IMPATT multiplier to 94 GHz. This is then amplified by an ELVA-1 IILA10/94/200 power amplifier to give the transmit signal. The IF signal is low-pass filtered to prevent aliasing and then sampled using a 500 kHz 12-bit National Instruments NIDAQCard-6062E PCMCIA multifunction data acquisition card. A schematic radar circuit diagram for AVTIS is shown in Figure 4.14.

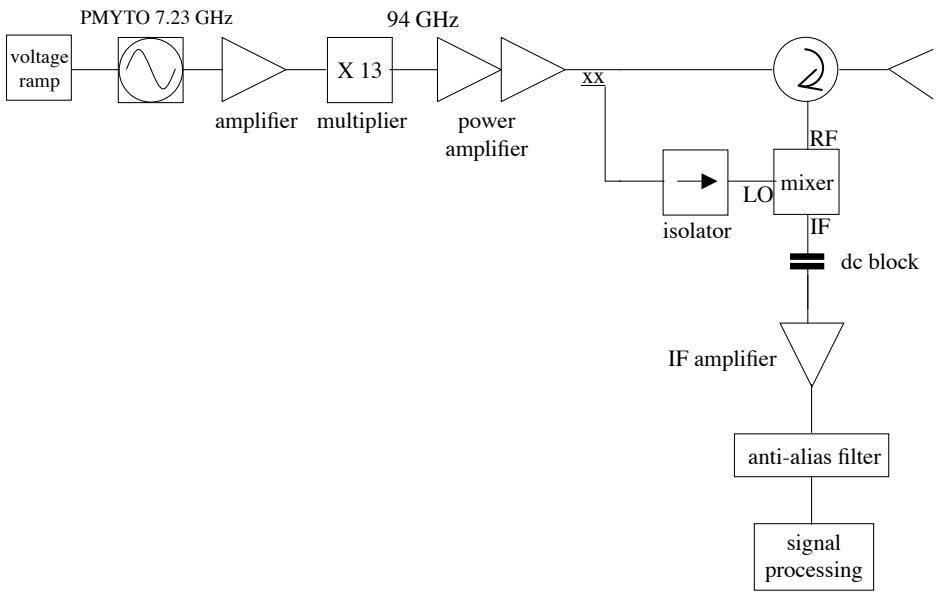

Figure 4.14: Schematic diagram of the AVTIS radar.

To obtain ground-truth data when imaging volcanoes, trihedrals are placed at points located with high-precision GPS, typically at 1 to 3 km range. The trihedrals are raster imaged to orientate the radar, and then the lava dome is imaged. To boresight the radar, a model of the beam shape is fitted to the raster scans of the trihedrals. This process provides ideal data for running the autofocus technique.

The method proposed in this chapter was used to compensate for any non-linearity in the AVTIS frequency chirp. The reference scatterer provided by the ground truth trihedral is at 1.4 km from the radar, and there is a 20×20 scan, providing 400 range profiles ranging from about -6 dB to full beam gain.

The chirp bandwidth was notionally 176 MHz and the chirp time was 32 ms. Hann window weighting was used. Accordingly, (2.12) gives the notional resolution as 1.2 m.

The data used in this subsection were collected several years ago by the developer and operator of AVTIS, Dr David Macfarlane.

The compensated range profile is shown with the original range profile in Figure 4.15. The sensitivity, resolution, dynamic range, and response shape have all been considerably improved. Without autofocus, the resolution is 3.6 m; with a single iteration of autofocus, the resolution is 1.8 m. The response shape is also much closer to ideal after autofocussing, and it is notice-

able that the dynamic range is improved. More iterations might yield further improvements, but the software on the AVTIS processor could not be modified to achieve this.

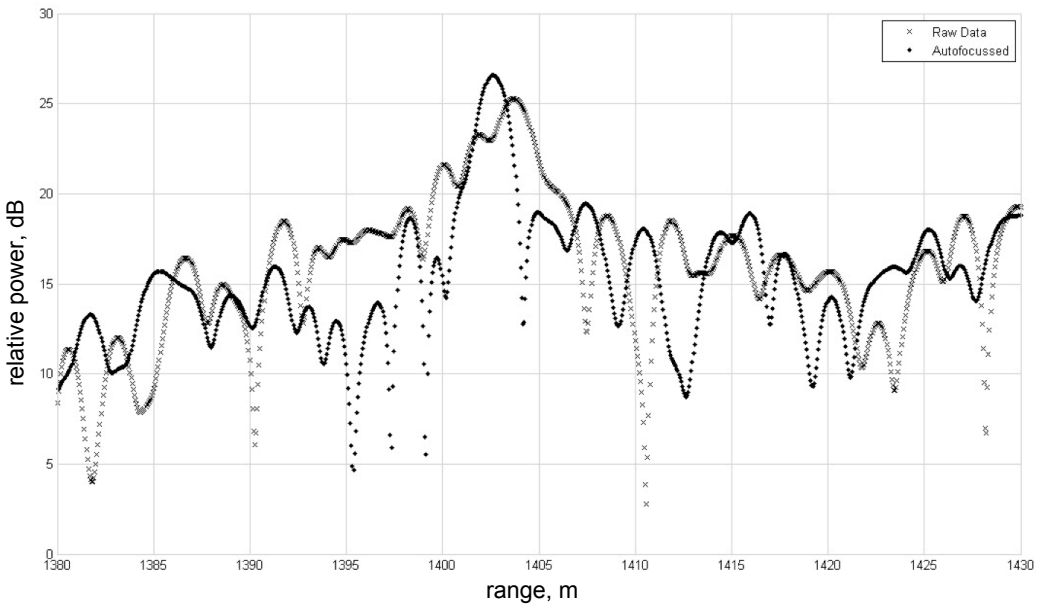

Figure 4.15: Point response of the AVTIS radar at 1400 m with and without a single iteration of the autofocus.

4.4 Conclusion

A combination of two established techniques, the Phase Gradient Algorithm and time-domain resampling, was presented and discussed as a method for characterizing and compensating for chirp nonlinearity in FMCW radars. Its validity in three representative cases was demonstrated.

The method was shown to be able to recover near-ideal resolution performance in a badly nonlinear case. It was also shown that the method can provide accurate estimates of the dynamic tuning curve of the FMCW radar.

In a demonstration on a typical radar, it was shown that the method can improve the quality of the point response at ranges much larger than that of the reference scatterer, returning the radar to near-ideal performance.

In the demonstration of retrospective application to the AVTIS data, the method worked well, giving a notable increase in resolution, dynamic range, and sensitivity for imagery at several kilometres range. Where suitable refer-

ence measurements have been made, archive data can be corrected for defocussing caused by chirp nonlinearity.

Chapter 5

Down conversion by subsampling and Moving Target Indication

In this chapter, I shall describe a method for reducing the sampling rate required to capture the IF radar signal of an FMCW radar. This technique requires only a band-pass filter and uses down conversion by subsampling to expand the operation of FMCW radars. I shall demonstrate the technique with Moving Target Indication, which is prone to high sampling rates. I shall also quantify the MTI problem for the case of AVTIS and long-range operation generally.

Part of the work presented in this chapter has been presented as an invited keynote paper at the 2010 IRMMW-THz International conference in Rome, Italy.

5.1 Introduction

In Chapter 2, it was shown that the frequency of the dechirped signal is given by

$$f_{\text{diff}} = \frac{2BR}{\mathrm{c}T}, \tag{5.1}$$

(i.e. (2.4)), which indicates that operation at fine resolution, at long range, with a short chirp, or some combination of all three, will result in high-frequency dechirped signals.

If single-channel real signal sampling is used (i.e. not I and Q sampling), then the sampling rate must be at least twice the highest signal component frequency. Additionally, it is often desirable to oversample the signals slightly

in order to make filter specification easier in the signal processing. So, the bare-minimum sampling rate for a signal (i.e. the unambiguous sampling rate) is double the frequency given in (5.1) for the farthest scatterer.

A fine-resolution radar might have $B = 1$ GHz, $T = 0.0001$ s, and $R = 5000$ m, which give the minimum sampling rate as 667 MHz. Sampling cards and processors for these data rates are rare and expensive.

In many applications, T can be increased to reduce the IF signal frequency to an acceptable value. Often T will be increased anyway, to maintain sufficient overlap of the transmitting and received signals as the standoff range is increased. However, sometimes it is necessary to use a short chirp, and in these cases it is useful to be able to reduce the required sampling rate in some way without reducing the range or degrading the resolution.

If the required information in the signal is band limited at some offset frequency, it is possible to band-pass filter the signal and down convert against a reference signal at the lowest required frequency. This means that only the useful part of the spectrum need be unambiguously sampled. For scenes with depth much smaller than the stand-off range, this offers a considerable reduction in the sampling rate. However, this approach requires a second oscillator and down conversion scheme, which are not always desirable or possible.

An alternative technique is possible under certain circumstances. This is to band-pass filter the signal leaving only the required information, then to deliberately under sample the IF signal so that the information-containing region of the spectrum aliases exactly into the fundamental region of the spectral analysis used to form the radar image.

The aliasing of signals is normally considered to be undesirable because information from one part of the spectrum ends up in another part of the spectrum where it isn't wanted. However, after band-pass filtering, the only information in the signal belongs to the region of interest.

This chapter is motivated by the requirement for a terrain-mapping homodyne FMCW radar, AVTIS [13], to be able to perform Moving Target Identification (MTI) on dust and rockfall on volcano lava domes from long, i.e. safe, standoff ranges. However, little or no modification to the hardware is possible owing to the radar already having been built. Other applications include surveillance radars that aim to detect moving reflectors in a small scene at long stand off ranges [24].

A technique to estimate the speed of scatterers in the scene was described

by Strauch [86]. It operates by detecting the rate of change of image phase over a set of successive range of profiles.

The successive range profiles must unambiguously sample the Doppler shifts to be resolved. As the Doppler shifts are proportional to the carrier frequency, this is a harder problem at high carrier frequencies (e.g. W band, like AVTIS) than at lower frequencies (e.g. X band).

To enable the estimation of high radial speeds, repeated range profiles must be formed in very quick succession, which requires a very short chirp, i.e. a small value of T. Because AVTIS must also operate at long range and with reasonably fine resolution, the IF sampling rate becomes unacceptably high. So, as part of the software to perform MTI, I incorporated the down conversion-by-undersampling technique described in this chapter.

This chapter has the following structure: I shall describe and quantify the subsampling technique, including a method of finding the smallest sampling rate that will give maximally aliased and minimally sampled signals. The method will also allow the user to specify the degree of oversampling.

I shall describe the MTI technique mentioned above, and I will calculate the FMCW radar signal properties assuming a constant radial component of velocity. Radially accelerating scatterers have been studied (Part C of) [73], but I will not consider them. I will show that a full calculation gives the same results as the simple calculation for all realistic MTI situations. I will describe simple rules for calculating the performance specification and describe how they can be used to find suitable parameter values for MTI operation.

I will demonstrate the operation of the MTI technique with subsampled signals using a numerical simulation of an example based on the required operation of AVTIS. I shall also simulate the effects of extreme operation (very wide relative bandwidths).

Finally, I shall demonstrate subsampled MTI operation with an educational demonstration radar, successfully detecting a moving scatterer.

5.2 Down conversion by subsampling

The idea behind the technique discussed in this chapter is to band-pass filter the IF signal, suppressing all frequency components that do not correspond to the interval in range (or frequency) of interest, and to sample the filtered radar IF signal so that it aliases into the unambiguous range of frequencies. This idea

is illustrated in Figure 5.1, which shows the equivalent spectral regions in a sampled signal. It is quite common to have an offset scene, for example, the air-field and volcano-imaging examples shown in Figure 5.2.

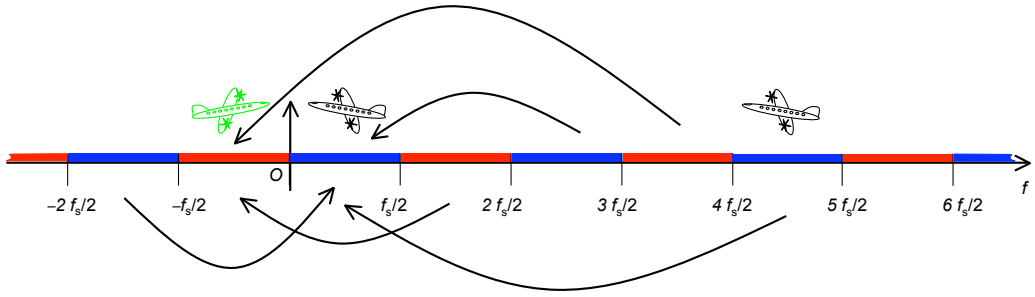

Figure 5.1: The equivalent spectral regions in a sampled system. The arrows indicate the origin and destination of aliased signal information. This is exploited in the down conversion-by-undersampling technique. The image of the black aeroplane is aliased into the pass band, giving the green aeroplane.

It is important to chose the sampling frequency to be as small as possible without having an alias point ($f_s/2$, $2f_s/2$, $3f_s/2$, $4f_s/2\ldots$) within the region required to be sampled. Of course, the sampling frequency must still satisfy the unambiguous sampling criterion for the information band.

Suppose that the required information in the IF signal lies between two frequencies: the lower frequency f_1 and the higher frequency f_2. Then the minimum (critical) sampling rate required is $f_{\text{crit.}}$, which is given by

$$f_{\text{crit.}} \geq 2(f_2 - f_1). \tag{5.2}$$

The aliased signal energy should be such that the Nth alias point is at or below f_1 and the $(N+1)^{\text{th}}$ alias point is at or above f_2, where N must be found. The actual sampling rate can be expressed as a scaled (≥ 1) critical sampling rate, so these conditions give the following pair of equations:

$$\frac{N f_{\text{crit.}} k}{2} \leq f_1, \tag{5.3}$$

and

$$\frac{(N+1) f_{\text{crit.}} k}{2} \geq f_2, \tag{5.4}$$

where $k \geq 1$ is the scaling.

The regions of k-N space allowed by these conditions are indicated by the green lines in Figure 5.3, in which N derived from (5.3) is plotted in blue and

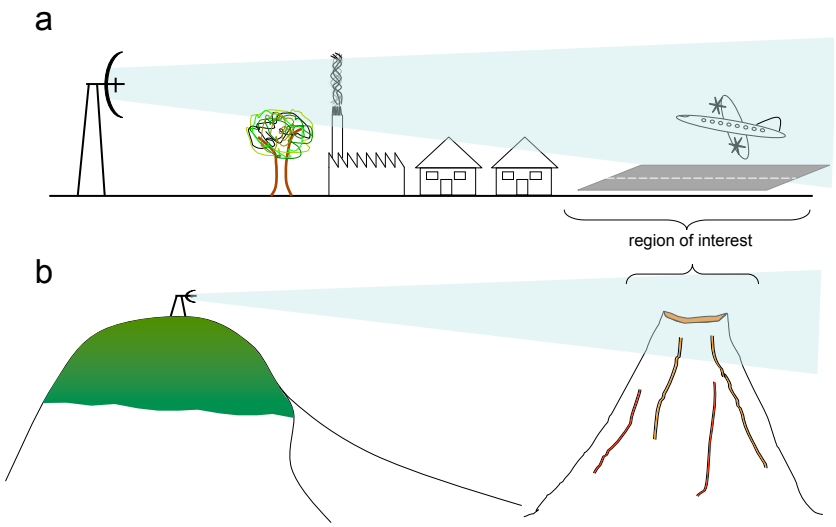

Figure 5.2: (a) A common radar imaging situation, with the scene to be imaged being offset from the radar. In this example, only the runway is of interest, objects nearer and farther than the indicated interval are not required to be imaged. (b) The situation for AVTIS, imaging a volcano from a neighbouring hill top. In this case there is a clear foreground, a relatively restricted scene depth compared to the standoff range, and there is nothing behind the region being imaged. This means the IF signal will only contain significant signal energy from the region being imaged.

N derived from (5.4) is plotted in red. It can be seen that the upper frequency aliasing point provides the lowest sampling rate. N.B., the plot in Figure 5.3 is a particular example, not a universal one.

Where the integer values of N intersect with the blue curve fixes the aliasing on the bottom frequency, and where the integer values of N intersect with the red curve fixes the aliasing points on the top frequency. All other places on the green lines give valid aliasing but with the aliasing points outside the f_1 to f_2 interval, and these correspond to sampling rates that oversample the IF signal.

The aim is usually to find the smallest possible value of $k \geq 1$ and the largest integer value of N that satisfy these equations. This is done by solving for the critical value of k in (5.4). The upper frequency gives the lowest value of k because the upper aliasing point increases faster than the lower aliasing point by a factor of $(N+1)/N$.

From (5.4), the number of aliases used is given by

$$N = \left\lfloor \frac{2f_2}{f_{\text{crit.}}} \right\rfloor - 1, \tag{5.5}$$

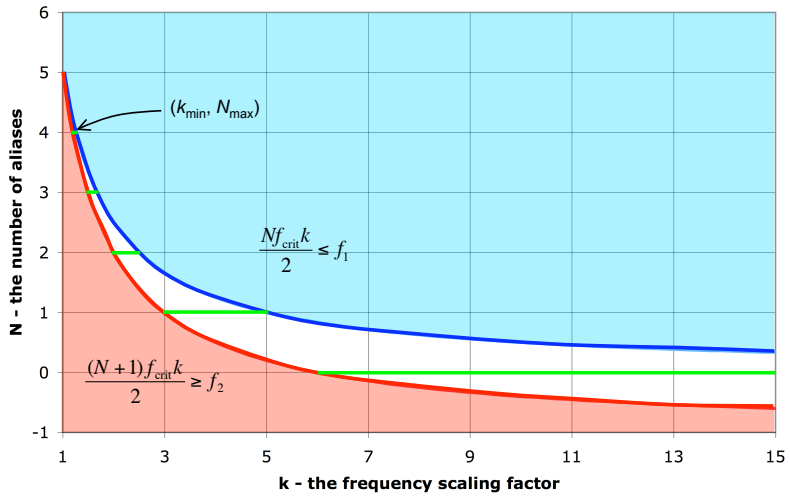

Figure 5.3: An example of a plot to illustrate the allowed regions (green lines) of k-N space for valid subsampling. The numbering on the N-axis is to indicate integer steps. In practice the values can be much bigger.

so the smallest value of k is given by

$$k_{\text{min}} = \frac{2f_2}{Nf_s}. \tag{5.6}$$

The parameter k indicates that the sampling frequency to be used should be f_s, where

$$f_s = kf_{\text{crit.}}. \tag{5.7}$$

If N is odd, the signal will alias into the negative frequency half of the spectrum; if it is even, the signal will alias into the positive half of the spectrum. Actually, there will be a reflection of the signal in the Fourier transform, as with all real signals, but the parity of N will indicate which half of the Fourier transform contains the unreflected copy.

For any values of k and N, the lowest frequency in the signal will be given by

$$f_{\text{lo}} = \frac{f_{\text{crit.}}kN}{2}, \tag{5.8}$$

and the highest frequency will be given by

$$f_{\text{hi}} = \frac{f_{\text{crit.}}k(N+1)}{2}. \tag{5.9}$$

The band-pass filter should be chosen to suppress signal energy not between f_{lo} and f_{hi}. There are a number of ways of achieving this, including

YIG-tunable filters, FPGA filters, electrically tunable BST filters, and simply switchable banks of hardware filters.

It is often useful to specify the lowest frequency as the aliasing point. For example, this would be useful for signal processing where the zero-range bin is specified. In this case, N is calculated using

$$N = \left\lfloor \frac{2f_1}{f_{\text{crit.}}} \right\rfloor, \tag{5.10}$$

derived from (5.3), with k then being given by (5.8).

5.3 MTI processing

The radar echoes from reflectors moving with constant radial speed (directly towards or away from the radar) are delayed and either stretched or compressed copies of the transmitted signal, depending on whether the reflector is receding or approaching. This signal modification introduces various artefacts, but the most obvious is a Doppler shift. In FMCW radar, the Doppler shift carries through the dechirping process and lowers or raises the IF frequency of the echo.

In FMCW radar, the range of a scatterer is found implicitly from the estimate of the round-trip time via the IF frequency of the echo. If the IF frequency is in part determined by the unknown radial speed of the scatterer, then there is a 'range-Doppler' ambiguity.

Several methods exist for resolving the ambiguity. In one method, the scene is imaged twice but with different chirp slopes. The frequency of each echo is the sum of the part due to the chirp and the part due to the Doppler shift. In narrow-band systems, the Doppler shift is determined mostly by the carrier frequency, so the total frequency of each echo will be different in the two images because the Doppler part remains constant and the nominal part changes. By pairing up the two images of each scatterer in the two different range profiles, the ambiguity can be resolved.

In a second method, the chirp rate is kept constant and a different carrier frequency is used to give two range profiles. Again, the total frequency of the IF signal of each scatterer will be different in the two range profiles. Pairing up the two images of each scatterer resolves the ambiguity.

However, these techniques are not suitable for complex scenes and distributed scatterers such as at volcano lava domes and rainfall [23, 62] be-

cause each scatterer requires a pair of distinguishable chirps, resulting in an unworkable system for more than a few scatterers. Another method, described by Strauch [86], enables a two-dimensional (range and radial speed) map of the scene to be formed. This technique, which will be called Fourier Cross Processing (FCP) from here onwards, exploits the linear dependence of the IF signal phase offset on the range of the scatterer from the radar. If the scatterer is repeatedly imaged at regular intervals, the phase offset will vary from chirp to chirp at a rate proportional to the radial speed of the scatterer. The best way to estimate the rate(s) of change of phase of a compound signal (maximizing SNR [49]) is to Fourier transform the signal. So, to estimate the rate of change of phase of the signal from chirp to chirp, the stack of IF signals (or the range profiles made from them) is Fourier transformed as a function of chirp repeat number. This is illustrated in Figure 5.4. This technique is best understood in terms of fast time and slow time, which are illustrated in Figure 5.5. Fast time is the time since the start of each chirp, whereas slow time is the time of the start of each chirp since the start of the whole data collection.

The two-dimensional signal phase, $\phi(t, t_s)$, can be written in terms of fast and slow time, t and t_s respectively, in three distinct contributions:

1. the nominal phase offset due to the range of the scatterer;
2. the nominal phase ramp due to the actual range of the scatterer;
3. the phase ramp due to the Doppler shift.

These give an approximate expression for the IF phase to within an overall phase offset, ϕ_{const},

$$\phi(t, t_s) \approx \phi_{\text{const}} + \underbrace{2\pi \frac{2 f_0 R_0(t_s)}{c}}_{\text{nominal phase offset}} + 2\pi \left[\underbrace{\frac{2BR_0(t_s)}{cT}}_{\text{nominal dechirped frequency}} - \underbrace{\frac{2 f_0 v}{c}}_{\text{Doppler shift}} \right] t, \tag{5.11}$$

where $R_0(t_s)$ is the range of the scatterer at the start of each chirp and v is the radial speed of the scatterer away from the radar.

The IF frequency within each chirp, i.e. the fast-time frequency, is given by

$$f_f = \frac{1}{2\pi} \frac{d\phi}{dt}, \tag{5.12}$$

which gives

$$f_f \approx \frac{2B}{cT} \left(R_0(t_s) - \frac{T f_0 v}{B} \right). \tag{5.13}$$

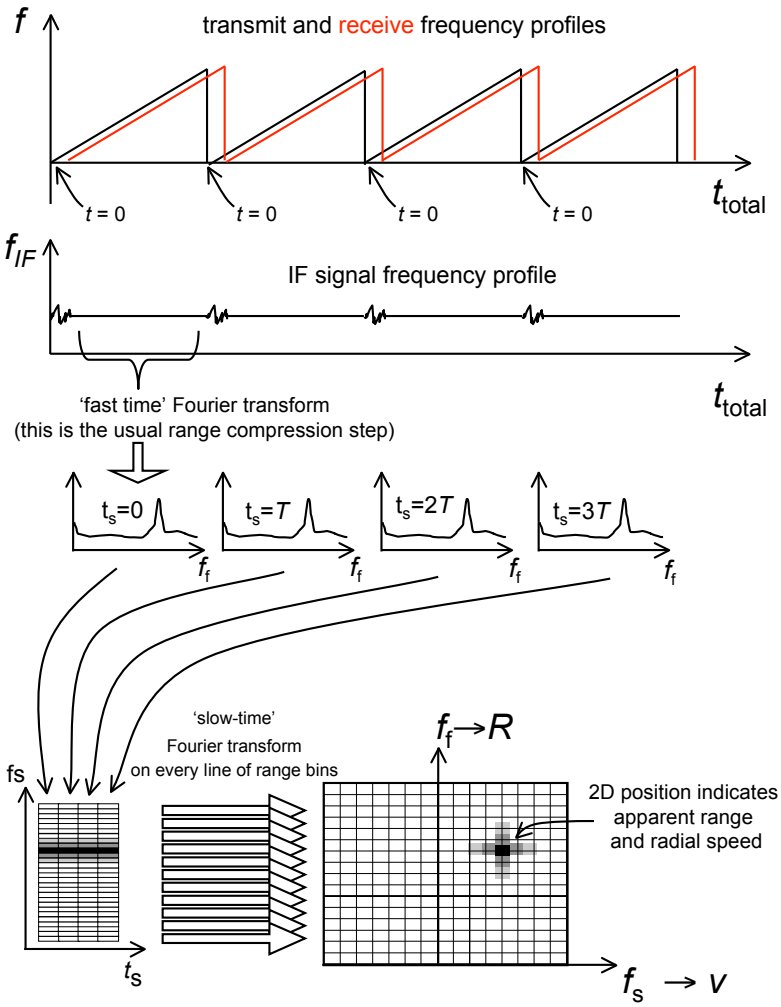

Figure 5.4: The Fourier Cross Processing (FCP) technique.

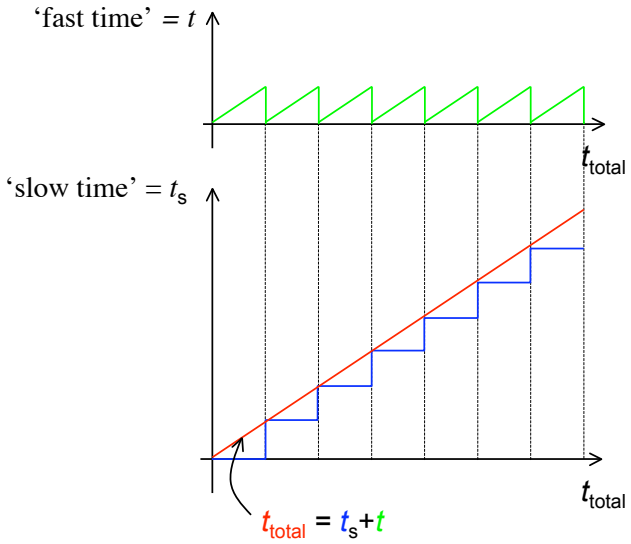

Figure 5.5: Fast and slow time for the contiguous chirp processing case.

N.B. If the FCP system is Doppler unambiguous, then the second part of (5.13) is $\leq \rho$, so could reasonably neglected.

Using (5.1), (5.13) gives

$$R_{\text{apparent}} \approx R_0(t_s) - \frac{T f_0 v}{B}. \tag{5.14}$$

Equation (5.14) allows the true range to be calculated from the IF frequency if the radial speed of the scatterer is known.

To estimate the radial speed of the scatterer, the slow-time frequency of the scatterers must be found. This is also done by Fourier transforming the signal but in the slow-time direction. The slow-time frequency is

$$f_s = \frac{1}{2\pi}\frac{\mathrm{d}\phi}{\mathrm{d}t_s}, \tag{5.15}$$

which gives

$$f_s \approx \frac{2v}{\mathrm{c}}\left(-f_0 + \frac{Bt}{T}\right). \tag{5.16}$$

For small relative bandwidths ($\leq 5\%$), the blurring introduced by the t-dependent term in (5.16) can be ignored, giving an expression for the speed

$$v \approx \frac{\mathrm{c} f_s}{2 f_0}, \tag{5.17}$$

Fourier transforming the stack of dechirped signals in the slow-time direction sorts the signal energy in each range bin by slow-time frequency and so by radial speed, too. So, the speed and true range can be found for the contents of every range cell in the range profile. The order of the Fourier transforms is unimportant to the operation of the FCP technique. However, for real signals, Fourier transforming in range first allows the array size that must be Fourier transformed in the slow-time direction to be halved: the negative frequencies are just a reflection of the positive ones, and ignoring the negative half of the spectrum is an implicit Hilbert transform on the real signal to give the complex signal. This Fourier transform order is desirable in practice because it reduces the computational load of the technique.

It can be seen from (5.16) that the slow-time frequency is proportional to the radial speed of the scatterer. Consequently, larger unambiguous speeds require larger slow-time frequency responses. This forces an upper limit on the time between chirps, which in turn increases the IF (fast-time) frequency. This provides the motivation for this chapter.

5.3.1 IF signals of moving scatterers

The planned application of AVTIS is fine-resolution, long-range MTI operation e.g. monitoring rock falls and eruptions. In this section, I shall calculate the IF signal phase directly from the transmitted and received signal phases of moving scatterers to give general expressions for the fast- and slow-time frequencies. I shall also quantify the technique to provide a means of calculating suitable operating parameters.

The radar transmits its signal towards the scene to be imaged. After propagating to a scatterer and back, the signal arrives at the radar as an echo. Each instant in the echo is just an instant in the transmitted signal delayed by some varying amount of time depending on the time of arrival. If an instant in an echo arrives at t, then it was transmitted at $\bar{t}$, where

$$\bar{t} = t - \tau \tag{5.18}$$

and τ is the round-trip time.

The round-trip time is given by the round-trip distance divided by the speed of light. If the position of the reflector at the beginning of the chirp ($t = 0$ at the beginning of the chirp) is given by

$$R = R_0 + vt, \tag{5.19}$$

where v is the radial speed of the reflector, then the round trip time for the instant in the signal transmitted at $\bar{t}$ and received at t is

$$\tau = \frac{2}{\mathrm{c}}\left(R_0 + v\frac{t+\bar{t}}{2}\right). \tag{5.20}$$

Solving (5.18) and (5.20) for $\bar{t}$ gives

$$\bar{t} = \frac{\mathrm{c}-v}{\mathrm{c}+v}t - \frac{2R_0}{\mathrm{c}+v}, \tag{5.21}$$

which is more conveniently written as

$$\bar{t} = \alpha t + \beta, \tag{5.22}$$

with

$$\alpha = \frac{\mathrm{c}-v}{\mathrm{c}+v}, \tag{5.23}$$

and

$$\beta = -\frac{2R_0}{\mathrm{c}+v}. \tag{5.24}$$

So, the received signal, $s_{\mathrm{rx}}(t)$, can be written in terms of the transmitted signal in the following way

$$s_{\mathrm{rx}}(t) = s_{\mathrm{tx}}(\alpha t + \beta). \tag{5.25}$$

The range of the reflector during the chirp is given by (5.19), but R_0 is a function of slow time and can be written as

$$R_0 = R_{00} + v t_{\mathrm{s}}, \tag{5.26}$$

where R_{00} is the range of the scatterer at the beginning of the whole MTI data collection.

In fact, it is only the phase of the signal that is of interest here, so the received phase can be written in terms of the transmitted phase,

$$\psi_{\mathrm{rx}}(t_{\mathrm{s}}, t) = \psi_{\mathrm{tx}}(\alpha t + \beta), \tag{5.27}$$

where the t_{s} dependence is via β.

The phase of the transmitted signal is given by

$$\psi_{\mathrm{tx}}(t) = 2\pi \int_0^t f(x)\mathrm{d}x, \tag{5.28}$$

where x is a dummy variable. With (2.1), this gives

$$\psi_{\text{tx}}(t) = 2\pi \left[\left(f_0 - \frac{B}{2} \right) t + \frac{B}{2T} t^2 \right]. \tag{5.29}$$

Using (5.27) and (5.29), the dechirped signal phase, which is given by

$$\Delta\psi = \psi_{\text{tx}}(t) - \psi_{\text{rx}}(t_{\text{s}}, t), \tag{5.30}$$

can be written as

$$\Delta\psi = \psi_0 + \psi_1 t + \psi_2 t^2, \tag{5.31}$$

where

$$\psi_0 = -2\pi \left[\left(f_0 - \frac{B}{2} \right) \beta + \frac{B\beta^2}{2T} \right], \tag{5.32}$$

$$\psi_1 = -2\pi \left[\left(f_0 - \frac{B}{2} \right) (\alpha - 1) + \frac{B\alpha\beta}{T} \right], \tag{5.33}$$

and

$$\psi_2 = -2\pi \left[\frac{B(\alpha^2 - 1)}{2T} \right]. \tag{5.34}$$

5.3.2 Exact expressions for R_0 and v

It is convenient to introduce a change of variables to refer the phase to the midpoint of the spectral analysis region. This has the advantage that the constant phase in the signal gives the constant phase in the spectrum, the first-order term gives the frequency offset, and the second-order term gives the defocussing quadratic phase.

Let $t' = t - \sigma$, which gives

$$\Delta\psi = \underbrace{\psi_0 + \psi_1\sigma + \psi_2\sigma^2}_{\psi'_0} + \underbrace{\left[\psi_1 + 2\sigma\psi_2\right]}_{\psi'_1} t' + \underbrace{\psi_2}_{\psi'_2} t'^2, \tag{5.35}$$

so

$$\Delta\psi = \psi'_0 + \psi'_1 t' + \psi'_2 t'^2. \tag{5.36}$$

In many cases, the spectral analysis region will simply be $t = 0$ to $t = T$. However, in extreme cases where there is only a small overlapping region of transmitted and received signal, only that region should be analysed, removing sharp discontinuities in the IF signal that would damage the range profile and contain no useful information.

In the following calculation, I shall assume that the centre of the spectral analysis region is aligned with the middle of the overlapping region of the transmitting and the received signals for the farthest reflector to be imaged. This gives

$$\sigma = \frac{T + 2R_{\max}/\mathrm{c}}{2}. \tag{5.37}$$

The quantity ψ_0' indicates the image phase (to within a phase offset determined by the radar), ψ_1' determines the frequency offset, and ψ_2' determines the QPE (as discussed in Chapter 3).

Assuming that $v \ll \mathrm{c}$ and making first-order approximations, the frequency offset of the response is $\psi_1'/(2\pi)$. Using (5.1), (5.23), (5.24), (5.33), (5.34), (5.35), (5.36), and (5.37), the apparent range is given by

$$R_{\text{apparent}} = \underbrace{R_0}_{\text{nominal range}} + \underbrace{\frac{vTf_0}{\mathrm{c}B}}_{\text{Doppler shift}} + \underbrace{\frac{vT}{2} + \frac{v}{\mathrm{c}}\left(R_{\max} - \frac{3R_0}{2}\right)}_{\text{negligible}}. \tag{5.38}$$

The frequency in the slow-time direction is given by (5.15), and the two-dimensional phase is given by (5.36), so, using (5.23), (5.24), (5.33), (5.34), (5.35), (5.36), and (5.37), again assuming that $v \ll \mathrm{c}$, and making first-order approximations,

$$f_{\mathrm{s}} = -\frac{2v}{\mathrm{c}}\left(f_0 + \frac{Bt}{T} + \frac{B(R_{00} + vt_{\mathrm{s}} + R_{\max})}{\mathrm{c}T}\right). \tag{5.39}$$

In this section, I have found expressions for the apparent range and the slow-time frequency of a moving scatterer assuming only that $v \ll \mathrm{c}$, which is generally an excellent assumption (usually better than 1 in 1 million). These approximations for α and β need not be made, but in that case the resulting expressions are much less intuitive. Also, as will be shown in Section 5.3.4, the FCP technique is not practical for extremely quickly moving scatterers.

5.3.3 Simplified expressions for R_0 and v

Although the expressions for the apparent range, (5.38), and slow frequency, (5.39), of moving scatterers are correct and apply to any valid configuration (e.g. very large B/f_0, large R_0 and large v), the resulting artefacts in the imagery mean that, to within various (quantifiable – see Section 5.3.4) uncertainties, the expressions derived in the simple analysis can be used for all valid applications of the technique.

Apparent range

The expression for the apparent range, (5.38), can be simplified. Firstly, the $vT/2$ part is always smaller than $c/(8f_0)$, which is in turn smaller than $c/(2B)$, the smallest possible range bin width. So, this error will always be smaller than even the ideal resolution. It is also smaller than the distance moved (and so blurred) by the scatterer during the entire data collection so can be neglected.

The $(v/c)(R_{max} - 3R_0/2)$ part can be neglected because $v \ll c$ will also be smaller than the blurring of the response as the scatterer moves in range throughout the whole data collection. This term can be neglected, giving

$$R_{apparent} = R_0 - \frac{vTf_0}{B} \tag{5.40}$$

to a very good approximation, which agrees with (5.14).

Radial speed

The expression for the slow-time frequency, (5.39), shows that, along with the 'classic' $f_s = -2vf_0/c$ part, there is also a symmetric blurring due to the chirping of the signal. This does not bias the measurement but smears it out so will be neglected here and dealt with in Section 5.3.4, which is concerned with the limitations of the FCP technique.

The $(R_{00} + R_{max})B/(cT)$ part of (5.39) biases the estimate of the velocity. It has a maximum value of $B(1-F)$, when $R_{00} = R_{max}$. Here the quantity F has been introduced. It is the fraction of the echo duration that overlaps with the transmitted chirp. This is given by

$$F = \frac{T - 2R_0/c}{T} = 1 - \frac{2R_0}{cT}, \tag{5.41}$$

or, with reference to Figure 2.1,

$$F = \frac{T - T_F}{T} = 1 - \frac{T_F}{T}. \tag{5.42}$$

Note that for many FMCW radar applications $F = 0.99$ is obtained, but for MTI applications F could be smaller than 0.5.

It can be shown that the blurring in slow frequency due to the

$$(R_{00} + R_{max})B/(cT)$$

part is no greater than that due to the chirping of the signal so in most cases can be ignored. If required, it could easily be taken into account by solving a quadratic equation in R_0.

The $Bvt_s/(\mathrm{c}T)$ part of (5.39) is small compared to the blurring due to the chirping because $v \ll \mathrm{c}$, so it can also be ignored.

Neglecting these terms, the radial speed can be related to the slow-time frequency by

$$v = -\frac{\mathrm{c}f_s}{2f_0} \tag{5.43}$$

to a very good approximation, which agrees with (5.17).

In this section, I have shown that, for most practical purposes, the exactly derived expressions for the apparent range and slow-time frequency of signals agree with the simply derived ones. In extreme configurations, the exactly derived expressions could be used.

5.3.4 Parameter specification and performance limitations

There are a number of limitations on the combinations of parameters that specify the range-speed measurement. These are driven by the frequency response of the FCP technique, the decreasing overlap of the transmitted and received signals, and the migration of the scatterers through range cells. For the purposes of parameter selection, a few relationships can be found and used to derive suitable parameters to obtain the required precision and range of operation.

In this section, I shall find some simple but useful relationships between the parameters of the measurement, and I shall describe a simple method for working through the parameters to specify a range-speed measurement task.

Maximum simultaneous range and speed precision

The limit on the range resolution is given by the larger of two quantities: the degraded nominal resolution, δR, determined by the decreased overlap (which affects all scatterers in the scene) and the blurring out of the response, ΔR, as the scatterers migrate through range cells during the slow-time extent of the whole measurement. The second limit increases as the slow-time extent of the signal increases. It is also proportional to the speed of the scatterer.

The degraded range bin depth (due to reduced signal overlap) is indicated by (2.12) and is given by

$$\delta R \geq \frac{\mathrm{c}}{2BF}. \tag{5.44}$$

The blurring in range due to motion of the scatterer through resolution cells is

$$\Delta R \geq v T_{\mathrm{s}}, \tag{5.45}$$

where

$$T_{\mathrm{s}} = \frac{\mathrm{c}}{2 f_0 \delta v}, \tag{5.46}$$

where δv is the speed bin width. So

$$\Delta R \delta v \geq \frac{v\mathrm{c}}{2 f_0}. \tag{5.47}$$

The defocussing due to the quadratic phase introduced by the radial motion (the $\psi_2' t'^2$ part of (5.36)) is limited to being no greater than $\pi B F^2/(2 f_0)$, which, for any real system, is negligible.

Similarly, the resolution in the radial speed is given by the larger of two quantities: the first is the lower limit on the radial speed resolution, δv, determined by the slow-time extent of the signal. This can be seen to be the same relationship as that driving the second lower limit on the range resolution, i.e. (5.47). The second is the blurring, Δv, due to the chirping of the signal.

The blurring of the radial speed resolution due to the chirping can be seen from (5.39) to be given by

$$\Delta v \geq \frac{F B v}{f_0}. \tag{5.48}$$

Multiplying (5.44) and (5.47) together gives

$$\delta R \Delta v \geq \frac{v\mathrm{c}}{2 f_0}. \tag{5.49}$$

The best resolution in R and v that can be achieved is always the larger of the bin width and the blurring. The bin width should be set equal to the blurring to obtain the best available resolution without oversampling the data: set $\Delta R = \delta R$ and $\Delta v = \delta v$. Equations (5.47) and (5.49) then give

$$\delta R \delta v \geq \frac{v_{\max}\mathrm{c}}{2 f_0}, \tag{5.50}$$

which allows the selection of suitable bin sizes and indicates the precision in the estimates of R and v.

If the specification in the FCP uses smaller values of bin spacing δR and δv than given by (5.50), then the resolutions no longer exactly match the bin spacing and revert to the values given by (5.47) and (5.49). I.E., attempting to over resolve R actually blurs v and vice versa. This is effectively a range-speed uncertainty principle: it is not possible simultaneously to measure both v and R with arbitrary precision for a given $v_{\max}$ and f_0 with this technique.

Maximum simultaneous speed and range

The maximum measurable slow-time frequency is

$$f_{\max} = \frac{1}{2T}. \tag{5.51}$$

The maximum slow-time frequency arising from radial scatterer motion is, using (5.43), given by

$$f_{\max} = \frac{2v_{\max}f_0}{\mathrm{c}}. \tag{5.52}$$

So, with (5.51) and (5.52), the maximum measurable radial speed is connected to the duration of the chirp.

Using (5.41), (5.51), and (5.52), the maximum measurable radial speed can be connected to the maximum range of operation and the overlap fraction. This gives

$$R_{\max}v_{\max} = \frac{\mathrm{c}^2(1-F)}{8f_0}. \tag{5.53}$$

Simple parameter selection method

Normally, the carrier frequency, f_0, and the maximum chirp bandwidth, B, of the radar are known, so it remains on a task-by-task basis to decide $R_{\max}$, $v_{\max}$, δR and δv.

As it is usual to specify the range of operation first, use (5.53) to find F. Next, F and the maximum chirp bandwidth can be used to obtain the desired range resolution and the corresponding speed resolution using (5.44) and (5.50). The value of B can then be relaxed to achieve the best compromise.

There are many ways in which the parameter selection can be ordered and achieved, and these can be developed for specific requirements.

5.3.5 Simulations and an example calculation

A computer program was written to generate realistic signals from a set of moving scatterers (ranges 1100 m, 1120 m, 1140 m, 1160 m, and 1180 m; and speeds -8 ms^{-1}, -5 ms^{-1}, 0 ms^{-1}, 5 ms^{-1}, and 8 ms^{-1}) for $B = 100$ MHz and $v_{\max} = 10$ ms^{-1}.

To illustrate the use of the simple rules in the previous sections, I shall calculate the various quantities for this simulated case.

The following quantities are chosen according to required performance: $B = 100$ MHz, $f_0 = 94$ GHz, $R_{\max} = 1190$ m, and $v_{\max} = 10$ ms^{-1}.

Using (5.53), F is found to be 0.9. Using (5.44), the highest allowable speed resolution is found to be $\delta v = 2.7 \times 10^{-3}$ ms^{-1}, which is much finer than usually necessary, so δv can be relaxed to 0.2 ms^{-1}.

The duration of the chirp, T, is found, using (5.50), to be 7.8×10^{-5} s. Using (5.39), the values of f_1 and f_2 are found to be 9.3 MHz and 10.0 MHz respectively. This gives a conventional sampling rate of 20.0 MHz. Using these values, the k-N plot can be found; it is shown in Figure 5.6. From this plot, suitable values of k and N can be found. In this case they are 1.083 and 10 respectively. With f_s given by (5.7), the sampling rate to achieve exact aliasing of the pass band is found to be 1.8 MHz.

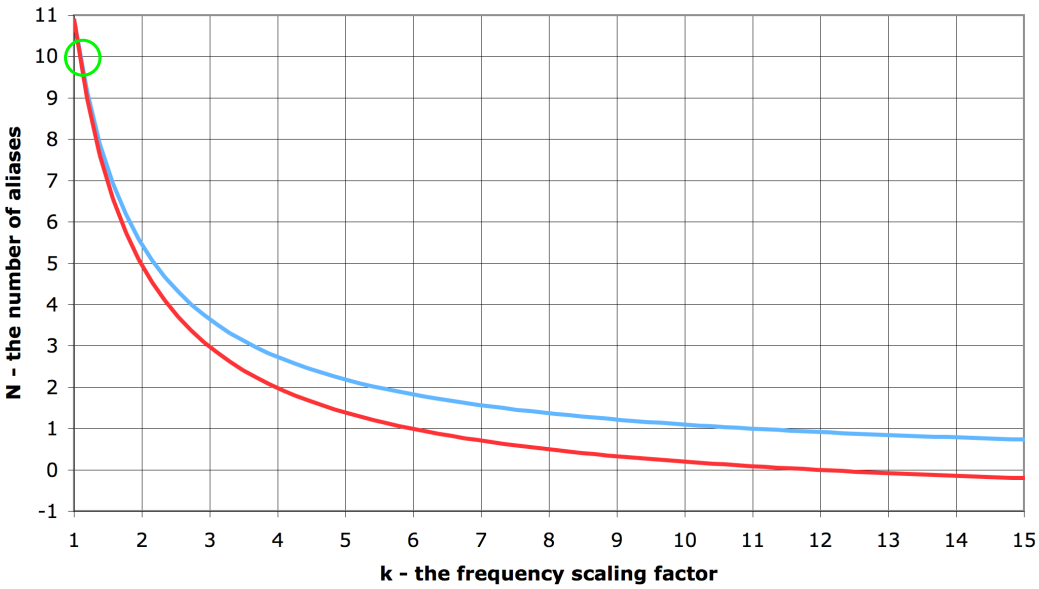

Figure 5.6: The k-N plot for the numerically simulated example. The largest possible number of aliasses is $N = 10$ (at $k = 1.083$), which is highlighted with the green ring.

The results of processing with subsampling ($f_s = 1.8$ MHz and $N = 10$) and without subsampling ($f_s = 20$ MHz and $N = 1$ giving a factor of 10 reduction in the required sampling rate) are shown in Figures 5.7 and 5.8. Slices through the response are shown for $R = 1180$ m both with and without subsampling in Figures 5.9 and 5.10 respectively.

It can be seen that there is good agreement between the plots, indicating that there are no undesirable artefacts due to the subsampling. Note that the power of each plot was normalized to aid comparison.

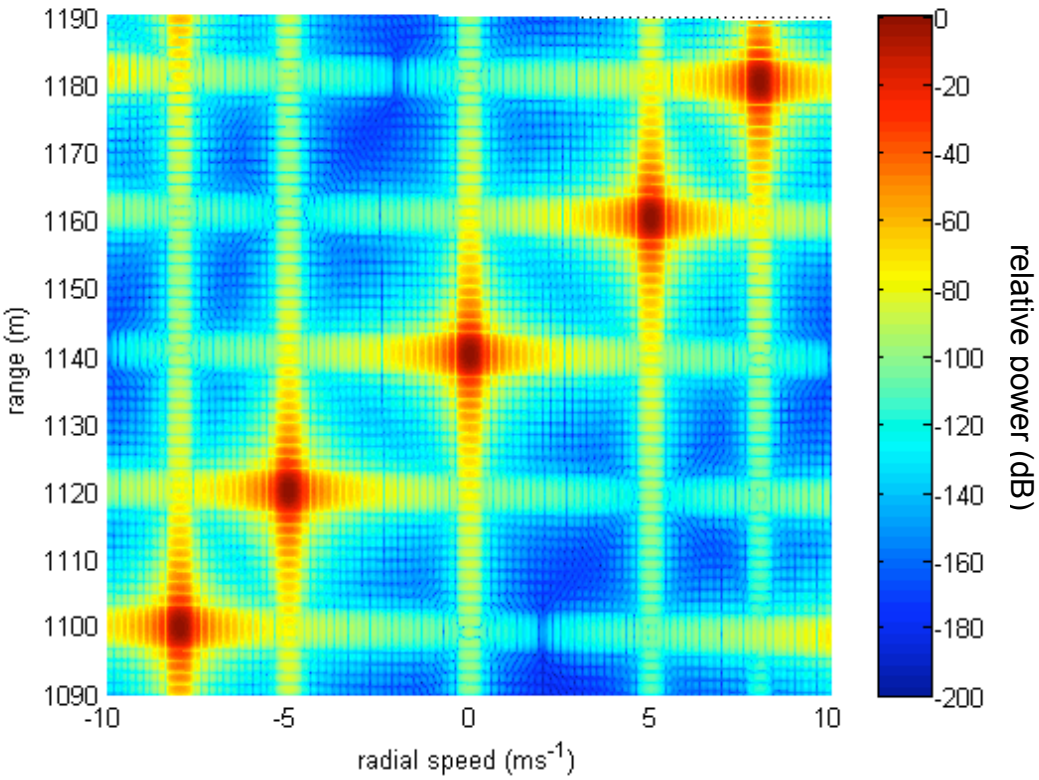

Figure 5.7: Speed-range plot for synthetic scatterers processed from normally sampled signals.

A deliberately extreme case, with large B/f_0 obtained by reducing f_0 and leaving all other parameters unchanged, was then simulated to demonstrate the resulting 'defocussing' effects. The parameter choice for this case was $v_{\max} = 30$ ms^{-1}, $B = 195$ MHz, $f_0 = 1$ GHz, $\delta v = 0.1$ ms^{-1}, and $F = 0.7$. Five moving scatterers were placed in 20 m steps up to the maximum range and given radial speeds of -10 ms^{-1}, -5 ms^{-1}, 0 ms^{-1}, 5 ms^{-1}, and 10 ms^{-1} respectively. The resulting range-speed profile is shown in Figure 5.11. In this case, the blurring in range and speed is larger than the bin widths. This is, of

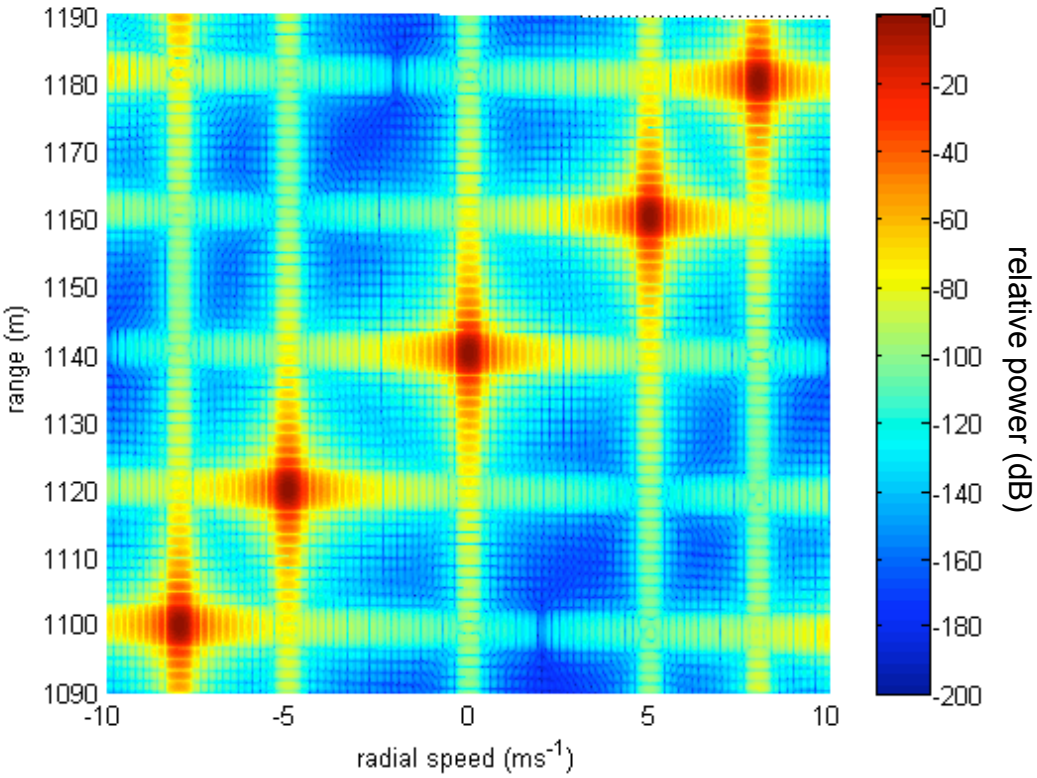

Figure 5.8: Speed-range plot for synthetic scatterers processed from subsampled signals.

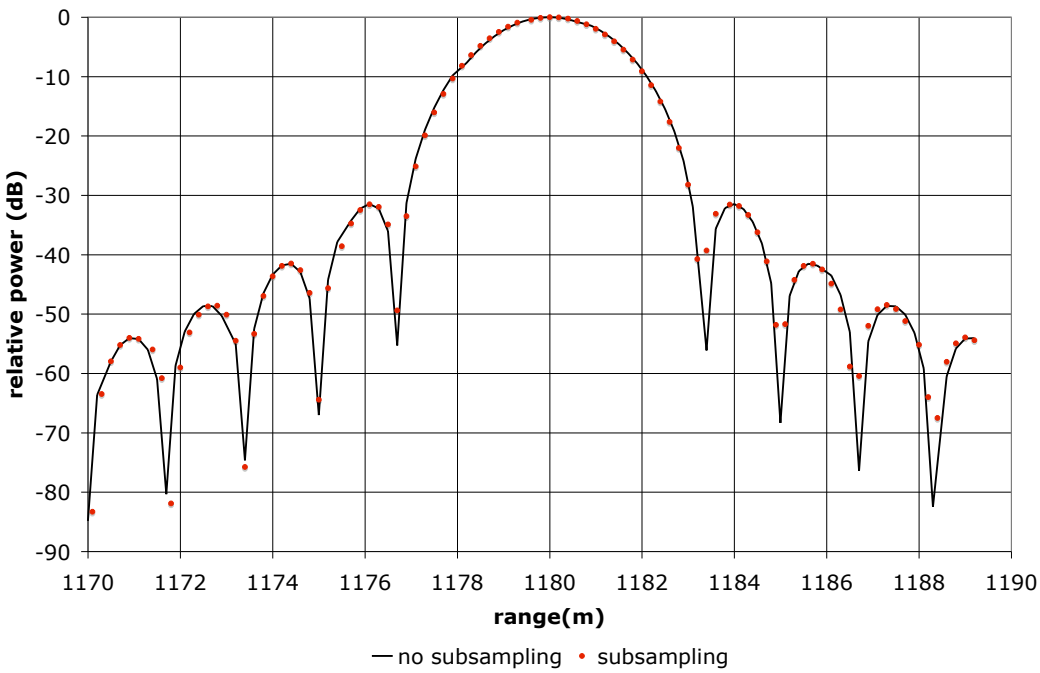

Figure 5.9: Comparison of the range response for the scatterer at $R = 1180$ m and $v = 8$ ms^{-1} taken with and without subsampling.

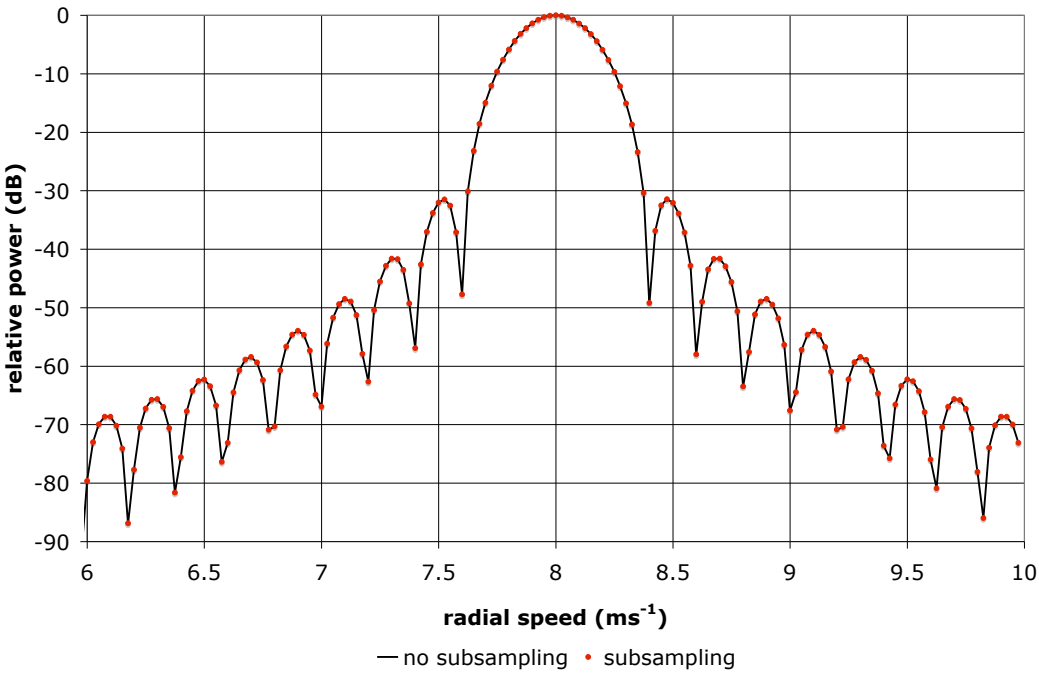

Figure 5.10: Comparison of the speed response for the scatterer at $R = 1180$ m and $v = 8$ ms^{-1} taken with and without subsampling.

course, a badly specified system, but it clearly illustrates the blurring.

The range and speed resolution were calculated using (5.47) and (5.48) to be 15 m and 1.4 ms^{-1} respectively, which agree reasonably well with the observed blurring of 16 m and 1.6 ms^{-1} respectively.

5.3.6 Radar demonstration

To demonstrate the technique on a real radar with a real moving scatterer, an educational demonstration radar, SAFIRE [87], was modified to perform MTI and subsampling.

A uniformly moving scatterer was achieved by attaching a trihedral reflector to a bicycle. SAFIRE's radar beam is a vertical fan, about 1° in azimuth and about 60° in elevation. The size of the beam helped to keep the moving scatterer illuminated during the data collection. However, the elevation extent of the beam also resulted in the ground being imaged, which in turn resulted in severe ground clutter at all ranges. It was not possible to filter the signal to remove all contributions from scatterers at other ranges, so the clutter at zero Doppler will be a mixture of the clutter at the ranges indicated by the range scale and the aliased signal energy.

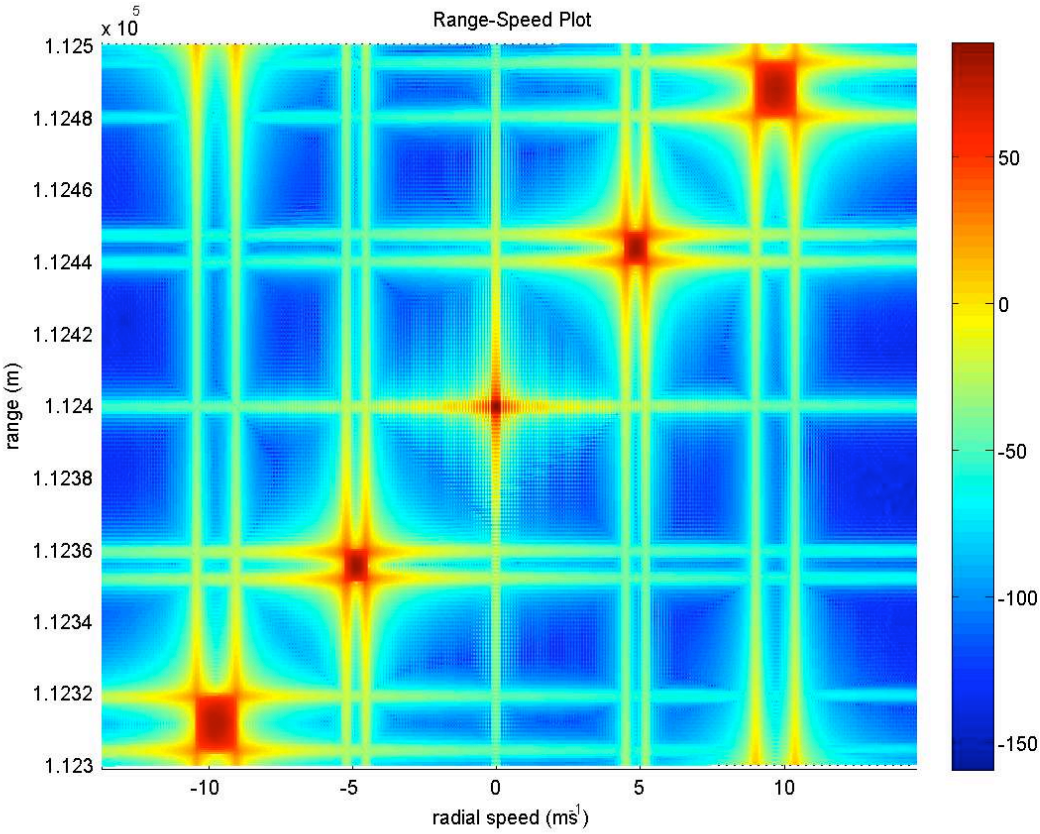

Figure 5.11: The effect of extreme operation on the localization of scatterer responses in the two dimensional range-speed plot.

The bicycle was ridden towards the radar, and the MTI data collection was run when the bike was (later measured to be) around (50 ± 5) m from the radar. The speed of the bike was (later approximately calibrated to be) about (4 ± 1) ms^{-1}.

The radar centre frequency, f_0, was 94 GHz, the bandwidth, B, was 98 MHz, the subsampling rate, f_s, was 600 kHz, the chirp time, T, was 80 µs, and there was one alias (it was not possible to operate at a farther range without the signal becoming too weak).

The resulting range-speed profile is shown in Figure 5.12, where it can be seen that there is a considerable amount of clutter in the zero Doppler bin but that the moving scatterer is clearly picked out. Another profile was collected with the same arrangement but with the scatterer receding. The profile is shown in Figure 5.13. It can be seen that the measured range and speeds are consistent with the estimated scatterer motion.

Whilst this was not a calibrated experiment (which could be done using the method described by Klugmann [88]), it provides a proof-of-principle demonstration. This simple illustration demonstrates that the MTI and subsampling techniques are compatible in a real radar application.

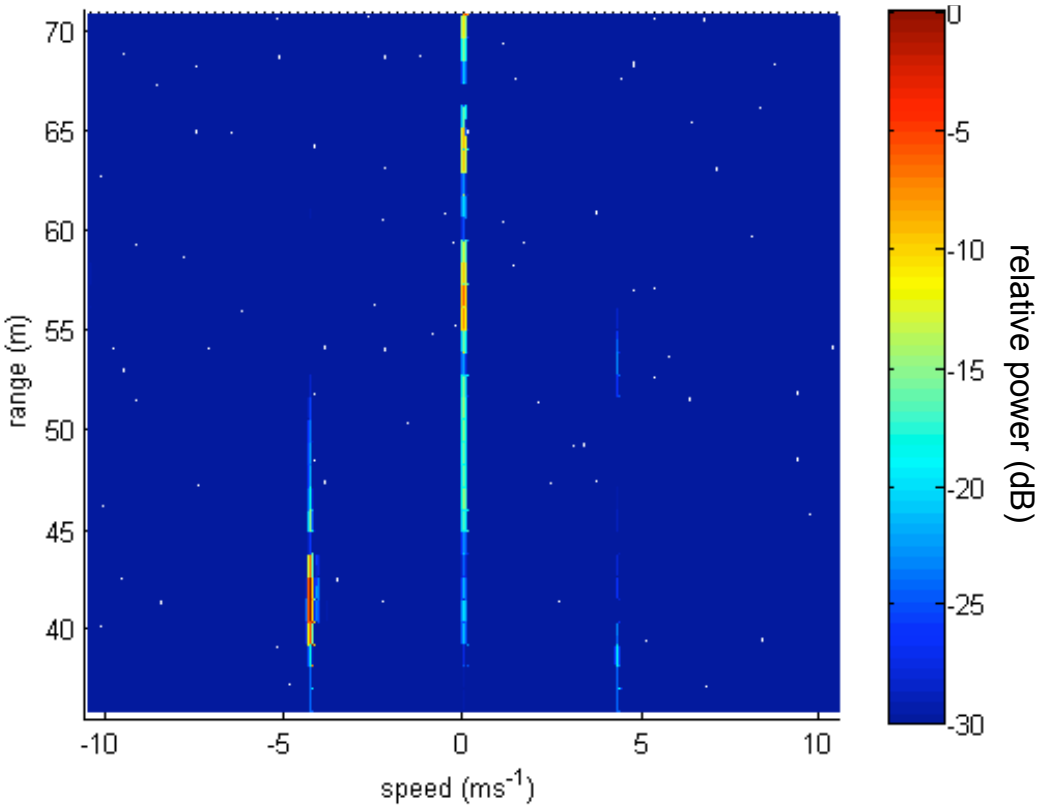

Figure 5.12: A range-speed profile for a real approaching scatterer computed from a subsampled radar signal. The scatterer was a 20 dBsm trihedral attached to the handle bars of a bicycle.

5.4 Conclusions

In this chapter, I have described and quantified a technique based on subsampling for down converting band-limited IF signals to reduce the IF sampling rates in homodyne FMCW radars.

I have described and quantified a particular application, MTI using FCP, and described rules for specifying the performance and operational range for arbitrary FMCW radar systems.

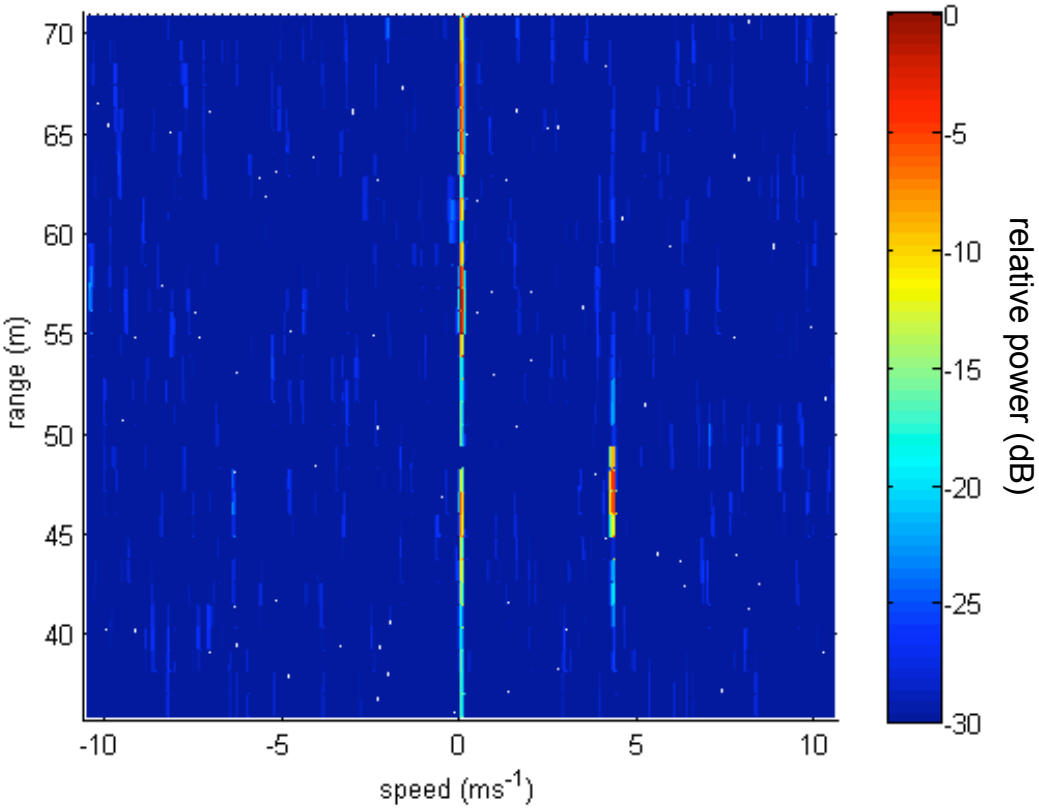

Figure 5.13: A range-speed profile for a real receding scatterer computed from a subsampled radar signal. The scatterer was a 20 dBsm trihedral attached to the parcel shelf of a bicycle.

I have demonstrated, in numerical simulations and a real radar demonstration, the validity of combining the FCP and subsampling techniques, providing long-range fine-resolution MTI capability for homodyne FMCW radars without extensive hardware modification.

Chapter 6

Synthetic Aperture Radar Test Bench

In this chapter, I shall describe work done to establish a mm wave homodyne FMCW synthetic aperture test bench instrumentation radar. I shall describe the mechanical construction and operation of the SAR test bench and the software to run experiments and perform data collection. I shall describe the RMA data processing algorithm and the modifications that I have made. I shall also describe a data simulator and a series of tests to investigate the sensitivity of the technique to typical signal errors. I shall investigate the phase noise properties of candidate signal sources, relating the chirp waveform voltage noise to the resultant sidebands in the range PSF of the radar. Finally, I shall demonstrate mm wave homodyne FMCW SAR imaging and evaluate the initial performance of the test bench.

6.1 Introduction

Synthetic Aperture Radar (SAR) is a signal processing technique for producing two-dimensional radar images from a coherent set of one-dimensional radar signals collected at different points in space. SAR uses the coherent set of signals to synthesize a narrow sliding or rotating virtual radar beam that is much narrower than the real beam.

In SAR imaging, there are two commonly used types of scene illumination:

1. stripmap mode: the scene is illuminated by a radar beam that is translated along the radar path. The longest synthetic aperture that can be

synthesized is equal to the footprint of the radar beam on the ground at the scene. In this mode, the along-track extent, L, of the scene can be infinite, but the resolution is limited by the beamwidth, θ_b, $\rho \geq \lambda\kappa/(4\sin(\theta_b/2))$;

2. spotlight mode: The scene is illuminated by a beam that is steered, as the radar moves along its path, in order to illuminate the same scene for the whole data collection. This allows for very long data collection intervals so allows very fine along-track resolution, too. However, the scene size is limited to the illuminated patch. In this mode, the resolution is limited by the carrier frequency, $\rho \geq \lambda/4$, and the scene size is limited by the beam width, $\Delta x \leq R\theta_b$.

The type of illumination used depends on the application: if very large regions of the ground must be imaged, then stripmap mode is suitable; if small regions of the ground must be imaged with very fine resolution, then spotlight mode is suitable.

Spotlight and stripmap mode SAR data collection geometries are illustrated in Figure 6.1.

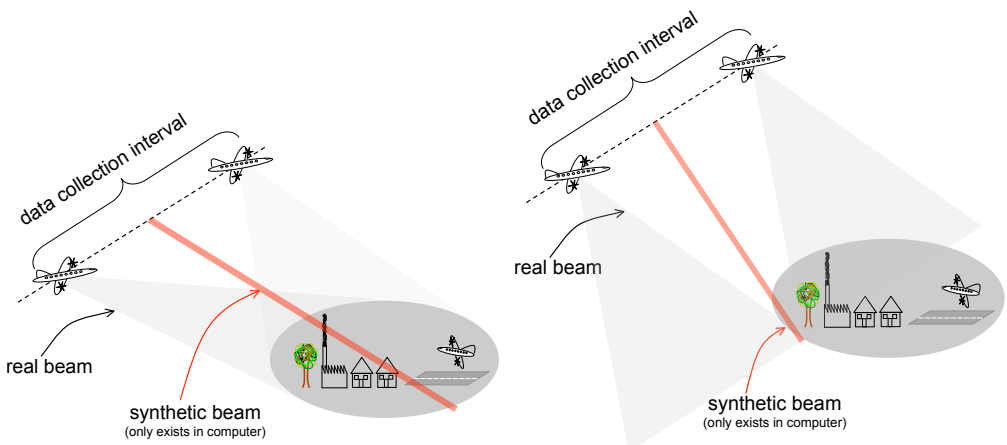

Figure 6.1: Left: spotlight mode radar imaging a scene from a number of different vantage points, in this case along a straight line. The virtual radar beam is shown in red. It exists numerically in the computation of the SAR image. Right: Stripmap mode radar imaging the same scene.

SAR processing can provide very high cross-range resolutions at very long ranges by collecting data from sufficiently long intervals in space. Consequently, there are many applications of SAR, including:

1. military: reconnaissance [89] and MTI [90, 91];
2. scientific: monitoring of pack ice [92], oceanographic flow [93, 94], and pollution measurement [95];
3. civil: crop mapping [96], flood plain mapping [97], and elevation mapping [98];
4. navigation.

SAR is useful because it enables radars to achieve fine resolution in the cross-range direction without the need for a very large antenna.

For instance, to form a 1 m cross-range resolution image at 1 km standoff range directly with a real beam at 94 GHz would require a 4.8 m diameter antenna. It is effectively impossible to manufacture and maintain such an antenna. However, to achieve this resolution using aperture synthesis would only require a small antenna and some means of translating the radar sideways through 2.4 m. Owing to the nature of the aperture synthesis, the resolution for a synthetic aperture is twice as fine as for a real antenna of the same width. The required aperture length scales with standoff range, so at 10 km standoff 1 m cross-range resolution requires a 48 m real antenna or a 24 m synthetic one. Clearly, the former is impossible, whereas the latter can be achieved by translating the radar on a vehicle or a specially constructed track.

SAR can be performed with radars (or sonars, giving Synthetic Aperture Sonar (SAS)) of more-or-less any type provided the requirements for coherence can be met. This allows the frequency of the radar to be chosen to suit the task. In many cases, this choice is driven by the nature of the scene being imaged, e.g. imaging through foliage (FoPen radar for **Fo**liage **Pen**etration) uses low-frequency electro-magnetic radiation (e.g. Carabas, which uses a 20 to 90 MHz signal) [99], whereas radars for imaging urban scenes often use radars operating at 10 GHz, e.g. TerraSar-X, giving low attenuation, small fractional bandwidth, and ease of construction [100].

mm-Wave radars can be used to collect data for SAR and have been shown to be highly suitable for applications such as the remote sensing of wave patterns [101] and the generation of digital terrain models [102]. Examples include SUMATRA, an unmanned air vehicle based SAR [103], and MEMPHIS, a fully polarimetric experimental radar [65].

An advantage of mm-waves is that they offer the ability to form high cross-range resolution images from relatively small synthetic apertures compared

to lower frequencies. This is because, for a given resolution, the required synthetic aperture is proportional to the carrier wavelength: a given resolution can be achieved by a 94 GHz SAR with an aperture roughly a ninth the length of that for a 10 GHz SAR.

The type of radar studied in this thesis is homodyne FMCW. As discussed in earlier chapters, this mode of operation has many advantages for radar imaging, including low cost, stability, robustness, operation at very high frequencies and wide bandwidths, and light computational requirements. However, these kinds of radar often transmit long chirps, which can be problematic for some SAR applications. In SAR, it is usual (although not always necessary) to make the 'Stop/Start' approximation. This is an assumption that the radar is stationary at each data collection point. For slow-moving radars and short chirps, this is a good assumption. However, this assumption can break down in the case of some (typically long-range) FMCW radar systems. Research has been done [66, 69] to modify the signal processing model, accommodating the long chirp duration.

With increased interest in mm-wave and FMCW SAR, it would be useful to investigate this technique for a variety of emerging applications, such as high-resolution terrain imaging. The aim of the work reported in this chapter is to develop a SAR-capability extension to the FMCW instrumentation radar. This SAR instrumentation radar is intended to provide a test bench on which to investigate the suitability of radar components for use in SAR applications and to investigate the properties of scatterers in SAR imaging situations. The FMCW instrumentation radar will form the basis of the SAR test bench, and the work described in this chapter is an attempt to provide the linear translation of the radar and the signal processing capability to produce two-dimensional imagery.

In this chapter, I shall discuss the available SAR processing algorithms and their benefits, selecting the Range Migration Algorithm (RMA) as a suitable processor to implement for the test bench. I shall then briefly outline the operation of the RMA and the signal requirements. I shall also discuss some simple modifications I have made to allow short along-track data extents and to accommodate drifting oscillator centre frequencies and homodyne FMCW radar data. I will describe a data simulator and use it to demonstrate the RMA implementation. I will then use the simulator and the RMA processor to investigate image quality tolerance to radar position error and drift in the centre frequency of the oscillator. Then I shall discuss the construction of

the radar translation and data collection system. Next, I shall discuss some tests to find a suitable oscillator for the radar, particularly with respect to frequency stability and phase noise. Finally, I shall present and discuss some initial demonstration SAR images produced by the test bench SAR.

6.2 SAR algorithm overview and selection

When a radar images a scene and produces a one-dimensional (range compressed) range profile, the voltage in each range bin is the sum of all of the voltages due to all of the scatterers in that range bin for the whole beam. This means that the voltage in each range cell is actually the beam-weighted integral over the range of beam angles. This is illustrated in Figure 6.2, from which it can be seen that the contents of the beam in each range cell are 'added' together to give an overall single value of the reflected power. The range profile gives no indication of the cross-range distribution of the reflectors. This is often the case for high range resolution compact mm-wave radars operating at long range, where the cross-range resolution is coarse compared with the range resolution [13].

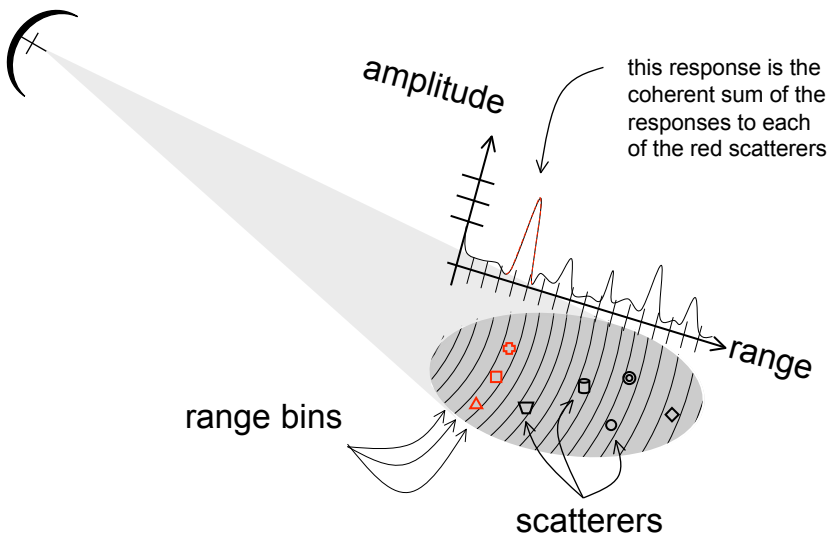

Figure 6.2: The range profile resulting from a radar illuminating a patch of scene containing multiple scatterers. The range profile does not describe the cross-range distribution of the scatterers.

There are several very different approaches to SAR processing, but they all have the same goal, which is to translate a coherent set of one-dimensional

radar measurements into a two-dimensional map of the RCS of the scene, i.e. the SAR image. N.B. here the word 'image' *does* refer to a two-dimensional map of reflected power.

Various algorithms exist to perform the inversion from radar data to image. The various algorithms prioritize different aspects of the problem. Mostly, though, the balance is among precision, generality, and computational load.

In the following discussion, it will be useful to refer to fast and slow time. This was discussed in Section 5.3 in the context of MTI. In this context, the fast time still refers to the time during the chirp (or the IF signal), and slow time still refers to the time between successive chirps. In fact, it is the *distance* between the IF signal collections that is important, not the time. However, it is usual to assume a constant along-track velocity for the radar, so slow time translates directly into along-track position.

There are essentially two types of SAR processor: those that operate in the time domain and those that operate in the wavenumber domain [104].

A popular time-domain method is called the Back Projection Algorithm (BPA). This approach operates by reversing the projection of received power along constant range curves onto the range profiles. The complex amplitude in each cell from each range profile collected is smeared out in the corresponding arc and added to an image that is built up by repeating this process for every range cell from every range profile. This can also be understood from the reverse point of view: for every image pixel, the value in the corresponding range bin of every range profile is added; effectively a voting system (i.e. a spatially variant matched filter) for the presence of a reflector in each image cell. The returns are coherent, so if there is a scatterer in a resolution cell, the corresponding contributions from all of the range profiles will add up. If there is no scatterer in that scene location, the contributions will tend to cancel. A filtering step finishes the process. The location of every image cell and the location of the radar at every range profile can be arbitrary. Consequently, this method has the potential to be very versatile, being able to cope with non-planar images (e.g. a hillside) and nonlinear trajectories. However, this is also a computationally very intensive method, having to sum over the range profiles for every resolution cell. Methods have been developed (e.g. the Fast Factorized BPA, [68, 105]) that attempt to accelerate the BPA. However, these are difficult to implement and require careful factorization of the problem if the resulting image quality is not to degrade unacceptably.

Wavenumber-domain processors generally transform the data by applying

phase corrections and distortions to the collected radar signals to obtain the Fourier conjugate (i.e. the spatial frequency response) of the scene. A computationally efficient two-dimensional FFT can then be used to form the image. This is one way of understanding how an FMCW radar forms a normal range profile.

Generally, matched filtering is a correlation search of the reflected signal (i.e. the echoes) for delayed and attenuated copies of the transmitted signal. This could be done directly as a time-domain correlation but would be very inefficient. However, it can also be done computationally efficiently in the frequency domain using FFTs and the following relationship:

$$f * g \equiv \mathrm{FT}^{-1}\left[\mathrm{FT}(f)\mathrm{FT}(g)\right], \tag{6.1}$$

where FT signifies Fourier transformation.

This allows the convolution of the received signal and the complex-conjugate of the time-reversed transmitted signal (i.e. the matched filter) to be done in the frequency domain, where the computationally efficient FFT can be used.

It is useful to think of the signal in this domain. When variously delayed signals (from scatterers at different ranges) are Fourier transformed, their Fourier transforms are all aligned. The only difference between them is a linear phase ramp with gradient proportional to their delay. This means that the same (multiplicative) matched filter can be applied simultaneously to cancel out the phase variation due to the transmitted (chirped signal). After the filter has been applied, each echo is just a pure signal tone, with frequency (i.e. phase ramp gradient) proportional to the range of the scatterer that reflected it. The signal is now the range-wavenumber-domain radar range profile. Fourier transforming it translates it back into the range domain, i.e. giving the range profile. This also applies for two-dimensional SAR signals.

The above description of matched filtering is true for signals that are not linearly chirped, for instance, the phase modulation could be a piece of music, or noise. However, in the case of linear FM, the radar illuminates the scene with a range of frequencies in continuous succession. Effectively, the first Fourier transform to convert the received echoes into a frequency representation has been done. It is then possible to remove the phase variation due to the chirp by down converting against the current transmitting signal, effectively applying the matched filter. After this, the signal only has linear phase variations, with the phase gradient being proportional to the delay, i.e. it is

the range-wavenumber-domain radar range profile. A single Fourier transform translates the signal back into the image domain, giving the required radar range profile.

So, in the case of the linear chirp, much of the signal processing can be done in analogue devices, principally the mixer, reducing the computational load dramatically compared to a general matched filter pulse compression system. As discussed in the introduction, this is a very important reason that (linear) FMCW is a powerful technique.

A particular wavenumber-domain processor, the Polar Format Algorithm (PFA), forms an image by taking the IF signals collected along the synthetic aperture and subtracting the phase of the scene centre from the phase histories of all the scatterers. A mapping is calculated to transform the signal from the f-t domain (the data collection coordinates) to the k_x-k_y domain, which is the Fourier conjugate of the image domain. The data is projected (and interpolated) onto the ground plane (doing this removes the change in phase due to the elevation of the radar) and can then be efficiently two-dimensional FFTd into the image. A final 'keystone' correction removes a range-dependent cross-range scaling in the image caused by the mapping of the data for all of the scene being done with a mapping calculated for the scene centre. This is essentially a range dependent stretch on the width of the image.

The PFA can produce excellent results from suitable data, is computationally efficient, and does not require excessive along-track sampling rates. However, owing to the approximate cross-range dechirping, which is only true for the scene centre, phase errors begin to degrade the resolution as the scene size is increased relative to the stand off range. The limit on the scene size for $\pi/2$ quadratic phase errors has been shown to be given by [67, 106]

$$L = \rho\sqrt{\frac{2R}{\lambda}}, \tag{6.2}$$

where ρ is the cross-range resolution, R is the stand off range, and λ is the carrier wavelength.

This method of processing the data is highly suitable for far-off, low-resolution, or small scene cases. However, for the experimental test bench, in which relatively large, short standoff range, fine resolution images will be processed, it is not suitable.

In an extreme experiment, the SAR test bench might be used with the following parameters: $\rho = 0.05$ m, $R = 3$ m, and $\lambda = 0.003$ m. This gives a

maximum scene size of 2.2 m, which is not sufficient. Doren [106] describes a technique for correcting the phase errors that limit the scene size. However, for the test bench, a transparent and exact approach with reasonable computational load is required.

6.3 Range Migration Algorithm

There are other wavenumber processing algorithms, but an algorithm called the Range Migration Algorithm (RMA) appears to be well-suited to the task of processing the data for the SAR test bench.

The RMA is not an especially computationally efficient algorithm, but it does offer exact processing for very wide, close scenes at an acceptable computational cost, provided the radar trajectory is straight.

My implementation and so the following analysis, too, are based on the description of the RMA in the textbook by Carrara et al. [67].

I shall briefly describe the signal processing performed by the implementation of the RMA for the SAR test bench, noting the small modifications that I have made to enable the use of oscillators with drifting centre frequency, real-sampled FMCW radar signals, and the shortest possible along-track data collection interval.

The RMA is based on a seismic imaging technique [107] and corrects for wavefront curvature. This is ideal for the test bench radar, which will be used to image close, wide scenes.

The RMA assumes a linear track, but this is not a problem because the test bench radar uses a highly linear (at least above the 0.1 mm scale) translation stage.

Whilst the RMA uses FFTs to compute the final image, this technique is computationally more demanding than the PFA. However, although very long computation times (i.e. significantly longer than the time required to collect the data) are not acceptable, fast image processing is not vital in the SAR test bench, whereas algorithmic transparency and precision are.

6.3.1 Overview of the standard RMA

The aim of the bulk of the RMA's signal processing is to manipulate a set of along-track radar signals into the k_x-k_y domain, which is the Fourier conjugate of the image domain. In this sense, 'image' refers to the two-dimensional

plot of the received radar power from each point in the scene that is being illuminated by the real radar beam. It is a short and computationally efficient step to perform a two-dimensional FFT on the k_x-k_y signal to give the x-y signal, i.e. the SAR image of the scene.

First, the RMA takes a two-dimensional signal (in one dimension the radial spatial wavenumber k_r, in the other dimension the along-track radar position x) and Fourier transforms it in the along-track direction to give a signal in the k_x-k_r domain. The signal emerges from the homodyne FMCW radar in the k_r domain but without the phase correction required for the RMA. A simple pre-processing step, which will be discussed in Section 6.3.2, effects the required correction.

Next, the phase variation due to platform motion is removed from each k_x-k_r signal component through multiplication by a matched filter. This is possible because, for a given range, the signals of scatterers at different along-track positions are identical apart from an along-track delay (due to their along-track position). The along-track Fourier transformed signal components are identical apart from a linear phase ramp, which encodes the along-track position of the scatterer that reflected that signal component.

Once this is done, the signal is in the k_x-k_r domain, and the signal phases are dependent only on the scatterer position and the wavenumber position, (x, y) and (k_x, k_y) respectively.

However, the signal is still stored on a k_x and k_r grid (coordinate system) which cannot be FFTd. The wavenumber domain signal must be resampled onto a k_x-k_y grid to yield the required Fourier conjugate of the image. Suitable window weighting is applied to the signal, which is then two-dimensional FFTd into the image domain.

6.3.2 Signal processing in the customized RMA

In this section, which follows the analysis given in Carrara [67], the signal of a representative sample scatterer is traced from the collected signal to the SAR image to indicate the operation of the RMA. I also describe the modifications that I have made to allow the RMA to process homodyne FMCW radar data.

The data collection geometry is illustrated in Figure 6.3, from which it can be seen that the radar trajectory is assumed to lie in the slant plane. SAR images produced from a linear aperture cannot resolve the location of the scatterers in the polar angle around the trajectory. It is assumed, then, that all

scatterers lie in this slant plane. In this simple analysis, it will be assumed that the imaging is broadside (at right angles to the radar path), which will be the arrangement for the SAR test bench.

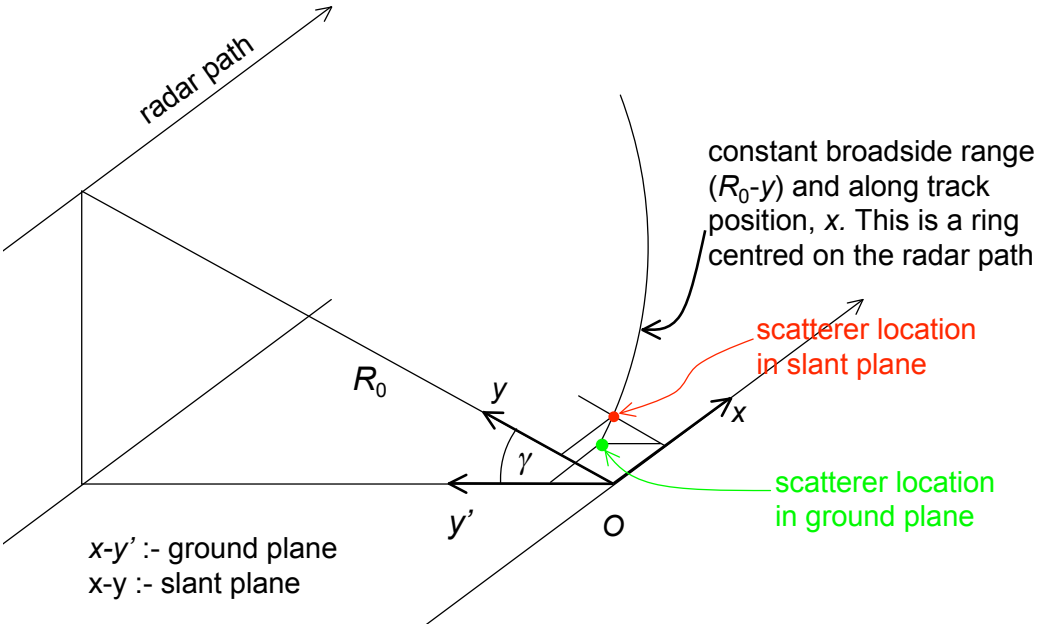

Figure 6.3: The geometry of the radar path and the slant plane. It is not possible to distinguish where on the circles around the radar path scatterers might be (other than that they must be in the beam), so it is assumed that they lie in the slant plane. Once the image is formed (in the slant plane), it can be mapped onto the ground.

The FMCW homodyne radar transmits a chirped signal with frequency profile given by

$$f_{\text{tx}}(t) = f_0 - \frac{B}{2} + \frac{Bt}{T}, \tag{6.3}$$

which is just (2.1).

The phase of this signal is given by

$$\phi_{\text{tx}}(t) = 2\pi \int_0^t f_{\text{tx}}(t')\mathrm{d}t', \tag{6.4}$$

which is

$$\phi_{\text{tx}}(t) = 2\pi \left[\left(f_0 - \frac{B}{2} \right) t + \frac{Bt^2}{2T} \right]. \tag{6.5}$$

The received echo from a scatterer in the scene has the same phase as the transmitted signal apart from the round trip delay, τ. This gives the phase of

the received signal,

$$\phi_{\mathrm{rx}}(t) = \phi_{\mathrm{tx}}(t-\tau), \tag{6.6}$$

so

$$\phi_{\mathrm{rx}}(t) = 2\pi\left[\left(f_0 - \frac{B}{2}\right)(t-\tau) + \frac{B(t-\tau)^2}{2T}\right]. \tag{6.7}$$

In homodyne FMCW radar, it is usual to deramp the received signals with the current transmitting signal. However, for the RMA to work, it is necessary to produce signals that are dechirped using a copy of the transmitting signal but delayed by a time corresponding to the round trip time to the scene centre, σ, giving zero phase variation for scatterers at the scene centre.

This gives

$$\phi_{\mathrm{tx}}(t-\sigma) - \phi_{\mathrm{rx}}(t) = 2\pi\left(f_0 - \frac{B}{2} + \frac{B}{T}(t-\sigma)\right)(\sigma-\tau) + \underbrace{\frac{\pi B}{T}(\sigma-\tau)^2}_{\text{'Residual Video Phase'}}. \tag{6.8}$$

The Residual Video Phase (RVP) is a small error part due to the dechirp-on-receive signal processing that can be ignored in the present application. In severe cases, the RVP can be removed by including a frequency dependent delay in the preprocessing steps (the inclusion of a phase correction of the form $\pi T f^2/B$ in (6.14)). However, the phase error, which is problematic if $\sigma - \tau$ changes sufficiently over the synthetic aperture, will not be very great for the minimal length data collection intervals planned for the short-baseline SAR test bench.

So, ignoring the RVP part, the dechirped (to an offset range) signal phase is

$$\phi_{\mathrm{d}}(t) = -2\pi\left[f_0 - \frac{B}{2} + \frac{B}{T}(t-\sigma)\right](\tau-\sigma). \tag{6.9}$$

From this the phase of the dechirped signal (for this sample scatterer) can be written in the following form

$$\phi_{\mathrm{d}}(t) = k_r(R_{\mathrm{s}} - R_{\mathrm{r}}), \tag{6.10}$$

where the reference scatterer range (used to dechirp the signal) is given by

$$R_{\mathrm{r}} = \frac{\mathrm{c}\sigma}{2}, \tag{6.11}$$

the sample scatterer range is given by

$$R_{\mathrm{s}} = \frac{\mathrm{c}\tau}{2}, \tag{6.12}$$

and k_r, the range wavenumber, is

$$k_r = -\frac{4\pi}{\mathrm{c}}\left[f_0 - \frac{B}{2} + \frac{B}{T}(t-\sigma)\right]. \tag{6.13}$$

N.B. this is just the spatial equivalent of the instantaneous carrier frequency of the radar signal that is illuminating the scene. In this view of radar imaging, the radar is measuring the frequency response of the scene in a similar manner to how a vector network analyser measures the S_{11} parameter of a device.

In many experimental FMCW radars, the IF signal is real. However, the following signal processing requires the signal to be complex. Additionally, it is often the case that the centre frequency of the oscillator will drift with the environmental parameters. This is true for many SAR systems, but usually the data for the whole aperture is collected in less than a minute, during which time the frequency drift will be negligible. However, in the test bench system, the aperture data may take twenty minutes to collect, during which time the frequency may have wandered by an unacceptable amount. This would degrade the coherence of the synthetic aperture and consequently defocus the SAR image in the cross-range direction.

A computationally light signal processing operation can be used to remove the carrier frequency drift, band-pass filter the IF signal, correct for RVP, and convert it into the complex form. This operation involves Fourier transforming each IF signal, applying a band-pass filter mask of the sort shown in Figure 6.4, and then multiplying the transformed signal by a phase correction term.

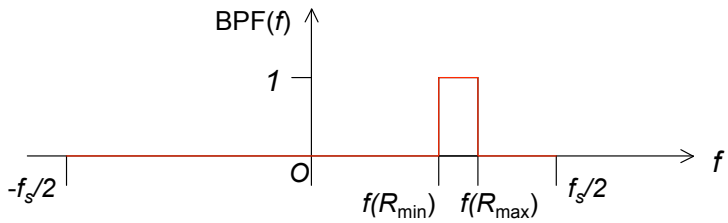

Figure 6.4: The band-pass filter to remove all frequencies of the IF signal other than the positive frequencies corresponding to the scene being imaged. N.B. this diagram is not to scale in the frequency direction.

If the nominal frequency is f_0 and the actual frequency is $f_0 + \delta f$, then the phase error to be removed is $\delta\phi = 4\pi R\delta f/\mathrm{c}$, where R is the range obtained

via (2.4). This operation can be summarized as follows

$$s(t) = \mathrm{FT}^{-1}\left[\mathrm{FT}\big(s_{\mathrm{raw}}(t)\big) \times \mathrm{BPF}(f) \times \exp -i\left(\underbrace{\frac{2\pi T \delta f f}{B}}_{f_0 \text{ drift correction}} + \underbrace{\frac{\pi T f^2}{B}}_{\text{RVP correction}}\right)\right], \tag{6.14}$$

which gives a complex signal that does not vary with drift in the oscillator frequency and has been band-pass filtered, leaving only signals originating in the ranges corresponding to the scene. This filtering step is useful because it removes all parts of the signal spectrum that do not correspond to scatterers from the scene.

This preprocessing correction also (subtractively) removes the Residual Video Phase error.

Another method for removing unwanted deterministic low-frequency signal components is also provided. This method involves coherently averaging the response of the radar to a 'null-scene' measurement (absorber over the receiver) and then numerically subtracting this average 'null-scene' response off the IF signal after sampling. Electronic subtraction prior to sampling might allow a better SNR. As will be discussed in Section 6.8, both corrections are necessary to form good SAR imagery.

Unfortunately, simple homodyne FMCW radar does not produce IF signals that conform to (6.10). Instead this gives signals with $\sigma = 0$.

The required signal phase is of the form

$$\phi_{\mathrm{RMA}} = \big(g + h.(t - \sigma)\big)(\sigma - \tau), \tag{6.15}$$

and the actual form is given by

$$\phi_{\mathrm{FMCW}} = \phi_{\mathrm{RMA}}|_{\sigma=0} = -\big(g + ht\big)\tau, \tag{6.16}$$

where

$$g = \frac{4\pi}{\mathrm{c}}(f_0 - B/2), \tag{6.17}$$

and

$$h = \frac{4\pi B}{\mathrm{c}T}(f_0 - B/2). \tag{6.18}$$

The FMCW signal can be modified to be in the correct form by adding in a correction term as follows,

$$\phi_{\mathrm{RMA}} = \phi_{\mathrm{FMCW}} + \text{correction}, \tag{6.19}$$

which gives

$$\text{correction} = g\sigma + h(t\sigma + \tau\sigma - \sigma^2). \tag{6.20}$$

However, τ is unknown and usually different for every echo. But for the SAR test bench application, τ and σ are similar and quite small, so the FMCW IF signal, $\mathrm{s}_{\mathrm{FMCW}}(t)$, can be corrected using

$$\mathrm{s}_{\mathrm{RMA}}(t) = \mathrm{s}_{\mathrm{FMCW}}(t)e^{i(g+ht)\sigma}, \tag{6.21}$$

making it suitable for processing with the RMA.

Once this correction has been applied, the signal is ready for processing in the RMA. The signal is two dimensional, varying in fast time (or range spatial frequency, k_r, from (6.13)) and varying with along-track position, x. So the signal can be written in the following way,

$$s(x, k_r) = a(x, t(k_r))e^{ik_r(R_\mathrm{r} - R_\mathrm{s}(x_\mathrm{s}, y_\mathrm{s}, x))}, \tag{6.22}$$

where the along-track dependence is introduced by $R_\mathrm{s}(x_\mathrm{s}, y_\mathrm{s}, x)$, the range from the radar to the scatterer. $t(k_r)$ is a rearrangement of (6.13). $(x_\mathrm{s}, y_\mathrm{s})$ is the location of the scatterer in the slant plane (where the ring of constant range that passes through the true location of the scatterer passes through the slant plane – this is illustrated in Figure 6.3). $R_\mathrm{s}(x_\mathrm{s}, y_\mathrm{s}, x)$ is given by

$$R_\mathrm{s}(x_\mathrm{s}, y_\mathrm{s}, x) = \sqrt{(R_0 - y_\mathrm{s})^2 + (x - x_\mathrm{s})^2}. \tag{6.23}$$

$a(x, k_r)$ gives the extent of the signal,

$$a(x, t) = \mathrm{rect}\left(\frac{x - L/2}{L}\right)\mathrm{rect}\left(\frac{t}{T}\right). \tag{6.24}$$

As discussed in the introduction, the aim is to transform the signal into the k_x-k_y domain so that it can be transformed into the image using a two-dimensional FFT. $s(x, k_r)$ can be Fourier transformed into the k_x domain as follows

$$S(k_x, k_r) = \int s(x, k_r)e^{-ik_x x}\mathrm{d}x. \tag{6.25}$$

Substituting (6.22) into (6.25) gives

$$S(k_x, k_r) = \int a(x, t(k_r))e^{i\left[k_r(R_\mathrm{r} - R_\mathrm{s}(x)) - k_x x\right]}\mathrm{d}x. \tag{6.26}$$

To evaluate this Fourier transform, a technique called the Principle Of Stationary Phase is used. This technique allows an approximate estimate of a certain kind of integral, a kind in which the integrand can be separated into two parts: the first part oscillating quickly and symetrically about zero with a slowly changing amplitude; the second part being any function that changes slowly compared with the first part. Where the first part oscillates rapidly about zero, the average integrated area over a few periods of the fast oscillation is approximately zero. However, if the phase of the quickly oscillating part has a stationary point (e.g. at the turning point, if the phase is quadratic), the oscillations will not cancel, and the integrand will contribute to the integral. This means that the integral can be approximated by a scaling factor and the value of the integrand at the turning point of the phase.

The stationary point, x_0, occurs when the slope of the phase is zero, i.e. when

$$\frac{\mathrm{d}}{\mathrm{d}x}\left[k_r\left(R_\mathrm{r} - R_\mathrm{s}(x)\right) - k_x x\right]\Big|_{x=x_0} = 0, \tag{6.27}$$

so using (6.23) gives

$$x_0 = x_\mathrm{s} - \frac{k_x(R_0 - y_\mathrm{s})}{\sqrt{k_r^2 - k_x^2}}, \tag{6.28}$$

where the negative root is chosen to associate higher along-track spatial frequency with scatterers at higher along-track positions.

The along-track Fourier transform of the signal is simply the product of a constant scaling and the value of the integrand at the stationary point:

$$S(k_x, k_r) = \Gamma a(x_0(x_\mathrm{s}), t(k_r))e^{i\left[k_r(R_\mathrm{r} - R_\mathrm{s}(x_0)) - k_x x_0\right]}, \tag{6.29}$$

where Γ is a scaling that is not important for this calculation.

Substituting for $R_\mathrm{s}(x_0)$ using (6.23) in the phase of $S(k_x, k_r)$ gives

$$S(k_x, k_r) = \Gamma a(x_0(x_\mathrm{s}), t(k_r))e^{i\left[k_r R_\mathrm{r} - k_x x_\mathrm{s} - \sqrt{k_r^2 - k_x^2}(R_0 - y_\mathrm{s})\right]}. \tag{6.30}$$

The next step is to remove any phase variations that are not due to the location of the scatterer in the scene. This means removing all of the signal phase other than the part that is of the form $(k_x x_\mathrm{s} + k_y y_\mathrm{s})$. Since $k_y = \sqrt{k_r^2 - k_x^2}$, the part to remove, i.e. the phase of the matched filter, is

$$\phi_\mathrm{MF} = k_r R_\mathrm{r} - k_x x_\mathrm{s} - \underbrace{\sqrt{k_r^2 - k_x^2}}_{\equiv k_y}(R_0 - y_\mathrm{s}) + (k_x x_\mathrm{s} + k_y y_\mathrm{s}), \tag{6.31}$$

which gives

$$\phi_{\mathrm{MF}}(k_r, k_{\mathrm{x}}) = k_r R_{\mathrm{r}} - \underbrace{\sqrt{k_r^2 - k_x^2}}_{\equiv k_y} R_0, \tag{6.32}$$

which is not specific to scatterer location and is removed from the phase of all the signal components as follows

$$S_{\mathrm{filtered}}(k_{\mathrm{x}}, k_r) = S(k_{\mathrm{x}}, k_r) e^{-i\phi_{\mathrm{MF}}(k_r, k_{\mathrm{x}})}, \tag{6.33}$$

which is equivalent to the dechirping operation in FMCW radar. This is the matched filtering step.

The filtered signal for the example scatterer is, then,

$$S_{\mathrm{filtered}}(k_{\mathrm{x}}, k_r) = \Gamma a\left(x_0(x_{\mathrm{s}}), k_r\right) e^{-i(k_x x_{\mathrm{s}} + \sqrt{k_r^2 - k_{\mathrm{x}}^2}\, y_{\mathrm{s}})}. \tag{6.34}$$

This signal has the right phase dependence (i.e. $\phi = k_x x + k_y y$, which is the phase of a signal displaced by x, y from the scene centre) but is in the wrong coordinate system. It is still represented in k_x-k_r space. To transform the signal into the Fourier conjugate of the image, the data is mapped using the relationship

$$k_y = \sqrt{k_r^2 - k_x^2}, \tag{6.35}$$

which is based on the assumption that the signal phase does not depend on the choice of coordinate system.

The mapping is done as a one-dimensional interpolative warping called the Stolt transform.

The signal is then window weighted and two-dimensional FFTd into the image, concluding the RMA.

It might also be desirable to remove the beam shape weighting and the $1/R^4$ weighting at this stage if required.

As can be seen from Figure 6.3, the slant plane, in which the RMA forms its image, is not the same as the ground plane (unless the radar path is at ground level). In some cases, it is desirable to map from (x, y) to (x', y'), which can be done by finding where the ring that passes through (x, y) passes through the ground, a surface that is neither necessary flat nor level.

In summary, the RMA and associated signal processing for the FMCW SAR test bench operate as follows:

1. Correct the raw signal to make FMCW radar data suitable for the RMA;

2. Apodize the signal (this is explained in Section 6.3.3);

3. Fourier transform the signal in the along-track direction;
4. Apply a matched filter;
5. Warp the data into the k_x-k_y domain;
6. Fourier transform the signal into the image domain;
7. Map the image into the ground plane.

Following this, the image can be presented to the user, including appropriate calibration, mapping, and feature extraction.

6.3.3 Signal extent and sampling rates

It is necessary to calculate the appropriate sampling rates and signal extent to give the required image specification. This calculation is useful in the design of radars, in the planning of imaging tasks, in the simulation of data, and in the processing of data into imagery.

In the case of the SAR test bench, the normal data collection geometry, in which sufficient along-track data is collected so that every point in the scene can be imaged with a synthetic aperture subtending the same absolute range of angles, is not appropriate. This is because the resulting collection interval would be much greater than the travel of the available translation stage. In this section, the general specification of the SAR data collection will be given and then modified to suit the purposes of the test bench, i.e. providing minimal data collection interval extents.

The starting point is the signal phase of a scatterer,

$$\phi(x_s, y_s, x) = k_r R(x_s, y_s, x), \tag{6.36}$$

where $R(x_s, y_s, x)$ is given by

$$R(x_s, y_s, x) = \sqrt{(R - y_s)^2 + (x - x_s)^2}. \tag{6.37}$$

The x and y wavenumbers are given by

$$k_x = \frac{\mathrm{d}\phi(x_s, y_s, x)}{\mathrm{d}x}, \tag{6.38}$$

and

$$k_y = \frac{\mathrm{d}\phi(x_s, y_s, x)}{\mathrm{d}y}, \tag{6.39}$$

which give

$$k_x = k_r \sin(\theta), \tag{6.40}$$

and

$$k_y = k_r \cos(\theta), \tag{6.41}$$

where x, y, x_s, y_s and θ are illustrated in Figure 6.5.

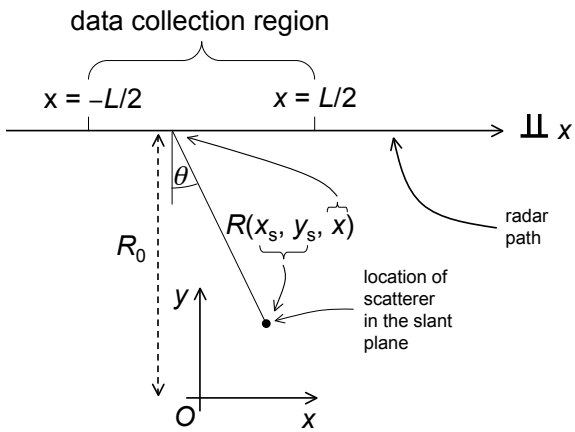

Figure 6.5: SAR data collection geometry.

As the radar moves along its path finding the radial frequency response of the scene from the range of spatial positions, the wavevector of the signal reflected back from the sample scatterer is swept out through a corresponding range of subtended angles. This is illustrated in Figure 6.6, in which k_r has been assumed to be positive. In the analysis above, k_r is negative, but this will not make any important difference to the analysis that follows.

It is usual in stripmap SAR processing to decide on the region of k_x-k_y to process and then to collect sufficient data that the signal extents of all of the scatterers in the required scene occupy at least this region. This results in map-like imagery with a sliding perspective, so all parts of the scene are viewed from the same angle. This is unlike the single-point, angular perspective view (e.g. how cameras see the world), in which the angle at which an object is viewed depends on its location relative to the viewer. For instance, railway tracks appear to converge in single perspective vision; in the usual SAR view of the world, the tracks remain parallel. In this mode of operation, sufficient along-track data is collected so that an image can be generated of the scene using the same absolute region of wavevector space. This means that there is a unique synthetic aperture for every point in the resulting image. However,

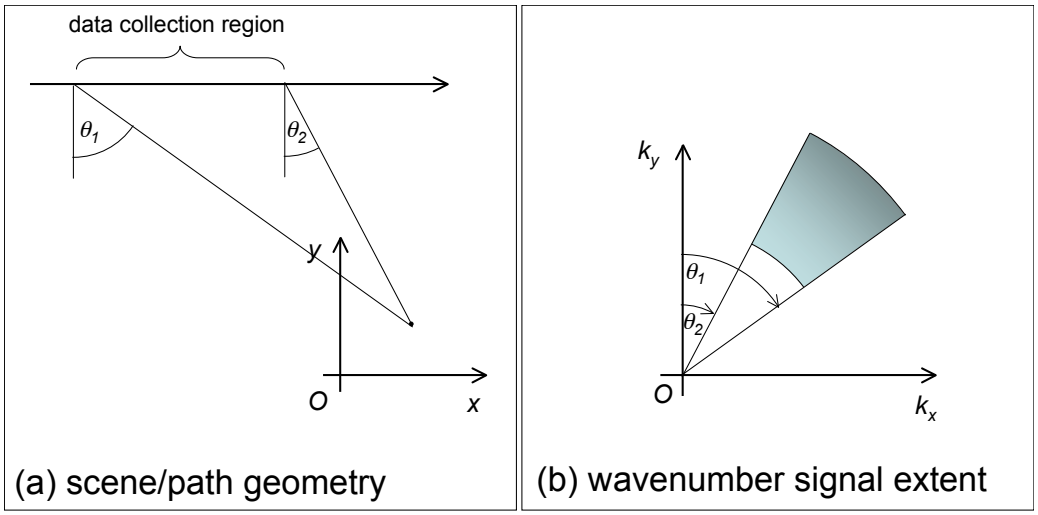

Figure 6.6: (a) The along-track signal extent and scatterer geometry, and (b) the corresponding wavenumber-domain signal extent. In this example, the data collected is 'squinted' because the mean value of θ is not zero.

this increases the amount of along-track data required to form the image: the data collection region length is the length of the synthetic aperture required to resolve the scatterers plus the along-track extent of the scene. This is the usual method of collecting and processing SAR data with the RMA and is called 'inscribed mode'. It is illustrated and explained in Figure 6.7.

For the purposes of the SAR test bench, this is unacceptable. Whilst radars carried on aeroplanes can be translated through very long distances with ease, the test bench radar will be translated on a screw-driven linear translation stage. In practice these are limited to about 1 m of travel, so for the implementation of the RMA for the test bench radar, a less usual mode of data collection will be used.

For the test bench radar, the same along-track data collection interval will provide the synthetic aperture for all points in the scene. This means that the position and extent of the wavevector signal will vary throughout the scene to give spatially variant resolution, viewing angle, and sensitivity. This is effectively a synthetic phased array antenna with transmit and receive at each node. In this case, the synthetic beam is rotated rather than slid to form the image. This method of data collection and processing, which is called 'exscribed mode', is illustrated and explained in Figure 6.8. The mode of data collection used in the SAR test bench is strip-map because the physical beam

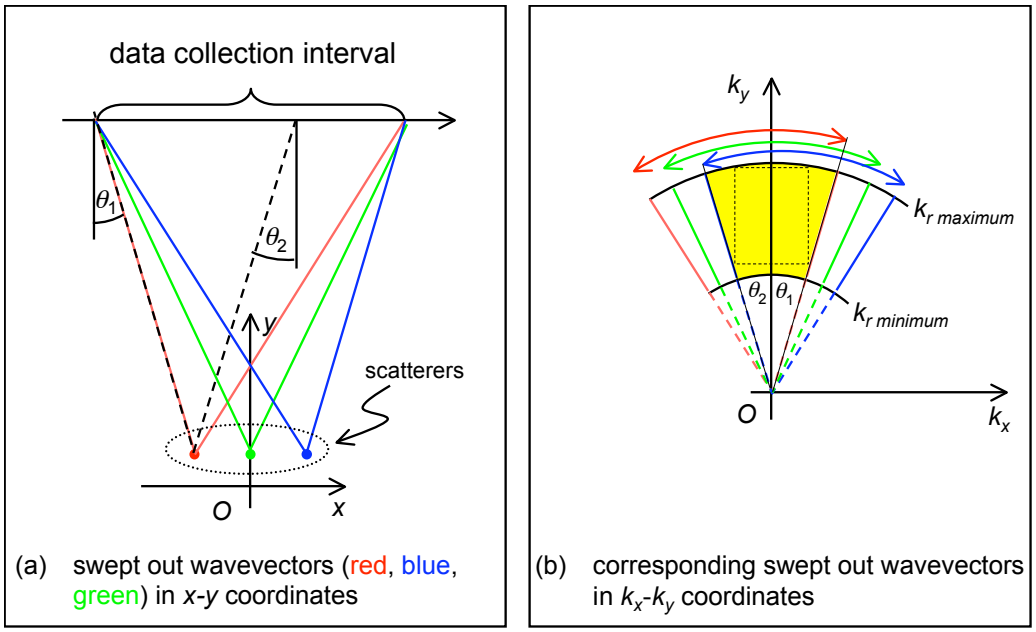

Figure 6.7: The usual (inscribed) data collection mode for SAR. (a) The radar illuminates and profiles all scatterers from at least the same range of angles, labelled θ_1 to $-\theta_2$. (b) The result is a range of wavevector signal extents which overlap in the required region. The yellow region is the intersection of the individual signals, and the dashed rectangle, which must inscribe the signal intersection, is a potential FFT region to generate a map-like SAR image of the three scatterers. Any (usually rectangular) region within the yellow overlapping extent region can be used, including ones rotated relative to the example shown.

is translated sideways along track without steering. However, since the radar is translated through a much smaller distance than the beam extent, the same patch of ground is assumed to be illuminated at all points in the along-track signal extent.

To find the length of synthetic aperture that should be used in the exscribed mode, the worst resolution required in the scene (it will vary from its best value at $(0, \Delta y/2)$ to its worst at one of $(\Delta x/2, \pm\Delta y/2)$) is related to the size of the synthetic aperture.

The relationship between FWHM resolution and signal extent in wavevector space is given by

$$\rho = \frac{2\pi\kappa}{\Delta k}, \tag{6.42}$$

where ρ is FWHM resolution and κ is a factor associated with the window function. This expression is equivalent to (2.12).

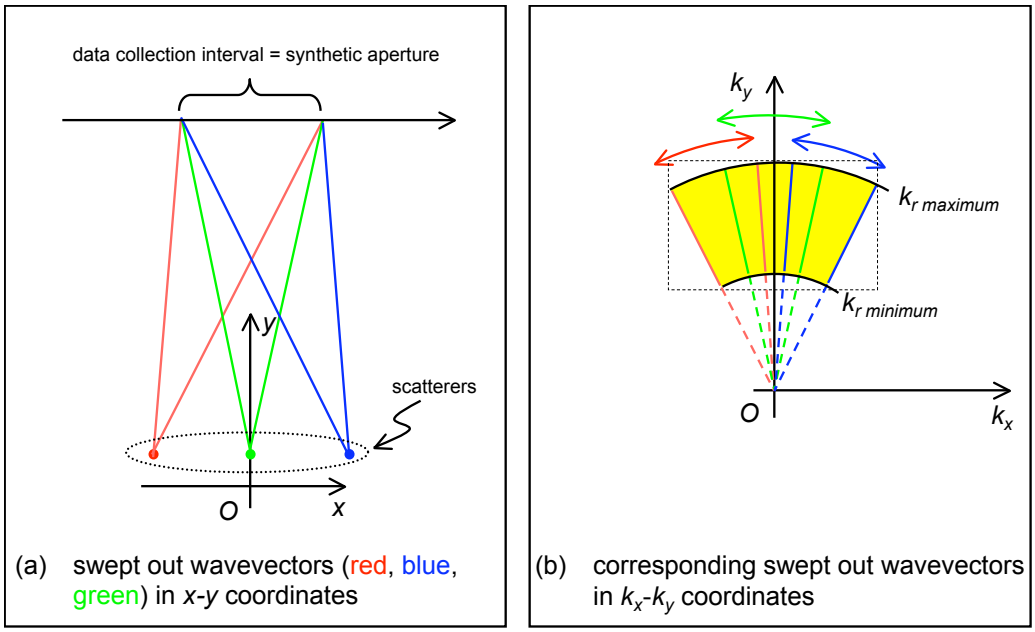

Figure 6.8: The minimal data (exscribed mode) collection mode for SAR. (a) The radar illuminates and profiles all scatterers from sufficiently closely spaced points in the synthetic aperture. (b) The result is a range of wavevector signal extents that do not necessarily overlap. The yellow region indicates the union of signals, all of which must be processed to yield the required resolution. The dashed rectangle, which must exscribe the union of the signals, is a potential FFT region to generate a single-point perspective, spatially-varying resolution SAR image of the three scatterers.

In the inscribed mode, x and y (or rotated combinations of x and y) resolutions can be specified for the whole scene. However, in the exscribed mode, these resolutions vary with location in the slant plane. Here it makes more sense to specify (and measure) radial and cross-radial resolution, as with PPI radars. In this case, though, the apparent aperture width reduces away from the zero azimuth angle, as with electronically scanned antennas, so the resolution degrades with increasing azimuth angle.

Because the resolution is spatially varying, it is usual to specify the worst acceptable resolution. This resolution can then be used to derive the synthetic aperture length and chirped bandwidth to use.

Using (6.42), the minimum radial resolution, ρ_{r}, and the minimum cross-radial resolution, ρ_{xr}, as illustrated in Figure 6.9, give the required wavenumber domain signal extents,

$$\Delta k_{\mathrm{r}} = \frac{2\pi\kappa}{\rho_{\mathrm{r}}}, \tag{6.43}$$

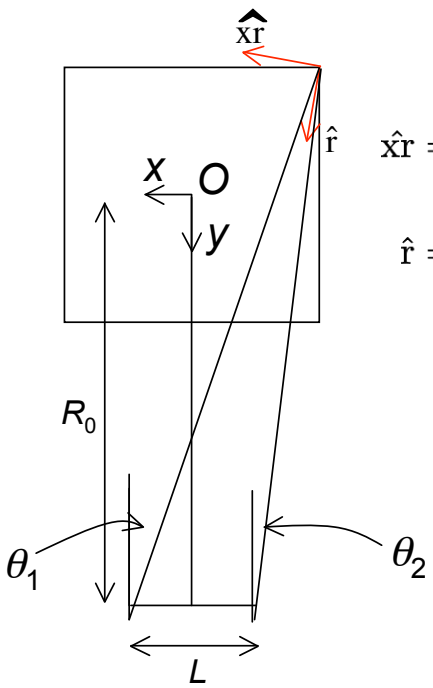

$$\hat{\mathrm{xr}} = \hat{x}\cos\left(\frac{\theta_1+\theta_2}{2}\right) - \hat{y}\sin\left(\frac{\theta_1+\theta_2}{2}\right)$$

$$\hat{\mathrm{r}} = \hat{x}\sin\left(\frac{\theta_1+\theta_2}{2}\right) + \hat{y}\cos\left(\frac{\theta_1+\theta_2}{2}\right)$$

Figure 6.9: The resolution direction as a function of position in the scene. The range and cross-range resolution are determined by the mean angle subtended by the synthetic aperture. This mean angle is not necessarily the angle from the middle of the aperture to the scatterer. However, in most applications, that would be a good approximation.

and

$$\Delta k_{\mathrm{xr}} = \frac{2\pi\kappa}{\rho_{\mathrm{xr}}}, \tag{6.44}$$

which are illustrated in Figure 6.10.

For the mm-wave systems that are to be tested using the SAR test bench, the relative bandwidth is mostly small, typically 1% to 5%. Since the range resolution and cross-range resolution are usually chosen to be the same or very similar, $\Delta\theta$ is limited to being of the order of a few degrees. In this case, approximate calculations of the required chirped bandwidth and the range of angles subtended by the synthetic aperture hold very well. If wider relative bandwidths or larger values of $\Delta\theta$ are required, more precise calculations can be done. The exact nature of those calculations will depend on the requirements of the particular task because there is not a unique way of specifying the resolution in the exscribed data collection mode.

Referring to Figure 6.10 and (6.43), the required chirped bandwidth can

be seen to be given to a very good approximation by

$$B = \frac{\kappa c}{2\rho_{\mathrm{r}}}. \tag{6.45}$$

Also, referring to Figure 6.10 and (6.44), it can be seen that the range of angles that must be subtended by the least well resolved scatterer (one at either a front or rear corner) is given to a very good approximation by

$$\Delta\theta = 2\tan^{-1}\left(\frac{c\kappa}{4f_0\rho_{\mathrm{xr}}}\right). \tag{6.46}$$

It should also be noted that, in the exscribed mode of signal processing, the range and along-track window functions must be applied in the fast- and slow-time domains. This is different to the usual RMA procedure, in which the window function is applied immediately before the two-dimensional Fourier transform into the image domain. Applying the window function in the time domain will result in slight distortion of the window functions but will apply the window function individually to the signal of each scatterer. When each signal fans out in the k_x-k_y domain, it effectively takes its window function with it. In exscribed mode, the shape and extent of the wavenumber domain signal will vary depending on the position of the scatterer in the scene. This results in spatially varying resolution and PSF shape. However, as will be demonstrated in Section 6.4.1, the effects of these variations are not usually too detrimental to the resulting image quality.

In the SAR test bench, wide radar beams with large scenes close to the radar are likely to be used. This means that an exact calculation of the required aperture length is desirable. Equation (6.47) provides an exact calculation of the minimum aperture length that will guarantee the specified range of angles subtended by the synthetic aperture to all scatterers in the scene.

$$L_{\pm} = 2\frac{R_0 \pm \Delta y/2}{\tan\Delta\theta}\left(-1 + \sqrt{1 + \tan^2\Delta\theta\left[1 + \left(\frac{\Delta x}{2(R_0 \pm \Delta y/2)}\right)^2\right]}\right). \tag{6.47}$$

To find this minimum aperture length, (6.47) is used twice with $\pm\Delta y/2$ as the y-coordinate of the test scatterer to give two values of L, the larger of which is taken as the correct value. This concludes the signal extent calculation.

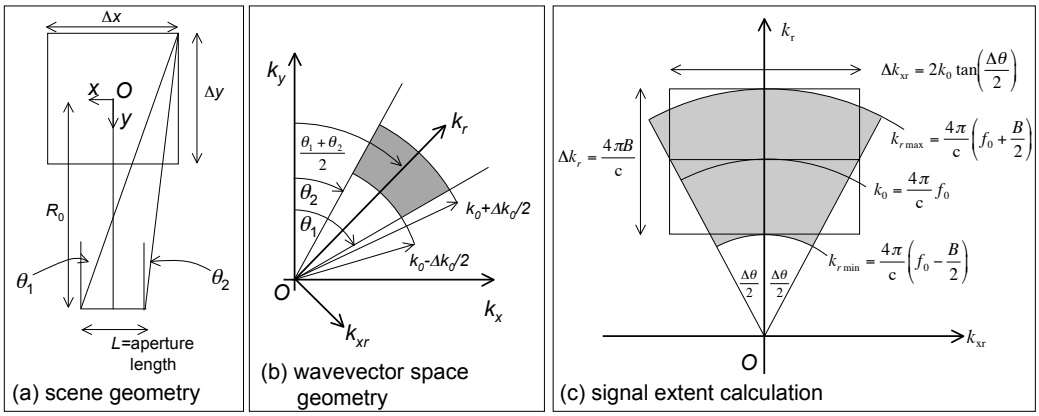

Figure 6.10: (a) The geometry of the aperture and the scatterer. (b) The wavenumber signal extent. (c) The wavenumber signal extent in the rotated coordinates system. Note that the rectangle specifying the wavenumber signal extent (shaded) is a very good approximation for realistic relative bandwidths, typically 1-5 % in mm-wave systems.

Note that, for small values of $\Delta\theta$, Δx, and Δy and for large values of R_0, i.e. the usual case for typical SAR imaging, (6.47) can be approximated by the more usual $L \approx R_0 \Delta\theta$.

In the range direction, the usual expression, (2.4), is used along with the maximum range present in the scene from any part of the synthetic aperture. So, the minimum sampling rate is given by

$$f_\mathrm{s} = \frac{4B}{\mathrm{c}T} R \left(-\frac{L}{2}, \frac{\Delta x}{2}, \frac{-\Delta y}{2} \right). \tag{6.48}$$

However, sampling at this rate should be accompanied by a physical low-pass filter to remove higher frequencies that would otherwise alias into the digitized signal. Ideally, a band-pass filter can be used to remove all signal energy not originating from the scene to be imaged, at either lower or higher frequencies.

The along-track frequency response is determined by the shape of the radar beam. It is necessary to decide the width of the beam beyond which the sensitivity is small enough that any signals aliasing into the image will be negligible. This width is called the unambiguous beam width, θ_u.

The unambiguous beam width must be chosen on a case-by-case basis. It is the width of the beam at which aliased signal energy will not degrade the image too severely for the purposes of the particular application. Clearly, this will depend on the shape of the beam, the nature of the scene, and the purpose of the imagery.

In the case of the SAR test bench, the beam is always broadside, so the range of spatial frequencies that can enter the measurement is the difference between the wavenumber of objects at the front of the beam and that of objects at the back of the beam. (6.40) gives the span as

$$\Delta k_{\mathrm{x}} = 2\max(k_{\mathrm{r}})\sin\left(\frac{\theta_{\mathrm{u}}}{2}\right). \tag{6.49}$$

The along-track spacing, δx, must unambiguously sample this, so

$$\delta x = \frac{2\pi}{\Delta k_{\mathrm{x}}}. \tag{6.50}$$

So, the along-track sample interval is given by

$$\delta x = \frac{\mathrm{c}}{4(f_0 + B/2)\sin(\theta_{\mathrm{u}}/2)}. \tag{6.51}$$

Whilst the along-track extent of the data collection is given by L, the along-track extent of the signal that must be processed (starting with the along-track Fourier transform prior to the matched filtering stage) must be large enough for the k-space sampling to be close enough to unambigously sample the k_x extent. Consequently, the along-track signal must be zero-padded out to the along-track length of the image to be processed. This is achieved by default in the normal SAR processing case, where inscribed data collection requires an along-track signal extent that is greater than the processed image. In the implementation for the test bench radar, all of the collected wavevector signal extent is processed to give an image of the full (unambiguous) beam contents. If required, only the parts of wavevector space corresponding to the image need be used, effectively low-pass filtering the beam and reducing its size. This can be done in the image domain, too.

Filtering is possible in either domain because the range of angles in wavevector space due to aperture extent is relatively small compared to the offset angle due to along-track position. But for simplicity, the whole data set is processed into the image domain, where the image can be cropped to give the required region. To avoid along-track aliasing, the along-track sampling rate is calculated using the unambiguous beam width, and the processed image extent is chosen to be the width of the unambiguous beam at the range of the scene.

6.4 Data simulator

It is very useful to be able to generate synthetic data when testing software, both to validate the software and also to investigate the results of particular specifications and the effects of test signal errors.

A simple program was written to generate realistic radar data that closely emulate the data expected from the FMCW radar, including radar position error and carrier frequency drift.

The data simulator is supplied with the required performance specification (scene size, beam width, resolution etc.), and the calculations described above are used to find the necessary parameter values. In this sense, the data simulator is also useful as a task planner, allowing the user to specify easily understood quantities like resolution and beam width and have the program find the required along-track sampling interval and aperture extent.

To generate the synthetic data, the following signal model is evaluated at each point in the two-dimensional signal for every scatterer simulated,

$$s_i(x,t) = A_i \cos\left(\underbrace{\frac{4\pi}{\mathrm{c}}\big(f_0 + \delta f(x)\big)R(x_\mathrm{s}, y_\mathrm{s}, x)}_{\text{slow-time phase}\to\rho_x} + \underbrace{\frac{4\pi B}{\mathrm{c}T}R(x_\mathrm{s}, y_\mathrm{s}, x)t}_{\text{fast-time phase}\to\rho_\mathrm{r}}\right), \quad (6.52)$$

where x is the along-track radar position, (x_i, y_i) are the coordinates of the scatterer for which data is being simulated, and $\delta f(x)$ is the error in the carrier frequency at each along-track position. A_i is the constant amplitude of the signal due to the ith scatterer. The range of the scatterer from the radar, $R(x_i, y_i, x)$ is given by

$$R(x_\mathrm{s}, y_\mathrm{s}, x) = \sqrt{\begin{array}{l}(R_0 + \delta y(x) - y_i)^2 + \\ (x + \delta x(x) - x_i)^2 + \\ (z + \delta z(x) - z_i)^2\end{array}} \quad (6.53)$$

where (x, R_0, z) is the nominal location of the radar and x parameterizes the nominal along-track position of the radar. $\big(\delta x(x), \delta y(x), \delta z(x)\big)$ is the error in the radar's position, expressed as a function of nominal along-track radar position.

The total simulated compound signal is given by

$$s(x,t) = \sum_i s_i(x,t). \quad (6.54)$$

Parameter	Value
R_0	30 m
Δx	10 m
Δy	10 m
f_0	94 GHz
B	1.2 GHz
T	1 ms
L	0.52 m
ρ_x	< 0.18 m
ρ_y	< 0.18 m

Table 6.1: Typical SAR test bench specification.

6.4.1 Ideal test case

To check that the SAR processor is operating correctly, a simple ideal data set was simulated and processed. A specification, given in Table 6.1, which is a typical test bench case, was used.

Radar data for five scatterers located at (0 m, 0 m) and ($\pm$4 m, $\pm$4 m) was simulated to give 0.18 m FWHM resolution in both the range and cross-range directions. It was then processed using the SAR processor described in Section 6.3. The result is shown in Figure 6.11.

In the x and y sections, shown in Figures 6.12 and 6.13, the ideal Hamming-weighted PSF shape is fitted to the observed point scatterer image located at $(0, 0)$. It can be seen that there is good agreement. The achieved resolution is 0.15 m in cross-range at the centre of the image and 0.18 m in range. The nominal resolution to achieve, given 1.2 GHz bandwidth, Hamming weighting ($\kappa = 1.43$), and square resolution, is < 0.18 m, which gives $\rho_x = 0.15$ m at the centre of the image.

There will be subtle differences between the actual and the model PSFs because the signal extent in the exscribed processing mode is not rectangular in the wavenumber domain and because the window function is not exactly applied but slightly distorted, as discussed in Section 6.3.3. However, it can be seen that the performance will be acceptable for realistic applications.

Note that the sampling rate is much higher in the x direction than in the y direction and is much smaller than the resolution. This is because the sampling must be unambiguous for the union of the k_x signal extents for all points in the scene, not just the k_x signal extent for any individual scatterer. If no further

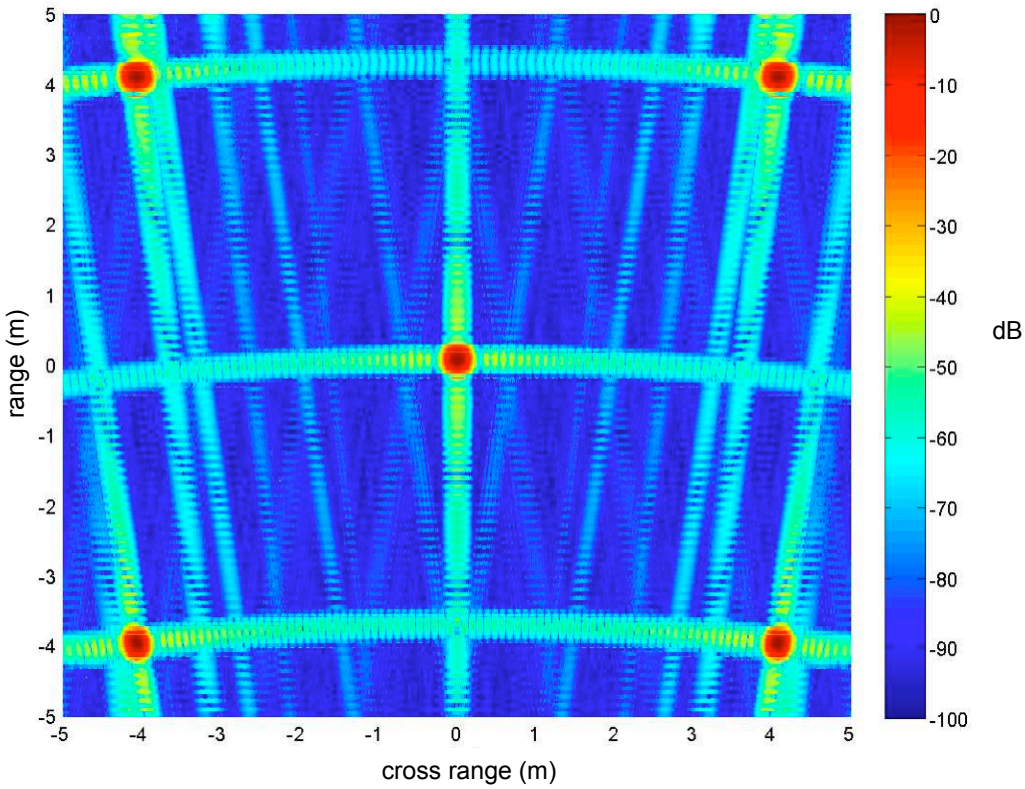

Figure 6.11: SAR image produced by the RMA implementation operating in exscribed data mode. There are five scatterers, at (0 m, 0 m) and at (±4 m, ±4 m). The data collection parameters are specified in Table 6.1.

coherent processing is required, the image can be down-sampled in the along-track direction.

Owing to the variation in the extent and orientation of the wavevector-domain signal as a function of scatterer location, the resolution, look angle, and sensitivity all vary throughout the image. The variation in resolution and look angle can be seen as the circumferential sidelobes and broadening response widths (in cross range) which are visible in Figure 6.11. The variation in sensitivity, although present, is too slight to see. The nominal performance specification is met.

It can be seen that the two-dimensional response to each scatterer resembles a cross. This is because the range window function applies in range and the cross-range window function applies in cross range. Both apply at angles in between, effectively giving double sidelobe suppression in directions other than the purely range or cross range ones.

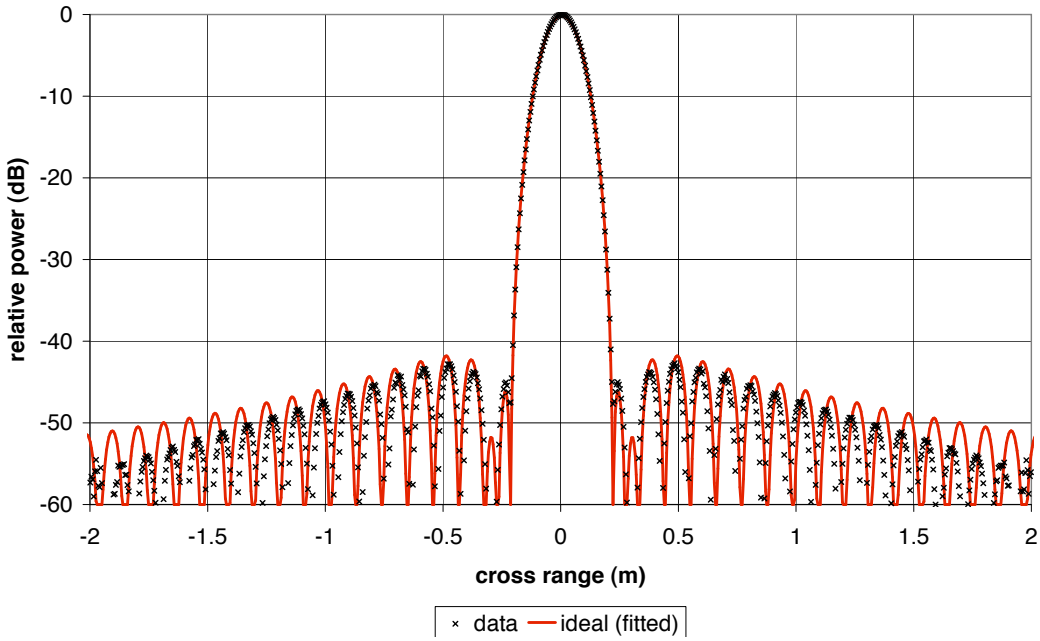

Figure 6.12: Synthetic SAR image and ideal Hamming weighted response in the x direction.

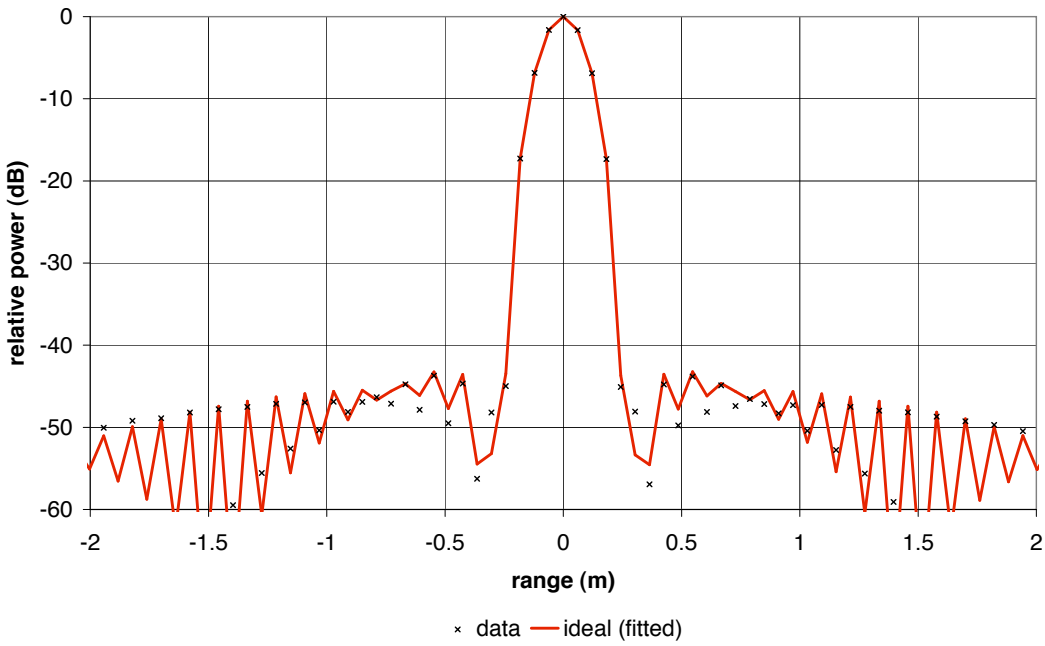

Figure 6.13: Synthetic SAR image and ideal Hamming weighted response in the y direction.

6.4.2 Frequency drift

To investigate the effect of frequency drift on the image quality and to validate the ability of the frequency correction method, data was simulated with a slowly-quadratically drifting carrier frequency and again with jittered carrier frequency. The ideal, unperturbed data for a scatterer at (0,0) simulated with the specification given in Table 6.1 was processed to give the SAR image shown in Figure 6.14.

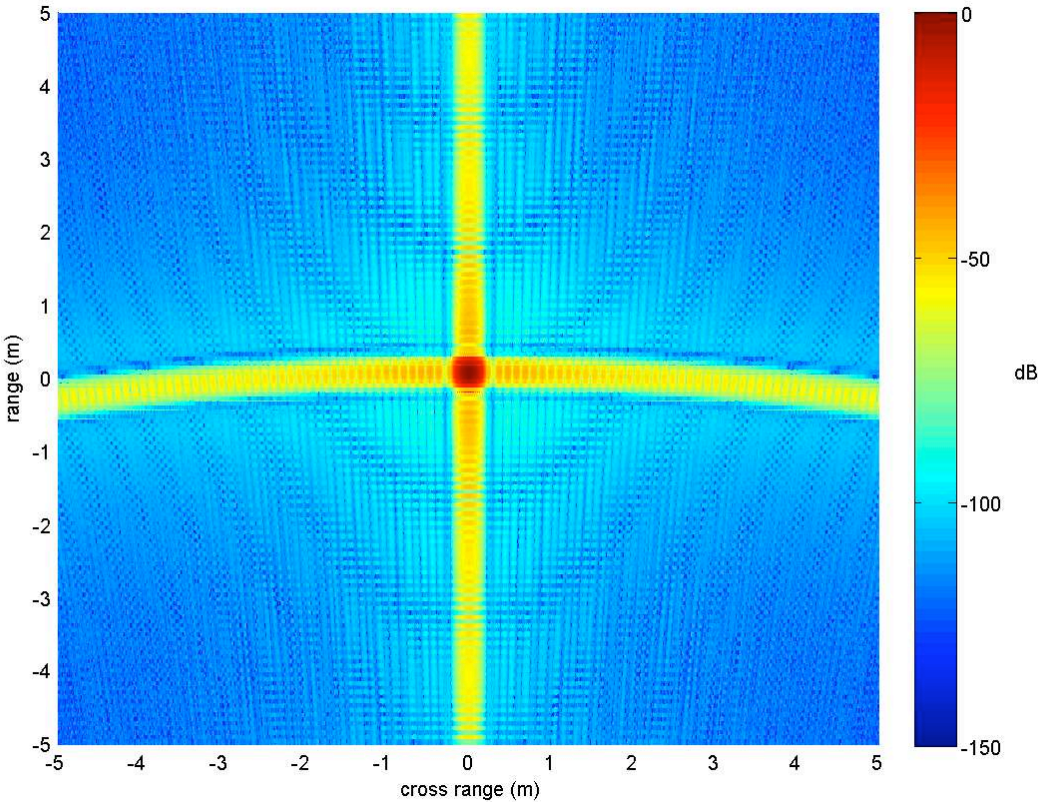

Figure 6.14: The ideal image processed from ideal data.

First, the carrier frequency was perturbed with a quadratic error, shown in Figure 6.15, that results in a $3\pi/2$ quadratic phase error in the along-track direction. The data was processed with the frequency correction, which is described by (6.14), disabled, giving the SAR image shown in Figure 6.16. The resulting SAR image can be seen to be badly defocussed in the cross-range direction. Notice that it is a circumferential defocus. The data was then processed again but with the frequency compensation enabled, giving the SAR

image shown in Figure 6.17, from which it can be seen that the image quality has been restored.

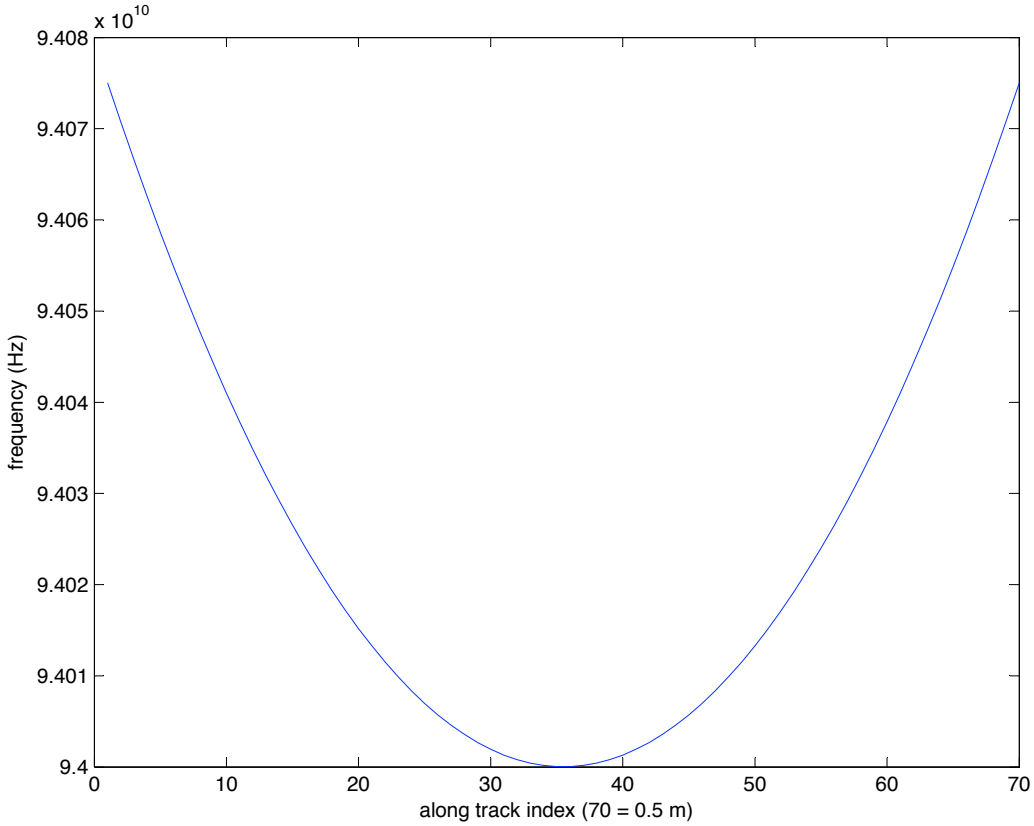

Figure 6.15: Slowly quadratically drifting carrier frequency.

Next, the effect of random carrier frequency discrepancies on the image is demonstrated. The carrier frequency was jittered, as shown in Figure 6.18, and the data processed without compensation, giving the SAR image shown in Figure 6.19. It can be seen that the random frequency jitter translates into a random phase noise giving raised sidebands. These sidebands predominantly affect the cross-range direction but have some effect in the range direction, too. The data was reprocessed with the compensation enabled, and the resulting image is shown in Figure 6.20, from which it can be seen that the image quality is restored.

These demonstrations show that, for extreme deterministic and random carrier frequency deviations, the built-in frequency compensation described by (6.14) satisfactorily corrects the data. This correction applies to all positions

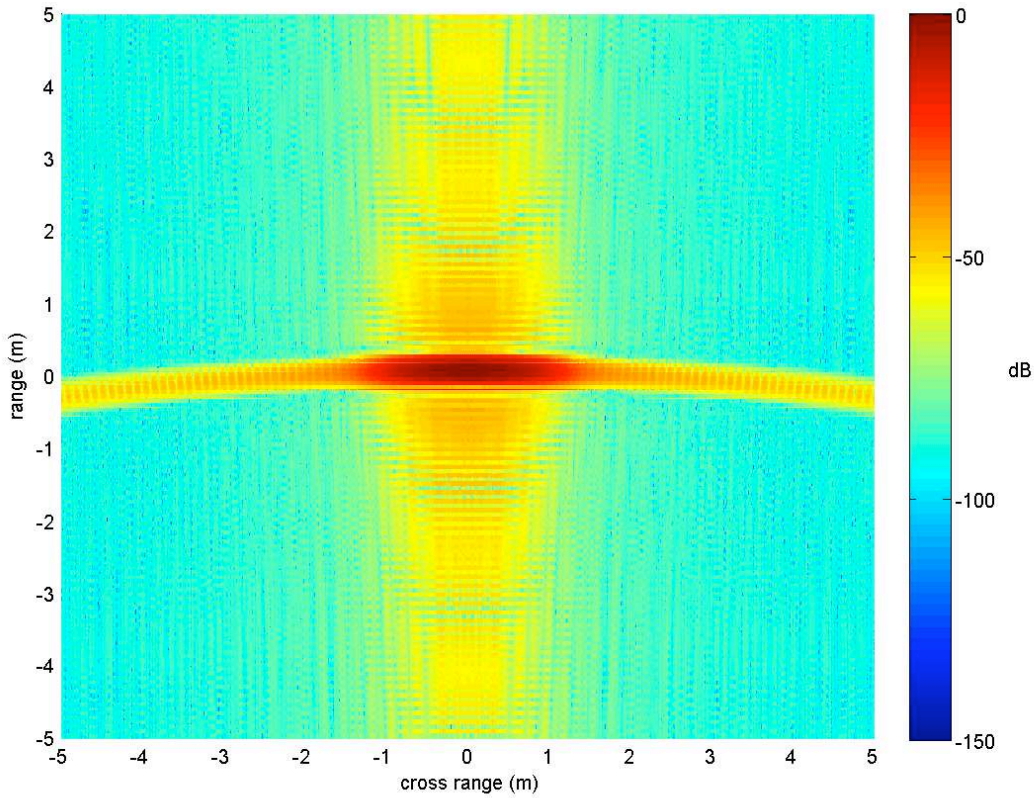

Figure 6.16: Result of processing SAR data with a slowly quadratically drifting carrier frequency. No correction was applied.

in the scene.

However, this technique does require that the centre frequency of the oscillator be measured, and this is not always convenient or possible. In such circumstances, modified autofocus techniques might be more suitable.

6.4.3 Platform position error

Another source of signal error is radar location error, which changes the range to each scatterer. To a good approximation, the resulting phase error affecting the radar signal is given by the phase due to the component of the radar position error in the direction of the scatterer from the nominal position of the

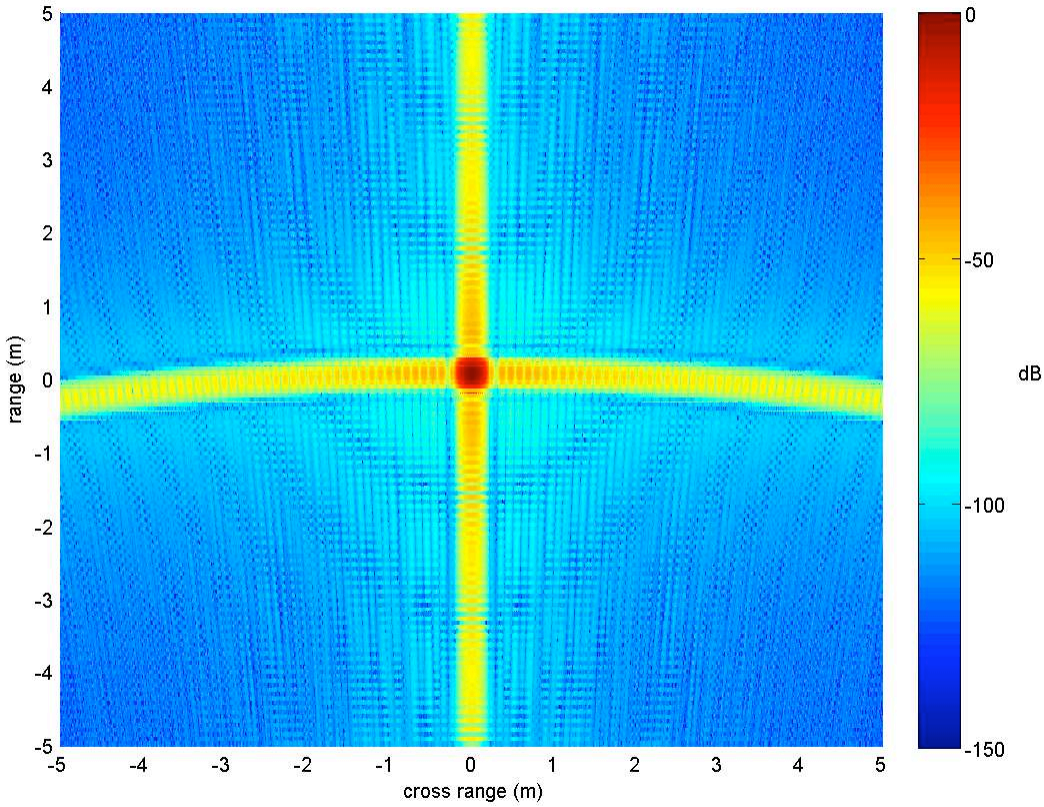

Figure 6.17: Result of processing SAR data with a slowly quadratically drifting carrier frequency with frequency correction enabled.

radar:

$$\delta\phi = \frac{4\pi f_0}{c} \begin{pmatrix} \delta x \\ \delta y \\ \delta z \end{pmatrix} \cdot \begin{pmatrix} x - x_s \\ y - y_s \\ z - z_s \end{pmatrix} \frac{1}{\sqrt{(x - x_s)^2 + (y - y_s)^2 + (z - z_s)^2}}. \tag{6.55}$$

In the case of the SAR test bench, radar position error is limited to small perturbations about the nominally linear track, owing to the construction using a linear translation stage.

In the typical arrangement for the test bench radar, indicated by the parameters shown in Table 6.1, only the y component is relevant. In fact, as shown by (6.55), as the geometry changes, the phase error picked up by echoes contains projections of the platform position error scaled into phase. So, for the purposes of this demonstration, I shall limit the presented results to the y-direction. Simulations were carried out for the x (cross range) and z (height)

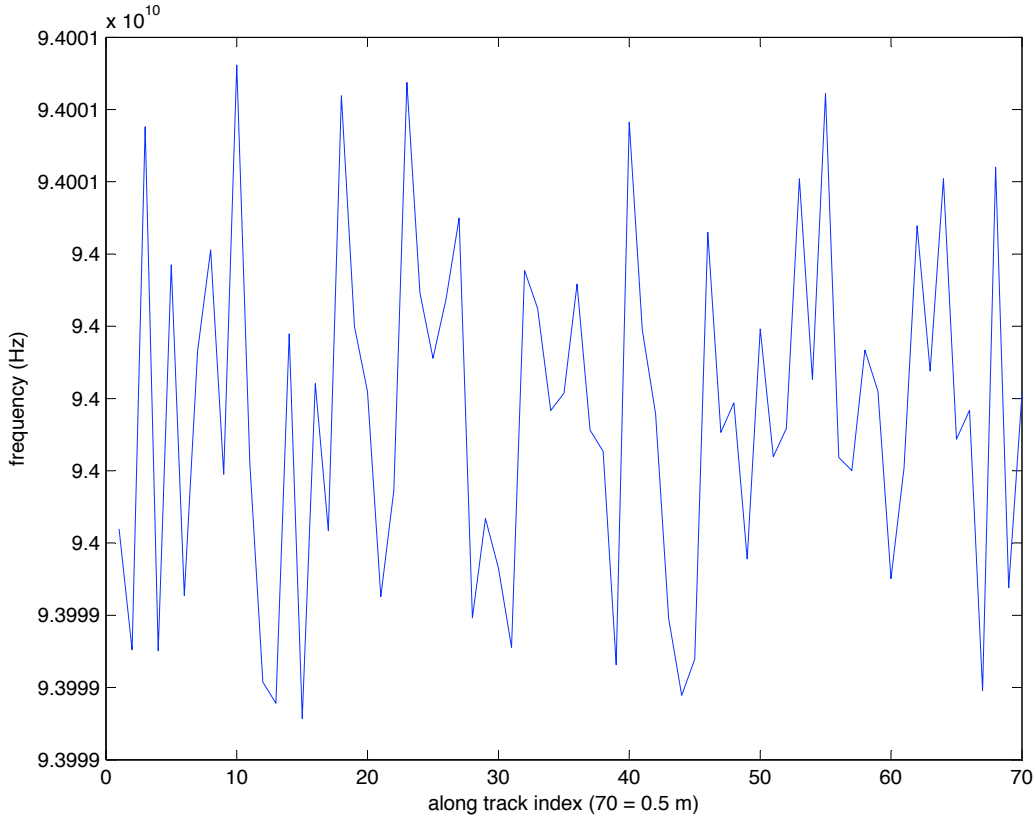

Figure 6.18: Rapidly jittering carrier frequency (±10 ppm peak-to-peak variation).

components, but as indicated by (6.55), for a large value of R_s compared to the scene size and the aperture size, typical errors in these directions have a much smaller effect on the PSF than comparable errors in the y direction.

Data sets were simulated with uniformly distributed radar position error (in the y-direction) for a range of amplitudes, and then the scene centre scatterer was profiled in the range and cross-range directions. The results are shown in Figures 6.21 and 6.22, from which it can be seen that the increasing position error increases the noise in the image (via phase noise sidebands). For the current scene-platform geometry, small random position errors in the x and z directions would have the same effect as those in the y direction, except that the resultant sidebands would be lower.

The data simulator could be used with different distributions and amplitudes of radar position error to investigate the effects on the resultant image quality. This is a useful facility: for a given imaging specification, the required position accuracy can be found.

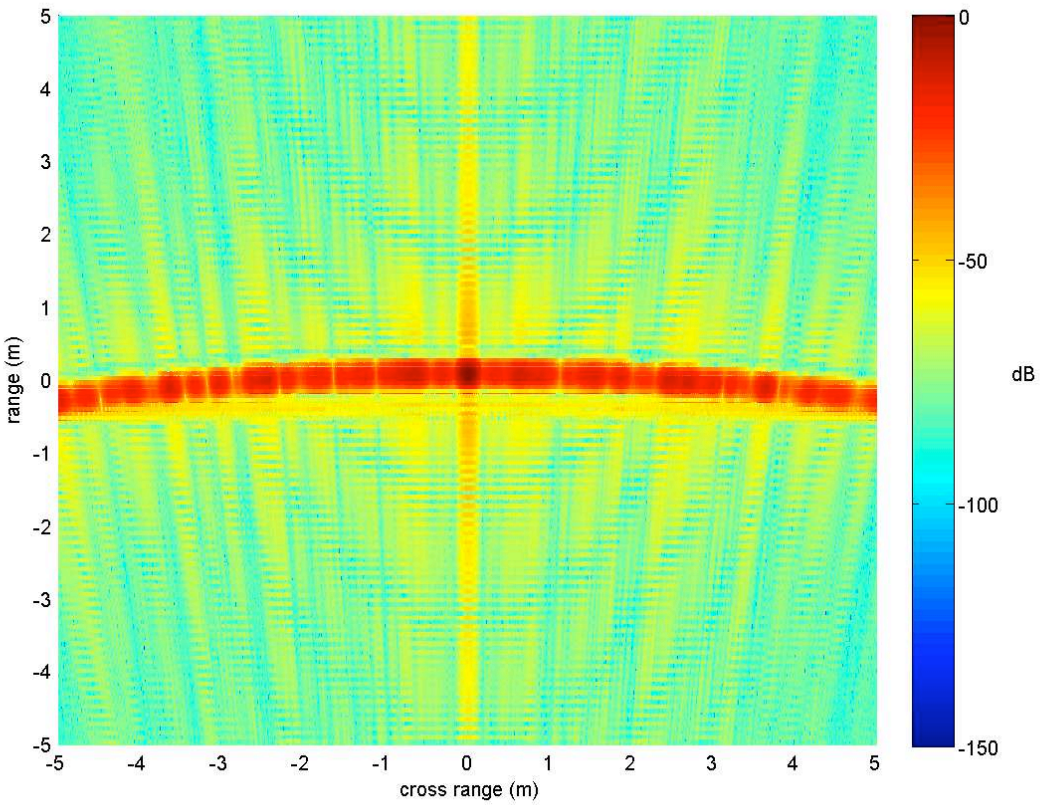

Figure 6.19: Result of processing SAR data with a rapidly jittered (±10 ppm peak-to-peak variation) carrier frequency. No correction was applied.

If required, (6.55) can be used to translate position errors into phase errors, and these can be translated into noise sidebands degrading the PSF. A similar calculation is described in Section 6.6.2 based on the work by Stove [11].

Along-track and vertical position errors are relatively unimportant, with 0.5 mm uniformly distributed errors in these directions being found to produce no discernible effects on the PSF. However, for the typical operation of the SAR test bench, it was found that position errors in the y direction should be limited to 0.2 mm to avoid undesirable noise floor levels due to position-error-induced spatial phase noise.

6.5 Practical aspects of the SAR test bench

There are three practical aspects to the construction of the SAR test bench:

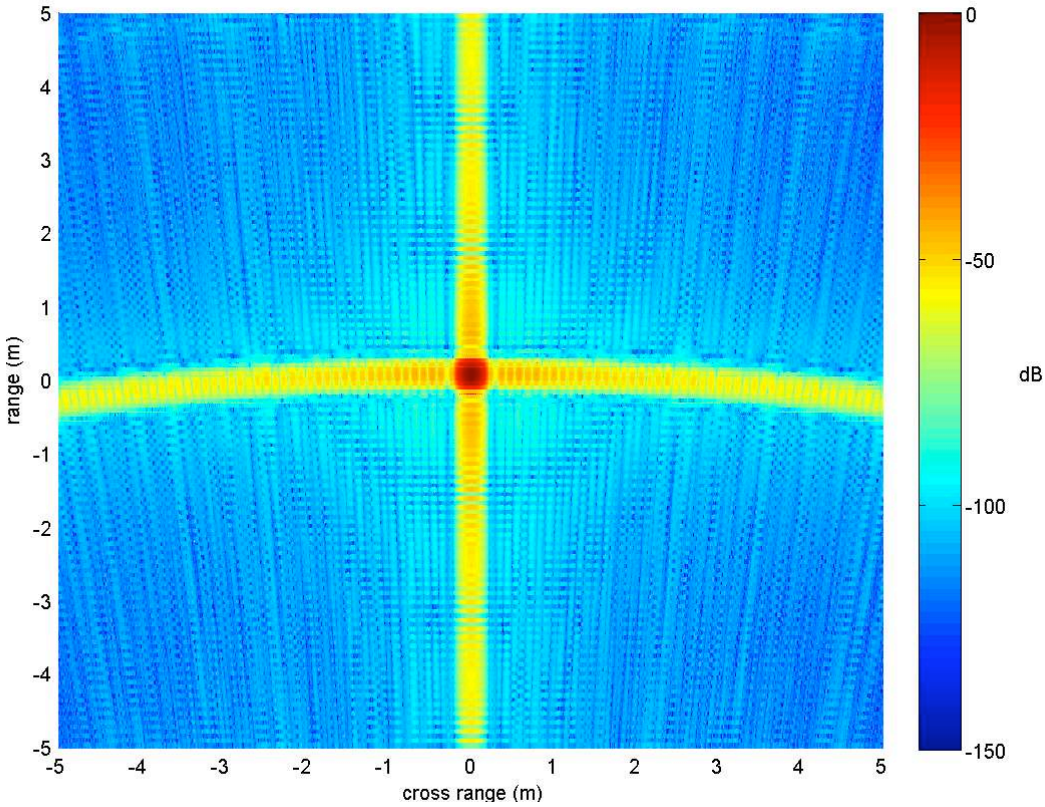

Figure 6.20: Result of processing SAR data with a rapidly jittered (±10 ppm peak-to-peak variation) carrier frequency with correction enabled.

1. the radar architecture;
2. the physical support and transportation of the radar;
3. the software to control the motion and data capture of the radar.

The radar itself is the dual horn/lens instrumentation radar reported by Robertson [76]. This is a comparatively light-weight device with excellent provision for customization and a well-documented performance history, all of which makes it ideal for this test bench application. The radar is described in Chapter 3, but here the pair of lenses have been removed to give a wide beam (20°) suitable for SAR imaging. The hardware is shown in Figure 6.23.

To support and transport the radar, care was taken to design a versatile but extremely rigid and substantial linear track arrangement. A custom linear screw-fed translation stage was bought to provide very precise range positioning (better than 0.2 mm accuracy as indicated by the simulated results in Sec-

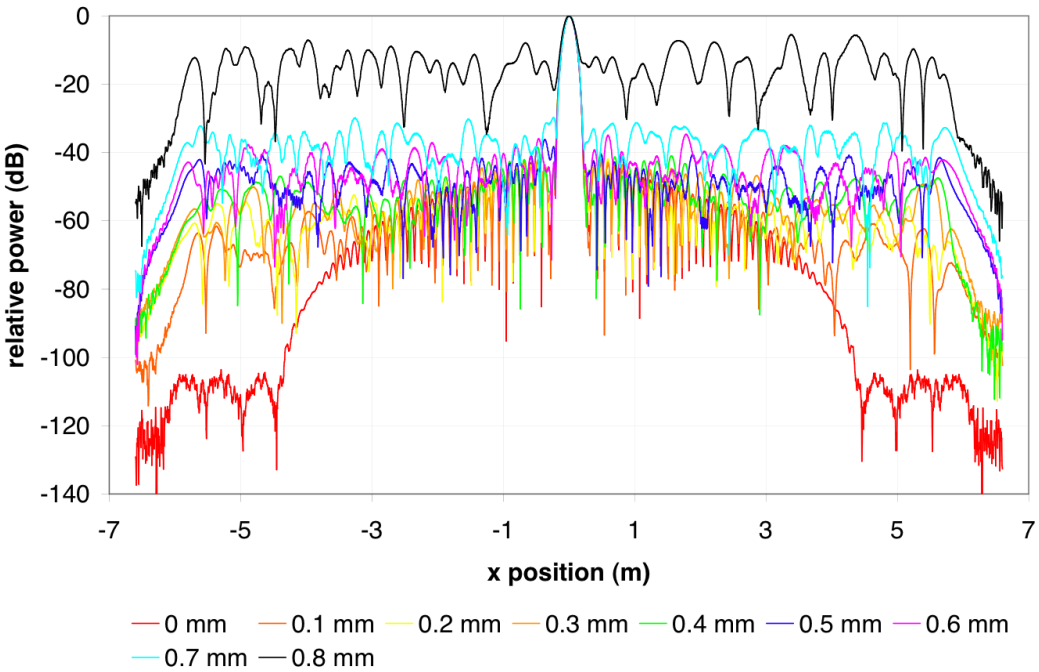

Figure 6.21: The cross-range profile of the point response given different y position errors.

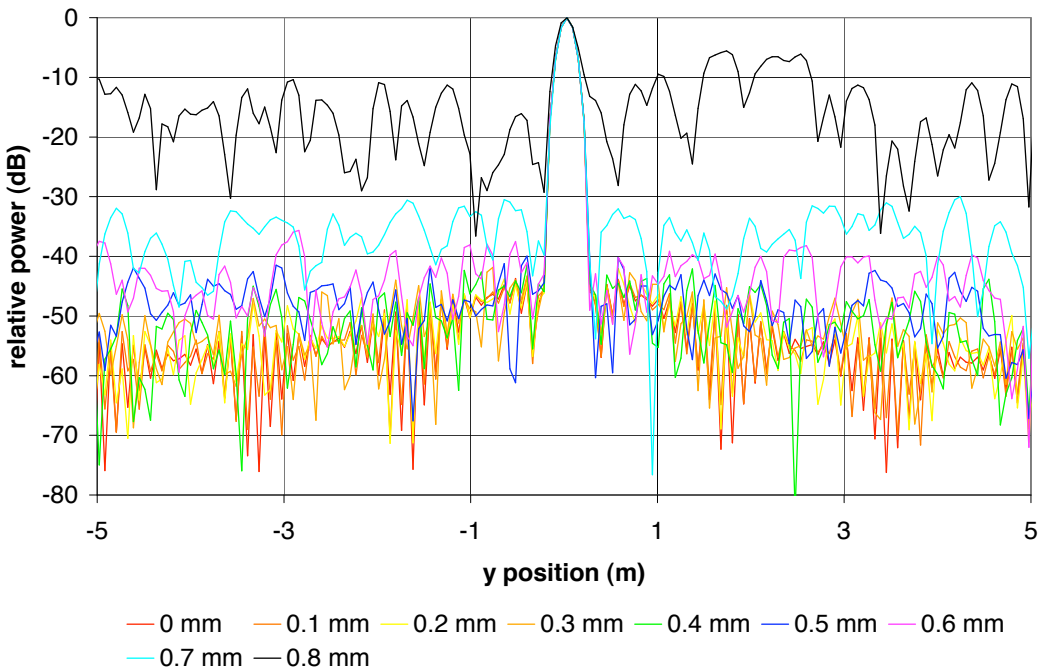

Figure 6.22: The range profile of the point response given different y position errors.

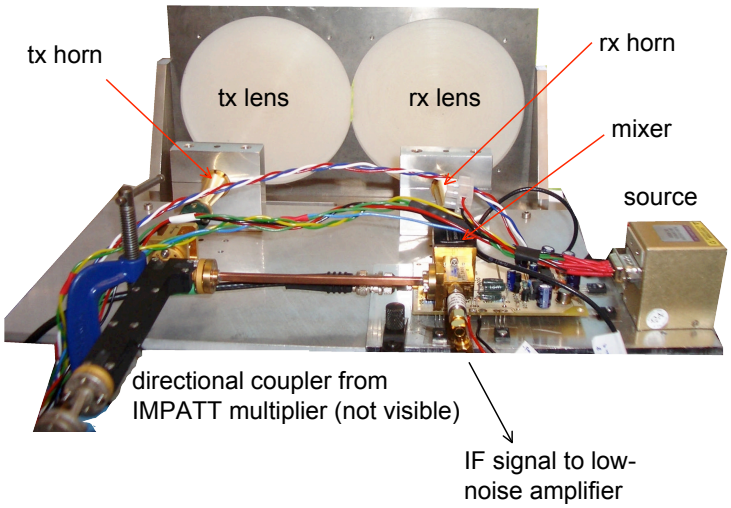

Figure 6.23: A photograph of the instrumentation radar hardware.

tion 6.4.3) and minimal position error in the cross-track and vertical direction. This was made possible by using plastic slide bearings that could be adjusted to minimize play. In the along-track direction, a precision screw (4 mm per turn) with pre-tensioned bearings giving zero backlash was used. The radar was always wound along in the same direction in any data collection task. This also reduces along-track position uncertainties. To wind the radar along, a stepper motor capable of 0.9° steps, giving a nominal along-track stepping precision of 0.01 mm, was used. This is perfectly sufficient for the SAR test bench, where accuracy and repeatability are more important than the precision of along-track position. The motor was powered and controlled by a standard control board that was modified to take TTL control signals from a computer, allowing computer-controlled along-track winding. Cut-out switches were fitted at either end of the track to prevent the motor from winding the radar too far, which could damage the bearings and the motor.

The motor and the linear track were mounted on a very heavy (50 kg) iron girder for extra rigidity and to suppress vibrations from the motor and motion of the radar. The motor was connected to the feed screw via a constant velocity flexible joint.

This arrangement was then bonded onto four very heavy (50 kg each) concrete optical-bench legs standing on the floor above a joist next to the window through which the radar would be pointed to collect data. This provides a very rigid, semi-permanent radar translation stage.

A computer program was written to control the radar's motion and operation, and also to collect and organize the signal data and meta data (parameters of operation and the time and centre frequency of each range profile data set).

This program controls the stepper motor by transmitting a stream of TTL pulses from the output channels of a digital sampling card to the 'direction' and 'step' terminals of the stepper motor control board. The stepping pulses are generated with increasing speed to reach the maximum stepping rate and then with decreasing speed to a halt to give smooth acceleration curves. This was done to prevent the stepper motor from slipping steps and was tested by commanding the stepper motor to wind the radar back and forth along the full length of the thread many times. The position of the radar at several points in the winding was checked at the start and end of the test. The radar was found to be in the correct position, indicating that no steps had been slipped.

Between each along-track data collection point, the radar is stationary, avoiding any question of the stop-start approximation being violated and reducing the chance of electrical interference from the stepper motor entering the radar signal. While the radar is stationary, a range profile is collected and digitized using the on-board digital sampling card, a 40MHz, 12-bit CH3150 ExacqDAQ model. This card is also used, via the digital output port, to control the stepper motor. Immediately after collecting the data, a frequency counter that monitors the centre frequency is queried for a measurement. The time and centre frequency are logged in the meta data file, and then the IF signal data is saved in a separate file named with the along-track position index. At the end of the data collection, the radar is wound back to the starting position, ready for the next data collection task.

The RMA is a batch-mode processor: it can only process the image once all of the range profiles have been collected and preprocessed. When data collection is complete, the implementation of the RMA processor reads the meta data file and processes the IF signals into a two dimensional complex image.

6.6 Test bench oscillator selection

Ideally, the oscillator used in the SAR test bench should have excellent signal characteristics if it is to provide a good indication of the performance of the

remainder of the system.

There were two available options: firstly, the usual instrumentation radar PMYTO [76], which is commonly used as a 'reference' oscillator. This has very good linearity and low phase-noise levels. This oscillator has been used in many experiments and has been found to give its best performance (in terms of spurious signal elements, noise floor, and linearity) when chirped using a TTi analogue waveform generator.

Secondly, advances in Direct Digital Synthesis (DDS) technology now mean that extremely-linearly chirped (limited only by the phase errors introduced by filters and amplifiers) and very-low-noise (especially when chirped) signals can be obtained in a highly controlled and repeatable manner (owing to the computer interface and exact numerical control of the waveform). The resulting signal does not require any linearization, and because it uses a STable Local Oscillator (STALO) that is tuned to a fixed frequency, the carrier stability is excellent.

The specific details of the two oscillators discussed in this section are as follows:

PMYTO A Micro Lambda Wireless MLPF-1463FM PMYTO device. It operates at 7.83 GHz and has tuning sensitivity 6.5 MHz/V over a ± 10 V range via a supplied voltage-to-current control circuit. The phase noise of the package is specified in the supplied data sheet as being -98 dBc at 10 kHz and -120 dBc at 100 kHz offset frequencies.

DDS An Analog Devices 9910 Evaluation board (Revision G) DDS device demonstration set used in an up-conversion scheme devised by D. A. Robertson, shown in Figure 6.24. The evaluation board is supplied with software to control the device, allowing the chirp rate and duration to be set via frequency step and time step controls. The board connects to a computer via the universal serial bus. The DDS has a 14-bit DAC and can sample out signals at frequencies as high as 400 MHz.

Both oscillators have good linearity, and at the typical operating ranges of 30 m, the linearity of either source will not be problematic.

The amplitude stability of both sources is good, so the remaining features that will determine the quality of the signal for SAR imaging purposes are

frequency stability and phase noise. In this section, I shall discuss and compare the phase noise and centre frequency drift of the two oscillators.

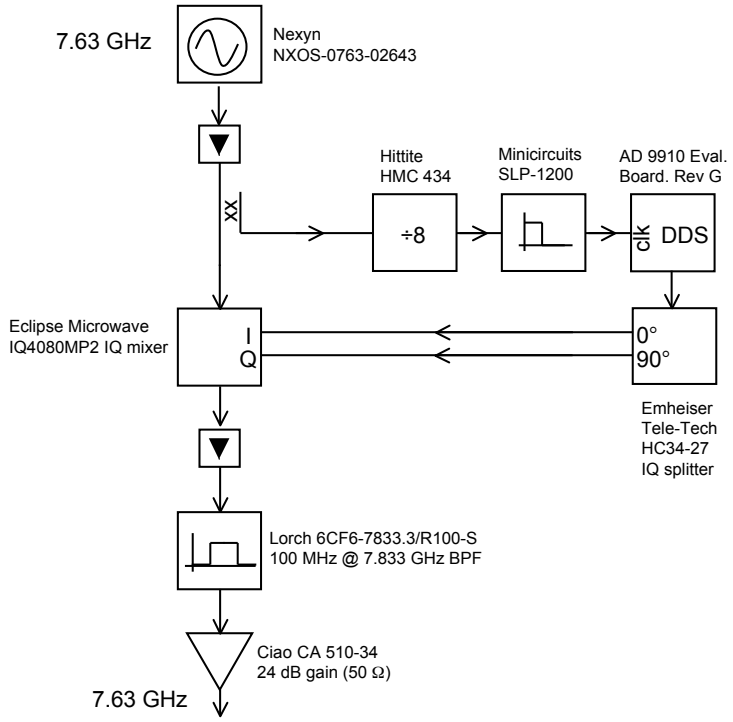

Figure 6.24: Upconversion scheme for the DDS-based source, devised by D. A. Robertson.

6.6.1 Centre frequency drift

It is important that the radar data remains sufficiently coherent over the duration of the synthetic aperture, as demonstrated in Section 6.4.2. Because of the nature of homodyne FMCW radars (they cancel the starting phase of the chirp in the dechirping process), if the centre frequency of the chirp is reasonably constant, then chirp-to-chirp IF coherence is maintained and an aperture can be synthesized.

From (6.36), the phase of a scatterer in the dechirped signal is seen to be ϕ, where

$$\phi = \frac{4\pi f_0 R}{c}, \tag{6.56}$$

so the frequency drift, δf_0, corresponding to a phase drift, $\delta\phi$, is given by

$$\delta f_0 = \frac{\delta\phi \, \mathrm{c}}{4\pi R}. \tag{6.57}$$

Assuming a maximum allowable QPE of $\pi/2$, as discussed in Chapter 3, with $R = 30$ m, (6.57) gives a maximum allowable drift of 1.25 MHz.

The quoted temperature dependent centre frequency drift for the PMYTO used in the instrumentation radar is 28 ppm. This corresponds to 2.7 MHz/°C. The temperature dependent centre frequency drift for the DRO driving the DDS is specified as ±5 ppm/°C, although the typical performance is ±1.5 ppm/°C. These correspond to 470 kHz/°C and 141 kHz/°C respectively. It is likely that the temperature would drift sufficiently during ten minutes (the typical data collection duration) to cause noticeable along-track phase errors, especially if the equipment is outside, which is often the case. Additionally, it might be desirable to coherently combine multiple SAR images, in which case a common fixed centre frequency is desirable for interferometry.

If the centre frequency at each along-track data collection point is known, then the frequency drift can be removed and the data can be made accurately coherent by applying a phase correction to the raw data. This correction has been implemented in the test bench SAR processor as part of the correction expressed by (6.14). Additionally, it should be possible to use autofocus techniques such as the PGA and Prominent Point Processing (PPP) [67] with modification (a range-dependent phase scaling) to estimate the centre frequency drift directly from the image.

The SAR test bench was built incorporating a microwave frequency counter that is queried by the controlling computer. The instantaneous STALO frequency is logged along with the IF signal data.

The PMYTO and the DDS both have good frequency stability, but only the DDS system lends itself to convenient centre frequency measurement (a small fraction of the STALO signal can be tapped off and measured with a frequency counter). In the PMYTO case, the centre frequency could be measured, but this would require some means of halting the ramp applied to the FM control of the oscillator. This is possible in principle but not convenient with the equipment available. In such a case, autofocus techniques might be preferable.

6.6.2 Oscillator phase noise

Ideally, oscillators produce a single 'tone' at a specified frequency, i.e. the signal phase increases linearly. Unfortunately, this is not realistic, and the signal phase includes errors such as the deterministic phase errors discussed in Chapter 3 and random (noise-like) phase errors. The latter are often due to thermal noise in the electronics and amplifiers. Phase noise is also inherently a property of the oscillator itself [108].

The effects of phase noise on the PSF and so on the range profile have been studied in depth. Stove [11] derives useful relationships between the Power Spectral Density (PSD) of the phase and the degraded point response. Stove shows that the spectrum of the frequency error (which is related to the phase error) maps into the PSF in the form of paired echoes either side of the main lobe. Depending on the nature of the frequency (or phase) error spectrum, the resulting distortion of the PSF degrades the resolution, sensitivity, dynamic range, and symmetry of the radar response.

The SAR signal is a two-dimensional signal and has a two-dimensional phase error. This results in noise sidebands in the SAR image in range and cross-range. So, as with many demanding (especially high-contrast) radar applications, it is desirable to choose a source with as low phase noise as possible.

In principle, it is possible to estimate the quality of the PSF of a radar from the quality of the source, usually using estimates of the linearity and phase noise. However, when the two sources are radically different and complicated, as in the case of the PMYTO and the DDS, it is simpler and more direct to test them in a radar imaging situation. This is a typical application of the instrumentation radar [76] mentioned elsewhere in this thesis.

Both the sources were used in the instrumentation radar to form high-resolution range profiles of a 30 dBsm point-like trihedral reference reflector. The range of the reflector, R, was 100 m, the chirped bandwidth, B, was 1.2 GHz (the largest bandwidth possible with the available electronics), and the chirp duration, T, was 5 ms. For each source, the target was imaged 100 times in quick succession and the results averaged, both coherently and incoherently. The results are shown in Figure 6.25. It can be seen that the coherent and incoherent averages for the DDS sources are very similar. This indicates that there is very little random noise in the signal derived from the DDS source. However, there is a marked difference between the coherent av-

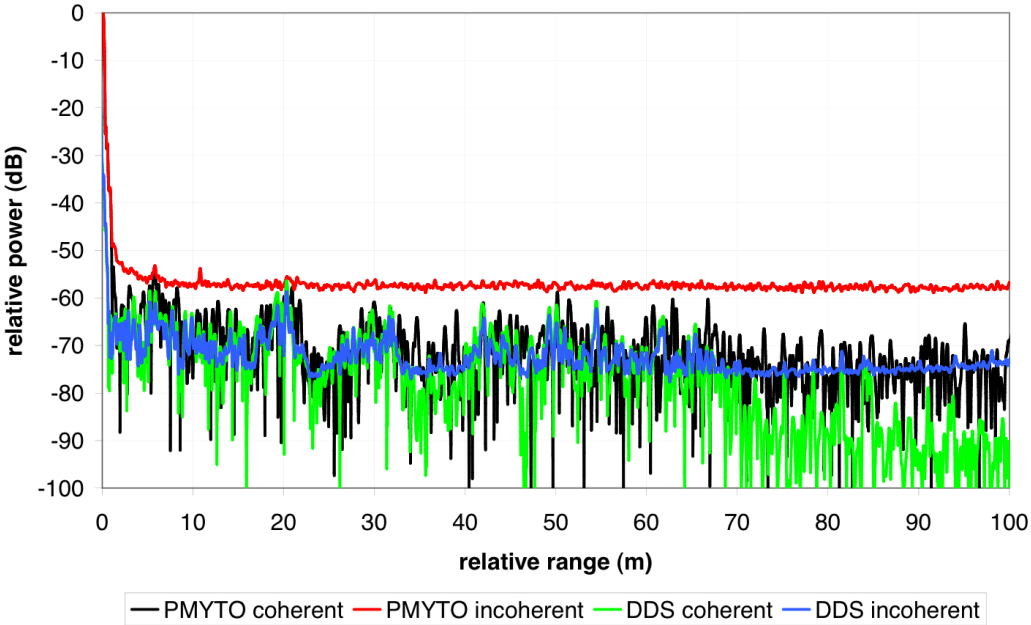

Figure 6.25: The (100 times) coherently and incoherently averaged range profiles of a 30 dBsm trihedral at 100 m range. Images for both the DDS source and the PMYTO source are shown. N.B. the range here corresponds to frequency above the carrier frequency.

erage of the PMYTO signal and the incoherent average. The difference is due to random noise in the PMYTO signal. It can also be seen that the coherent average of the PMYTO and DDS images are very similar. This indicates that neither is introducing (different) deterministic spurious signals. The low level structure is either clutter or a common effect.

Analysis has been done [109, 110] to investigate and quantify the signal artefacts introduced by DDS techniques in FMCW radar systems. These artefacts originate in phenomena such as quantization noise and phase truncation spurs. However, whilst these artefacts appear sometimes to be problematic in the constant frequency case, they appear to be less problematic in the chirped case. This is thought [111] to be because the chirping makes the phase truncation errors non-periodic and removing the periodicity removes the spurs. Analysis has been done [112, 113] that suggests that DDS FMCW radar systems should obtain excellent (i.e. low) spurious signal levels.

Similarly, DAC errors, which tend to cause harmonic spurs, are attenuated by the combined chirping and dechirping action, which smears out the cross terms (i.e. any fundamental or harmonic in the echo being dechirped by any-

thing other than itself) in the frequency domain. Because energy is conserved by Fourier transforms, smearing in frequency (or range) results in a decreased amplitude. The exact cross terms of spurs are usually small enough to ignore because they are second-order terms at most.

The phase noise sidebands degrading the PSF of the PMYTO are very clear from the comparison shown in Figure 6.25. The performance of the PMYTO does not match expectations based on the specified noise performance. The specified noise level in the signal generated by the PMYTO is -98 dBc at 10 kHz and -120 dBc at 100 kHz. N.B. there is an extra $20\log_{10}(N = 12)$ dB due to the twelve-times frequency multiplication.

To check that the PMYTO was operating correctly, a phase noise measurement set (HP 4352B signal analyser, HP43521A downconverter and HP8664A reference signal generator) was used to characterize the PMYTO and the DDS. Both of the sources were operating in constant-frequency mode at the central transmit frequency (7.833 GHz), i.e. there was no frequency modulation. The results are shown in Figure 6.26, from which it can be seen that the PMYTO phase noise is within specification and that the DDS phase noise is noticeably lower.

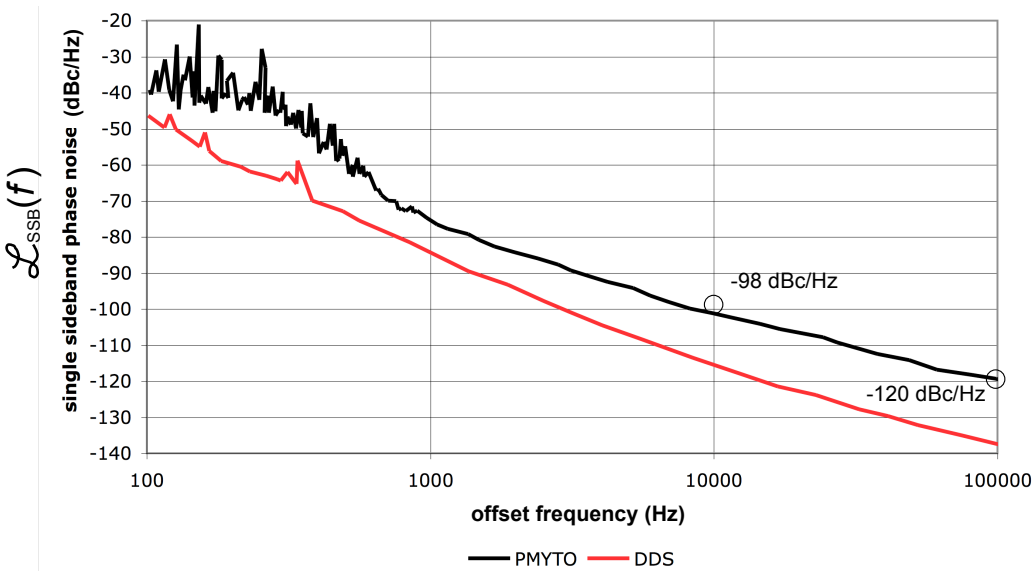

Figure 6.26: The phase noise spectra of the PMYTO and the DDS-based systems measured at 7.83 GHz. The PMYTO is measured to agree with its manufactured specification. The jagged structure below 1 kHz in the PMYTO spectrum is thought to be due to driver noise.

An obvious remaining route for phase errors to enter the PMYTO signal is via the tuning voltage. This is provided by a TTi TG210 analogue waveform generator. An investigation was carried out to find the best signal generator to chirp the PMYTO. A range of tests investigating the linearity, noise, and spurious signal content of a range of digital and analogue waveform generators and waveforms (sawtooth, triangular, rounded) were carried out. In the tests, the waveform generators and waveforms were ranked according to each of these metrics, and these rankings were compared against a definitive ranking of the actual performance of the PSF obtained when chirping the oscillator with each waveform generator and waveform. In each case there was no correlation. It was concluded that either there is some important factor (other than linearity, noise, and spurious signals obvious from the spectra of the waveforms) that was not investigated, or, more likely, the relationship between the oscillator and the waveform generator is complicated and important. The waveform generators were all measured into a dummy impedance equal to that of the PMYTO's built-in driver circuitry, 10 kΩ, and this approach was possibly too simplistic. The results of the radar field trials indicated that the TTi waveform generator producing a triangle wave was the best option for overall performance.

To estimate the noise in the triangular waveform, a simple measurement arrangement was set up, as shown in Figure 6.27. The method was to high-pass filter the triangular waveform to suppress the triangle wave, leaving the wideband noise part that is to be measured.

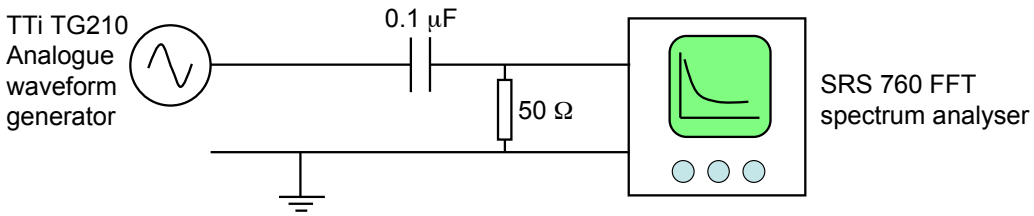

Figure 6.27: The measurement arrangement to estimate the noise in the triangle wave generated by a TTi TG210 waveform generator.

The spectral analysis region (4 ms) of the SRS 760 was arranged to fit symmetrically within one upstroke (which was also used in the radar imaging tasks) of the 10 ms triangular waveform, using the TTi trigger output and an appropriate trigger delay. By removing the large nominal signal content, the SRS 760's internal amplifiers/attenuators could be set to high sensitivity to

measure the comparatively small noise part. Coherent and incoherent averages were made to identify the spectrum due to the residual nominal signal (which is deterministic). The results are shown in Figure 6.28, where it can be seen that the noise floor of the measurement (i.e. the noise coming from the spectrum analyser, the high-pass circuit, and a 50 Ω dummy load) is much smaller than the noise coming from the TTi.

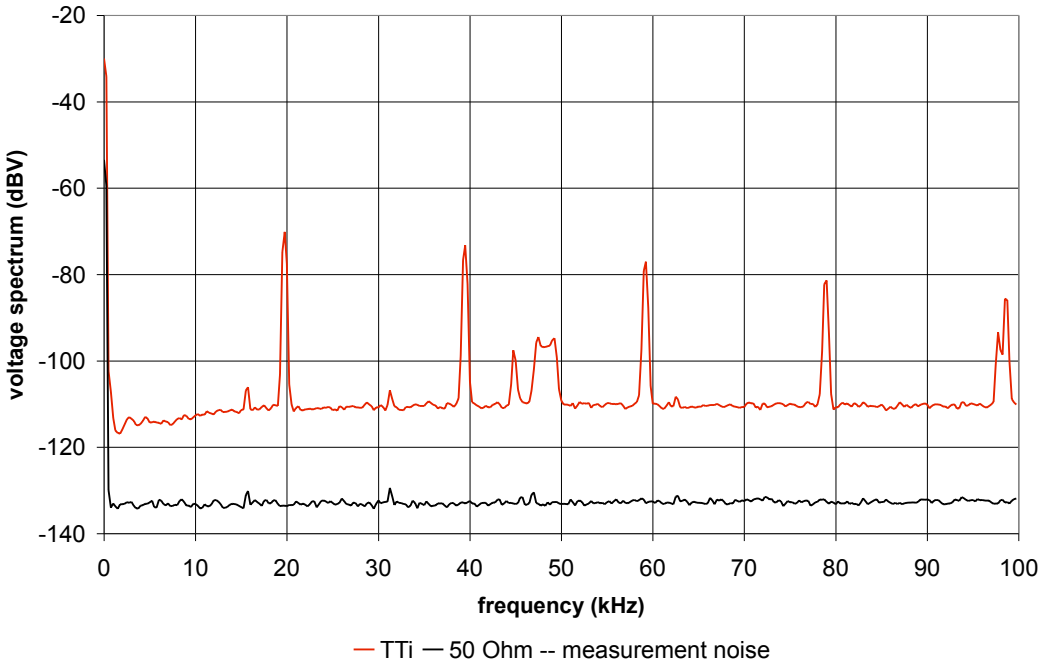

Figure 6.28: The voltage spectrum of the noise of the TTi TG210 waveform generator estimated using the measurement arrangement shown in Figure 6.27. The frequency bins are 250 Hz wide (a 4 ms spectral analysis region was used in the FFT spectrum analyser).

To estimate the effect that this voltage noise will have on the PSF, a simple analysis based on the method described by Stove [11] is used. The calculation is as follows.

The VCO converts the applied voltage into the frequency (according to the tuning curve) of a phase-continuous signal which is then frequency-multiplied to give the transmit signal. Labelling the VCO centre frequency f_0, the tuning sensitivity β, and the frequency multiplication factor N, the phase of the transmitted signal at time t after the start of the chirp can be written as

$$\phi(t) = 2\pi N \int_0^t \left(f_0 + \beta[v(t') + \delta(t')]\right) \mathrm{d}t' + \phi_0, \tag{6.58}$$

where $v(t) = v_0.(t/T - 1/2)$ is the nominal control voltage and $\delta(t)$ is the voltage noise. t' is a dummy variable and ϕ_0 is an arbitrary phase offset. This gives

$$\phi(t) = \underbrace{2\pi N \int_0^t f_0 \mathrm{d}t' + \phi_0}_{\phi_\mathrm{i}(t)=\text{nominal phase}} + \underbrace{2\pi N\beta \int_0^t [v(t') + \delta(t')]\mathrm{d}t'}_{\epsilon(t)=\text{phase error}}. \tag{6.59}$$

So, with reference to Chapter 2 and ignoring the amplitude, the dechirped signal, $s_\mathrm{d}(t)$, is of the form

$$s_\mathrm{d}(t) = \cos\big(\phi_\mathrm{i}(t) - \phi_\mathrm{i}(t-\tau) + \epsilon(t) - \epsilon(t-\tau)\big). \tag{6.60}$$

The ideal part of (6.60) can be written in the form $2\pi f_\mathrm{R} t$, where f_R is the frequency determined by the range of the reflector. If the phase error,

$$\Delta\epsilon = \epsilon(t) - \epsilon(t-\tau), \tag{6.61}$$

is assumed to be small, $\ll \pi$, then (6.60) can be approximated by

$$s_\mathrm{d}(t) = \cos(2\pi f_\mathrm{R} t) - \Delta\epsilon \sin(2\pi f_\mathrm{R} t). \tag{6.62}$$

The voltage noise can be represented in terms of its spectrum,

$$\delta(t) = \sum_{i=0} a_i \cos(2\pi f_i t + \theta_i). \tag{6.63}$$

$\Delta\epsilon(t)$ is given by (6.59) and (6.61). Along with (6.63), this gives

$$\Delta\epsilon(t) = 2N\beta \sum_{i=0} \frac{a_i}{f_i} \sin(\pi f_i \tau) \sin(2\pi f_i t + \theta_i), \tag{6.64}$$

where θ_i are not the same phase offsets as in (6.61). But the absolute phases of the signal components are not important in this calculation.

Substituting for $\Delta\epsilon$ in (6.62) and rearranging gives

$$s_\mathrm{d}(t) = \underbrace{\cos(2\pi f_\mathrm{R} t)}_{\text{ideal part}} + \underbrace{N\beta \sum_{i=0} \frac{a_i}{f_i} \Big[\cos\big(2\pi(f_\mathrm{R} + f_i)t - \theta_i\big) - \cos\big(2\pi(f_\mathrm{R} - f_i)t - \theta_i\big)\Big]}_{\text{paired echoes due to control voltage noise}}, \tag{6.65}$$

which indicates that each phase noise spectral component results in a pair of antisymmetric sidebands upconverted to the nominal signal frequency. These

are often called 'paired echoes' and are illustrated in Figure 6.29. As indicated by (6.65), the amplitude of the pair of sidebands relative to carrier is given by

$$b_i = \frac{N\beta a_i \sin(\pi f_i \tau)}{f_i}, \tag{6.66}$$

which can be seen to be a modified version of the voltage error spectrum defined by (6.63). For small values of $f_i\tau$, this can be approximated by

$$b_i = \pi\beta\tau N a_i. \tag{6.67}$$

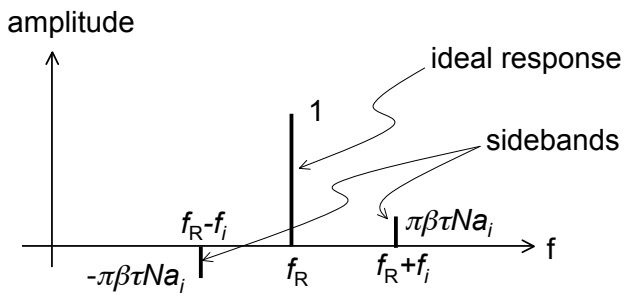

Figure 6.29: The paired echoes due to the ith voltage noise component.

The representation of a random noise process as a set of discrete frequency components is a useful technique, but there is not really a sine wave at each frequency. In fact, the representative amplitude at each frequency gives a sine wave that will have the same power as all of the distributed frequency components in the same bin. Assuming that the spectral power density is uniform across each frequency bin, then the signal power density in the ith frequency bin, σ_i, is given by

$$\frac{1}{2}a_i^2 = \sigma_i \Delta f, \tag{6.68}$$

where the 1/2 comes from the RMS power of a normalized sine wave and Δf is the bin width.

Equations (6.67) and (6.68) give the expected amplitude relative to the peak,

$$b_i = \sqrt{2\Delta f}\,\pi\beta\tau N\sigma_i. \tag{6.69}$$

From Figure 6.28, it can be seen that the noise floor of the TTi signal is about -110 dBV in 250 Hz bins. This gives $\sigma = -110$ dBV $-10\log_{10}(250\text{ Hz}) = -134$ dBV/$\sqrt{\text{Hz}}$.

However, the input impedance of the measurement arrangement (high-pass filter and spectrum analyser) is 50 Ω, whereas the PMYTO control circuit has a high impedance (≈ 10 kΩ) input. The output impedance of the waveform generator is 50 Ω, so this results in a factor of ≈ 2 difference in the effective voltage presented to the VCO. This factor of 2 in voltage accounts for 6 dB less power in the measurement compared to that presented to the input of the PMYTO. This gives -128 dBV/$\sqrt{\text{Hz}}$ as the voltage noise density presented to the VCO input.

Using (6.69) with the above values gives -55 dBc. This agrees reasonably well with the observed incoherently averaged signal noise level, as shown in Figure 6.25, suggesting that the observed noise is determined primarily by voltage noise in the triangular voltage waveform applied to the VCO to provide the chirp. This calculation suggests that use of a dedicated low-noise, highly linear variable triangle wave signal generator would dramatically improve the noise levels in the performance of the PMYTO as a radar source.

6.6.3 Source selection conclusions

In comparison to the PMYTO-based system, the DDS-based system offers a low-noise, highly linear, precisely-specified, repeatable chirp. Based on these points and considering the ease with which the carrier frequency can be measured, the DDS-based source was chosen for the SAR test bench.

6.7 Processing real SAR data

To demonstrate the operation of the SAR test bench, a scene was laid out as shown in Figure 6.30 with nine 20 dBsm reference trihedrals on a grassy, reasonably level piece of ground. The radar was then run with maximum bandwidth (1.2 GHz) and translated over 0.88 m in the along-track direction. This gives range and cross-range resolution respectively of 0.18 m and 0.078 m, assuming Hamming weighting. The scene was 30 m from the radar, which had beam width, θ_b, 20°. The radar was about 2 m above the scene, which at 30 m gives a grazing angle $\gamma = 2.8°$. Because the ground at the scene is neither perfectly flat nor level and because the grazing angle is small, no mapping into the ground plane (or surface) was done, the image being left in the slant plane. The imaging specification is tabulated in Table 6.2, and the resulting SAR image is shown in Figure 6.31.

Name	Symbol	Value
Carrier frequency	f_0	94 GHz
Bandwidth	B	1.2 GHz
Range resolution	ρ_r	≤ 0.178 m
Along-track data extent	L	0.880 m
Along-track resolution	ρ_{xr}	≤ 0.088 m
Chirp time	T	5 ms
Beam width	$\theta_b = \theta_u$	20°
Along-track measurement spacing	δx	0.004 m
Fast-time sampling rate	f_s	4 MHz

Table 6.2: Imaging parameters used for Scene A. N.B. the beam falls off rapidly, so $\theta_b = \theta_u$ is a good assumption.

The 'calibration' of the SAR image shown in Figure 6.31 and the calibration of all the other calibrated images (those with the dependent variable measured in dBsm) was achieved by scaling the response such that known large RCS scatterers (trihedral reference scatterers) have the correct size.

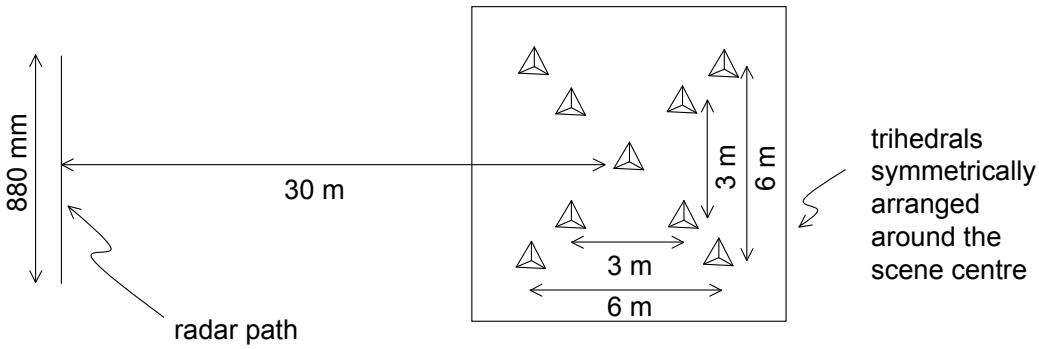

Figure 6.30: Scene A: Arrangement of the scatterers for both the real and the simulated data cases. The radar is 2 m above the ground plane.

The same situation was simulated (with exactly the same parameters) and the signal processed to form an image, which is shown in Figure 6.32.

Comparing the images shown in Figures 6.31 and 6.32, it can be seen that the images made from simulated and real data agree to within slight misalignments in the placement of the scatterers. The error in the apparent position of the scatterers is not a processor artefact, as can be seen from the correct placement of the scatterer images in the image generated from the simulated data. The ground was not particularly flat, and the physical arrangement of

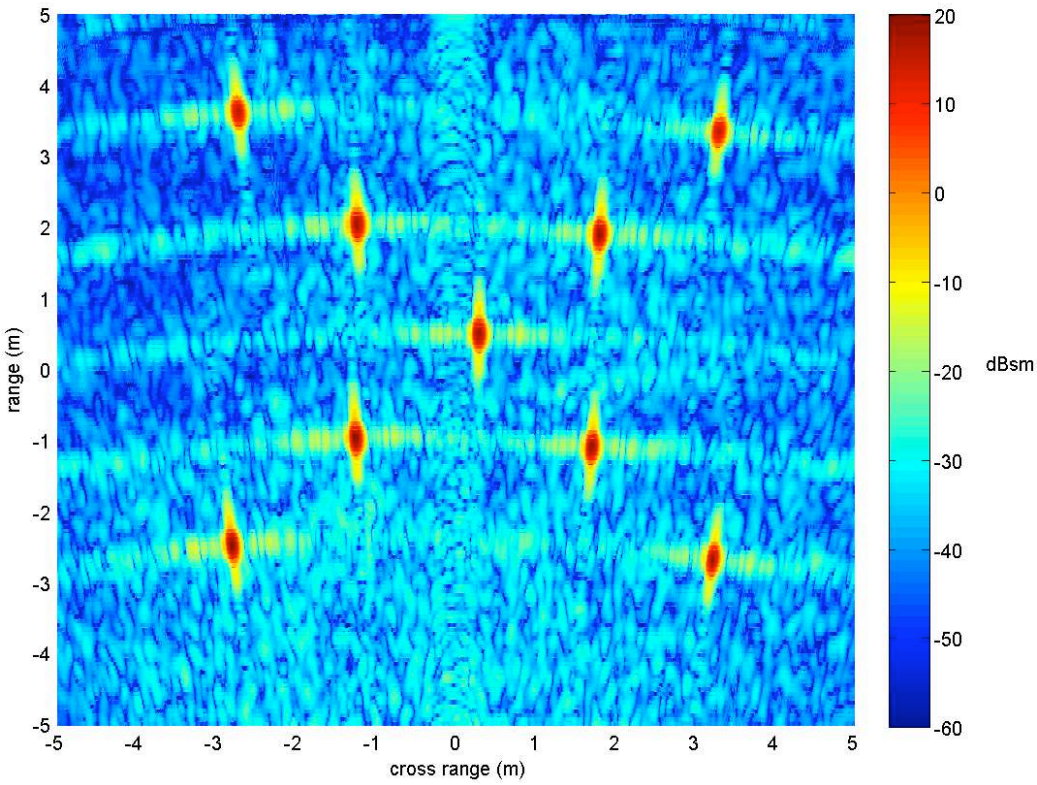

Figure 6.31: SAR image of Scene A generated from real data collected with the test bench radar.

the scatterers was slightly wrong because I did not survey the scene sufficiently accurately. The PSFs in cross range and range (x and y) of the central scatterer in the images generated from the synthetic and real data are compared in Figures 6.33, 6.34, and 6.35 respectively. It can be seen that there is a reasonable correspondence between the simulated PSFs and the measured PSFs. The noise and clutter levels are clearly higher in the real case, and the resolution in the real case is inferior to that in the synthetic case.

The increased sidebands of the range PSF are undesirable. This could be phase noise introduced into the signal after the source, perhaps in the frequency multiplier. However, the same multiplier was used in many experiments, some of them described in this thesis, and it was not previously found to introduce significant phase noise.

As shown in the SAR images processed from simulated radar data, radar position jitter introduces sidebands similar to those seen in Figures 6.31, 6.33, and 6.35. By comparing the sidebands due to radar position jitter and those

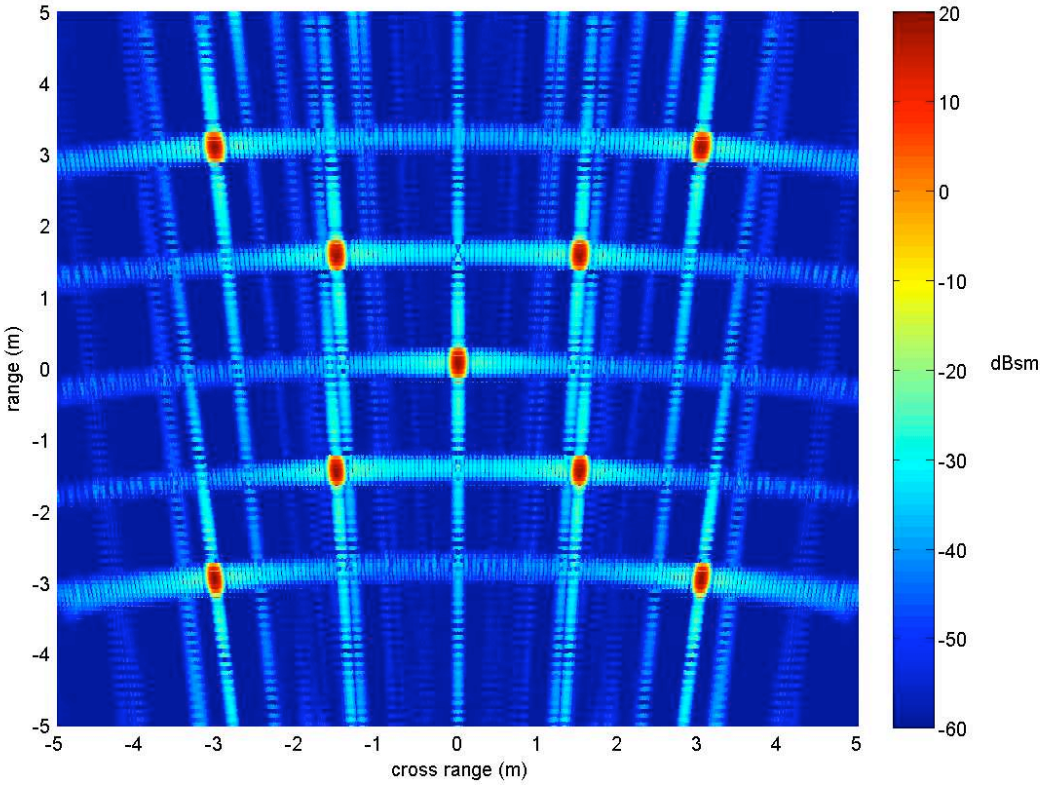

Figure 6.32: SAR image generated from simulated Scene A data.

in the imagery, it appears that radar position error might be the cause of the degradation.

The radar translation stage was chosen to have as little vibration as possible, but some is inevitable. The radar sits on a bracket mounted on top of the slide table of the linear translation stage. While effort was made to make the radar as steady as possible, it is very likely that the antennas vibrated between and during along-track data points, effectively adding broadband along-track noise to the signal. This is a problem with the mechanical design and could be investigated further to yield significant improvements. Ideally, the antennas would be mounted more directly to the translation stage, and the microwave hardware mounted on top. This would decrease the lever arm between the slide table and the antennas, reducing the effect of any vibration.

The nominal and achieved resolution in the cross-range and range directions are shown in Table 6.3, from which it can be seen that the cross-range resolutions broadly agree between images generated from the simulated and

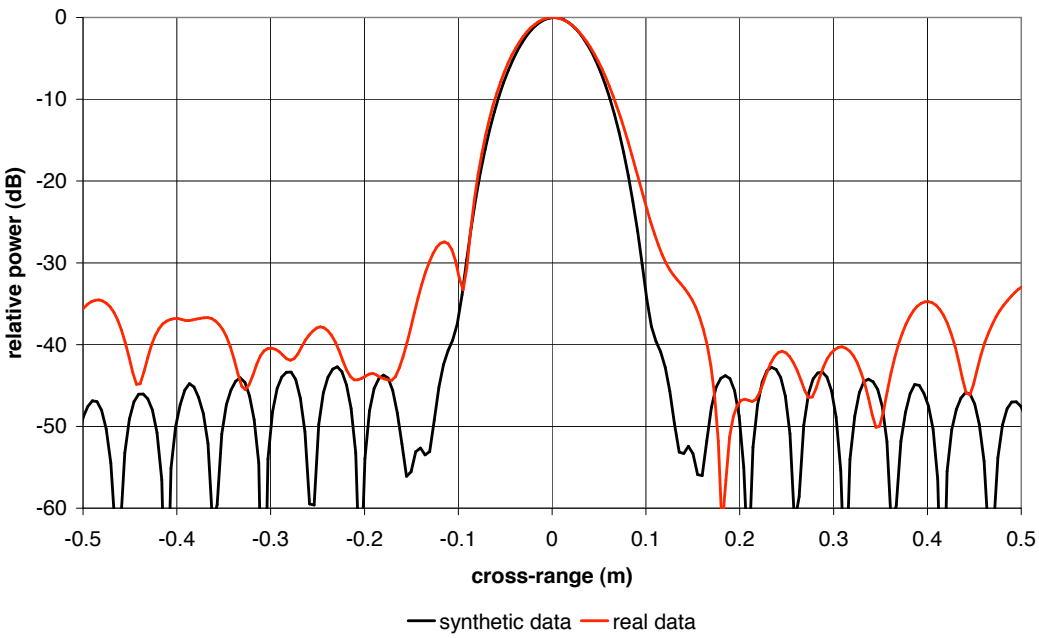

Figure 6.33: Close-in view of the x direction PSFs of the centre scatterer images made from simulated and from real data.

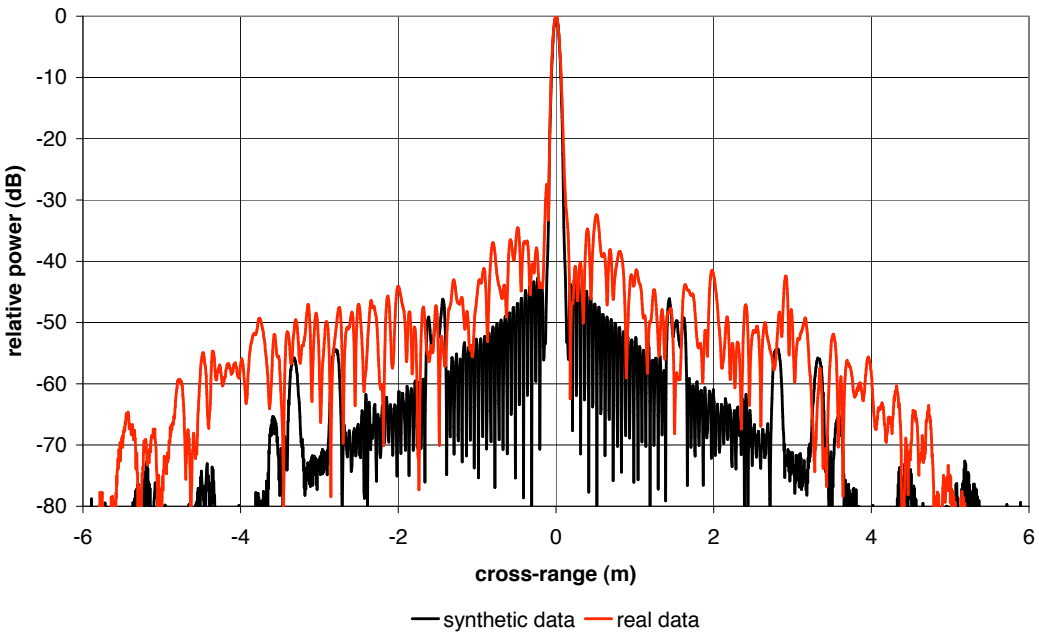

Figure 6.34: Full-image-width x direction PSFs of the centre scatterer images made from simulated and from real data. The noise floor in the real data signal can be seen to be significant.

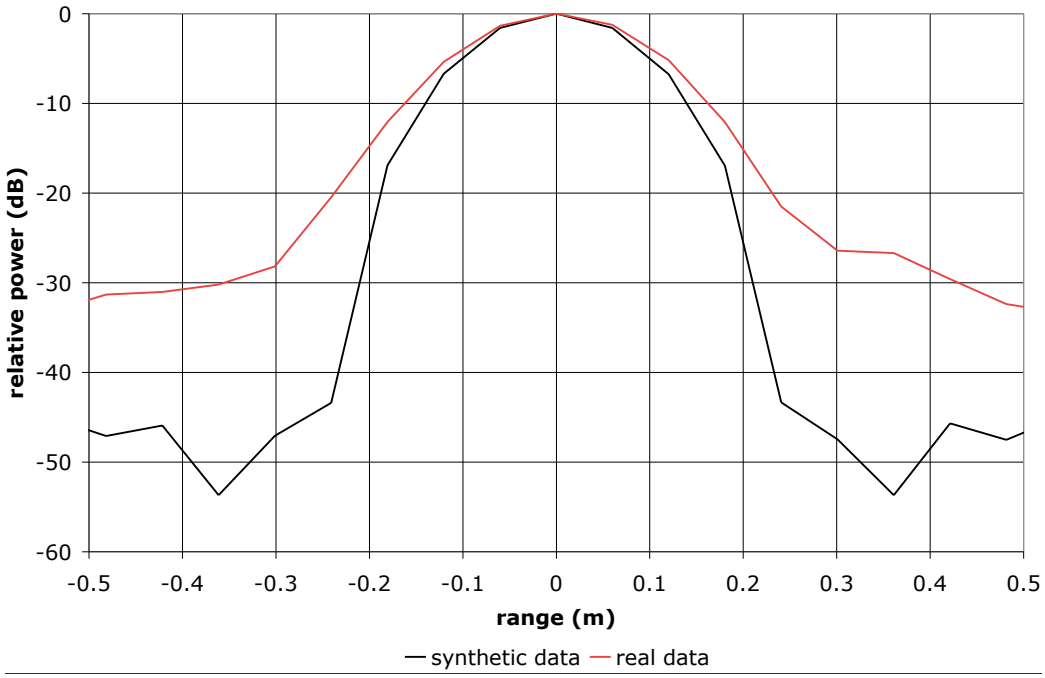

Figure 6.35: Full-image-width y direction PSFs of the images made from simulated and from real data.

the measured data.

The range resolution in the real SAR image is broader than the designed value by about 20%. There are several possible reasons for this, the most likely being that the actual chirped bandwidth is smaller than nominal owing to amplitude roll off towards the edges of the pass band of the transmitter. If the frequency sweep rate were different from the designed value, then there would be implications for the frequency-range scaling, too. However, this appears not to be the case. The most likely cause is loss of signal power of the IMPATT frequency multiplier towards the edge of its pass band. To verify this, the frequency response of the IMPATT frequency multiplier was measured, and the PSF was calculated from the resulting AM (from sweeping the frequency in the linear chirp) using (3.4) and the ideas presented in Chapter 3. The frequency response of the IMPATT and the estimated PSF given Hamming window weighting are shown in Figures 6.36 and 6.37 respectively. The ideal Hamming weighted signal PSF is also shown in the latter. The degraded response is 15% broader than the ideal one. While this does not account completely for the discrepancy between the nominal and the actual range resolution (which is about 15% to 20%), it suggests that this could be responsible

Resolution			
Direction	**Nominal** (m)	**Simulated** (m)	**Real** (m)
cross-range slice at the centre	≤ 0.078	0.078	0.078
range slice at the centre	≤ 0.178	0.176	0.203
cross-range slice at (3, −3)	≤ 0.088	0.086	0.085
range slice at (3, −3)	≤ 0.178	0.170	0.214

Table 6.3: Specified and achieved resolution. In SAR images of Scene A processed from the real and simulated data.

for a large part of it. Additionally, the response was measured quasi-statically and might differ from the dynamic frequency response. In further work, the dynamic frequency response could, if need be, be evaluated from the IF time series of single scatterer imaging tasks, which should show the frequency response as a function of time. The signal amplitude for a single scatterer can be obtained by inverse Fourier transforming a small image section centred on a single bright scatterer.

The bandwidth could be recovered to some degree by dividing out the frequency response in the frequency domain, but this would be at a cost to the SNR, because noise in the roll-off regions would be amplified.

6.8 Additive signal error correction

It can be seen that there is a small spurious response up the middle of the SAR image shown in Figure 6.31. It is more evident in a SAR image produced from data collected when a piece of W-band absorber is placed over the transmitting antenna. This image is shown in Figure 6.39, where the scaling has been chosen to be consistent for comparison with other figures. The presence of the artefact even when the transmitting antenna is covered suggests that it is introduced by the electronics, e.g. by the W-band mixer responding to the chirping Local Oscillator (LO) signal.

The processor implementation was provided with a means of removing spurious dc signal responses. The method, described by (6.14), is simply to band-pass filter all of the fast time signals, leaving only the part of the spectrum that corresponds to the scene. This correction is extremely important: the resulting imagery would be unusable without it because spurious responses would strongly dominate even scenes containing very high-RCS scat-

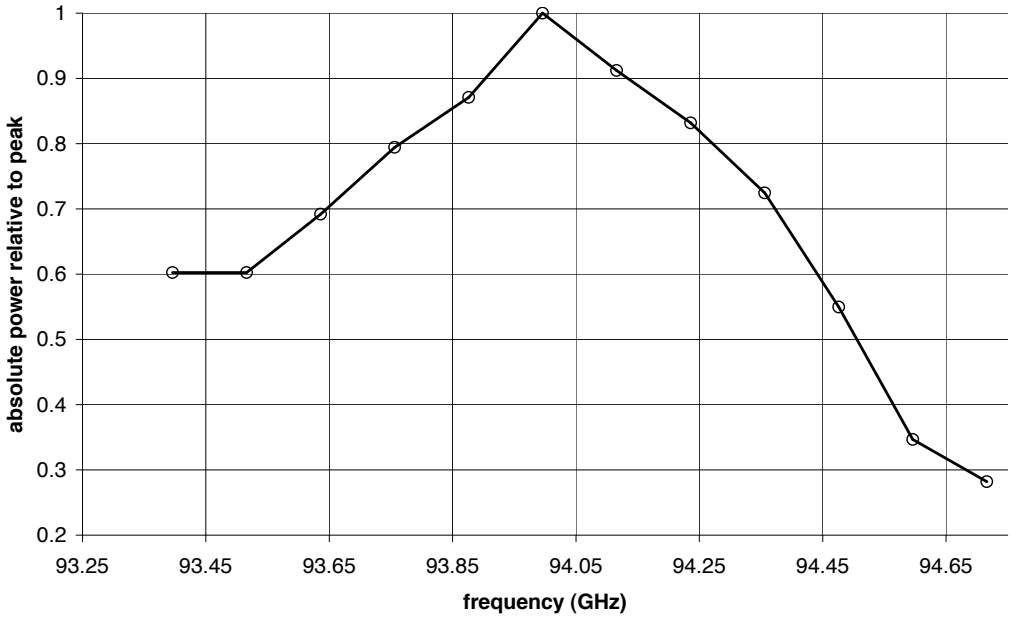

Figure 6.36: The normalized absolute frequency response of the IMPATT frequency multiplier over the operational range used in the SAR radar experiments.

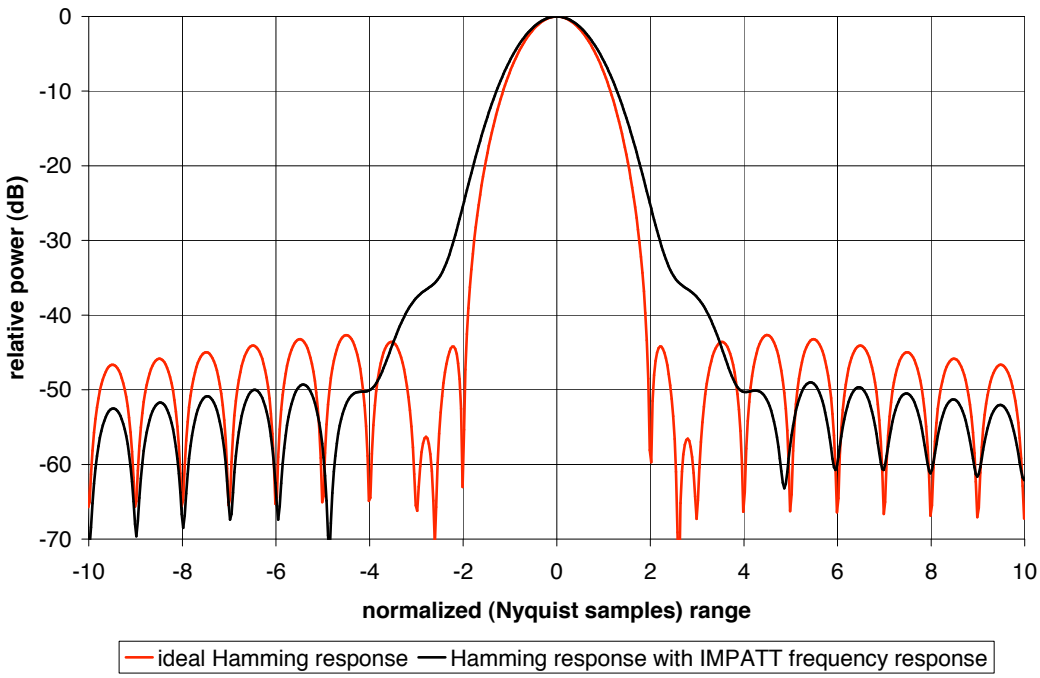

Figure 6.37: The ideal and degraded PSF given Hamming weighting and the AM due to the non-uniform frequency response of the IMPATT frequency multiplier. The degraded response is 15% wider than the ideal one.

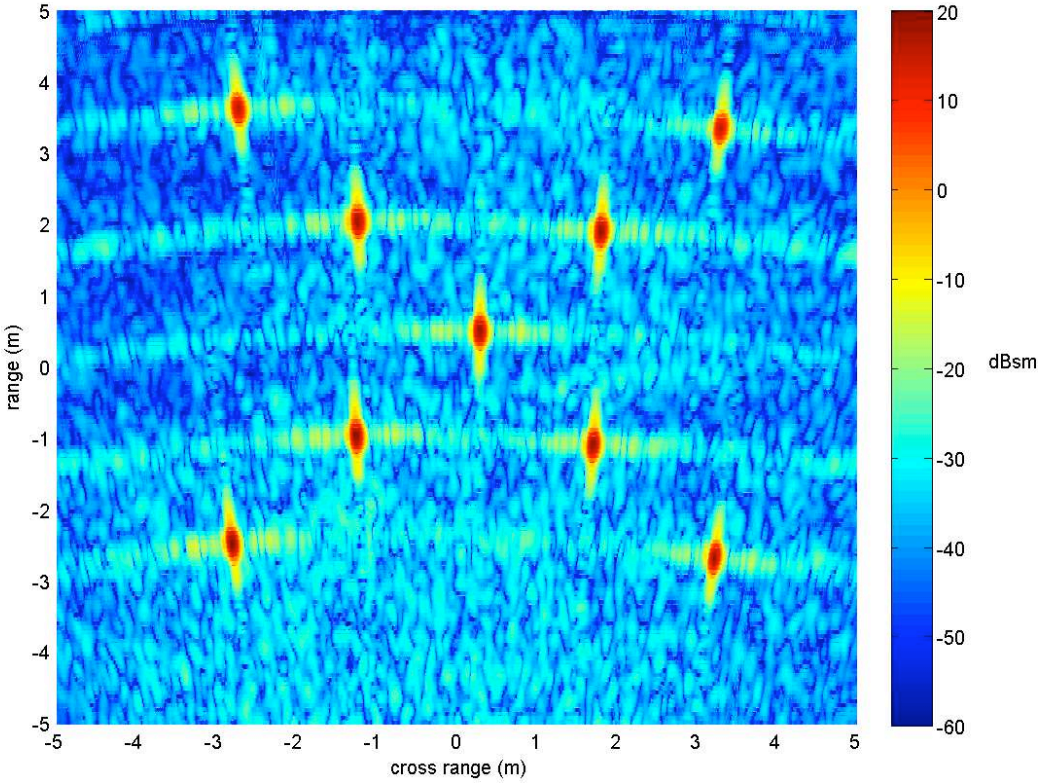

Figure 6.38: Image of Scene A processed from the same data as the image shown in Figure 6.31 but with signal correction applied. The correction can be seen to remove the artefact running the depth of the image at cross-range position $x = 0$.

terers.

Although the band-pass filter can completely remove components of the signal that are *not* in its pass band, it cannot remove (to any degree) those that *are* in its pass band. It appears that the artefact is a ringing due to a signal from outside the pass-band. To remove this signal, an additional error correction technique was implemented in the SAR signal processing software. This second method involves estimating the common part of the response of the radar from all along-track positions. This is done by averaging the fast-time IF signal in the along-track direction when there is no return from the scene. This can be achieved by collecting data as usual but with absorber preventing the radar from transmitting. Once the common error component of the IF signals has been found, it can be subtracted from each of the IF signals in the data preprocessor before entering the RMA.

A correction was estimated using the data collected with the transmitting

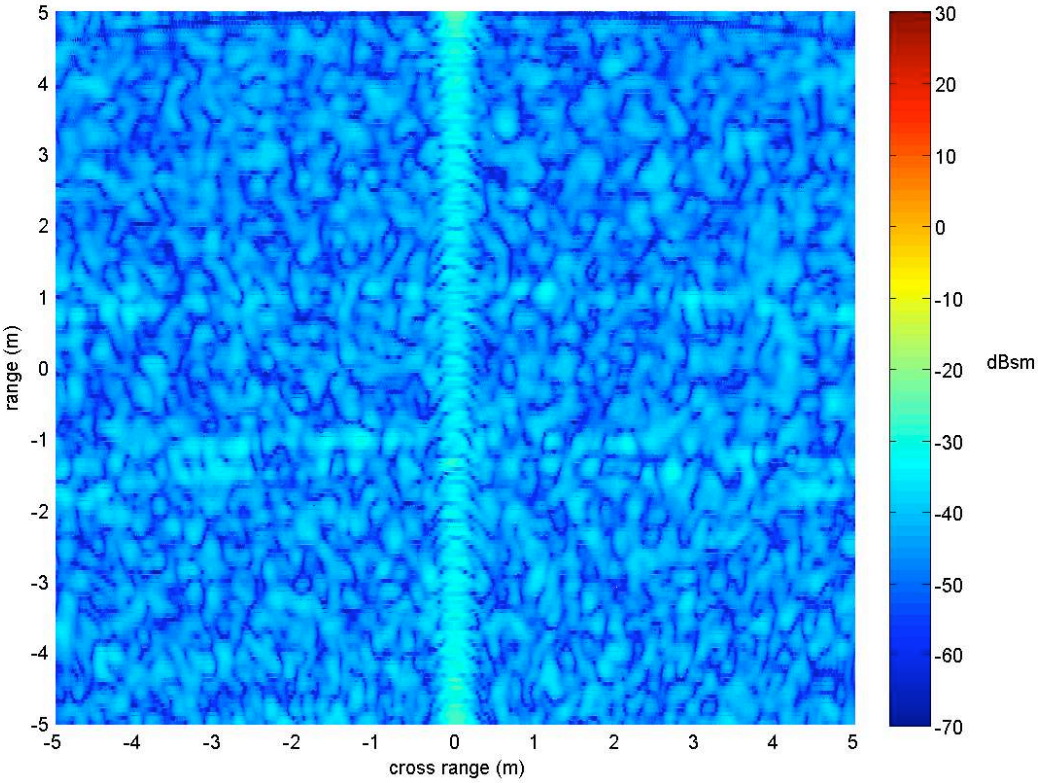

Figure 6.39: Result of imaging the empty scene with a piece of absorber on the transmit antenna.

antenna covered, and then three cases were reprocessed with the correction applied. The cases were the covered transmitting antenna case (before: Figure 6.39 and after: Figure 6.40), the Scene A case (before: Figure 6.31 and after: Figure 6.38), and a case in which an empty field was imaged, (before: Figure 6.41 and after: Figure 6.42).

In every case, it can be seen that the large artefact has been removed, whilst the correct image remains undisturbed. The correction is subtractive not multiplicative: it does not suppress all signal energy at the affected area but instead subtracts the spurious signal, leaving only the signal due to scatterers in the scene.

The error affecting the signals was estimated from two data sets collected on different days, one for Scene A data and one with the transmitter covered, both operating with the same swept bandwidth and chirp time. It can be seen from Figure 6.43 that the error is very similar apart from an overall dc offset. This suggests that the error is a highly repeatable artefact. It is thought to be

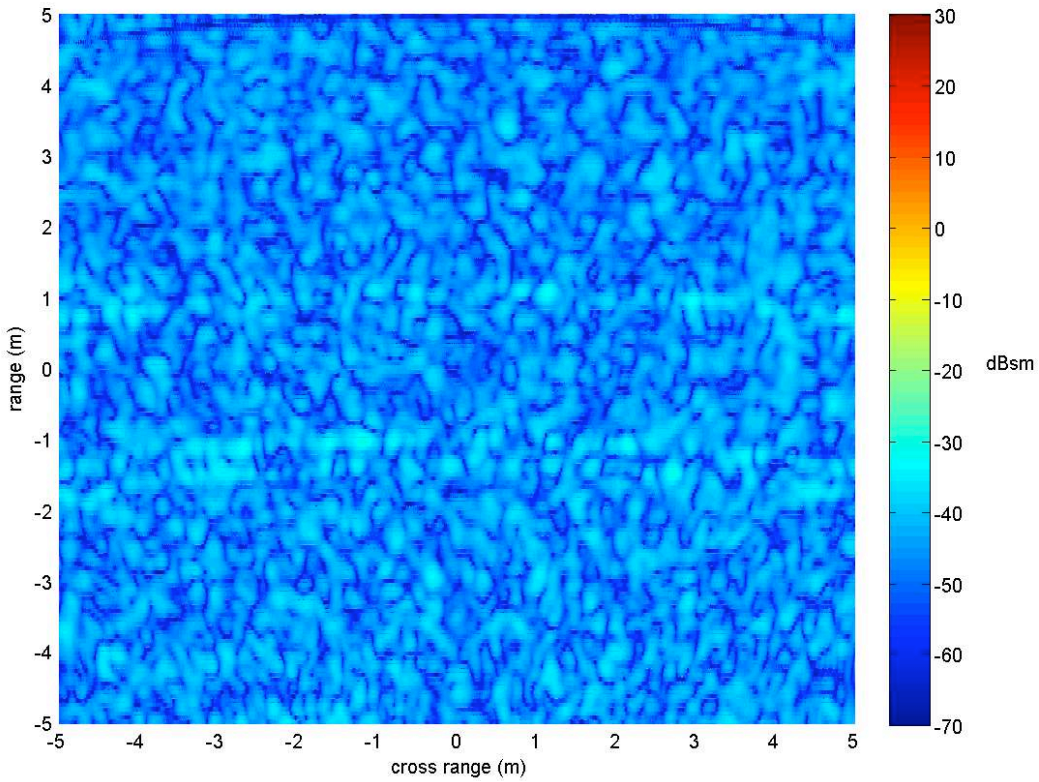

Figure 6.40: Result of imaging the empty scene with a piece of absorber on the transmit antenna and with signal correction applied.

related to the W-band mixer.

Ideally, this artefact would be removed before the signal is sampled. This is because the error part is larger than the IF signal corresponding to scatterers. This means that, currently, the dynamic range of the sampling card must accommodate the spurious response from the mixer (or whatever its origin) and not just the signal. This reduces the dynamic range and SNR of the resultant SAR image.

6.9 Radar sensitivity

The sensitivity of the radar indicates how large an object must be before it can be discerned from the noise in an image. So it is a useful quantity to know. To demonstrate the sensitivity of the SAR test bench, a range of scatterers was arranged in a scene, labelled Scene B, as shown in Figure 6.44. The scene

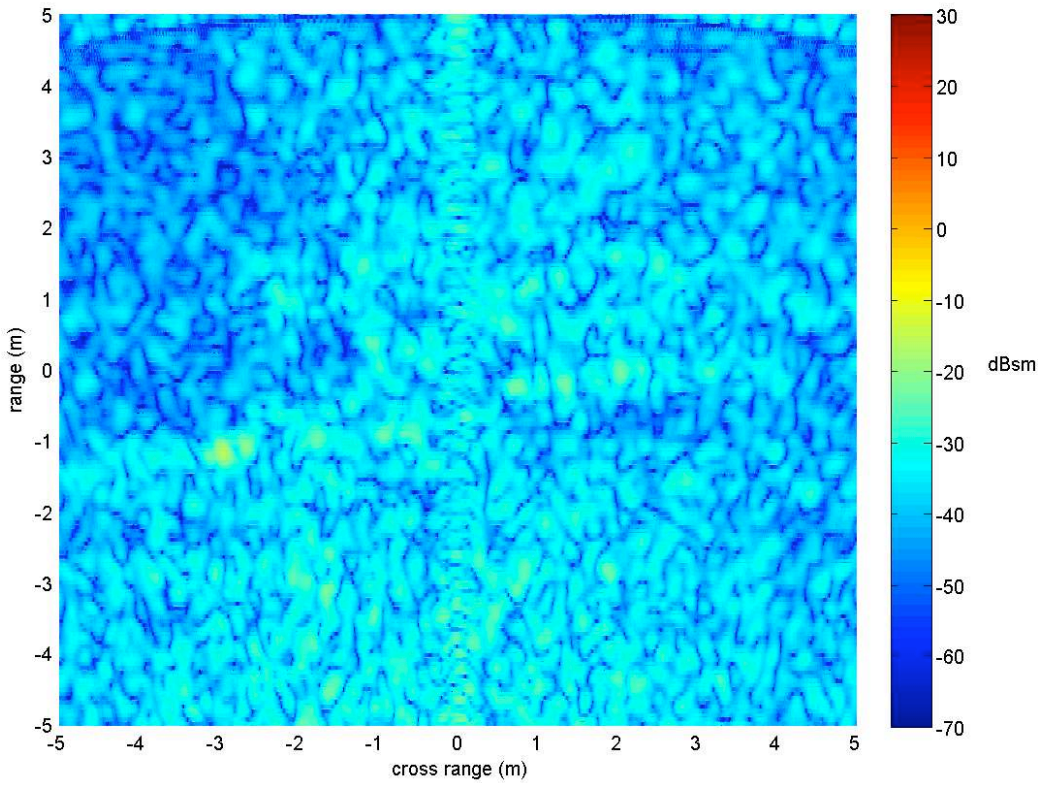

Figure 6.41: SAR image of the empty scene.

was imaged with the parameters shown in Table 6.4. The resulting SAR image (with signal correction enabled, the error estimate being derived from the covered transmitter case data) is shown in Figure 6.45. It can be seen from this image that, although the high-RCS scatterers are clearly visible, even down to the 0 dBsm scatterer, the more natural objects (cardboard boxes, collections of small metal objects) are much less obvious above the clutter/noise return.

To investigate the properties of the radar sensitivity further, the statistics of a SAR image of a weakly reflecting scene were studied.

The radar reflectivity histograms for the empty (i.e. grass-filled) scene image and the covered-transmitter image were found and compared with an independently estimated histogram of radar reflectivity for the same patch of grass, imaged with a conventional 94 GHz radar at the same grazing angle (2.8°). Note that all of the radar images were formed with vertical polarization on transmission and reception, i.e. VV data were used.

The two radar images do not have the same resolution, so the quantity to

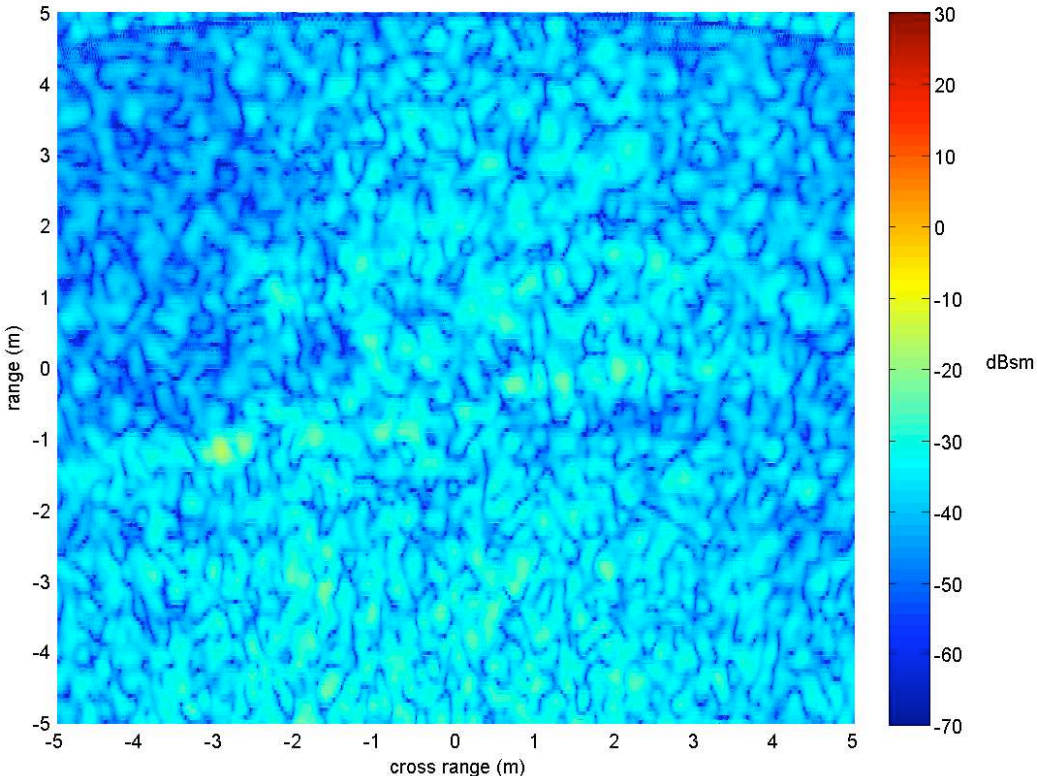

Figure 6.42: SAR image of the empty scene processed from the same data as Figure 6.41 but with signal error compensation enabled.

Name	Symbol	Value
Carrier frequency	f_0	94 GHz
Bandwidth	B	1.2 GHz
Range resolution	ρ_{r}	≤ 0.178 m
Along-track data extent	L	0.520 m
Along-track resolution	ρ_{xr}	≤ 0.178 m
Chirp time	T	5 ms
Beam width	$\theta_{\mathrm{b}} = \theta_{\mathrm{u}}$	20°
Along-track measurement spacing	δx	0.004 m
Fast-time sampling rate	f_{s}	4 MHz

Table 6.4: Imaging parameters used for Scene B. N.B. the beam falls off rapidly, so $\theta_{\mathrm{b}} = \theta_{\mathrm{u}}$ is a good assumption.

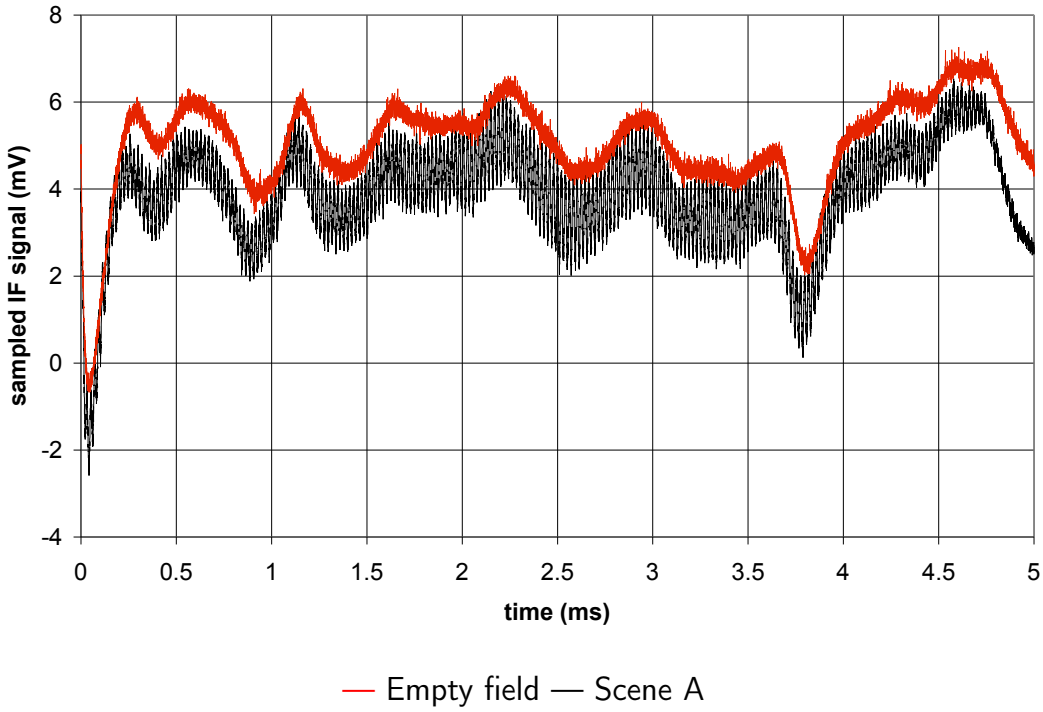

Figure 6.43: The signal errors estimated from the data collected from the Scene A data (black) and from the empty field data (red). The high frequency vibrations in the Scene A signal are the echoes off the scatterers.

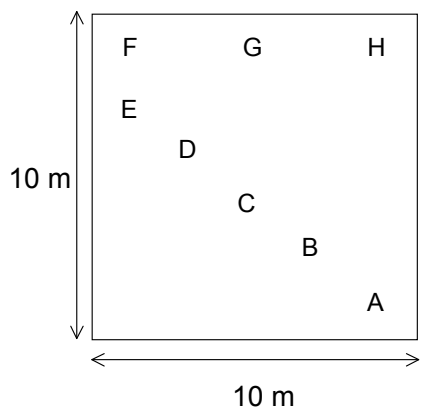

Object	Description
A	20 dBsm trihedral
B	20 dBsm trihedral
C	30 dBsm trihedral
D	10 dBsm trihedral
E	0 dBsm trihedral
F	80 cm cardboard box
G	20 cm cardboard box of metal scrap
H	20 cm cardboard box

Figure 6.44: Scene B: The arrangement of the assorted scattering objects.

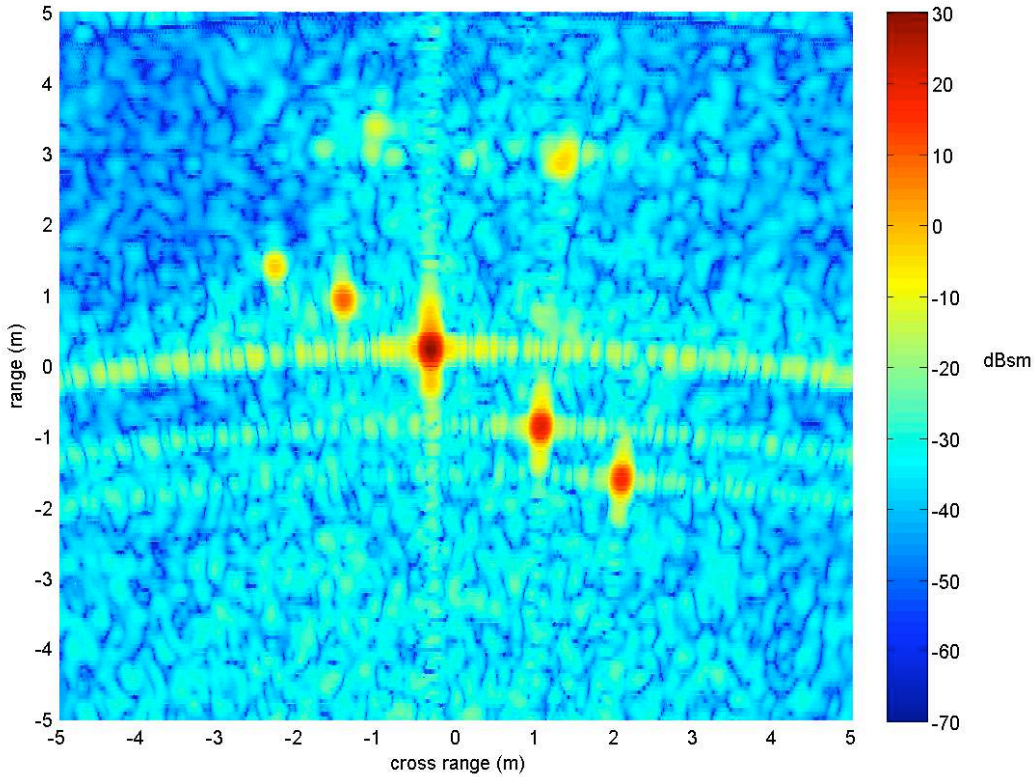

Figure 6.45: SAR image of Scene B produced from radar data collected by imaging a range of scatterers. The scatterers are labelled in Figure 6.44. The dc signal correction was used in processing this image.

compare is the radar reflectivity, which for sufficiently large resolution cells is independent of resolution. The radar reflectivity, σ^0, is defined by the equation

$$\sigma = \sigma^0 A, \tag{6.70}$$

where σ is the RCS and A is the effective area of the scattering material that contributes to each resolution cell [114].

The distribution of σ^0 was found for three images:

1. a SAR image of grass;

2. a SAR image formed with the same specifications as the grass image but with the transmitter obscured with mm-wave absorbing material;

3. a conventional radar PPI image formed using an instrumentation radar (the one used to build the SAR test bench and described in [76]) oper-

ating at 94 GHz with 0.365 m range resolution and approximately 1 m cross-range resolution.

To estimate σ^0, the images, which were scaled to give the correct RCS for a known scatterer at the scene centre, were compensated for five effects to allow (6.70) to be used. The five effects are:

1. $1/R^4$ dependence;
2. two-dimensional beam shape dependence (this is applied differently for the SAR and the real-beam radar cases);
3. R dependence of the azimuth resolution;
4. squint dependence of the azimuth resolution (only in the SAR case);
5. grazing angle dependence of the range resolution.

The value of A was derived from the scene centre resolutions and appropriate 'beam shape' scaling factors [114], which were found numerically.

The resulting histograms of σ^0 are shown in Figure 6.46. It can be seen that there is a contribution to the SAR image from the noise and from the grass. The conventional grass image indicates that the grass contributes a response in the -20 to -35 dB region. There is a local peak in the histogram for the SAR image of grass at -20 dB.

This agrees with the small amount of data available from the literature. For example, Brooker (after Curie et al.) [115] shows model predictions and measured data. The model curves and the measured data are shown in Figure 6.47, from which it can be seen that grass at very low grazing angles is about -20 dB. The noise (covered-transmitter) histogram indicates that there is a noise contribution in the -50 to -40 dB region, and this is roughly indicated in the grass histogram.

The grass in the scene was about 4 cm high and part of a roughly mown sportsfield. In all the cases, the grass was lush but not damp.

The histogram shown in Figure 6.46 suggests that the SAR grass imagery is consistent with other imagery of grass and that the radar's performance is acceptable. The histograms also indicate that the SAR measurement is sensitive to scatterers that have RCS greater than $\sigma_{\min}$, where

$$\sigma_{\min} = \big(-35 + 10\log_{10}(A)\big) \text{ dBsm}, \tag{6.71}$$

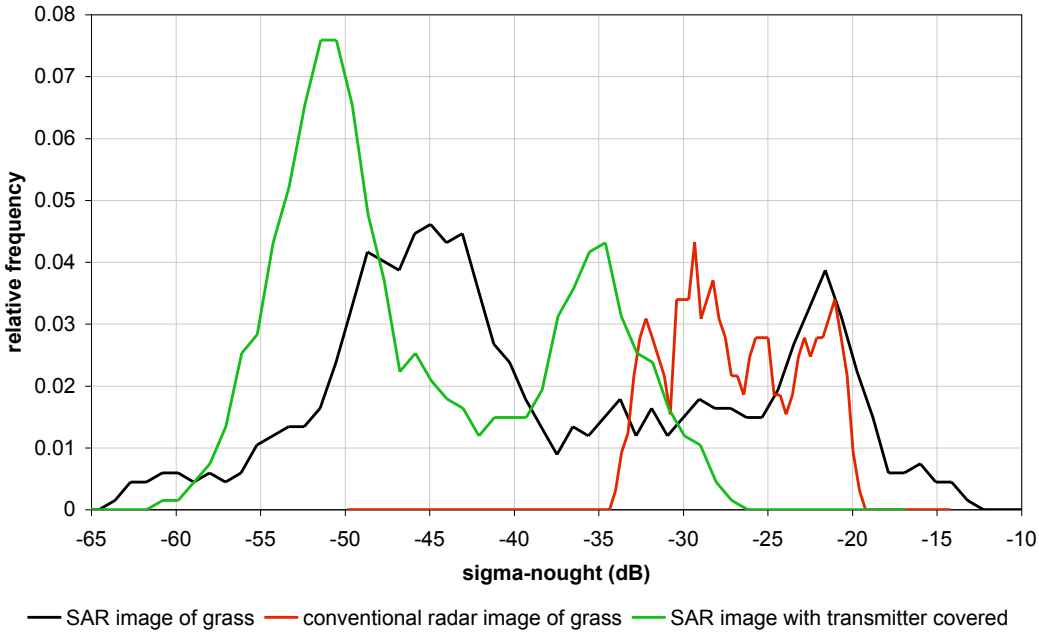

Figure 6.46: Histograms of σ^0 distribution for the three images: a SAR image of grass, a SAR noise image (transmitter covered), and a conventional radar image of grass.

where -35 dB is the smallest reflectivity that is not dominated by noise.

Typically, operating at 1 GHz swept bandwidth and synthetic aperture 0.3 m at 30 m standoff range, $A = 0.09$ m^2, so typically the smallest RCS that can be measured by the radar is about -45 dBsm.

6.10 Conclusions

In this chapter, I discussed SAR processing and selected the RMA as the most suitable SAR image processor for a SAR test bench based on its ability to process very-high-resolution imagery for very wide beam widths without a prohibitive computational load. For lower resolution, larger standoff ranges, and smaller scenes, the PFA and BPA would give acceptable image quality and offer lower computational loads and more versatile image and data collection geometries respectively.

I modified the RMA to make it more suitable for the purposes of a SAR test bench. These modifications allow real homodyne FMCW radar data to be processed and minimal along-track data collection intervals to be used. They also provide both a compensation for drifting source centre frequencies

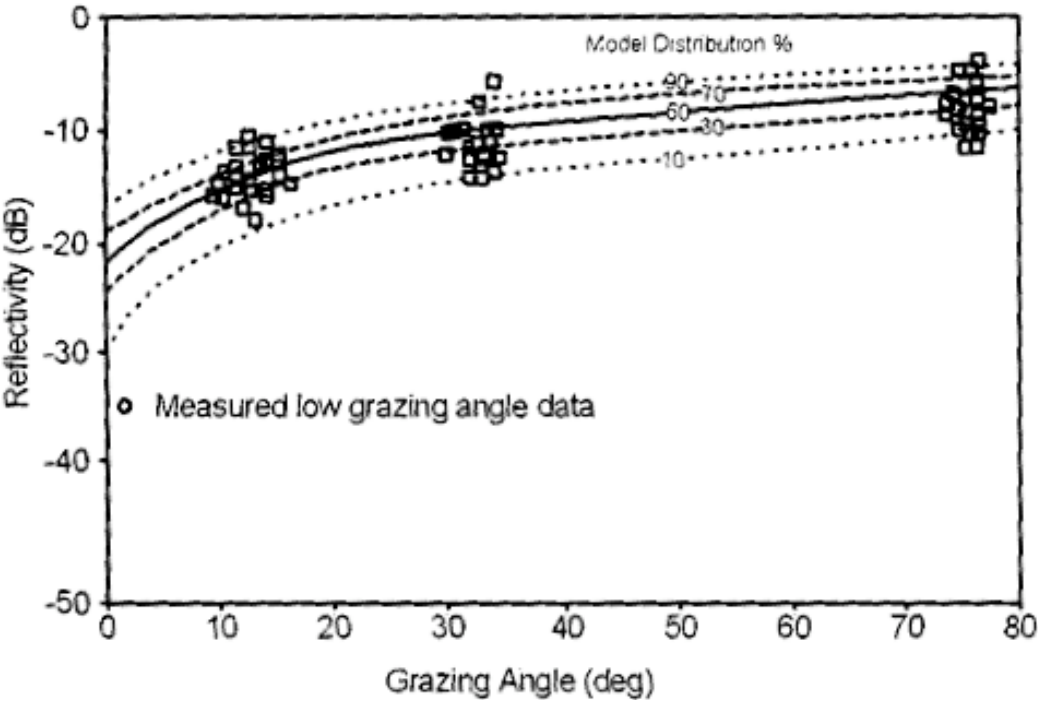

Figure 6.47: Model curves (based on work done at the Georgia Institute of Technology and measured data) (after Brooker [115]). These data suggest that $\sigma^0 = -20$ dB for grass at very low grazing angles (1° to 5°).

and several methods for correcting for signal errors, i.e. frequency drift and variation in the dc part of the signal. I found the appropriate data-sampling rates and extents for the purposes of the SAR test bench.

I wrote a computer program that synthesizes data which emulate the raw data collected from a typical homodyne FMCW radar, and I demonstrated that the modified RMA operates to give acceptable imagery (meeting specifications). I also tested the sensitivity of the image quality to radar position error and centre frequency drift and jitter. The centre frequency correction was shown to operate correctly, and sensible limits on the tolerable radar position error were found. The performance of the RMA and the data specification appear to be acceptable.

I demonstrated the connection between the ramp voltage noise and the degraded PSF for the PMYTO, which along with other considerations led to the selection of a DDS-based source for the test bench radar.

I constructed and automated a linear translation stage and heavy mount for the SAR system to allow easy data collection and to ensure accurate signal

phases respectively. A range of simple test images were formed that demonstrated that the system gives geometrically accurate and sensitive measurements.

The SAR test bench is intended to provide a platform for experiment and investigation. Further work on the apparatus is inherently part of its future. A more sturdy translation arrangement might reduce the two-dimensional phase errors degrading the SAR image PSF.

Chapter 7

Summary, Conclusions and Further Work

Introduction

The aim of the work reported in this thesis was to extend and improve the operation of homodyne dechirp on receive linearly frequency modulated radars without the need for significant hardware provision or modification.

The work is multi-themed: every chapter deals with a different problem, but the underlying theme of all the work is that appropriate parameter value selection and suitable signal processing techniques can be used to solve some of the problems in FMCW radar.

In the remainder of this chapter, I shall summarize the aims and results of the earlier chapters, drawing conclusions about the successfulness of the work and commenting on how the work might be carried on.

Chapter 3: Range Standoff Diagrams

In Chapter 3, I discussed the effect that phase errors have on the PSF and the significance of the choice of window weighting function. I then developed a simple technique for accurately and precisely calculating the effect of arbitrary phase errors on the PSF. This technique, referred to in this thesis as the Range Standoff diagram calculation, was demonstrated to work well for a number of different examples. Additionally, a simple technique for calculating an exact parametric representation of the PSF resulting from cosine-family window

weighted signals was found.

The simplicity of the Range Standoff diagrams suggests a trivial extension to predict the effect of amplitude modulation and also to predict the image phase. These remain to be demonstrated experimentally.

Chapter 4: Range autofocus

In Chapter 4, I developed a computational technique, based on two existing techniques, for measuring and compensating for chirp nonlinearity. This technique uses the ability of the PGA to estimate the phase error degrading a PSF and performs phase correction by resampling to linearize the phase ramps of dechirped signals. This allows the compensation for nonlinear chirps completely in software. This should be of great use where it is undesirable or impossible to provide hardware linearization.

Additionally, the technique provides a convenient method for chirp nonlinearity measurements to be made when the radar is operating in its normal fashion.

Because the technique is entirely software based and uses the PGA to estimate the defocussing phase errors, suitable archive data can be autofocussed retrospectively.

The technique was demonstrated for mildly and badly nonlinear-chirps and was shown to work well. The technique was also demonstrated retrospectively on an old (archive) data set and succeeded in significantly improving the quality of the PSF.

Future work might implement the generalization of the chirp error estimation stage discussed in Section 4.2.5 and the correction technique described by Meta [84].

Chapter 5: Down conversion

In Chapter 5, I developed and demonstrated a simple rule for finding suitable sampling rates for down conversion by subsampling. It was shown that, where suitable (i.e. reasonably narrowband) IF signals exist, significant reductions in the necessary signal sampling rate can be achieved. This technique was developed for an MTI application and demonstrated in software simulations and a practical experiment.

I also developed some simple rules for suitable specification of the MTI imaging parameters to achieve appropriate results. I showed that a detailed calculation of the properties of the Doppler shifted signals is approximated very well by the traditional calculation for most ordinary cases but that in extreme situations the exact expressions exist to provide a more accurate description of the signals.

Whilst this technique offers a method for reducing sampling rates without major hardware modification, it relies on the ability to band-pass filter the signal (if it isn't inherently narrowband). Further work could usefully be directed at developing software configurable band-pass filters.

Chapter 6: SAR test bench radar

In Chapter 6, I presented and discussed a wide range of topics related to the development of a test bench synthetic aperture radar.

The RMA, a standard SAR image processing algorithm, was modified to allow the smallest possible along-track signal extents to be used. Additionally, a correction was found for drifting centre frequency, persistent spurious IF signals, and IF noise. This correction was included in a pre-processing routine that also modified the homodyne FMCW radar IF signal so that it conforms to the RMA's signal model.

The construction of a simple radar translation stage was described, as was software to run the radar and the translation stage mechanism.

The centre frequency and phase noise stability of each radar source were investigated for the purposes of the SAR test bench, and a DDS-based system was selected. As part of this discussion, the control voltage noise and the resultant PSF degradation were connected for a PMYTO. This provides a useful and simple indication of the acceptable voltage control noise.

A data simulator was written to generate data on which to test the modified RMA SAR processor implementation. The processor was shown to work correctly. The simulated data was then used with varying degrees of frequency and radar position error to form test imagery. The frequency drift correction was seen to be able to correct a wide range of frequency errors, from a large slow drift to large random jittering. Provision was made in the software that runs the test bench to collect centre frequency data where possible. The simulated data was also used to investigate the sensitivity of the radar to random

position error. It was found that 0.2 mm in the line-of-sight direction and 0.5 mm perpendicular to this were acceptable for basic imaging purposes. The algorithm implementation performed correctly on the synthetic data.

The SAR test bench was used to image a series of test scenes, and the resulting imagery was measured and found mostly to meet the nominal performance specifications. The range response was found to be broadened slightly, but this is believed to be due to frequency response roll off in the frequency multiplication stage of the radar.

The sensitivity of the test bench was estimated and found to be acceptable, with the typical smallest detectable RCS being -45 dBsm.

References

[1] J. C. Wiltse. History of millimetre and sub-millimetre waves. *IEEE Transactions on microwave theory and techniques*, MTT-32(9):1118–1127, 1984.

[2] K. B. Cooper, N. Llombart, R. J. Dengler, and P. H. Siegel. Beam width robustness of a 670 GHz imaging radar. In *Electromagnetics in Advanced Applications, 2009. ICEAA '09. International Conference on*, pages 611–612, sep. 2009.

[3] E. Im, S. L. Durden, C. Wu, and T. R. Livermore. The 94-GHz cloud profiling radar for the CloudSat mission. In *IEEE Aerospace Conference, Big Sky, Montana, USA*, volume 4, pages 411803–411809, 2001.

[4] A. G. Stove, A. L. Hume, and C. J. Baker. Low probability of intercept radar strategies. *IEE Proc.-Radar Sonar Navig.*, 151(5), 2004.

[5] G. M. Brooker, R. Hennessey, C. Lobsey, M. Bishop, and E. Widzyk-Capehart. Seeing through dust and water vapor: Millimeter wave radar sensors for mining applications. *Journal of field robotics*, 24(7):527–557, July 2007.

[6] G. M. Brooker, S. Scheding, M. V. Bishop, and R. C. Hennessy. Development and application of millimeter wave radar sensors for underground mining. *Sensors Journal, IEEE*, 5(6):1270 – 1280, December 2005.

[7] M. E. Russell, A. Crain, A. Curran, R. A. Campbell, C. A. Drubin, and W. F. Miccioli. Millimeter-wave radar sensor for automotive intelligent cruise control (ICC). *Microwave Theory and Techniques, IEEE Transactions on*, 45(12):2444–2453, December 1997.

[8] J. Wenger. Automotive mm-wave radar: status and trends in system design and technology. In *Automotive Radar and Navigation Techniques, IEE Colloquium on*, pages 1/1 –1/7, London, UK, feb. 1998.

[9] G. Brooker. Understanding millimetre wave FMCW radar. In *Proc. 1st Int. Conf. on Sensing Technology*, pages 152–157, Palmerston, New Zealand, November 2005.

[10] D. G. Macfarlane and D. A. Robertson. Long range, high resolution 94 GHz FMCW imaging radar (AVTIS). In *Proc. Int. Conf. IRMMW-THz*, volume 1, pages 201–202, Karlsruhe, Germany, September 2005.

[11] A. G. Stove. Linear FMCW radar techniques. *Radar and Signal Processing, IEE Proc. F*, 139(5):343–346, October 1992.

[12] H. D. Griffiths. New ideas in FM radar. *Electronics and Communication Engineering Journal*, 2(5):185–194, October 1990.

[13] D. A. Robertson and D. G. MacFarlane. AVTIS: All-weather volcano topography imaging sensor. In *Infrared and Millimeter Waves, 2004 and 12th International Conference on Terahertz Electronics*, pages 813–814, September and October 2004.

[14] K. Van Caekenberghe, K. F. Vrakora, and K. Sarabandi. A 94 GHz OFDM frequency scanning radar for autonomous landing guidance. In *Proc. Radar Conference*, pages 248–253, April 2007.

[15] L. Q. Bui, D. Uecker, E. Loose, and Y. Alon. Test results of an experimental autonomous aircraft landing system utilizing a 94 GHz FM-CW imaging radar. In *IEEE MTT-S*, pages 857–860, 1993.

[16] F. Sadjadi, M. Helgeson, J. Radke, and G. Stein. Radar synthetic vision system for adverse weather aircraft landing. *IEEE Transactions on aerospace and electronic systems*, 35(1):2–14, January 1999.

[17] K. L. Koester and W. Vaillancourt. Talons 95 GHz radar sensor for autonomous landing guidance. In *Aerospace and Electronics Conference, 1992. NAECON 1992., Proceedings of the IEEE 1992 National*, pages 310–315, May 1992.

[18] A. Pagels, M. Hagelen, G. Briese, and A. Tessmann. Helicopter assisted landing system - millimeter-wave against brown-out. In *Proceedings of the German Microwave Conference*, pages 1–3, March 2009.

[19] M. Rangwala, J. Lee, and K. Sarabandi. Design of FMCW millitmeter-wave radar for helicopter assisted landing. In *Proc. Int. Conf. IGARSS Geoscience and remote sensing symposium*, pages 4183–4186, Barcelona, Spain, July 2007.

[20] A. Foessel, S. Chheda, and D. Apostolopoulos. Short-range millimeter-wave radar perception in a polar environment. In *Proceedings of the Field and Service Robotics Conference*, August 1999.

[21] C. A. Cardenas Mansilla, M. Jennett, K. Schunemann, and J. Winkelmann. Instruments and methods: Sub-ice topography in patriot hills, west antarctica: first resutls of a newly developed high-resolution FM-CW radar ssytem. *Journal of Glaciology*, 55(195):162–166, 2010.

[22] N. Galin, A. Worby, R. Massom, G. M. Brooker, C. Leuschen, S. P. Gogineni, and P. Jansen. 2–8 GHz FMCW radar for estimating snow depth on Antarctic sea ice. In *Int. Conf. Radar 2008*, Adelaide, Australia, September 2008.

[23] D. Klugmann. A compact 94-GHz FM-CW Doppler cloud radar using semiconductor devices for power generation. In *Geoscience and Remote Sensing Symposium, 2000. Proceedings. IGARSS 2000. IEEE 2000 International*, volume 5, pages 1801–1803, 2000.

[24] E. N. Grossman and A. J. Miller. Active millimeter-wave imaging for concealed weapons detection. In *Passive Millimeter-Wave Imaging Technology VI and Radar Sensor Technology VII*, volume 49, pages 1581–592, Orlando, FL, USA, 2003. SPIE.

[25] S. Stanko, D. Notel, A. Wahlen, J. Huck, F. Kloppel, R. Sommer, M. Hagelen, and H. Essen. Active and passive mm-wave imaging for concealed weapon detection and surveillance. In *Infrared, Millimeter and Terahertz Waves, 2008. IRMMW-THz 2008. 33rd International Conference on*, pages 1–2, September 2008.

[26] R. Appleby and H. B. Wallace. Standoff detection of weapons and contraband in the 100 GHz to 1 THz region. *IEEE Trans. on Antennas and Propagation*, 55(1):2944–2956, 2007.

[27] T. W. du Bosque, J. M. Lopez-Alonzo, and G. D. Boreman. Millimetre wave imaging system for land mine detection. *Applied Optics*, 45(22):5686–5692, August 2006.

[28] H.H. Meinel. Millimeter-wave technology advances since 1985 and future trends. *Microwave Theory and Techniques, IEEE Transactions on*, 39(5):759–767, May 1991.

[29] H. D. Griffiths. Radar imaging for combatting terrorism, 2006.

[30] R. Mende and H. Rohling. New automotive applications for smart radar sytems. Technical report, Smart Microwave Sensors, 2007.

[31] I. Gresham, N. Jain, T. Budka, A. Alexanian, N. Kinayman, B. Ziegner, S. Brown, and P. Staecker. A compact manufacturable 76–77 GHz radar module for commercial ACC applications. *IEEE Trans. MTT*, 49(1):44–58, 2001.

[32] M. Schneider. Automotive radar – status and trends. In *German Microwave Conference*, Ulm, Germany, 2005.

[33] M. J. Basten. Low cost implementation of an acc automotive radar. In *MM-Wave Products and Technologies, 2006. The Institution of Engineering and Technology Seminar on*, pages 1–6, November 2006.

[34] M. G. Walden. Development of millimetre-wave radar products. In *MM-Wave Products and Technologies, 2006. The Institution of Engineering and Technology Seminar on*, pages 81–86, nov. 2006.

[35] W. H. Haydl, M. Neumann, L. Venveyen, A. Bangert, S. Kudszus, M. Schlechtweg, A. Hulsmann, A. Tessmann, W. Reinert, and T. Krems. Single-chip coplanar 94-GHz FMCW radar sensors. *Microwave and Guided Wave Letters, IEEE*, 9(2):73–75, February 1999.

[36] M. Caniade, D. Domnesque, P. F. Alleame, A. Mallet, D. Pons, and H. Dambkes. Full MMIC millimeter-wave front end for a 76.5 GHz

adaptive cruise control car radar. In *IEEE MTT-S International Microwave Symposium Digest*, volume 4, pages 1489–1492, Anaheim, CA, USA, June 1999.

[37] G. Wadge, D. G. Macfarlane, D. A Robertson, A. J. Hale, H. Pinkerton, R. V. Burrell, G. E. Norton, and M. R. James. AVTIS: A novel millimetre-wave ground based instrument for volcano remote sensing. *Journal of Volcanology and geothermal research*, 146(4):307–318, 2005.

[38] D. A. Robertson and D. G. MacFarlane. A 94 GHz dual-mode imaging "radarometer" for remote sensing. In *SPIE Defense and Security Symposium*, Orlando, USA, April 2006.

[39] D. G. MacFarlane and D. A. Robertson. A 94 GHz dual-mode active/passive imager for remote sensing. In *SPIE Europe*, Orlando, FL, USA, April 2006.

[40] P. D. L. Beasley, G. Binns, R. D. Hodges, and R. J. Badley. Tarsier, a millimetre wave radar for airport runway debris detection. In *EURAD*, pages 261–264, 2004.

[41] P. D. L. Beasley. Advances in millimetre wave FMCW radar. In *MRRS Symposium*, pages 246–249, Kiev, Ukraine, September 2008.

[42] F. Perez-Marinez, M. Burgos-Garcia, and A. Asensio-Lopez. Group delay effects on the performance of wideband CW–LFM radars. *IEE Proc.-Radar Sonar Navig.*, 148(2):95–100, April 2001.

[43] J. R. Klauder, A. C. Price, S. Darlington, and W. J. Albersheim. The theroy and design of chirp radars. *The Bell Systems Technical Journal*, xxxix(4):745–808, 1960.

[44] N. M. Blackman and G. A. McAlpine. The spectrum of a high-index FM waveform: Woodward's theorem revisited. *IEEE Trans. Commumication Technology*, Com-17(2):201–209, April 1969.

[45] N. D. Wallace. Performance prediction method for a class of FM-CW radars. *IEEE Transactions on aerospace and navigational systems*, ANE:36–44, March 1963.

[46] S. O. Piper. Homodyne FMCW radar range resolution effects with sinusoidal nonlinearities in the frequency sweep. In *Proc. IEEE Int. Radar Conf.*, 1995.

[47] A. Scheiblhofer, S. Schuster, and A. Stelzer. Effects of systematic FMCW radar sweep nonlinearity on bias and variance of target range estimation. In *IEEE MTT-S International Microwave Symposium Digest*, pages 1418–1421, 2006.

[48] M. Pichler, A. Stelzer, P. Gulden, and M. Vossiek. Influence of systematic frequency-sweep non-linearity on object distance estimation in FMCW/FSCW radar systems. In *Proc. 33rd European Radar Conf.*, pages 1203–1206, 2003.

[49] N. Levanon and E. Mozeson. *Radar Signals*. Wiley, 2004.

[50] P. J. Burke. Ultra-linear chirp generation via VCO tuning predistortion. In *Proc. IEEE MTT-S*, 1994.

[51] M. J. Withers. Method of measuring the phase errors in linear frequncy-modulated and pulse compression radar systems. *Electronics letters*, 2(2):50–51, February 1966.

[52] K. S. Kulpa, A. Wojtkiewicz, M. Nalecz, and J. Misiurewicz. The simple analysis method of nonlinear frequency distortions in FMCW radar. In *13th Microwaves, Radar and Wireless Communications Conference*, volume 1, pages 26–29, Wroclaw, 20000.

[53] J. Yang, X. Yang, Y. Ding, and S. Huang. High-resolution 35 GHz coherent LFM-CW radar for two-dimensional imaging. *Journal of electronics*, 14(2):148–153, April 1997.

[54] J. Fuchs, K. D. Ward, and M. P. Tulinand R. A. York. Simple techniques to correct for VCO nonlinearities in short range FMCW radars. In *Proc. IEEE MTT-S*, 1996.

[55] W. J. Caputi. Stabilized linear FM generator. *IEEE Transactions on aerospace and electronic systems*, AES-9(5):670–678, September 1973.

[56] M. Christmann, M. Vossiek, M. Smith, and G. Rodet. SAW based delay locked loop concept for VCO linearization in FMCW radar sensors. In

Microwave Conference, 2003. 33rd European, volume 3, pages 1135–1138, Munich, Germany, Oct. 2003.

[57] H. Ruser and V. Magori. Sweeep linearization of a microwave FMCW doppler sensor by an ultrasonic reference. In *Proc. IEEE Frequency Control Symp.*, Orlando, USA, 1997.

[58] M. Vossiek, P. Heide, M. Nalezinzki, and V. Magori. Novel FMCW radar system concept with adaptive compensation of phase errors. In *Proc. 26th EuMC*, Prague, Czech Republic, September 1996.

[59] Coherent frequency modulated continuous wave radar. World Patent WO 2006/103391 A1, 2000.

[60] C. V. Jakowatz et al. *Spotlight-mode synthetic aperture radar: a signal processing approach*. Kluwer Academic, 1996.

[61] C. G. Newhall and W. G. Melson. Explosive activity associated with the growth of volcanic domes. *Journal of Volcanology and Geothermal Research*, 17(1–4):111–131, September 1983.

[62] M. Hort and R. Seyfreid. Volcanic eruption velocities measured with a micro radar. *Geophysical Research Letters*, 25(1):113–116, January 1998.

[63] R. Seyfried and M. Hort. Continuous monitoring of volcanic eruption dynamics: a review of various techniques and new results from a frequency-modulated radar doppler system. *Bulletin of Volcanology*, 60:627–639, 1999.

[64] X Xu and R. M. Narayanan. FOPEN SAR imaging using UWB step-frequency and random noise waveforms. *Aerospace and Electronic Systems, IEEE Transactions on*, 37(4):1287 –1300, October 2001.

[65] H. Schimpf, H. Essen, and S. Boehmsdorff. MEMPHIS – a fully polarimetric experimental radar. In *IEEE Geoscience and remote sensing symposium IGARSS*, pages 1714–1716, June 2002.

[66] C. Zaugg and D. G. Long. Theory and application of motion compensation for LFM-CW SAR. *IEEE Transactions on geoscience and remote sensing*, 46(10):2990–2998, October 2008.

[67] W. G. Carrara et al. *Spotlight synthetic aperture radar radar*. Artech House, 1995.

[68] L. M. H. Ulander, H. Hellsten, and G. Stenstrom. Synthetic-aperture radar processing using fast factorized back-projection. *Aerospace and Electronic Systems, IEEE Transactions on*, 39(3):760 – 776, July 2003.

[69] A. Meta, P. Hoogeboom, and L. P. Ligthart. Signal processing for FMCW SAR. *IEEE Transactions on geoscience and remote sensing*, 45(11):3519–3532, November 2007.

[70] D. R. Bolton, P. A. S. Cruikshank, D. A. Robertson, and G. M. Smith. Sub-nanosecond coherent pulse generation at millimetre-wave frequencies. *Electronics letters*, 43(6), 2007.

[71] E. A. Uliana, B. S. Yaplee, N. C. Chu, and M. H. Newkirk. 95-GHz short pulse radar. *IEEE Transactions on geoscience and remote sensing*, 28(4):729–731, July 1990.

[72] F. J. Harris. On the use of windows for harmonic analysis with the discrete Fourier transform. *Proc. IEEE*, 66(1):51–83, 1978.

[73] K. S. Kulpa and A. Wojtkiewicz. Use of polynomial phase modeling to FMCW radar. In *RTO MP-070*, Warsaw, Poland, April 2001.

[74] W. Chen, S. Xu, D. Wang, and F. Liu. Range performance analysis in linear FMCW radar. In *2nd International Conference on Microwave and Milllimetre wave technology proceedings*, pages 654–657, 2000.

[75] P. D. L. Beasley, A. G. Stove, B. J. Reits, and B-O As. Solving the problems of a single antenna frequency modulated CW radar. *IEEE interrnational radar conference*, pages 391–395, 1990.

[76] D. A. Robertson, R. J. C. Middleton, and D. G. Macfarlane. A 94 GHz FMCW instrumentation radar. In *IRMMW-THz*, pages 919–921, Cardif, Wales, September 2007.

[77] L. A. Hoffman, K. H. Hurlbut, D. E. Kind, and H. J. Wintroub. A 94 GHz radar for space object identification. *IEEE Trans. MTT*, 17(12):1145–1149, 1969.

[78] R. J. C. Middleton and D. A. Robertson. Predicting range point response from chirp nonlinearity. In *Int. Radar Conf.*, pages 128–132, Adelaide, Australia, September 2008.

[79] S. Scheiblhofer, S. Schuster, and A. Stelzer. High speed FMCW radar frequency synthesizer with DDS based linearization. *IEEE Microwave and wireless components letters*, 17(5):3897–399, May 2007.

[80] C. Wagner, A. Stelzer, and H Jager. PLL architecture for 77-GHz FMCW radar systems with highly-linear ultra-wideband frequency sweeps. In *Proc. IEEE MTT-S*, pages 399–402, San Fransisco, USA, 2006.

[81] T. Musch, I Rolfes, and B. Schiek. Fractional divider conepts with phase-lock-crontrol for the generation of precise linear fequency ramps. In *28th European Microwave Conf.*, volume 1, pages 451–456, 1998.

[82] D. E. Wahl, P. H. Eichel, D. C. Ghiglia, and C. V. Jakowatz Jnr. Phase gradient autofocus – a robust tool for high resolution sar phase correction. *IEEE Transactions on aerospace and electronic systems*, 30(3):827–835, July 1994.

[83] P. H. Eichel. and C. V. Jakowatz Jnr. Phase-gradient algorithm as an optimal estimator of the phase derivative. *Optics Letters*, 14(20):1101–1103, October 1989.

[84] A. Meta, P. Hoogeboom, and L. P. Ligthart. Range non-linearities correction in FMCW SAR. *IEEE IGARS Int. Conf.*, pages 403–406, 2006.

[85] D. A. Robertson and D. G. Macfarlane. A 94 GHz real aperture 3D imaging radar. In *Proc. EuRAD*, pages 154–157, Manchester, England, 2006.

[86] R. G. Strauch. *Theory and application of the FM-CW Doppler Radar*. PhD thesis, University of Colorado, Colorado, USA, 1976.

[87] D.G. Macfarlane and D.A. Robertson. SAFIRE: A close range real time millimetre wave radar for public education. In *Infrared and Millimeter Waves, 2007 and the 2007 15th International Conference on Terahertz Electronics. IRMMW-THz. Joint 32nd International Conference on*, pages 924–925, sep. 2007.

[88] D. Klugmann and R. Stephan. Calibration of portable FM-CW doppler radar profilers with an artificial target. In *Geoscience and Remote Sensing Symposium, 2004. IGARSS '04. Proceedings. 2004 IEEE International*, volume 6, pages 3953 – 3955 vol.6, sep. 2004.

[89] A. R. Brenner and J. H. G. Ender. Demonstration of advanced reconnaissance techniques with the airborne SAR/GMTI sensor PAMIR. *IEE Proc.-Radar Sonar Navig.*, pages 152–162, April 2006.

[90] M. Jahangir, D. Coe, A. P. Blake, P. G. Kealey, and C. P. Moate. PodSAR: A versatile real-time SAR GMTI surveillance and targetting system. In *Proc. IEEE Radar Conference*, pages 1–6, Rome, Italy, May 2008.

[91] W. J. Miceli and L. A. Gross. Test results from the AN/APY-6 SAR/GMTI surveillance, tracking and targeting radar. In *Proc. IEEE Radar Conference*, pages 13–17, Atlanta, Ga, USA, May 2001.

[92] A. D. Nichols, J. W. Wilhelm, T. W. Gaffield, D. R. Inkster, and S. K. Leung. A SAR for real-time ice reconaissance. *IEEE TransGeoscience and remote sensing*, 24(3):383–389, January 1986.

[93] R. M. Goldstein, H. A. Zebker, and T. P. Barnett. Remote sensing of ocean currents. *Science*, 246(4935):1282–1285, December 1989.

[94] J. A. Rodenas and R. Garello. Wavelet analysis in SAR ocean image profiles for internal wave detection and wavelength estimation. *IEEE Trans. Geoscience and remote sensing*, 35(4):933–945, July 1997.

[95] O. M. Johannessen, H. A Espeda, A. D. Jenkins, J. Knulst, T. Hamre, and S. Sandven. SAR surveillance of ocean sufrace slicks. In *ERS Applictions Proceedings of the 2nd international workshop*, London, 1996.

[96] T. Le Toan, F. Ribbes, W. Li-Fang, N. Floury, D. Kung-Hau, K. Jin Au, M. Fujita, and T. Kurosi. Rice crop mapping and monitoring using ERS-1 data based on experiment and modeling results. *IEEE Trans. Geoscience and remote sensing*, 35(1):41–56, Jan 1997.

[97] H. M. Galy and R. A. Sanders. Using SAR imagery for flood modelling. In *Proceedings of RGS-IBG Annual Conference*, 2000.

[98] N. Marechal. Tomographic formulation of interferometric sar for terrain elecation mapping. *IEEE Trans. Geoscience and remote sensing*, 33(3):726–739, May 1995.

[99] J. E. S. Fransson, F. Walter, and L. M. H. Ulander. Estimation of forest parameters using CARABAS-II VHF SAR data. *Geoscience and Remote Sensing, IEEE Transactions on*, 38(2):720 –727, March 2000.

[100] A. Burini, C. Putignano, F. Del Frate, M. Lazzarini, G. Licciardi, G. Schiavon, D. Solimini, F. De Biasi, and P. Manunta. TerraSAR-X Imaging for Unsepervised Land Cover Classification and Fire Mapping. In *Geoscience and Remote Sensing Symposium, 2008. IGARSS 2008. IEEE International*, volume 3, pages 660–663, July 2008.

[101] H. Essen, H.H. Fuchs, and A. Pagels. High resolution millimetrewave SAR for the remote sensing of wave patterns. In *IEEE Geoscience and remote sensing symposium*, pages 963–966, Barcelona, Spain, July 2007.

[102] G. Nico, D. Leva, J. Fortuny-Gausch, G. Antonello, and D Tarchi. Generation of digital trrain models with a ground-based SAR system. *IEEE Trans. Geoscience and remote sensing*, 43(1):45, January 2005.

[103] H. Essen, M. Brautigam, R. Sommer, A. Wahlen, W. Hohannes, J. Wilcke, M Schlechtweg, and A. Tessmann. SUMATRA, a W-band SAR for UAV application. In *Surveillance for a safer world*, pages 1–4, Bordeaux, France, October 2009.

[104] M. Albuquerque et al. Applications of time-domain back-projection SAR processing in the airborne case. In *7th European Conference on Synthetic Aperture Radar*, Friedrichshafen, Germany, June 2008.

[105] A. J. Hunter, M. P. Hayes, and P. T. Gough. A comparison of fast factorised back projection and wavenumber algorithms for sas image reconstruction. *IGARSS*, 2008.

[106] N. E. Doren, C. V. Jakowatz Jnr, D. E. Wahl, and P. A. Thompson. General formulation for wavefront curvature correction in polar-formatted spotlight-mode SAR images using space-variant post-filtering. In *Proc. Int. Conf. Image Processing*, 1997.

[107] C. Cafforio, C. Prati, and F. Rocca. SAR data focussing using seismic migration techniques. *IEEE Transactions on aerospace and electronic systems*, 27(2):194207, 1991.

[108] W. P. Robins. *Phase noise in signal sources*. Peter Peregrinus (for the IEE), 1984.

[109] H. T. Nicholas and H. Samueli. An analysis of the output spectrum of direct digital frequency synthesizers in the presence of phase-accumulator truncation. In *41st Annual Frequency Control Symposium*, pages 494–502, 1987.

[110] A. Torosyan and A.N. Willson. Exact analysis of DDS spurs and SNR due to phase truncation and arbitrary phase-to-amplitude errors. In *Proc. IEEE Int. Conf. Frequency Control Symposium*, August 2005.

[111] Jordi Figueras i Ventura and Herman Russchenberg. Improvement of the performance of FM-CW radar systems by using direct digital synthesizers: Comparison with voltage controlled oscillators. In *Radar Symposium, 2006. IRS 2006. International*, pages 1–4, May 2006.

[112] M. M. Abousetta and D. C. Cooper. Noise analysis of digitized FMCW radar waveforms. *IEE Proc.-Radar Sonar Navig.*, 145(4):209–215, August 1998.

[113] J. L. Jimenez, J. Gismero, D. Ramirez, and J. M. Pardo. Large time-bandwidth product DDS chirp waveform generator for high resolution radars. In *Radar 2004 – International conference on radar systems*, Toulouse, France, 2004.

[114] N. C. Currie, R. D. Hayes, and R. N. Trebits. *Millimeter-wave radar clutter*. Artech House, 1992.

[115] G. Brooker. *Introduction to sensors for ranging and imaging*. SciTech, 2009.